

Luminescent Single and Dual Sensors for *In Vivo* Imaging of pH and pO₂

**Dissertation zur Erlangung des Doktorgrades der Naturwissenschaften
(Dr. rer. nat.)
an der Fakultät für Chemie und Pharmazie der Universität Regensburg**



vorgelegt von

Robert Johannes Meier

Regensburg, Mai 2011

Luminescent Single and Dual Sensors for *In Vivo* Imaging of pH and pO₂

Doctoral Thesis

By

Robert Johannes Meier

Submitted to

Faculty of Chemistry and Pharmacy

University of Regensburg

June 2011

Diese Doktorarbeit entstand im Zeitraum von Oktober 2007 bis Mai 2011 am Institut für Analytische Chemie, Chemo- und Biosensorik der Universität Regensburg

Die Arbeit wurde angeleitet und begleitet von Prof. Dr. Otto S. Wolfbeis

Promotionsgesuch eingereicht am:

Juni 2011

Kolloquiumstermin:

7. Juli 2011

Prüfungsausschuß:

Vorsitzender:

Prof. Dr. F.-M. Matysik

Erstgutachter:

Prof. Dr. O. S. Wolfbeis

Zweitgutachter:

Prof. Dr. J. Wegener

Drittprüfer:

Prof. Dr. J. Heilmann

Danksagung

Mein ganz besonderer Dank gilt meinem Doktorvater Herrn **Prof. Dr. Otto S. Wolfbeis** für die Bereitstellung des äußerst interessanten Themas, die intensiven wissenschaftlichen als auch nicht wissenschaftlichen Diskussionen, die sehr guten Arbeitsbedingungen am Lehrstuhl, sowie für die hervorragende Betreuung meiner Arbeit.

Dr. Stephan Schreml möchte ich für die für die exzellente wissenschaftliche Zusammenarbeit, die äußerst fruchtbaren Diskussionen, die sogar nachts oder am Wochenende stattfanden, als auch für seine unermüdliche Begeisterungsfähigkeit danken.

Der nächste Dank muss in englischer Sprache erfolgen: Thank you so much my brothers „**James**“ **Xu-Dong Wang** and „**Sayed**“ **El Sayed Saleh**. You guys really made the university a better place for me. Also thanks for the scientific discussions and the collaboration.

Ein weiterer Dank gilt Herrn **Dr. Philipp Babilas** der das gemeinsame DFG Projekt von Klinikums Seite aus ins Rollen gebracht und sehr gut betreut hat betreut hat.

Danke noch an meine Projektpartner von der Dermatologie, **Dr. Stephan Schreml** und **Dr. Philipp Babilas**, für Patientenrekrutierung und die Hilfe bei der Durchführung sowie die Interpretation der *in vivo* Messungen.

Danke an die **Deutsche Forschungsgemeinschaft** für die finanzielle Unterstützung.

Dr. Stefan Nagl und **Dr. Matthias Stich** möchte ich für die Einführung in die große Welt der Imaging-Technologien danken.

Danke an alle Freiwilligen, Freunde und Kollegen die als Testpersonen für die Strippingmessungen herhalten mussten.

Außerdem danke ich allen Mitarbeitern des Lehrstuhls für die ausgezeichnete kollegiale Arbeitsatmosphäre, die Hilfestellungen und fortwährende Unterstützung, die zur Vollendung der Dissertation beigetragen haben. Speziell genannt werden müssen hierbei **Sabine Rudloff** und **Edeltraud Schmid** sowie den technischen Angestellten **Gisela Hierlmeier** und **Barbara Goricnik**.

Danke Liebe Kaffeerrunde, dass ihr meine Sprüche ertragen habt.

Ein spezieller Dank geht noch an meine Kollegen **Dr. Mark-Steven Steiner**, **Dominik Grögl**, **Lorenz Fischer**, **Judith Stolwijk**, **Dr. Petra Schremkhammer**, **Dr. Doris Burger** und **Daniela Achatz** für die zahllosen geführten wissenschaftlichen und nicht wissenschaftlichen Diskussionen.

Danke an **Raphaela Liebherr**, **Dagmar Flittner** und **Sven Kochmann** für die unterstützende Arbeit während ihrer Diplom-, Bachelor- oder Forschungspraktika-Arbeiten

Und danke an meine Freundin, dass sie mir in der ganzen Zeit den Rücken frei gehalten und mich immer unterstützt hat.

Diese Arbeit ist meiner Familie gewidmet.

Table of contents

1. Introduction

1.1	Motivation	1
1.2	Standard techniques for oxygen and pH	3
1.2.1	The Clark electrode	3
1.2.2	pH electrode	5
1.2.3	Electrodes vs. optical sensing and imaging	6
1.3	State of the art in optical imaging of pO₂, pH, and dual pO₂/pH	8
1.3.1	pO ₂ sensors	8
1.3.2	pH sensors	11
1.3.3	Dual sensors for pO ₂ and pH	13
1.4	Methods for referenced imaging	15
1.4.1	Fluorescence ratiometric imaging (FRIM)	16
1.4.2	Luminescence (Fluorescence) lifetime imaging (FLIM or LLI)	17
1.4.3	Time domain Dual lifetime referencing (tdDLR)	20
1.5	References	21

2. Instruments and Methods

2.1	pH meter	32
2.2	Knife coating devices for sensor fabrication	32
2.3	Spectrometers	34
2.3.1	Absorbance measurements	34
2.3.2	Fluorescence spectrometer	34
2.4	Calibration chamber	35
2.5	Time-gated imaging setup	36
2.6	RGB imaging setup	37
2.7	References	38

3. 2D luminescence imaging of pH *in vivo*

3.1	Introduction	39
3.2	Results and Discussion	42
3.2.1	Luminescence imaging of pH	42
3.2.2	Material design	45
3.2.3	<i>In vitro</i> characterization	49
3.2.4	Biocompatibility	52
3.2.5	<i>In vivo</i> validation	56
3.2.6	Luminescence imaging of pH in cutaneous wound healing.....	57
3.3	Materials and methods	61
3.3.1	Microparticle preparation.....	61
3.3.2	Preparation of sensor foils	61
3.3.3	Time response, spectra and photostability	62
3.3.4	Luminescence measurement and calibration	62
3.3.5	Dye leaching and particle leakage	63
3.3.6	Cytotoxicity.....	64
3.3.7	Cellular uptake.....	65
3.3.8	Singlet oxygen detection	66
3.3.9	Study subjects	66
3.3.10	<i>In vivo</i> luminescence imaging	67
3.3.11	Statistics	68
3.4	Conclusion	68
3.5	Additional studies using the pH sensor	69
3.6	References	70

4. 2D luminescent pO₂ sensor for *in vivo* imaging in physiological wound oxygenation

4.1	Introduction	73
4.2	Results and Discussion	75

4.2.1	Material design and <i>in vitro</i> characterization	75
4.2.2	Biocompatibility	81
4.2.3	<i>In vivo</i> imaging of wound healing.....	82
4.2.4	<i>In vivo</i> imaging of skin during stratum corneum removal.....	84
4.3	Materials and Methods.....	85
4.3.1	Microparticle preparation.....	85
4.3.2	Preparation of the sensor foils	86
4.3.3	Luminescence imaging of pO ₂ and calibrations	86
4.3.4	Cytotoxicity	87
4.3.5	<i>In vivo</i> luminescence imaging	87
4.3.6	Study participants	88
4.3.7	Assessment of the pO ₂ on wound surface.....	88
4.3.8	Measurement of the epidermal oxygen barrier pO ₂	88
4.3.9	Statistics	89
4.4	Conclusion	89
4.5	References	90

5. Dual sensor for pO₂ and pH *in vivo* using a time-gated approach

5.1	Introduction.....	93
5.2	Results and Discussion.....	95
5.2.1	General sensor concept.....	95
5.2.2	Signal separation	96
5.2.3	<i>In vitro</i> characterization	97
5.2.4	Imaging of a skin graft donor site	100
5.2.5	Imaging of chronic ulcers	101
5.3	Materials and methods	104
5.3.1	Microparticle preparation.....	104
5.3.2	Preparation of sensor foils	104
5.3.3	Luminescence imaging of pH/pO ₂ and calibrations.....	104
5.3.4	Study participants	105
5.3.5	<i>In vivo</i> luminescence imaging.....	106
5.4	Conclusion	106

5.5	References	106
-----	------------------	-----

6. Ratiometric RGB imaging

6.1	Photographing oxygen distribution	109
6.1.1	Introduction	109
6.1.2	Results and discussion	110
6.1.3	Methods and materials.....	117
6.1.4	Discussion	118
6.2	Absorbance- and emission-based RGB imaging of CO ₂	119
6.2.1	Imaging of CO ₂	119
6.2.2	Methods and materials	123
6.3	RGB imaging of pH	125
6.3.1	Material design.....	125
6.3.2	Materials and methods	127
6.4	References	128

7. Dual RGB imaging of oxygen and pH in vivo

7.1	Introduction.....	132
7.2	Main text	133
7.2.1	RGB dual imaging and material design.....	134
7.2.2	Cytotoxicity	142
7.2.3	<i>In vitro</i> characterization	147
7.2.4	<i>In vivo</i> imaging	150
7.3	Materials and Methods.....	153
7.3.1	Microparticle preparation.....	153
7.3.2	Preparation of the sensor foils	154
7.3.3	Imaging and data processing	154
7.3.4	Dye leaching and particle leaching.....	155
7.3.5	Cytotoxicity	156
7.3.6	Cellular uptake.....	157
7.3.7	Singlet oxygen detection	157

7.3.8	<i>In vitro</i> sensor characterization	158
7.3.9	Study on human subjects	159
7.3.10	Sensor application <i>in vivo</i>	159
7.3.11	Statistics	160
7.4	Conclusion	160
7.5	References	161
<hr/>		
8.	Summary	162
<hr/>		
9.	Zusammenfassung	164
<hr/>		
10.	Curriculum Vitae	167
<hr/>		
11.	List of Publications and Presentations	
<hr/>		
	Diploma thesis	169
	Papers	169
	Abstracts and Posters	171
<hr/>		
12.	Appendix	
<hr/>		
12.1	Partial pressure – a conversion table for oxygen	172
12.2	Source code for the ImageJ RGB macro	173
12.3	Video stills	173

1. Introduction

1.1 Motivation

Interdisciplinarity is the idea of a unified science, general knowledge, synthesis and the integration of knowledge¹. Chemistry and its interdisciplinary applications are in close alliance during the last centuries. Applied chemistry and applied natural sciences in general determine our everyday life. The impact on our lives ranges from basic things like CO₂ in sparkling water, soap for washing, or road salt for iced streets, to very sophisticated modern techniques for instance quantum physics based techniques such as semiconductor transistors for computers, LEDs for electric lighting or TV sets, or optical sensors. The transfer of a technique from the lab bench to its application is a most important as well as a very fascinating process for human scientific progress.

Since the middle of the 1990s extensive research on development of optical sensing and imaging techniques has been performed at the Institute of Analytical Chemistry, Chemo-, and Biosensors at the University of Regensburg. Sensors for determination of pO₂, pH, Ions, CO₂ and various biological species as well as multi-analyte sensors have been realized²⁻⁵. Further, various new techniques for sensing and imaging have been developed⁶⁻⁸. Continuing this research, the aim of this thesis was to develop new luminescent *in vivo* sensors and imaging techniques for clinical application.

pH (Latin: *pondus hydrogenii*) and pO₂ (oxygen partial pressure) are parameters of great interest especially in biosciences. They can act as diagnostic or surrogate parameters in surgery or can further understanding of physiological and biological processes. Although, more and more physiological processes are unveiled during the last decades and centuries, there are still many fundamental human disease patterns whose processes suffer from a lack of understanding. An important group of these disease patterns are chronic wounds and skin defects.

Chronic wounds are defined as wounds that show no tendency in healing after 4 to 8 weeks⁹. Most chronic wounds are cutaneous ulcers at the lower extremities of patients. They are chiefly caused by chronic venous insufficiency, arterial occlusive

disease, microangiopathies (such as diabetes mellitus), or vasculitis¹⁰. Chronic wounds are highly resistant to therapy and require long-term treatment. Approximately 1% of Europe's population suffers from chronic wounds. Besides the impact on the quality of life, chronic wounds are a fundamental economic burden with nearly 2% of the total health care budget being spent on chronic wound treatment^{11,12}. In North America, even one-third of the total dermatological budget is spent on this issue. This exceeds the money that is spent for all melanoma and other types of skin cancer combined¹³.

Cutaneous wound healing is basically divided into three major phases which overlap during healing¹⁴:

- (i) initial inflammatory phase (cytokines, chemokines, etc.)
- (ii) proliferative phase (neoangiogenesis, fibroblast proliferation, reepithelialization)
- (iii) final tissue remodeling phase (extracellular matrix reorganization)

Chronic wounds remain often in a sustained inflammatory phase¹⁵.

The parameters of pH and pO₂ play an essential role in healing of wounds^{11,15,16}. For example, the wound fluid¹⁷ and its varying pH are known to greatly affect healing¹⁴: pH affects the epidermal barrier self-regulation and stratum corneum integrity¹⁸, alters the activity and conformations of proteinases during the tissue remodeling phase¹⁹. Low pH levels limit the cell proliferation²⁰ and elevated pH values tend to higher risks of bacterial infections and thus the formation of chronic wounds^{15,21}. Oxygen plays an immense role in wound repair, too²²: generally, hypoxia largely impairs wound healing²³, oxygen converted to reactive oxygen species (ROS) via neutrophils regulates bactericidal defense against wound pathogenesis²⁴, further, oxygen is needed for regulation of collagen synthesis²⁵, angiogenesis²⁶, and reepithelization²⁷. Although, there are numerous publications on the molecular and cellular events during cutaneous wound healing²⁸ the basic clinical parameters like pO₂ and pH are not completely unveiled in this context.

The aim of this work was to develop optical *in vivo* sensors for imaging of pH and pO₂ during physiological wound healing and in chronic wounds. Further, novel sensors for simultaneous imaging of pH/pO₂ using optical dual sensors were developed. These

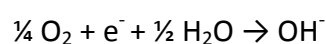
sensors were implemented in clinical studies on dermatological problems in cooperation with the Institute of Dermatology at the University Hospital of Regensburg.

1.2 Standard techniques for oxygen and pH

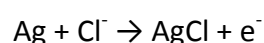
1.2.1 The Clark electrode

Oxygen is one of the most fundamental species for life on earth. Numerous different techniques for determination of oxygen were invented during the last century. Among those were mass spectrometric, gas chromatographic, paramagnetic methods and solid state electrodes^{29,30} that were only suitable for measuring oxygen in the gas phase. Dissolved oxygen (e.g. in natural waters), mostly is determined by Winkler-Titration³¹ or via colorimetric methods³², that, unfortunately, were limited to discontinuous measurements and thus prohibit on-line monitoring. Nowadays, amperometric sensors³³⁻³⁵ were most frequently used for continuous as well as discontinuous determinations of dissolved oxygen. In principle, those sensors are based on the electrochemical reduction of oxygen at a polarized electrode. An electric current is generated, that is proportional to the pO_2 in the sample. Different types of amperometric electrodes are available. Membrane coated electrodes such as the Clark electrode^{33,36} more and more supersede plain electrodes³⁴.

The Clark electrode (**Fig. 1.1**) is a two electrode system consisting of a platinum, gold or silver working electrode (cathode) and a reference electrode (silver; anode). Both electrodes are submersed by a neutral or basic electrolyte solution (mostly KCl). The electrodes are covered by an oxygen permeable membrane made of Teflon® or silicone that separates the electrodes from the test solution. Oxygen diffuses through the membrane into the electrolyte solution and is reduced at the Pt cathode:



The anode reaction is:



If the electrodes are polarized with a potential between -0.6 and -0.8 V, the electric current is proportional to the oxygen partial pressure. The Clark electrodes are widely used due to their simple and straightforward design. They offer a linear dynamic range over several orders of magnitude, have limits of detection (LODs) in the lower ppm range, and often single point calibrations are sufficient.

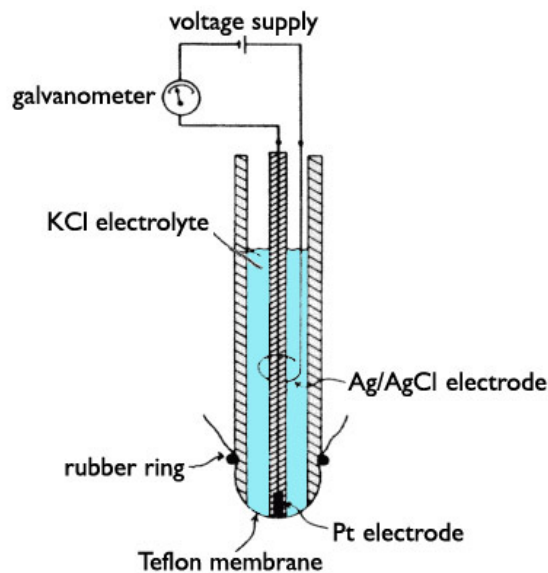


Figure 1.1 | Schematic drawing of a Clark type electrode for dissolved oxygen.

Despite the fact that Clark electrodes are widely used, they also have numerous drawbacks. First, they consume oxygen and thus solutions have to be stirred to obtain correct results. This causes errors when low pO_2 values have to be detected. Further, the electrode is cross sensitive towards gaseous CO_2 , H_2S and Cl_2 which partly can be compensated or minimized by the use of specific electrolyte compositions. *In vivo* experiments are also problematic, since proteins and other biological substances may cover the membrane and in consequence limit the operational lifetime of the electrodes.

1.2.2 pH electrode

A second analytical parameter of extraordinarily importance to industry, chemical laboratories, medicine, microbiology, biology, etc. is the pH value (“pH”). pH is used as a surrogate parameter in clinical analysis, especially in blood³⁷ and other body fluid^{38,39} analytics, or in monitoring food quality (milk^{40,41}, meat^{42,43}, and tap water^{44,45}). Further, pH is essential in environmental analysis, for instance in determination of acidic rain⁴⁶, industrial waste waters⁴⁷, or in control of bodies of water⁴⁸⁻⁵⁰.

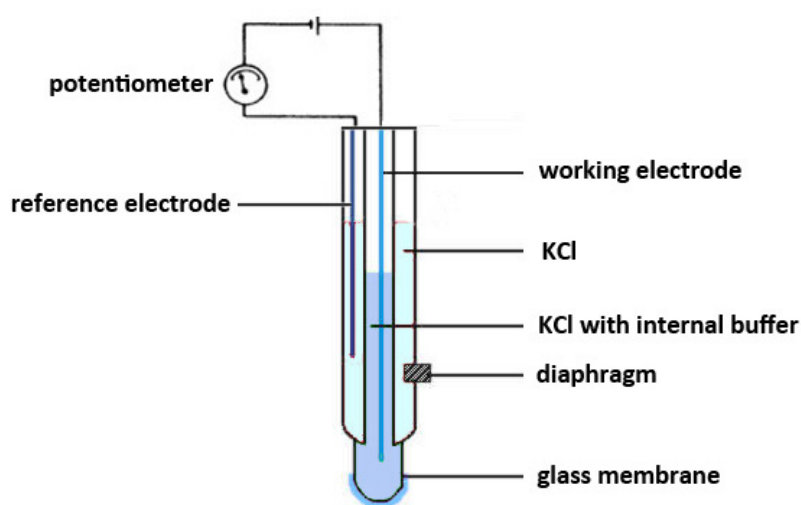


Figure 1.2 | Schematic drawing of a pH glass electrode

The most common tool to determine pH^{51,52} is the glass electrode. It was first described by Haber⁵³, Cremer⁵⁴, MacInnes and Dole⁵⁵ in the first decades of the 20th century. The glass electrode is a potentiometric two electrode system consisting of an Ag⁺/AgCl working electrode and an Ag⁺/AgCl reference electrode (**Fig. 1.2**). Both electrodes are immersed in KCl solutions. The electrolyte solution of the inner electrode additionally contains a buffer with a defined pH (mostly phosphate buffer of pH 7). The outer solution is connected with the analyte solution via a small diaphragm that allows for electrical connection but hinders material exchange. The inner electrode is separated from the analyte solution via a glass membrane. Generally, the glass membrane prevents penetration by protons, but water partly swells the glass surface. If the pH values of the

analyte solution are lower than those of the internal buffer solutions, protons diffuse into the outer surface of the glass membrane and versatile Na^+ ions are pushed back inside the glass. Thus an electric potential is generated. If the pH value of the analyte solution is higher than the internal buffer, the polarization of the membrane is inverted^{56,57}. The electrochemical series inside the glass electrode is: Ag/AgCl/KCl (buffered) | glass membrane | analyte solution | diaphragm | Ag/AgCl/KCl.

Glass electrodes for pH measurements offer the advantage that they show Nernstian response behavior (linearity) towards pH. Thus, they allow for straightforward two-point calibrations. Further, they show high sensitivity, have a very wide dynamic range (linear behavior from pH 2 to 12), have small power requirements and measures activities rather than concentrations. However, they also have numerous drawbacks that complicate or even prevent the use of pH electrodes in certain applications. They are sensitive to electromagnetic fields, show difficulties in remote sensing and sensor miniaturization, need a reference electrode, can be interfered by heavy metal ions, proteins or H_2S , and show an acidic and a basic failure with extreme pH values. Moreover, they potentially create a risk of undesirable electric shocks during *in vivo* measurements.^{56,58,59}

1.2.3 Electrodes vs. optical sensing and imaging

There is one major drawback for the use of electrodes besides the disadvantages already mentioned in the previous sections. Electrodes only allow for single spot measurements, that makes imaging and thus visualization of 2D analyte distributions nearly impossible. Although, 2D images can be obtained with electrodes via scanning of surfaces, but it is very tedious, time consuming and spatial resolutions are severely limited. Other approaches for the spatial visualization of analyte distributions have to be taken in account.

The use of optical sensors, so called optrodes, represents a promising alternative^{2,59-64}. Generally, optrodes are chemical sensors based on optical signal transduction. A chemical sensor is defined via two official definitions:

On the one hand the IUPAC definition, which is a global definition matching nearly all analytical devices:

"A chemical sensor is a device that transforms chemical information, ranging from the concentration of a specific sample component to total composition analysis, into an analytically useful signal. Chemical sensors usually contain two basic components connected in series: a chemical (molecular) recognition system (receptor) and a physicochemical transducer⁶⁵."

On the other hand, a more precise definition, the Cambridge definition:

"Chemical sensors are miniaturized devices that can deliver real time and on-line information on the presence of specific compounds or ions in even complex samples⁶⁶."

A sensor is more than just a simple indicator dye or probe. A sensor consist at least of (i) a receptor layer (including the indicator) reacting with the analyte to generate a signal, (ii) a transducer that converts this specific signal into an electrical signal, which (iii) is often amplified or integrated and (iv) then converted and evaluated in a computer system^{29,62}.

The signal of an optrode is generated either from changes in intrinsic or extrinsic optical properties. Using intrinsic optical signals is the most elementary way for optical analyte determination. For instance, the photosynthesis activity can be directly determined by the luminescence of chlorophyll (Kautsky effect)⁶⁷, blood oxygenation is monitored via colorimetric read-out or pulse oximetry^{68,69}, or in a more sophisticated way, temperature can be observed by tilted Bragg-grated fibers⁷⁰. Unfortunately, most analytes do not display intrinsic optical signals. Labels or indicators have to be used to convert the analyte (e.g. pH, oxygen, ect.) concentration or distribution into a useful optical signal. The spectral properties of those indicators may vary in absorbance, reflectance or luminescence. The gross of optical sensors and probes uses either luminescence intensity⁷¹⁻⁷⁹ or luminescence lifetime^{2,3,6,59,80-83} for extrinsic analyte determination.

Optrodes are versatile. The indicator can be embedded in a membrane or in micro- or nanoparticles. The specific behavior, response times, dynamic ranges, and cross

reactivity of the indicator thus can be tuned and controlled by choosing a proper microenvironment.

Optrodes offer numerous benefits. They (i) can easily be miniaturized, (ii) do not consume the analyte (whereas the Clark electrode consumes oxygen), (iii) are non-invasive, (iv) are cheap and thus can be fabricated as disposable sensors, (v) do not require an additional reference element (such as the reference electrode), (vi) are not interfered by high pressure, electric or magnetic fields, (vii) can transmit multiple signals at the same time, and (viii) in fact offer a smaller dynamic range, but have a better resolutions compared to electrodes. On the contrary, optical sensors also implicate some disadvantages. They (i) can be interfered by ambient light or scattered excitation light, (ii) have limited dynamic range, (iii) offer limited operational lifetime due to possible photobleaching or bleeding (i.e. leaching of probes out of the sensor), and (iv) measure concentrations instead of activities.^{62,84-90}

Optical sensors show great promise for *in vivo* visualization of pH and oxygen distributions in human tissue, inter alia, since the physiological range is limited and high spatial resolution should be gained. Further, possible simultaneous multianalyte analysis and 2D imaging is essential for the scope of this thesis.

1.3 State of the art in optical imaging of pO₂, pH, and dual pO₂/pH

1.3.1 pO₂ sensors

The interest in sensing and imaging of oxygen immensely increased during the last four decades since its first description by Bergman in 1968⁹¹. pO₂ sensors are used in many fields of research⁸³. They are used in medical care⁹²⁻⁹⁴ and cancer research⁹², in environmental analysis⁹⁵⁻⁹⁷, in industrial process monitoring⁹⁸, in biology^{99,100} and biotechnology¹⁰¹⁻¹⁰³, but also in less obvious areas such as in coal mines⁹¹, food packaging¹⁰⁴, and marine research¹⁰⁵. Further, oxygen is also imaged and sensed in so

called pressure sensitive paints¹⁰⁶ for automotive and aeronautic research and in glucose determination using enzyme-based biosensors⁵.

Practically all optrodes for oxygen are based on the use of luminescence^{3,80}. The signal is generated by collisional quenching of luminescence. The indicator molecules in their excited triplet state collide with triplet oxygen. Therefore the energy is transferred from the dye to the oxygen molecules resulting in radiationless deactivation of the excited state. Thus, no oxygen is consumed during the measurement. The signal change can be observed by a change in luminescence intensity or in luminescence lifetime.

The first pO₂ sensor from Bergman⁹¹ used unreferenced fluorescence intensity based read-out of fluoranthene absorbed on a polyethylene film. The properties of sensors can be modified by the use of specific polymers as matrix materials for the indicators. Typically, oxygen indicators are incorporated in non-polar and oxygen permeable polymers. For instance, silicone rubbers, polystyrene (PS), poly(vinyl chloride) (PVC), cellulose derivatives, poly(methyl methacrylate) (PMMA) or various co-polymers are used^{83,107-114}. Silicone rubbers provide an excellent oxygen permeability that is at least two orders of magnitude higher than those of the other polymers mentioned^{115,116}. This results in an enormous quenching efficiency. Nevertheless, the other polymer materials (PS, PMMA, PVC, etc.) are widely used, because they are transparent, less rigid, chemically and biologically inert, and do not swell in aqueous solution⁸³. Further sol-gel based optrodes are available that are used for gas phase and aqueous measurements¹¹⁷⁻¹¹⁹. Those sol-gel matrices reduce long response times and indicator leaching^{118,120}.

There is a great variety of dyes that are quenched by oxygen but unfortunately merely a manageable quantity of indicators really fits the requirements of a probe for oxygen sensing. The indicators need (i) a sufficient quenching efficiency and rate, (ii) high photostability, (iii) a luminescence lifetime at least in the μs range, (iv) high luminescence quantum yield and (v) molar absorbance. Further, they have to be (vi) compatible with cheap and straightforward excitation light sources (such as LEDs) and (vii) should be soluble in the sensor matrix or polymer used.^{83,121}

Organometallic dyes are a widely used class of oxygen probes. They largely meet the requirements mentioned in previous paragraph. Generally, organometallic oxygen

probes can be divided in two major groups: polypyridyl complexes and metalloporphyrins. Polypyridyl complexes of transition metals (Ru^{2+} , Os^{2+} , or Ir^{2+}) with ligands such as 2,2'-bipyridyl, 1,10-phenanthroline or 4,7-diphenyl-1,10-phenanthroline possess good oxygen sensing properties^{83,122-125}. They offer moderate to high quantum yields of up to 0.5, luminescence lifetimes of up to several μs (1 - 7 μs), are relatively stable to photodecomposition, and are excitable with UV or blue light. Besides, they offer large Stokes shifts (> 150 nm), which allows for easy separation of excitation and emission light. Unfortunately, the emission bands are very broad (550 - 700 nm) which hampers its combination with other dyes to form multiple parameter sensors. Usually, lipophilic ion pairs of these charged polypyridyl based indicators with anions such as 3-(trimethylsilyl)-1-propanesulfonate are formed to incorporate the dyes in non-polar polymers^{126,127}. The second group of oxygen probes is the group of metalloporphyrins. The mainly used metalloporphyrins consist of a (modified) porphyrin framework with Pt^{2+} or Pd^{2+} as central ion¹²⁸⁻¹³⁰. They display moderate quantum yields (up to 0.15) and have a Soret band and a Q-band for excitation. The Soret band displays higher molar absorption (molar absorbance coefficients up to 320,000)^{73,131}. Fluorinated porphyrins show excellent photostability¹³². Metalloporphyrins offer excellent quenching rates due to their extremely long luminescence lifetimes of 50 to 1,000 μs . The complexes are mostly lipophilic and thus are soluble in the particular oxygen sensor polymers. Further they offer excitation bands in the near UV and the VIS region. Metalloporphyrins possess relatively narrow emission bands. Thus, they easily enable possible multi parameter sensing and imaging.

The general fact that luminescence quenching of oxygen indicator probes affects both, quantum yield and also decay time, enables intrinsically referenced measurements based on lifetime determination. These measurements offer high sensor signal stability and reproducibility, which is mandatory for possible *in vivo* imaging where conditions are quite variable.

Besides simple one-spot oxygen sensing, determination of spatial distributions, so called imaging, of pO_2 gained increased popularity during the last two decades¹³³. 2D oxygen sensors are of great interest in aeronautics and automobiles^{4,80,134},

microbiology^{99,100} and particularly for the medical field for *in vivo* imaging of tumor biology (tumor microenvironment)¹³⁵⁻¹³⁹ and skin research^{74,81,140}, to name but a few.

In vivo imaging of pO₂ based on optical read-out goes from strength to strength. Rumsey⁷⁴, Wilson^{71,141}, and Intaglietta¹⁴² have established first *in vivo* 2D imaging methods for oxygen in tissue in the 1990s. Oxygen sensitive probes were injected intravenously in animals and imaged unreferenced via fluorescent read-out. Itoh *et al.*¹⁴³ applied tris(1,10-phenanthroline)ruthenium(II) chloride absorbed in silica gel. Stücker, Hartmann, and Lübbers¹⁴⁴⁻¹⁴⁶ embedded ruthenium phenanthroline complexes in polymer matrices (ethyl cellulose, PS or silica gels). These approaches were used to image tissue pO₂ of intact human skin or in malignant melanoma on skin. Babilas *et al.*^{81,147,148} used platinum(II)-octaethyl-porphyrines in planar polystyrene films for tumor imaging in animals and imaging of blood microcirculation in human skin.

1.3.2 pH sensors

Optical pH sensors typically consist of indicator dyes that are covalently bound to, adsorbed to, or physically entrapped in a proton permeable polymer matrix. Generally, the indicator molecules are weak acids or bases that undergo reversible changes in their optical properties (absorbance or fluorescence intensity) upon protonation and deprotonation. They can be read out via absorbance, reflectance, or fluorescence measurements, or via energy transfer or change of the refractive index⁶². Non-bleeding pH indicator test-strips were regarded as first type of optical pH sensors. The signal is read-out in a very rudimentary way via the eye of the beholder. In 1977, Peterson *et al.*¹⁴⁹ developed a first regular optic pH sensor. The fiber optic sensor is based on absorbance measurement of phenol red covalently bound to polyacrylamide microspheres. The sensor was used to determine blood pH *in vitro* and *in vivo*¹⁵⁰. Although, many absorbance based pH sensors using phenol red, bromothymol blue and other probes exist¹⁵¹⁻¹⁵⁷, fluorescence is still the method of choice. The first fluorescence based pH optrode was described by Saari and Seitz¹⁵⁸ in 1982 using 5-aminofluorescein covalently attached to controlled-pore glass and cellulose membranes.

Fluorescence based methods, in contrast to absorption measurements, offer higher sensitivity, work with lower indicator concentrations, and need less complex experimental setups using illumination as well as detection from the same side instead of light transmission in absorption measurements. Most frequently used pH indicators for fluorescence read-out are HPTS (8-hydroxypyrene-1,3,6-trisulfonate), various fluorescein derivatives (fluoresceins, aminofluoresceins, carboxyfluoresceins, halogenated fluoresceins, ect.), hydroxycoumarines, seminaphthorhodafluors (SNARFs)^{75,159-164}. The choice of a proper pH indicator dye for a specific sensor is mainly governed by its pK_a value, quantum yield, molar absorbance, photostability, excitation and emission wavelength, and the Stokes shift. The polymer matrix also exerts extreme influence on the properties of the resulting pH sensor. The microenvironment resulting from the sensing layer or particles used can affect the pK_a values of the indicators and cause shifts of several units by stabilizing the acid or base form. Further, the response times and recovery times are altered due to different diffusion rates and hydrophobicities. Widely used polymer matrices for pH include hydrophobic plasticized PVC¹⁶⁵, poly(vinyl alcohols) (PVA)¹⁶⁶, sol-gels^{167,168}, ion-exchange materials¹⁶⁹, polyurethane^{170,171} or pHEMA based hydrogels^{160,172}, and cellulose derivatives^{173,174}.

Optrodes for pH are available in various formats such as directly injected indicators¹⁷⁵, fiber optic sensors^{2,85,176}, coated microtiter plates^{177,178}, and planar sensor membranes¹⁷⁹. Fiber optic sensors allow for precise measurements in environments with high local resolution. Microtiter plate formats allow for high-throughput screening.

Regarding optical 2D imaging of pH with high spatial resolution, only direct injection and planar sensors come into consideration. In the first approach mentioned, indicators are added directly to the sample. The direct injection is a more or less “invasive” approach. Basically, optical sensors are described as “non-invasive”, since the signals are transduced contactless. Taking this into account, the labeling “invasive” is slightly controversial. In this thesis, the label “invasive” marks the circumstance of indicators being in direct contact with the sample (i.e. human tissue) whereas approaches with indicators being separated from the sample via membranes or particles embedded membranes are called “non-invasive”.

In recent years, many invasive approaches for *in vivo* imaging were implemented. Most of them are based on microscopic imaging using scanning techniques. In 1990, Bassnett et al.¹⁸⁰ used carboxysemaphthorhodafluor-1 (SNARF-1) to image intracellular pH using ratiometric wavelength read-out. 2D luminescence lifetime imaging of fluorescein derivatives has been used for high-resolution mapping in studies on cells, tissue samples, tumors, and artificial skin constructs^{175,181-188}. These techniques are, however, difficult to implement in studies on live human subjects, because of long scanning times, highly sophisticated measurements setups (confocal microscope, laser, etc.), and the necessity of a spatially fixed sample. To overcome these issues, planar optical sensor membranes can be used^{179,189-192}. The planar sensor membranes either consist of a sensor layer with the indicator dyes directly embedded in a matrix, or are composed of indicator dyes incorporated in micro- or nanoparticles which are then embedded in a planar sensor matrix layer. Only a few planar pH sensors for 2D imaging have been realized yet. Liebsch¹⁹⁰ and Schröder^{193,194} used fluorescein derivatives embedded in polyurethane hydrogels as pH optodes. The pH dependent signal is referenced via a second signal from a ruthenium diphenylphenanthroline complex in oxygen blocking microparticles via a td-DLR method (see section 1.4.3). Hulth¹⁸⁹ and Zhu¹⁷⁹ used ratiometric read-out (see section 1.4.1) of HPTS in PVA membranes.

1.3.3 Dual sensors for pO₂ and pH

As mentioned in section 1.2.3 optical imaging allows for multiple analyte analysis or imaging. Generally, signals can be divided either spectrally due to their excitation or their emission wavelengths, or on the basis of different luminescence lifetimes. Diverse wavelengths primarily are divided via the use of optical filters, or different excitation sources¹³⁴, or RGB cameras that act as rudimental spectrometers¹⁹⁵. Different lifetimes are separated using time-gated detection, such as the modified dual lifetime referencing described by Borisov et al.⁸.

Two general concepts for the design of multiple analyte sensor membranes exist: a double-layer concept^{196,197} and a monolayer concept^{7,198,199}. In the double-layer sensors,

the sensor chemistry for each analyte is located in a different layer. The second layer covers a first one that is immobilized on a sensor support. The monolayer sensor type contains all sensor materials in one matrix layer. This sensor format is a more straightforward approach, the fabrication process is less tedious and the response times of the sensors are faster due to limited diffusion distances.

Dual sensing often implicates difficulties from the material side. For example, oxygen optodes (i.e. indicators, in contrast to optrodes that are referred to the “whole” sensor) need polymers that are permeable to oxygen but impermeable for protons and water. For pH indicators, the strategy has to be other way around. Matrix polymers have to be permeable for protons. Temperature indicators have to be shielded towards oxygen to prevent cross reactivity. The use of micro- or nanoparticles can circumvent those problems by generating the desired microenvironment for the specific purpose.

Recently, several multiple-analyte sensors have been developed. The major combination of analytes is pO_2 /temperature^{80,197,200}. Basically, all optical indicator dyes are more or less sensitive to temperature changes⁸². Thus, oxygen signals can be temperature-compensated to get precise and accurate data. Fiber-optic sensors^{85,196} as well as planar sensor membranes for 2D imaging^{7,134} exist. These sensors basically use two organometallic complexes. A highly oxygen sensitive complex is embedded in an oxygen permeable polymer resulting in the oxygen optode. A second fairly oxygen sensitive complex is embedded in oxygen blocking polymer particles (for instance poly acrylonitrile) to form the temperature optode.

Further, sensors for pCO_2/pO_2 ^{196,201} had been developed, too. Generally, carbon dioxide is measured with pH indicators. These indicators are embedded in polymers that cannot be penetrated by protons. According to this, the indicator is shielded towards pH and the signal changes exclusively result from CO_2 and its equilibrium with HCO_3^- in aqueous solution. Schröder et al.⁹⁰ developed a dual sensor for pCO_2 and pO_2 using HPTS and $Ru(dpp)_3TMS_2$ embedded in one ethyl cellulose matrix layer.

Only a few sensors for the combination of pH and pO_2 were described up to now. In 1988 a US patent²⁰² described a first pH/ pO_2 sensor for blood analysis. Tian et al.²⁰³ reported polymerizable dye/polymer hybrid for imaging. Unfortunately, the signals are

read out unreferenced via fluorescence intensity measurements. In 2006, Vasylevskaya et al.^{204,205} developed referenced fiber-optic dual micro sensors for pH/pO₂. The sensor was also used to monitor bacterial growth in a microtiter plate approach¹⁰³. The results from the dual sensors are generated by a modified dual luminophore referencing method which relates phase shifts that are measured at two different frequencies to pH and to oxygen. Regrettably, the method only allows for single spot measurements. In 2006, Schröder et al.²⁰⁶ described the first planar pH/pO₂ dual sensor. The sensor utilizes a lipophilic carboxyfluorescein derivative as pH indicator and a platinum(II)mesotetrakis (pentafluorophenyl)porphyrin for oxygen determination in polyurethane hydrogel. The planar optrode was used to study sediments in marine research. Both sensors from Schröder (pH/pO₂- and pCO₂/pO₂-sensor) are read-out via rapid lifetime determination (for oxygen; see section 1.4.2) and a modified td-DLR scheme (for pCO₂/pH; see section 1.4.3). While the oxygen signal is intrinsically referenced, the pH signal is referenced in a very circumstantial way. Cumbersome mathematical procedures including several iteration steps have to be made to refer the pH dependent intensity signal to the oxygen dependent signal. Up to now, no planar pH/pO₂ sensor exists, that allows for separately referenced and straightforward detection of 2D analyte distributions. Even sensor membranes for pH/pO₂ for *in vivo* use were not realized yet.

1.4 Methods for referenced imaging

Regularly, optical 2D-sensors are read out by charge coupled device (CCD) cameras as detectors, whereas each single photosensitive element (i.e. pixel) of the CCD chip acts like a single spot detector. Referencing each signal of all these single measurement spots is necessary. Various referencing techniques for optical imaging have been developed.

Luminescence intensity signals and lifetime signals are the most common parameters that are determined in optical imaging. Intensity follows the Parker's law:

$$\text{Equation 1.1:} \quad I = I_0 * \phi * k * \epsilon * d * c$$

I represents the luminescence intensity, I_0 the light intensity for excitation, ϕ the quantum yield of the luminophore (between 0 and 1), k is a geometric factor for the setup used, ε depicts the extinction coefficient, d stands for the diameter of the penetrated medium, and c gives the concentration of the luminophore. Hence, intensity measurements offer high light intensity along with strong excitation sources. Further, intensity measurements are inexpensive, simple and numerous indicators are available. Unfortunately, luminescence intensity is prone to errors such as irregular indicator concentration, differing experimental geometry, or inhomogeneous sensor films. Additionally, the illumination light field has to be very homogeneous. In contrast, Lifetime signals are intrinsically referenced, thus result in defined values. Lifetime measurements are independent from the measurement setup and excitation light source or intensity, but they need more sophisticated and expensive time-gated read-out. Last of all, the number of indicators with lifetimes long enough for lifetime determination (μs -range) is very limited.²⁰⁷ There are numerous oxygen and temperature indicators available displaying μs -lifetimes, but only a few do exist for pH or CO_2 ²⁰⁸⁻²¹¹.

Referencing imaging signals is mandatory especially for *in vivo* imaging on human subjects. Clinical conditions are quite variable in contrast to fixed samples or measurement systems while calibrating sensors on the lab bench.

1.4.1 Fluorescence ratiometric imaging (FRIM)

FRIM is the most basic and simple technique for referenced imaging^{121,212}. Generally, FRIM is an intensity based measurement that uses a second analytical wavelength to reference the signal. The reference wavelength has to be independent of the analyte concentration. There are two fundamental principles for referencing: (i) detection of two different emission wavelengths with a fixed excitation wavelength, and (ii) detection of one emission wavelength with two different excitation wavelengths. These principles reference variations in the indicator concentrations, alterations in measurement geometry, and fluctuations in light source intensity. Unfortunately, background fluorescence, light scattering and reflections cannot be compensated with FRIM.

However, to obtain 2D-images, either modifications of the optical system during measurements or the use of an image splitter are necessary to separate the signals. Instruments for fluorescence analysis, such as microscopes, or scanning devices are often equipped with dual excitation devices or switchable emission filter sets, thus enabling FRIM. Regarding (macroscopic) 2D analyte determination, changing filters or light sources is tedious and implies that images are created whereas data have not been acquired at the same time.

There are two approaches for FRIM. The first technique is referencing an indicator signal to a second reference dye, since a large number of indicators show only one fluorescent form, the acidic or the basic form. Among those are fluorescein derivatives, resorufins, coumarins, etc. The reference dye should be inert and non-responding to the analyte. Further the reference should either offer an overlapping excitation spectrum with a distinguishable emission wavelength, or, other way around, corresponding emission wavelength and discrete excitation. These methods may suffer from Förster resonance energy transfer (FRET), and most importantly from differential photobleaching of indicator/reference dyes. The second approach uses dual wavelength probes. Dyes like HPTS, seminaphthocarboxyfluoresceins, or seminaphtharhodafluors, offer different spectroscopic behavior in their protonated or deprotonated form. The ratio of their two emission intensities represents an intrinsically referenced signal. Problems of the indicator/reference approach are avoided when using this method.

1.4.2 Luminescence (Fluorescence) lifetime imaging (FLIM or LLI)

The luminescence lifetime τ reflects the average period of time a molecule remains in its excited state until it reaches its ground state via radiation of luminescence. More precisely, τ is defined as the length of time when $1/e$ of an amount of initial excited molecules still exists in their electronically elevated state²¹³. The time-dependent luminescence intensity $I(t)$ is related to the lifetime τ via following equation with I_0 equals the luminescence intensity at time $t=0$:

Equation 1.2:
$$I(t) = I_0 * e^{\frac{-t}{\tau}}$$

The use of lifetime as analytical signal overcomes many problems with intensity-based measurements. Neither scattering or reflections, nor indicator concentration or excitation light intensity interfere the measurement. Lifetime signals are determined either in the time domain or the frequency domain²¹⁴. Frequency domain measurements provide very accurate results and are the method of choice for fiber optic sensors. Regarding imaging techniques, frequency domain read-out via CCD cameras requires very complex and expensive setups such as integrated sinusoidal modulated image intensifiers. Hence, frequency domain imaging is out of the question for the work in this thesis.

Determination of τ in the time domain is a straightforward approach and the preferable method in 2D imaging. τ can be detected either via phase delay rationing (PDR)^{6,145} or rapid lifetime determination (RLD)^{6,215}. Both approaches make use of pulsed excitation light and two defined time-gated images. In PDR one time-gated image is acquired during the excitation phase (light source on) and a second image is taken in the emission phase (light source off). The ratio of the gathered light intensities of the two gates is rationed. The ratio is dependent on the luminescent decay time and stands for the intrinsically referenced sensor response^{212,216}. A major disadvantage of PDR is the detection of background fluorescence within the first time gate during the excitation phase. Background fluorescence is a limiting factor concerning medical imaging (such as imaging of blood or tissue, etc.), since most biological media includes fluorescent substances.

However, RLD in combination with μs decaying indicators circumvents the disturbances caused by background fluorescence. When using the RLD method both time gates are acquired during the emission phase (see **Fig. 1.3**) after pulsed excitation^{6,207,212,213}. Short-lived background fluorescence (< 200 ns) is hardly recorded due to a short time gap of typically 250 ns after the excitation pulse. Then, after the background luminescence has decayed, the long-living luminescence (mainly phosphorescence) of the indicators is collected. The ratio of the integrated intensities of the two time gates (A_{em1} and A_{em2}), depicted in two gathered intensity images, is dependent on the lifetime. Thus, the ratio expresses the intrinsically referenced sensor

signal. The lifetime τ can be calculated via the following equation with t_1 and t_2 representing the periods of time from the end of excitation pulse to the start of acquiring the respective image and A_{em1} and A_{em2} reflecting the intensities gathered during the image acquisition:

$$\text{Equation 1.3:} \quad \tau = \frac{t_2 - t_1}{\ln \frac{A_{em1}}{A_{em2}}}$$

There are limitations for this equation. First, both time gates have to have the same length. Second, true τ values can only be obtained for luminophores with mono-exponential decay²¹⁷⁻²¹⁹. Unfortunately, mono-exponential decay is an exceptional case for organometallic indicators. Sharman et al.²²⁰ presented a method to obtain more accurate data for bi-exponential decay. A 50 % overlap of the two time gates improves the results for τ immensely. Further experiments on positioning and length of the time gates were made for multi-exponential decay²²¹. Nevertheless, determining relative changes rather than calculating exact τ values is sufficient for most imaging applications. Oftentimes, only the ratio of the two images or of the detected τ values is empirically determined for calibration^{222,223}.

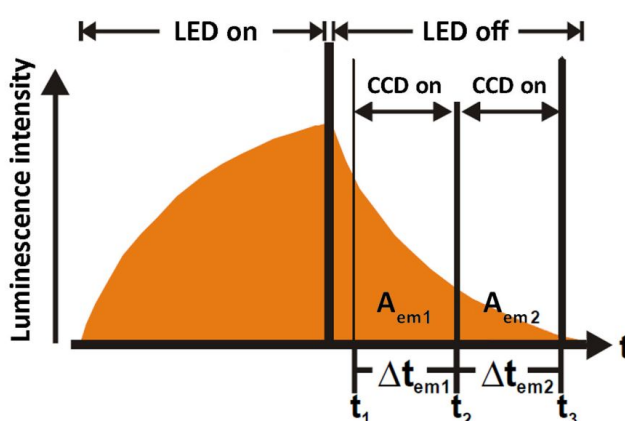


Figure 1.3 | Schematic drawing of the rapid lifetime determination (RLD) imaging scheme, where LED represents the light source and CCD is the detection device.

The RLD gathers all the mentioned advantages from lifetime based signals, including independency from measurement geometries, light field distribution and intensity, indicator concentrations, sensor thickness, or background fluorescence^{6,224}. Further, RLD signals are independent from photobleaching. For instance, if an indicator is bleached for 50 %, the ratio between A_{em1} and A_{em2} remains stable, because the intensities were reduced in the same proportional way. Apart from that, RLD even allows for measurements at ambient light, because the background can be corrected via subtraction of dark images (i.e. without excitation pulse)²⁰⁷.

1.4.3 Time domain Dual lifetime referencing (tdDLR)

Lifetime-referenced imaging of fluorescence indicators is challenging as many of the luminophores (especially those for pH and CO₂) exhibit luminescence lifetimes that are too short for LLI methods, which do not utilize microscopic scanning techniques. To overcome this issue, Liebsch et al.^{6,190} described a time-domain dual lifetime referencing (tdDLR) method. The tdDLR method requires the following prerequisites: (i) a indicator and (ii) a reference dye that are (iii) simultaneously excitable with one light source, and (iv) allow for the use of one single detector and emission filter setup. The two dyes need (iv) largely different luminescence lifetimes. Typically, the indicator is a fluorescent dye with a lifetime in the ns range and the reference is a phosphorescent dye with a μ s-lifetime. Further, (v) the reference has to be inert and (vi) decay time and quantum yield have to be unaffected by the analyte. At least, (vii) both luminophores have to be in close spatial proximity, and (viii) the ratio of the concentration has to be constant over the whole sensor membrane.²¹²

tdDLR detects two different images: one image during excitation phase (light source on), comprising the short-living indicator signal and the long-lasting reference signal, and a second image during emission phase but consisting of the long-lasting reference phosphorescence. Luminescence intensity was integrated in two time gates: one during excitation (A_{ex}) and one during emission (A_{em}). Given the fact that during excitation the integrated signal intensity reflects the combination of indicator and

reference signals, A_{ex} is $A_{ex}(ind) + A_{ex}(ref)$. However, approximately 250 ns after turning the LED off, fluorescence of the indicator has decayed, and only the reference signal is detected, so that A_{em} is $A_{em}(ref)$ (**Fig. 1.4**). The ratio R of A_{ex}/A_{em} denotes a referenced integrated signal intensity ratio.

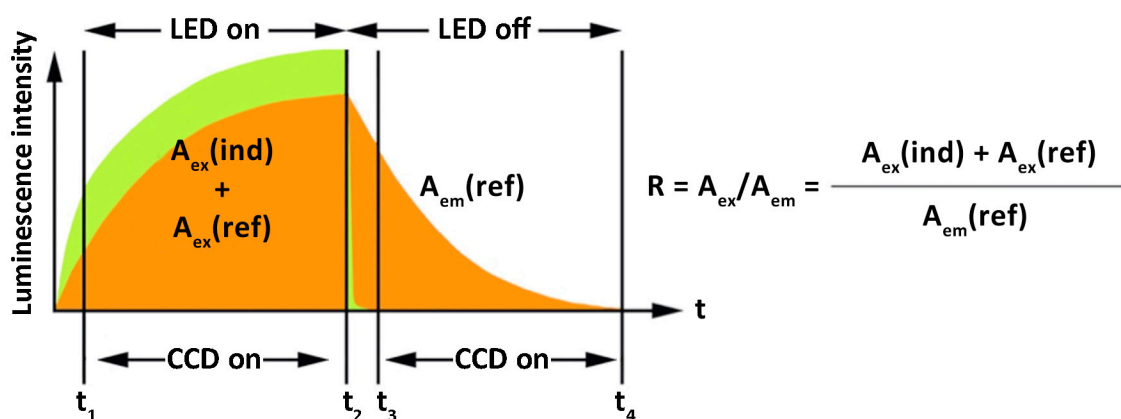


Figure 1.4 | Schematic drawing of the time-domain dual lifetime referencing (tdDLR) imaging scheme.

The tdDLR method thus transfers non-referenced intensity signals into lifetime-referenced signals. Thus, little irregularities in particle distribution or illumination of the sensor do not alter the measured ratio R . This fact is a major advantage, especially if the density of the sensor particles differs locally, or if illumination cannot be controlled as precisely as in a laboratory setting. Unfortunately, negative effects such as indicator leaching or differential photo bleaching that may vary the measured ratio R are not referenced by tdDLR. Those concerns have to be minimized and specially investigated for each new sensor type.

1.5 References

- 1 Thompson Klein, J. Interdisciplinarity: History, theory, and practice. *Bloodaxe Books, West Sussex*, (1990).
- 2 Wolfbeis, O. S. Fiber-optic chemical sensors and biosensors. *Analytical Chemistry* **76**, 3269-3284, (2004).

- 3 Wolfbeis, O. S. Materials for fluorescence-based optical chemical sensors. *J Mater Chem* **15**, 2657-2669, (2005).
- 4 Stich, M. I. J., Fischer, L. H. & Wolfbeis, O. S. Multiple fluorescent chemical sensing and imaging. *Chem Soc Rev* **39**, 3102-3114, (2010).
- 5 Borisov, S. M. & Wolfbeis, O. S. Optical biosensors. *Chem Rev* **108**, 423-461, (2008).
- 6 Liebsch, G. Time-resolved luminescence lifetime imaging with optical chemical sensors: Set-up, controlling, concepts and applications *Ph.D. Thesis, University of Regensburg*, (2000).
- 7 Nagl, S., Stich, M. I. J., Schäferling, M. & Wolfbeis, O. S. Method for simultaneous luminescence sensing of two species using optical probes of different decay time, and its application to an enzymatic reaction at varying temperature. *Anal Bioanal Chem* **393**, 1199-1207, (2008).
- 8 Borisov, S. M., Neurauder, G., Schroeder, C., Klimant, I. & Wolfbeis, O. S. Modified dual lifetime referencing method for simultaneous optical determination and sensing of two analytes. *Appl Spectrosc* **60**, 1167-1173, (2006).
- 9 Lippert, H. Wundatlas, wunde-wundbehandlung und wundheilung. *Verlag J. A. Barth*, (2001).
- 10 Schreml, S., Szeimies, R.-M., Prantl, L., Landthaler, M. & Babilas, P. Wound healing in the 21st century. *J Am Acad Dermatol* **63**, 866-881, (2010).
- 11 Schreml, S. *et al.* The impact of the ph value on skin integrity and cutaneous wound healing. *J Eur Acad Dermatol* **24**, 373-378, (2010).
- 12 Menke, N. B., Ward, K. R., Witten, T. M., Bonchev, D. G. & Diegelmann, R. F. Impaired wound healing. *Clin Dermatol* **25**, 19-25, (2007).
- 13 Bickers, D. R. *et al.* The burden of skin diseases: 2004 - a joint project of the american academy of dermatology association and the society for investigative dermatology. *Journal of the American Academy of Dermatology* **55**, 490-500, (2006).
- 14 Singer, A. J. & Clark, R. A. Cutaneous wound healing. *N Engl J Med* **341**, 738-746, (1999).
- 15 Schreml, S. *et al.* Oxygen in acute and chronic wound healing. *Br J Dermatol* **163**, 257-268, (2010).
- 16 Schreml, S. *et al.* The role of oxygen in wound healing and chronic wound pathogenesis. *J Am Acad Dermatol*, (2009, in press).
- 17 Winter, G. D. Formation of the scab and the rate of epithelization of superficial wounds in the skin of the young domestic pig. *Nature* **193**, 293-294, (1962).
- 18 Hachem, J. P. *et al.* Ph directly regulates epidermal permeability barrier homeostasis, and stratum corneum integrity/cohesion. *J Invest Dermatol* **121**, 345-353, (2003).
- 19 Dissemond, J., Witthoff, M., Brauns, T. C., Haberer, D. & Goos, M. Ph-wert des milieus chronischer wunden. *Der Hautarzt* **54**, 959-965, (2003).
- 20 Akatov, V. S., Lezhnev, E. I., Vexler, A. M. & Kublik, L. N. Low ph value of pericellular medium as a factor limiting cell proliferation in dense cultures. *Exp Cell Res* **160**, 412-418, (1985).
- 21 Halbert, A. R., Stacey, M. C., Rohr, J. B. & Jopp-McKay, A. The effect of bacterial colonization on venous ulcer healing. *Australas J Dermatol* **33**, 75-80, (1992).
- 22 Hopf, H. W. & Rollins, M. D. Wounds: An overview of the role of oxygen. *Antioxid Redox Sign* **9**, 1183-1192, (2007).
- 23 Schugart, R. C., Friedman, A., Zhao, R. & Sen, C. K. Wound angiogenesis as a function of tissue oxygen tension: A mathematical model. *Proc Natl Acad Sci U S A* **105**, 2628-2633, (2008).
- 24 Allen, D. B. *et al.* Wound hypoxia and acidosis limit neutrophil bacterial killing mechanisms. *Arch Surg-Chicago* **132**, 991-996, (1997).
- 25 Myllyla, R., Tuderman, L. & Kivirikko, K. I. Mechanism of the prolyl hydroxylase reaction. 2. Kinetic analysis of the reaction sequence. *Eur J Biochem* **80**, 349-357, (1977).

- 26 Knighton, D. R. *et al.* Oxygen tension regulates the expression of angiogenesis factor by macrophages. *Science* **221**, 1283-1285, (1983).
- 27 [Anon]. Regulation of tgf-beta and its signaling components by oxygen tension and steroids in skin cells. *Wound Repair Regen* **13**, 42-42, (2005).
- 28 Schreml, S., Szeimies, R. M., Prantl, L., Landthaler, M. & Babilas, P. What the new millenium taught us about cutaneous wound healing. *J Am Acad Dermatol*, (2009, in press).
- 29 Gründler, P. Chemische sensoren: Eine einführung für naturwissenschaftler und ingenieure *Springer, Berlin*, (2004).
- 30 Oehme, F. Chemische sensoren. *Vieweg, Braunschweig*, (1991).
- 31 Winkler, L. W. *Bericht Deutsche Chemische Gesellschaft*, 2834, (1888).
- 32 Goodfellow, G. I. & Webber, H. M. Absorptiometric determination of low oxygen concentrations in power-station waters. Part i. Manual method. *Analyst*, 1105-1118, (1979).
- 33 Clark, I. C., Jr., Wolf, R., Granger, D. & Taylor, Z. Continous recording of blood tensions by polarography. *J Appl Physiol* **6**, 189-193, (1953).
- 34 Tödt, F. Elektrochemische sauerstoffmessungen. *Walter de Gruyter, Berlin*, (1958).
- 35 Clark, L. C. Monitor and control of blood and tissue oxygenation. *Tr Am Soc Artif Intern Org*, 41-45, (1956).
- 36 Clark, L. C., Jr. Continuous recording of blood oxygen content. *Surg Forum* **11**, 143-144, (1960).
- 37 Koch, G. & Wendel, H. Comparison of ph carbon dioxide tension standard bicarbonate and oxygen tension in capillary blood and in arterial blood during neonatal period. *Acta Paediatr Scand* **56**, 10-&, (1967).
- 38 Kristens.M. Continuous intragastric ph determination .I. Ph of gastric juice determined in situ and following aspiration. *Acta Med Scand* **177**, 415, (1965).
- 39 Durham, R. M. & Weigelt, J. A. Monitoring gastric ph levels. *Surgery Gynecology & Obstetrics* **169**, 14-16, (1989).
- 40 Eldaher, N., Nawas, T. & Alqaderi, S. The effect of the ph of various dairy-products on the survival and growth of brucella-melitensis. *Ann Trop Med Parasit* **84**, 523-528, (1990).
- 41 Benoit, E. & Bessiere, J. Analytical study of ph-metric properties of a dissolving reagent of milk and dairy-products. *Analisis* **18**, 136-141, (1990).
- 42 Young, O. A., Thomson, R. D., Merhtens, V. G. & Loeffen, M. F. Industrial application to cattle of a method for the early determination of meat ultimate ph. *Meat Sci* **67**, 107-112, (2004).
- 43 [Anon]. Testing ph and temperature of meat products. *Food Aust* **58**, 166-166, (2006).
- 44 Putzien, J. Precise ph-measurement in drinking-water. *Z Wasser Abwass For* **21**, 1-6, (1988).
- 45 Canete, F., Rios, A., Decastro, M. D. L. & Valcarcel, M. Determination of analytical parameters in drinking-water by flow-injection analysis .2. Simultaneous determination of calcium and magnesium. *Analyst* **112**, 267-270, (1987).
- 46 Marinenko, G. & Koch, W. F. A critical-review of measurement practices for the determination of ph and acidity of atmospheric precipitation. *Environ Int* **10**, 315-319, (1984).
- 47 Anderson, G. K. & Yang, G. Ph control in anaerobic treatment of industrial waste-water. *J Environ Eng-Asce* **118**, 551-567, (1992).
- 48 Serra, G., Schirone, A. & Boniforti, R. Fiberoptic ph sensor for sea-water monitoring using a single dye. *Anal Chim Acta* **232**, 337-344, (1990).
- 49 [Anon]. Monitoring and controlling level and ph in effluent water. *Water Serv* **85**, 610, (1981).
- 50 Tedesco, D., Pece, R. & Avino, R. Radon, ph and temperature monitoring in water wells at campi flegrei caldera (southern italy). *Geochem J* **30**, 131-138, (1996).

- 51 Sørensen, S. P. L. Enzyme studies. li. The measurement and importance of the hydrogen ion concentration in enzyme reactions. *Biochemische Zeitschrift*, 131-304, (1909).
- 52 Kober, F. Serensen and ph. *Praxis der Naturwissenschaften, Chemie* **40**, 43-45, (1991).
- 53 Haber, F. & Klemensiewicz, Z. On the electrical phase limit powers. *Zeischr. f physik. Chemie* **67**, 385, (1909).
- 54 Cremer, M. Über die ursache der elektromotorischen eigenschaften der gewebe, zugleich ein beitrag zur lehre von den polyphasischen elektrolytketten. *Zeitschrift für Biologie* **2**, 562 - 608, (1906).
- 55 MacInnes, D. A. & Dole, M. Tests of a new type glass electrode. *Ind. Eng. Chem. Anal.*, 57 - 59, (1929).
- 56 Schwedt, G. Analytische chemie: Grundlagen, methoden und praxis. *Wiley-VCH* (2008).
- 57 Kratz, L. Die glaselektrode und ihre anwendungen. *Steinkopff*, (1950).
- 58 Wolfbeis, O. S. Fiber optic chemical sensors and biosensors. *CRC Press* **1**, (1991).
- 59 Wolfbeis, O. S. Optical sensors: Industrial, environmental and diagnostic applications (springer series on chemical sensors and biosensors). *Springer, Berlin*, 1 - 34, (2003).
- 60 Homola, J. Optical biochemical and chemical sensors: Europt(r)ode x. *Anal Bioanal Chem* **398**, 1861-1862, (2010).
- 61 Savvin, S. B., Kuznetsov, V. V., Sheremet'ev, S. V. & Mikhailova, A. V. Optical chemical sensors (micro- and nanosystems) for analysis of liquids. *Russ J Gen Chem+* **78**, 2418-2429, (2008).
- 62 McDonagh, C., Burke, C. S. & MacCraith, B. D. Optical chemical sensors. *Chem Rev* **108**, 400-422, (2008).
- 63 Bogue, R. Optical chemical sensors for industrial applications. *Sensor Rev* **27**, 86-90, (2007).
- 64 Gauglitz, G. Optical biochemical and chemical sensors - europt(r)ode viii. *Anal Bioanal Chem* **386**, 1199-1200, (2006).
- 65 Thevenot, D. R., Toth, K., Durst, R. A. & Wilson, G. S. Electrochemical biosensors: Recommended definitions and classification - (technical report). *Pure Appl Chem* **71**, 2333-2348, (1999).
- 66 Cammann, G. G., Guilbault, E. A., Hal, R., Kellner, H. & Wolfbeis, O. S. The cambridge definition of chemical sensors. *Cambridge Workshop on Chemical Sensors and Biosensors, Cambridge University Press*, (1996).
- 67 Kautsky, H. & Hirsch, A. Energy transformations on boundary surfaces. Iv. Interaction of excited dyestuff molecules and oxygen. *Chemische Berichte*, 2677-2683, (1931).
- 68 Kienle, A. *et al.* Why do veins appear blue? A new look at an old question. *Appl Optics* **35**, 1151-1160, (1996).
- 69 Severinghaus, J. W. History and recent developments in pulse oximetry. *Scand J Clin Lab Inv* **53**, 105-111, (1993).
- 70 Trpkovski, S., Wade, S. A., Baxter, G. W. & Collins, S. F. Dual temperature and strain sensor using a combined fiber bragg grating and fluorescence intensity ratio technique in er³⁺-doped fiber. *Rev Sci Instrum* **74**, 2880-2885, (2003).
- 71 Vinogradov, S. A. *et al.* Noninvasive imaging of the distribution in oxygen in tissue in vivo using near-infrared phosphors. *Biophys J* **70**, 1609-1617, (1996).
- 72 Vinogradov, S. A. & Wilson, D. F. Metallo-tetrabenzoporphyrins - new phosphorescent probes for oxygen measurements. *J Chem Soc Perk T 2*, 103-111, (1995).
- 73 Papkovsky, D. B., Ponomarev, G. V., Trettnak, W. & O'Leary, P. Phosphorescent complexes of porphyrin ketones - optical-properties and application to oxygen sensing. *Analytical Chemistry* **67**, 4112-4117, (1995).
- 74 Rumsey, W. L., Vanderkooi, J. M. & Wilson, D. F. Imaging of phosphorescence - a novel method for measuring oxygen distribution in perfused tissue. *Science* **241**, 1649-1651, (1988).

- 75 Han, J. & Burgess, K. Fluorescent indicators for intracellular pH. *Chem Rev* **110**, 2709-2728, (2010).
- 76 Snee, P. T. *et al.* A ratiometric CdSe/ZnS nanocrystal pH sensor. *J Am Chem Soc* **128**, 13320-13321, (2006).
- 77 Nivens, D. A., Schiza, M. V. & Angel, S. M. Multilayer sol-gel membranes for optical sensing applications: Single layer pH and dual layer CO₂ and NH₃ sensors. *Talanta* **58**, 543-550, (2002).
- 78 Malins, C. & MacCraith, B. D. Dye-doped organically modified silica glass for fluorescence based carbon dioxide gas detection. *Analyst* **123**, 2373-2376, (1998).
- 79 Mills, A. & Chang, Q. Fluorescence plastic thin-film sensor for carbon-dioxide. *Analyst* **118**, 839-843, (1993).
- 80 Wolfbeis, O. S. Sensor paints. *Adv Mater* **20**, 3759-3763, (2008).
- 81 Babilas, P. *et al.* In vivo phosphorescence imaging of pO₂ using planar oxygen sensors. *Microcirculation* **12**, 477-487, (2005).
- 82 Rai, V. K. Temperature sensors and optical sensors. *Applied Physics B* **88**, 297-303, (2007).
- 83 Amano, Y. Probes and polymers for optical sensing of oxygen. *Microchim Acta* **143**, 1-12, (2003).
- 84 Weidgans, B. M. New fluorescent optical pH sensors with minimal effects of ionic strength. *Ph.D. Thesis, University of Regensburg*, 15, (2004).
- 85 Wolfbeis, O. S. & Weidgans, B. Fiber optic chemical sensors and biosensors: A view back, in: *Optical chemical sensors. NATO science series: Series 2, Mathematics, physics and chemistry; Springer, Berlin* **224**, 17-44, (2006).
- 86 Narayanaswamy, R. Optical chemical sensors - transduction and signal-processing. *Analyst* **118**, 317-322, (1993).
- 87 Blum, L. J. & Coulet, P. R. Biosensor principles and applications. *Marcel Dekker, Inc., New York*, 163-165, (1991).
- 88 Pasic, A., Koehler, H., Klimant, I. & Schaupp, L. Miniaturized fiber-optic hybrid sensor for continuous glucose monitoring in subcutaneous tissue. *Sensor Actuat B-Chem* **122**, 60-68, (2007).
- 89 Borisov, S., Vasylevska, A., Krause, C. & Wolfbeis, O. Composite luminescent material for dual sensing of oxygen and temperature. *Adv Funct Mater* **16**, 1536-1542, (2006).
- 90 Schroeder, C. R., Neurauder, G. & Klimant, I. Luminescent dual sensor for time-resolved imaging of pCO₂ and pO₂ in aquatic systems. *Microchim Acta* **158**, 205-218, (2007).
- 91 Bergman, I. Rapid-response atmospheric oxygen monitor based on fluorescence quenching. *Nature* **218**, 396, (1968).
- 92 Zhang, G. Q., Palmer, G. M., Dewhurst, M. & Fraser, C. L. A dual-emissive-materials design concept enables tumour hypoxia imaging. *Nat Mater* **8**, 747-751, (2009).
- 93 Sorensen, B. S. *et al.* Influence of oxygen concentration and pH on expression of hypoxia induced genes. *Radiother Oncol* **76**, 187-193, (2005).
- 94 Peterson, J. I., Fitzgerald, R. V. & Buckhold, D. K. Fiber-optic probe for in vivo measurement of oxygen partial pressure. *Analytical Chemistry* **1**, 62-67, (1984).
- 95 Li, H. *et al.* A novel nano-Au-assembled gas sensor for atmospheric oxygen determination. *Analyst* **126**, 1747-1750, (2001).
- 96 Guo, L. Q. *et al.* A novel sensor based on the porous plastic probe for determination of dissolved oxygen in seawater. *Talanta* **74**, 1032-1037, (2008).
- 97 Girard, J. Principles of environmental chemistry. *Jones & Bartlett, Boston*, (2009).
- 98 Narayanaswamy, R., Wolfbeis, O.S. Optical sensors for industrial, environmental and clinical applications. *Springer, Berlin*, (2003).
- 99 Epstein, R. J. Human molecular biology: An introduction to the molecular basis of health. *Cambridge Univ. Press, Cambridge, UK*, (2003).
- 100 Periasamy, A., Clegg, R. M. Flim microscopy in biology and medicine. *CRC Press, Boca Raton, FL*, (2009).

- 101 Riegel, E. R. & Kent, J. A. Handbook of industrial chemistry and biotechnology. *Springer, Berlin*, (2007).
- 102 Ge, X. D. *et al.* Validation of an optical sensor-based high-throughput bioreactor system for mammalian cell culture. *J Biotechnol* **122**, 293-306, (2006).
- 103 Kocincova, A. S. *et al.* Multiplex bacterial growth monitoring in 24-well microplates using a dual optical sensor for dissolved oxygen and ph. *Biotechnol Bioeng* **100**, 430-438, (2008).
- 104 Mills, A. Oxygen indicators and intelligent inks for packaging food. *Chem Soc Rev* **34**, 1003-1011, (2005).
- 105 Moore, T. S. *et al.* Marine chemical technology and sensors for marine waters: Potentials and limits. *Annu Rev Mar Sci* **1**, 91-115, (2009).
- 106 Liu, T., Sullivan, J.P. Pressure and temperature sensitive paints. *Springer, Berlin*, (2005).
- 107 Schaffar, B. P. & Wolfbeis, O. S. A fast responding fibre optic glucose biosensor based on an oxygen optrode. *Biosens Bioelectron* **5**, 137-148, (1990).
- 108 Borisov, S. M. & Klimant, I. Ultrabright oxygen optodes based on cyclometalated iridium(iii) coumarin complexes. *Anal Chem* **79**, 7501-7509, (2007).
- 109 Douglas, P. & Eaton, K. Response characteristics of thin film oxygen sensors, pt and pd octaethylporphyrins in polymer films. *Sensor Actuat B-Chem* **82**, 200-208, (2002).
- 110 Mills, A. Controlling the sensitivity of optical oxygen sensors. *Sensor Actuat B-Chem* **51**, 60-68, (1998).
- 111 Mills, A. & Lepre, A. Controlling the response characteristics of luminescent porphyrin plastic film sensors for oxygen. *Analytical Chemistry* **69**, 4653-4659, (1997).
- 112 Borisov, S. M. *et al.* Springer series on fluorescence, vol. 4: Fluorescence of supermolecules, polymers, and nanosystems *Springer, Berlin, Heidelberg*, (2008).
- 113 Schrenkhammer, P. New optical biosensors for uric acid and glucose. *Ph.D. Thesis, University of Regensburg*, (2008).
- 114 Xu, W. Y., Mcdonough, R. C., Langsdorf, B., Demas, J. N. & Degraff, B. A. Oxygen sensors based on luminescence quenching - interactions of metal-complexes with the polymer supports. *Analytical Chemistry* **66**, 4133-4141, (1994).
- 115 He, H. R., Fraatz, R. J., Leiner, M. J. P., Rehn, M. M. & Tusa, J. K. Selection of silicone polymer matrix for optical gas-sensing. *Sensor Actuat B-Chem* **29**, 246-250, (1995).
- 116 Brandrup, J., Immergut, E. H. & Grulke, E. A. Polymer handbook. *Wiley-VCH New-York* (1999).
- 117 Pang, H. L. *et al.* Ormosil oxygen sensors on polystyrene microplate for dissolved oxygen measurement. *Sensor Actuat B-Chem* **123**, 120-126, (2007).
- 118 Ding, J. J., Li, B., Zhang, H. R., Lei, B. F. & Li, W. L. Oxygen-sensing properties of ormosil hybrid materials doped with ruthenium(ii) complexes via a sol-gel process. *Mater Lett* **61**, 3374-3377, (2007).
- 119 Al-Jowder, R., Roche, P. J. R. & Narayanaswamy, R. Use of an artificial neural network to model the quenching of a ru.Dpp : Ormosil-based optrode to gaseous and dissolved oxygen. *Sensor Actuat B-Chem* **127**, 383-391, (2007).
- 120 Jiang, Y. Q. *et al.* Luminescence quenching behavior of oxygen sensing ormosil films based on ruthenium complex. *Chem Res Chinese U* **17**, 374-379, (2001).
- 121 Schröder, C. R. Luminescent planar single and dual optodes for time-resolved imaging of ph, pco2 and po2 in marine systems *Ph.D. Thesis, University of Regensburg*, (2006).
- 122 Garcia-Fresnadillo, D., Marazuela, M. D., Moreno-Bondi, M. C. & Orellana, G. Luminescent nafion membranes dyed with ruthenium(ii) complexes as sensing materials for dissolved oxygen. *Langmuir* **15**, 6451-6459, (1999).
- 123 Zhong, W., Urayama, P. & Mycek, M. A. Imaging fluorescence lifetime modulation of a ruthenium-based dye in living cells: The potential for oxygen sensing. *J Phys D Appl Phys* **36**, 1689-1695, (2003).

- 124 Amao, Y. & Okura, I. Optical oxygen sensing properties of tris(4,7'-diphenyl-1,10'-phenanthroline) ruthenium (ii)-polyacrylic acid complex thin film. *Polym J* **32**, 452-455, (2000).
- 125 Mcgee, K. A., Veltkamp, D. J., Marquardt, B. J. & Mann, K. R. Porous crystalline ruthenium complexes are oxygen sensors. *J Am Chem Soc* **129**, 15092, (2007).
- 126 Klimant, I. & Wolfbeis, O. S. Oxygen-sensitive luminescent materials based on silicone-soluble ruthenium diimine complexes. *Analytical Chemistry* **67**, 3160-3166, (1995).
- 127 Papkovsky, D. B. New oxygen sensors and their application to biosensing. *Sensor Actuat B-Chem* **29**, 213-218, (1995).
- 128 Amao, Y., Asai, K. & Okura, I. Oxygen sensing based on lifetime of photoexcited triplet state of platinum porphyrin-polystyrene film using time-resolved spectroscopy. *J Porphyr Phthalocya* **4**, 292-299, (2000).
- 129 Amao, Y., Asai, K., Miyakawa, K. & Okura, I. Oxygen sensing using palladium porphyrin with long alkyl chain self-assembled film. *J Porphyr Phthalocya* **4**, 19-22, (2000).
- 130 Borisov, S. M., Nuss, G. & Klimant, I. Red light-excitable oxygen sensing materials based on platinum(ii) and palladium(ii) benzoporphyrins. *Analytical Chemistry* **80**, 9435-9442, (2008).
- 131 Lai, S. W. *et al.* Electronic spectroscopy, photophysical properties, and emission quenching studies of an oxidatively robust perfluorinated platinum porphyrin. *Inorg Chem* **43**, 3724-3732, (2004).
- 132 Lee, S. K. & Okura, I. Photostable optical oxygen sensing material: Platinum tetrakis (pentafluorophenyl) porphyrin immobilized in polystyrene. *Analytical Communications* **34**, 185-188, (1997).
- 133 Stich, M. I. J. & Wolfbeis, O. S. Pressure sensitive paints: Standardization in fluorometry: State-of-the art and future challenges. *Springer, Berlin*, chapter 20, (2007).
- 134 Stich, M. I. J., Nagl, S., Wolfbeis, O. S., Henne, U. & Schaeferling, M. A dual luminescent sensor material for simultaneous imaging of pressure and temperature on surfaces. *Adv Funct Mater* **18**, 1399-1406, (2008).
- 135 Redford, G. I. Imaging tumor cells using a fast fluorescence lifetime microscope. *Biophys J* **86**, 609a-609a, (2004).
- 136 Graves, E. E., Weissleder, R. & Ntziachristos, V. Fluorescence molecular imaging of small animal tumor models. *Curr Mol Med* **4**, 419-430, (2004).
- 137 Conklin, M. W., Provenzano, P. P., Eliceiri, K. W., Sullivan, R. & Keely, P. J. Fluorescence lifetime imaging of endogenous fluorophores in histopathology sections reveals differences between normal and tumor epithelium in carcinoma in situ of the breast. *Cell Biochem Biophys* **53**, 145-157, (2009).
- 138 Deliolanis, N. C. *et al.* In-vivo imaging of murine tumors using complete-angle projection fluorescence molecular tomography. *J Biomed Opt* **14**, -, (2009).
- 139 Vaupel, P., Kallinowski, F. & Okunieff, P. Blood flow, oxygen and nutrient supply, and metabolic microenvironment of human tumors: A review. *Cancer Res* **49**, 6449-6465, (1989).
- 140 Lee, S. K. & Okura, I. Photoluminescent determination of oxygen using metalloporphyrin-polymer sensing systems. *Spectrochim Acta A* **54**, 91-100, (1998).
- 141 Wilson, D. F. & Cerniglia, G. J. Localization of tumors and evaluation of their state of oxygenation by phosphorescence imaging. *Cancer Res* **52**, 3988-3993, (1992).
- 142 Kerger, H., Torres, I. P., Rivas, M., Winslow, R. M. & Intaglietta, M. Systemic and subcutaneous microvascular oxygen-tension in conscious syrian golden-hamsters. *Am J Physiol-Heart C* **268**, 802-810, (1995).
- 143 Itoh, T., Yaegashi, K., Kosaka, T., Kinoshita, T. & Morimoto, T. In-vivo visualization of oxygen-transport in microvascular network. *Am J Physiol-Heart C* **267**, 2068-2078, (1994).
- 144 Stücker, M. *et al.* Flim of luminescent oxygen sensors: Clinical applications and results. *Sensors and Actuators B: Chemical* **51**, 171-175, (1998).

- 145 Hartmann, P., Ziegler, W., Holst, G. & Lubbers, D. W. Oxygen flux fluorescence lifetime imaging. *Sensor Actuat B-Chem* **38**, 110-115, (1997).
- 146 Smolle, J. *et al.* Non-invasive imaging of tissue po₂ in malignant melanoma of the skin. *Melanoma Research* **16**, 479-486, (2006).
- 147 Babilas, P. *et al.* Transcutaneous po₂ imaging during tourniquet-induced forearm ischemia using planar optical oxygen sensors. *Exp Dermatol* **17**, 265-265, (2008).
- 148 Geis, S. *et al.* Transcutaneous po₂ measurement during tourniquet-induced venous occlusion using dynamic phosphorescence imaging. *Clin Hemorheol Microcirc* **40**, 249-258, (2008).
- 149 Peterson, J. I. & Goldstein, S. R. Fiber optic ph sensor. *Fed Proc* **36**, 496-496, (1977).
- 150 Peterson, J. I., Goldstein, S. R., Fitzgerald, R. V. & Buckhold, D. K. Fiber optic ph probe for physiological use. *Analytical Chemistry* **52**, 864-869, (1980).
- 151 Jordan, D. M., Walt, D. R. & Milanovich, F. P. Physiological ph fiberoptic chemical sensor based on energy-transfer. *Analytical Chemistry* **59**, 437-439, (1987).
- 152 Wolthuis, R., Mccrae, D., Saaski, E., Hartl, J. & Mitchell, G. Development of a medical fiberoptic ph sensor based on optical-absorption. *Ieee T Bio-Med Eng* **39**, 531-537, (1992).
- 153 Kostov, Y., Tzonkov, S. & Yotova, L. Dynamic-model of an optical absorption-based ph sensor. *Analyst* **118**, 987-990, (1993).
- 154 Sotomayor, P. T., Raimundo, I. M., Neto, G. D. & de Oliveiira, W. A. Evaluation of fibre optical chemical sensors for flow analysis systems. *Sensor Actuat B-Chem* **51**, 382-390, (1998).
- 155 Lobnik, A., Majcen, N., Niederreiter, K. & Uray, G. Optical ph sensor based on the absorption of antenna generated europium luminescence by bromothymolblue in a sol-gel membrane. *Sensor Actuat B-Chem* **74**, 200-206, (2001).
- 156 Liu, Z. H., Liu, J. F. & Chen, T. L. Phenol red immobilized pva membrane for an optical ph sensor with two determination ranges and long-term stability. *Sensor Actuat B-Chem* **107**, 311-316, (2005).
- 157 BenDavid, O., Shafir, E., Gilath, I., Prior, Y. & Avnir, D. Simple absorption optical fiber ph sensor based on doped sol-gel cladding material. *Chem Mater* **9**, 2255-2257, (1997).
- 158 Saari, L. A. & Seitz, W. R. Ph sensor based on immobilized fluoresceinamine. *Analytical Chemistry* **54**, 821-823, (1982).
- 159 Weidgans, B. M., Krause, C., Klimant, I. & Wolfbeis, O. S. Fluorescent ph sensors with negligible sensitivity to ionic strength. *Analyst* **129**, 645-650, (2004).
- 160 Vasylevska, A. S., Karasyov, A. A., Borisov, S. M. & Krause, C. Novel coumarin-based fluorescent ph indicators, probes and membranes covering a broad ph range. *Anal Bioanal Chem* **387**, 2131-2141, (2007).
- 161 Whitaker, J. E., Haugland, R. P. & Prendergast, F. G. Spectral and photophysical studies of benzo[c]xanthene dyes - dual emission ph sensors. *Anal Biochem* **194**, 330-344, (1991).
- 162 Wolfbeis, O. S., Furlinger, E., Kroneis, H. & Marsoner, H. Fluorimetric analysis .1. A study on fluorescent indicators for measuring near neutral (physiological) ph-values. *Fresen Z Anal Chem* **314**, 119-124, (1983).
- 163 Xu, Z., Rollins, A., Alcalá, R. & Marchant, R. E. A novel fiber-optic ph sensor incorporating carboxy snaf1-2 and fluorescent wavelength-ratiometric detection. *J Biomed Mater Res* **39**, 9-15, (1998).
- 164 Zhujun, Z. & Seitz, W. R. A fluorescence sensor for quantifying ph in the range from 6.5 to 8.5. *Anal Chim Acta* **160**, 47-55, (1984).
- 165 Papkovsky, D. B., Ponomarev, G. V. & Wolfbeis, O. S. Protonation of porphyrins in liquid pvc membranes: Effects of anionic additives and application to ph-sensing. *J Photoch Photobio A* **104**, 151-158, (1997).
- 166 Liu, Z. H., Luo, F. L. & Chen, T. L. Polymeric ph indicators immobilized pva membranes for optical sensors of high basicity based on a kinetic process. *Anal Chim Acta* **519**, 147-153, (2004).

- 167 Wencel, D., MacCraith, B. D. & McDonagh, C. High performance optical ratiometric sol-gel-based ph sensor. *Sensor Actuat B-Chem* **139**, 208-213, (2009).
- 168 Rottman, C., Turniansky, A. & Avnir, D. Sol-gel physical and covalent entrapment of three methyl red indicators: A comparative study. *J Sol-Gel Sci Techn* **13**, 17-25, (1998).
- 169 Moreno, M. C., Jimenez, M., Conde, C. P. & Camara, C. Analytical performance of an optical ph sensor for acid-base titration. *Anal Chim Acta* **230**, 35-40, (1990).
- 170 Draxler, S. & Lippitsch, M. E. Effect of polymer matrices in lifetime based sensing. *Proc SPIE*, 363 - 368, (1995).
- 171 Werner, T. *et al.* Novel optical ph-sensor based on a boradiaz-indacene derivative. *Fresen J Anal Chem* **359**, 150-154, (1997).
- 172 Parker, J. W. *et al.* Fiberoptic sensors for ph and carbon-dioxide using a self-referencing dye. *Analytical Chemistry* **65**, 2329-2334, (1993).
- 173 Carofiglio, T., Fregonese, C., Mohr, G. J., Rastrelli, F. & Tonellato, U. Optical sensor arrays: One-pot, multiparallel synthesis and cellulose immobilization of ph and metal ion sensitive azo-dyes. *Tetrahedron* **62**, 1502-1507, (2006).
- 174 Kostov, Y., Tzonkov, S., Yotova, L. & Krysteva, M. Membranes for optical ph sensors. *Anal Chim Acta* **280**, 15-19, (1993).
- 175 Hanson, K. M. *et al.* Two-photon fluorescence lifetime imaging of the skin's stratum corneum ph gradient. *Biophys J* **82**, 494-494, (2002).
- 176 Wolfbeis, O. S., Kovács, B., Goswami, K. & Klainer, S. M. Fiber-optic fluorescence carbon dioxide sensor for environmental monitoring. *Microchim Acta* **129**, 181-188, (1998).
- 177 Arain, S. *et al.* Characterization of microtiterplates with integrated optical sensors for oxygen and ph, and their applications to enzyme activity screening, respirometry, and toxicological assays. *Sensor Actuat B-Chem* **113**, 639-648, (2006).
- 178 Arain, S., Ley, B. H. & Benz, K. Online monitoring of oxygen and ph during cell cultivation in multiwell plates. *Tissue Eng Pt A* **15**, 728-729, (2009).
- 179 Zhu, Q., Aller, R. C. & Fan, Y. High-performance planar ph fluorosensor for two-dimensional ph measurements in marine sediment and water. *Environ. Sci. Technol* **39**, 8906-8911, (2005).
- 180 Bassnett, S., Reinisch, L. & Beebe, D. C. Intracellular ph measurement using single excitation-dual emission fluorescence ratios. *Am J Physiol* **258**, C171-C178, (1990).
- 181 Bowyer, W. J., Xu, W. & Demas, J. N. Determining proton diffusion in polymer films by lifetimes of luminescent complexes measured in the frequency domain. *Anal Chem* **81**, 378-384, (2009).
- 182 Niesner, R. *et al.* 3d-resolved investigation of the ph gradient in artificial skin constructs by means of fluorescence lifetime imaging. *Pharm Res* **22**, 1079-1087, (2005).
- 183 Carlsson, K. & Liljeborg, A. Simultaneous confocal lifetime imaging of multiple fluorophores using the intensity-modulated multiple-wavelength scanning (ims) technique. *J Microsc* **191**, 119-127, (1998).
- 184 Ohman, H. & Vahlquist, A. In vivo studies concerning a ph gradient in human stratum corneum and upper epidermis. *Acta Derm Venereol* **74**, 375-379, (1994).
- 185 Behne, M. J. *et al.* Nhe1 regulates the stratum corneum permeability barrier homeostasis. Microenvironment acidification assessed with fluorescence lifetime imaging. *J Biol Chem* **277**, 47399-47406, (2002).
- 186 Zhang, X., Lin, Y. & Gillies, R. J. Tumor ph and its measurement. *J Nucl Med* **51**, 1167-1170, (2010).
- 187 Nakabayashi, T., Wang, H.-P., Kinjo, M. & Ohta, N. Application of fluorescence lifetime imaging of enhanced green fluorescent protein to intracellular ph measurements. *Photoch Photobio Sci* **7**, 668-670, (2008).
- 188 Niesner, R. *et al.* 3d-resolved investigation of the ph gradient in artificial skin constructs by means of fluorescence lifetime imaging. *Pharm Res-Dord* **22**, 1079-1087, (2005).

- 189 Hulth, S., Aller, R. C., Engstrom, P. & Selander, E. A ph plate fluorosensor (optode) for early diagenetic studies of marine sediments. *Limnol Oceanogr* **47**, 212-220, (2002).
- 190 Liebsch, G., Klimant, I., Krause, C. & Wolfbeis, O. S. Fluorescent imaging of ph with optical sensors using time domain dual lifetime referencing. *Analytical Chemistry* **73**, 4354-4363, (2001).
- 191 Cardwell, T. J., Cattrall, R. W., Deady, L. W., Dorkos, M. & Oconnell, G. R. A fast response membrane-based ph indicator optode. *Talanta* **40**, 765-768, (1993).
- 192 Safavi, A. & Sadeghi, M. Development of an optode membrane for high ph values. *Spectrochim Acta A* **66**, 575-577, (2007).
- 193 Schroder, C. R., Weidgans, B. M. & Klimant, I. Ph fluorosensors for use in marine systems. *Analyst* **130**, 907-916, (2005).
- 194 Stahl, H. *et al.* Time-resolved ph imaging in marine sediments with a luminescent planar optode. *Limnol Oceanogr-Meth* **4**, 336-345, (2006).
- 195 Stich, M. I. J., Borisov, S. M., Henne, U. & Schaferling, M. Read-out of multiple optical chemical sensors by means of digital color cameras. *Sensor Actuat B-Chem* **139**, 204-207, (2009).
- 196 Wolfbeis, O. S., Weis, L. J., Leiner, M. J. P. & Ziegler, W. E. Fiber-optic fluorosensor for oxygen and carbon-dioxide. *Analytical Chemistry* **60**, 2028-2030, (1988).
- 197 Borisov, S. M., Vasylevska, A. S., Krause, C. & Wolfbeis, O. S. Composite luminescent material for dual sensing of oxygen and temperature. *Adv Funct Mater* **16**, 1536-1542, (2006).
- 198 Hradil, J., Davis, C., Mongey, K., McDonagh, C. & MacCraith, B. D. Temperature-corrected pressure-sensitive paint measurements using a single camera and a dual-lifetime approach. *Meas Sci Technol* **13**, 1552-1557, (2002).
- 199 Nagl, S. & Wolfbeis, O. S. Optical multiple chemical sensing: Status and current challenges. *The Analyst* **132**, 507 (2007).
- 200 Kose, M. E., Omar, A., Virgin, C. A., Carroll, B. F. & Schanze, K. S. Principal component analysis calibration method for dual-luminophore oxygen and temperature sensor films: Application to luminescence imaging. *Langmuir* **21**, 9110-9120, (2005).
- 201 Borisov, S. M., Krause, C., Arain, S. & Wolfbeis, O. S. Composite material for simultaneous and contactless luminescent sensing and imaging of oxygen and carbon dioxide. *Adv Mater* **18**, 1511, (2006).
- 202 Kane, J. *US Pat.*, 4785814, (1988).
- 203 Tian, Y. *et al.* Dually fluorescent sensing of ph and dissolved oxygen using a membrane made from polymerizable sensing monomers. *Sensors and Actuators B: Chemical* **147**, 714-722, (2010).
- 204 Kocincova, A. S., Borisov, S. M., Krause, C. & Wolfbeis, O. S. Fiber-optic microsensors for simultaneous sensing of oxygen and ph, and of oxygen and temperature. *Analytical Chemistry* **79**, 8486-8493, (2007).
- 205 Vasylevska, G. S., Borisov, S. M., Krause, C. & Wolfbeis, O. S. Indicator-loaded permeation-selective microbeads for use in fiber optic simultaneous sensing of ph and dissolved oxygen. *Chem Mater* **18**, 4609-4616, (2006).
- 206 Schroder, C. R., Polerecky, L. & Klimant, I. Time-resolved ph/po(2) mapping with luminescent hybrid sensors. *Analytical Chemistry* **79**, 60-70, (2007).
- 207 Stich, M. I. J. Preparation and calibration of pressure-sensitive and temperature-sensitive paints for fluorescence lifetime imaging applications. *Ph.D. Thesis, University of Regensburg*, page 18, (2009).
- 208 de Carvalho, I. M. M., Diogenes, I. C. N., Moreira, I. D. & Gehlen, M. H. Effect of the ph in the luminescence of ruthenium tris-bipyridine derivatives. *J Photoch Photobio A* **171**, 107-112, (2005).
- 209 Bai, G. Y., Wang, K. Z., Duan, Z. M. & Gao, L. H. Luminescent ph sensing and DNA binding properties of a novel ruthenium(ii) complex. *J Inorg Biochem* **98**, 1017-1022, (2004).

- 210 Clarke, Y., Xu, W. Y., Demas, J. N. & DeGraff, B. A. Lifetime-based pH sensor system based on a polymer supported ruthenium(II) complex. *Analytical Chemistry* **72**, 3468-3475, (2000).
- 211 Kosch, U., Klimant, I. & Wolfbeis, O. S. Long-lifetime based pH micro-optodes without oxygen interference. *Fresen J Anal Chem* **364**, 48-53, (1999).
- 212 Schäferling, M. & Duerkop, A. Springer series on fluorescence, vol 5: Intrinsically referenced fluorimetric sensing and detection schemes: Methods, advantages and applications. *Springer, Berlin*, 373-414, (2008).
- 213 Lakowicz, J. R., Szmacinski, H., Nowaczyk, K., Berndt, K. W. & Johnson, M. Fluorescence lifetime imaging. *Anal Biochem* **202**, 316-330, (1992).
- 214 Lakowicz, J. R. Principles of fluorescence spectroscopy 2nd edition. *Springer, Berlin*, (1999).
- 215 Liebsch, G., Klimant, I., Frank, B., Holst, G. & Wolfbeis, O. S. Luminescence lifetime imaging of oxygen, pH, and carbon dioxide distribution using optical sensors. *Appl Spectrosc* **54**, 548-559, (2000).
- 216 Hartmann, P. & Ziegler, W. Lifetime imaging of luminescent oxygen sensors based on all-solid-state technology. *Anal. Chem* **68**, 4512-4514, (1996).
- 217 Ballew, R. M. & Demas, J. N. An error analysis of the rapid lifetime determination method for the evaluation of single exponential decays. *Analytical Chemistry* **61**, 30-33, (1989).
- 218 Chan, S. P., Fuller, Z. J., Demas, J. N. & DeGraff, B. A. Optimized gating scheme for rapid lifetime determinations of single-exponential luminescence lifetimes. *Analytical Chemistry* **73**, 4486-4490, (2001).
- 219 Chan, S. P., Fuller, Z. J., Demas, J. N., Ding, F. & DeGraff, B. A. New method of rapid luminescence lifetime determination using square-wave excitation. *Appl Spectrosc* **55**, 1245-1250, (2001).
- 220 Sharman, K. K., Periasamy, A., Ashworth, H., Demas, J. N. & Snow, N. H. Error analysis of the rapid lifetime determination method for double-exponential decays and new windowing schemes. *Analytical Chemistry* **71**, 947-952, (1999).
- 221 Moore, C., Chan, S. P., Demas, J. N. & DeGraff, B. A. Comparison of methods for rapid evaluation of lifetimes of exponential decays. *Appl Spectrosc* **58**, 603-607, (2004).
- 222 Woods, R. J., Scypinski, S., Love, L. J. C. & Ashworth, H. A. Transient digitizer for the determination of microsecond luminescence lifetimes. *Analytical Chemistry* **56**, 1395-1400, (1984).
- 223 Wang, X. F., Uchida, T., Coleman, D. M. & Minami, S. A 2-dimensional fluorescence lifetime imaging-system using a gated image intensifier. *Appl Spectrosc* **45**, 360-366, (1991).
- 224 Demas, J. N., Jones, W. M. & Keller, R. A. Elimination of quenching effects in luminescence spectrometry by phase resolution. *Analytical Chemistry* **58**, 1717-1721, (1986).

2. Instruments and Methods

2.1 pH meter

The pH values of solutions for the calibration experiments were determined using a digital GC 840 pH meter with internal temperature compensation from Schott (Mainz, Germany; www.schott.com). The pH meter was calibrated with standard buffer solutions of pH 7.00 and pH 4.00 from Carl Roth at $T = 20 \pm 2$ °C. pH measurements for *in vivo* experiments were conducted using a mobile Handylab 12 pH meter along with a Blue Line 27 flat membrane pH electrode (both Schott). The Blue Line 27 electrode has a flat diaphragm on the glass electrode tip that allows for measurements on various kinds of surfaces like skin, leather, paper and textiles.

2.2 Knife coating devices for sensor fabrication

Two different knife coating devices were used to fabricate the planar sensor films. A first device (**Fig. 2.1**) serves for preparing standard sized sensor foils of a maximum size of 4 cm x 8 cm.

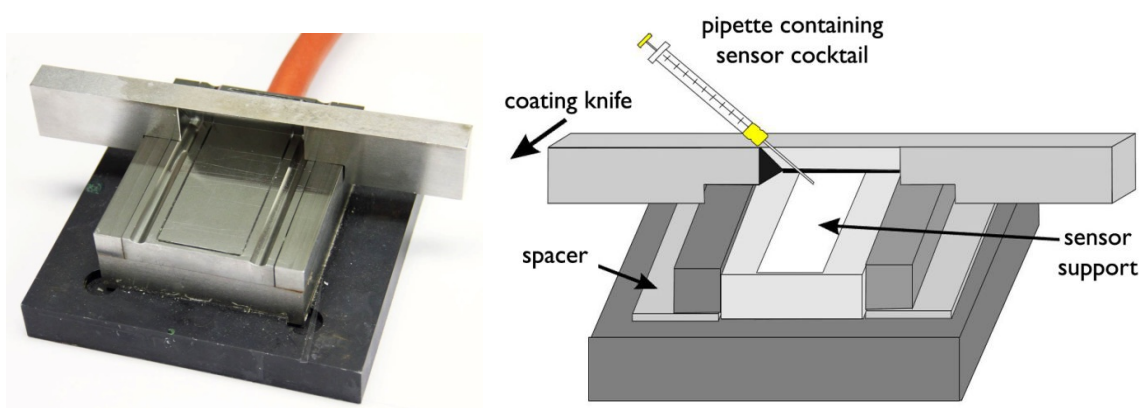


Figure 2.1 | Photo (left) and schematic drawing (right) of the knife coating device for standard sizes.

A dust free sensor support (consisting of a poly(ethylene glycol terephthalate MYLAR[®] foil or a poly(vinylidene chloride) SARAN[®] wrap) is placed on the surface of the knife coating device. Vacuum assures excellent contact of the foil and the device. It prevents bubbles and thus resultant inhomogeneous sensor layer thickness. The spacer consists on the one hand of the sensor support and on the other hand of additional spacers to adjust the desired wet film thickness of the sensor membrane. The sensor cocktail is pipetted onto the sensor support and subsequently spread over the support using the coating knife. The sensors remain on the device for evaporation of the matrix solvent.

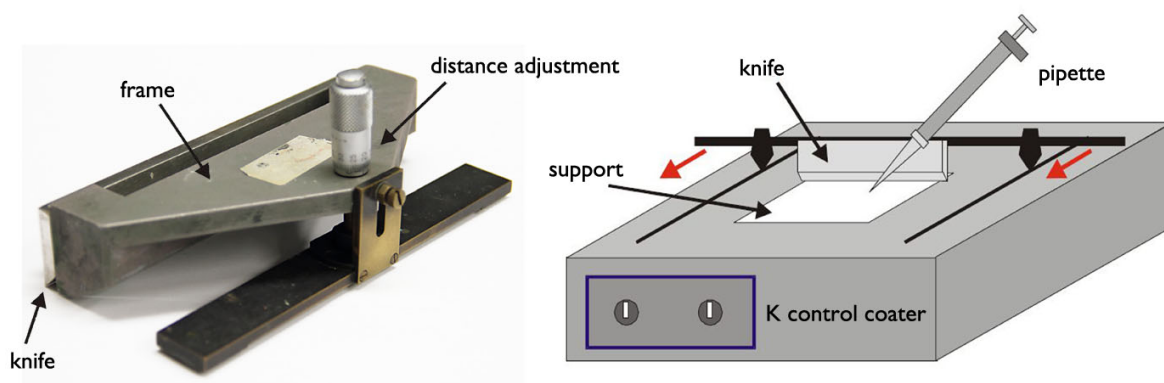


Figure 2.2 | Photo of the custom-made knife (left) and the K control coater.

A second device (**Fig. 2.2**) for fabrication of large scale *in vivo* sensors of scales up to 12 cm x 20 cm consists of a K Control Coater model 101 knife coating device (RK Print-Coat Instruments Ltd., Litlington, UK) and a custom-made coating knife. The SARAN[®] foil is adapted to the surface of the K control coater. The surface of the coater is previously wetted with ethanol and bubbles underneath the foil were removed by smoothing out the foil with a moist (ethanol) kitchen roll. The wet layer thickness of the film is defined using an adjustable screw on the coating knife slide. The micrometer screw varies the tilt angle of the slide and thus changes the distance between knife and sensor support foil.

2.3 Spectrometers

2.3.1 Absorbance measurements

Absorbance spectra were acquired on a Cary 50 Bio UV-visible spectrophotometer from Varian (Agilent Technologies Inc., Santa Clara, CA, USA; www.agilent.com). Measurements were performed in standard quartz cuvettes (1 x 1 x 3 cm) with the samples being diluted up to 1 ml.

2.3.2 Fluorescence spectrometer

Fluorescence measurements, as well as emission and absorption measurements of particles in sensor films were realized using an Aminco Bowman AB2 luminescence spectrometer (Thermo Spectronic, Rochester, NY, USA; www.thermo.com) equipped with a 150-W continuous wave xenon lamp as the excitation source. Fluorescence spectra from solutions or suspensions were recorded in standard fluorescence or semi micro cuvettes. Particles in films were investigated with the AB2 spectrometer along with fibre optics and a custom-made flow through cell (**Fig. 2.3**)

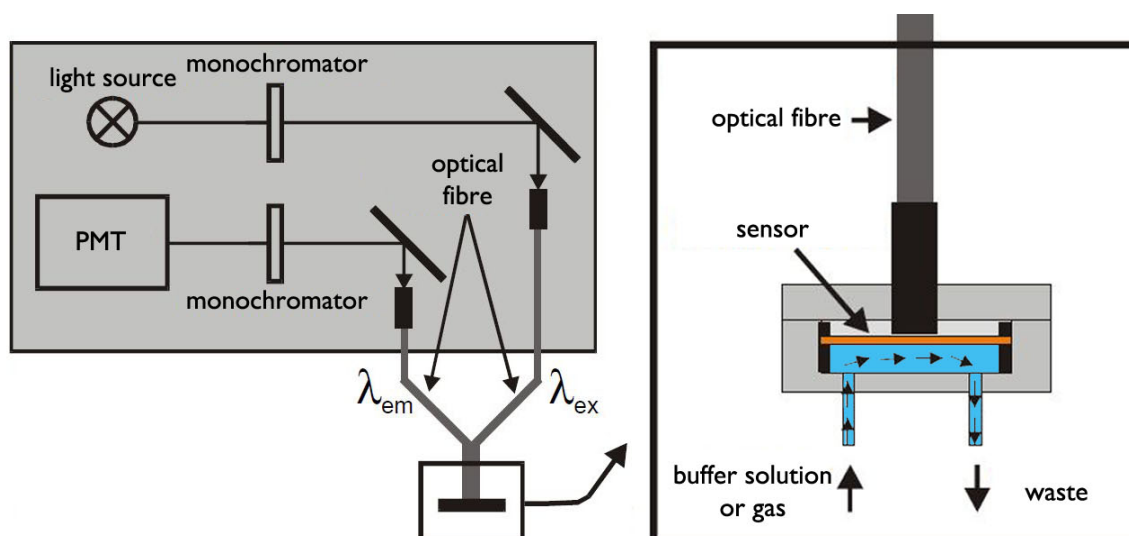


Figure 2.3 | Schematic drawing of the fluorescence spectrometer combined with fibre optics and a custom-made flow through cell.

The excitation light passes a monochromator, is coupled into one branch of a bifurcated fiber bundle. The end of the fiber is positioned in the flow through cell pointing at the backside of a sensor. The sensor responds to passing buffer solutions or gases flowing through the cell. The buffer solutions were transported to the sensor film by a peristaltic pump (Minipuls; Gilson Inc., Middleton, WI, USA; www.gilson.com). Gas atmospheres were generated using a gas mixing device (MKS; Andover, MA, USA www.mksinst.com). Emission light of the photoexcited sensor is guided back to the spectrometer via the other branch of the fiber, passes a monochromator and is gathered by a photo multiplier tube.

2.4 Calibration chamber

The calibrations of pO_2 , pH and dual sensors were accomplished in a custom-made calibration chamber (**Fig. 2.4**). The chamber is temperature controlled by a Lauda Ecoline RE 104 (Lauda, Lauda-Königshofen, Germany; www.lauda.de). The defined oxygen atmospheres in the chamber were generated by a MKS gas mixing device using nitrogen, oxygen and argon gasses from Linde (Pullach, Germany; www.linde-gase.de) under atmospheric pressure.

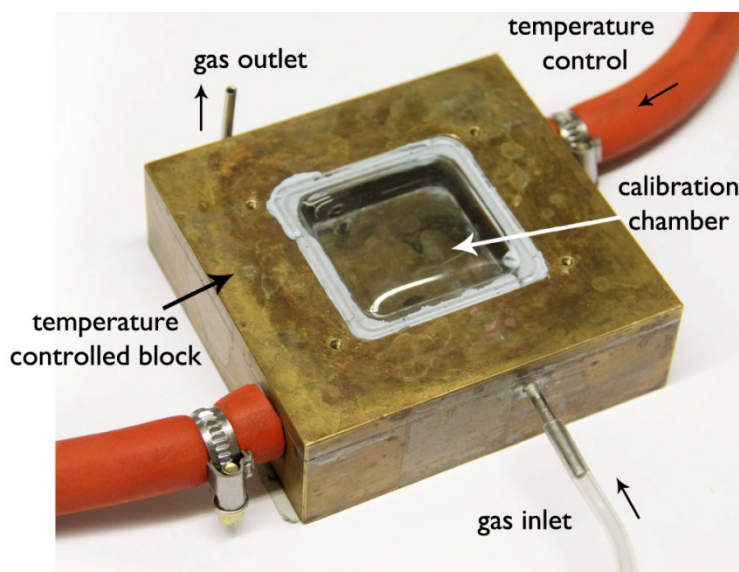


Figure 2.4 |
Custom-made calibration chamber.

2.5 Time-gated imaging setup

The principle of the time-gated imaging setup is shown in **Fig. 2.5**. A sensor is excited with a light source that passes an excitation filter. The emitted light is filtered through an emission filter in order to block reflected excitation light or undesired signals of other wavelengths from the sensor response. The emitted and filtered light is collected on a grayscale camera. The images are processed on a computer. The detailed basic principle of imaging setups used for time-gated 2D imaging (RLD and tdDLR) is described by Liebsch¹, Holst², Schröder³, and Nagl⁴. In this section a short overview on adaptations and modifications made is given.

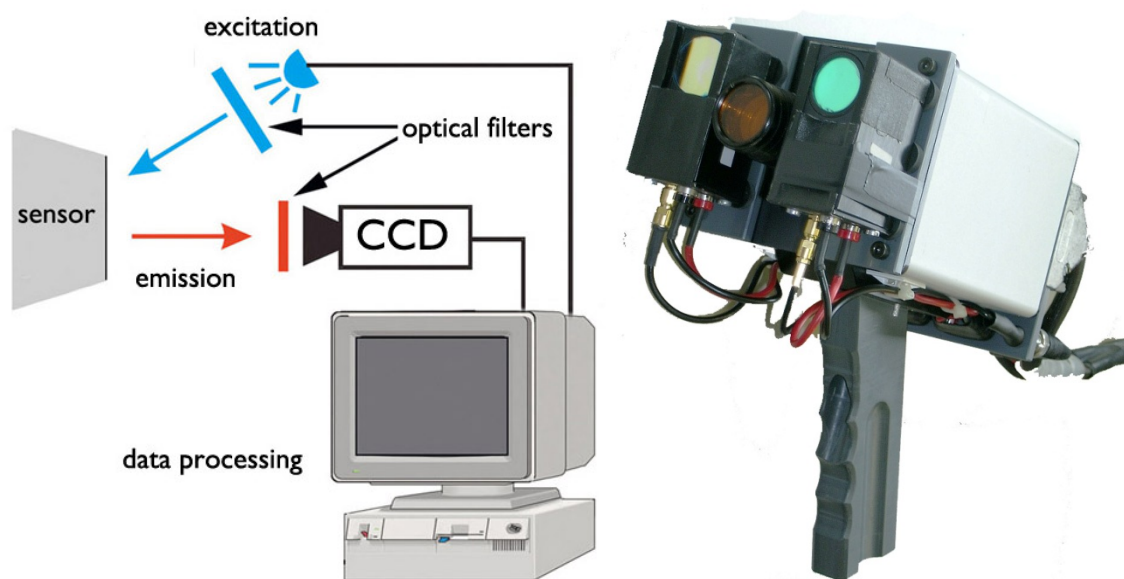


Figure 2.5 | Scheme of the imaging setup (left) and a photo of the camera head equipped with excitation LEDs and filters (right).

A customized setup based on an ImageX Time-gated Imaging system (TGI, Photonic Research Systems, Salford, UK; www.prsbio.com) is used in this work. The system is equipped with a cooled 12 bit CCD chip camera with a resolution of 640*480 pixels. The camera is able to shutter time gates of a minimum of 0.2 μ s. The camera is sensitive to light of wavelengths ranging from 350 nm to 900 nm with a higher sensitivity in the range

of 430 to 700 nm. The camera is able to image and detect signals even IR light emitting probes. A custom-made handhold is attached on the camera head, to ease measurements in clinical applications. The camera is combined with a light emitting 460 nm LED array (Luxeon V Star LXHL-LB5C, 5W, Philips Lumileds Lighting Company, San Jose, CA, USA; www.philipslumileds.com). The LEDs are directly mounted on the customized camera head to minimize the size of the imaging system. FITCA filters (Schott) for excitation filter excitation light. A filter holder for easy change of emission filters is mounted on the camera lens. A 1.4 / 16mm Pentax TV lens (Pentax Europe GmbH, Hamburg, Germany, www.pentaxcctvus.com) is used. Focal distance starts from 8 to 80 cm. Data is processed using ImageX software (Microsoft Corporation, Redmond, WA, USA; www.microsoft.com)

2.6 RGB imaging setup

A straightforward imaging system for referenced FRIM measurements is developed. The setup comprises only of a standard digital camera equipped with a battery-operated ring light for excitation and an emission filter. The principle of the RGB imaging setup is shown in **Fig 2.6**.

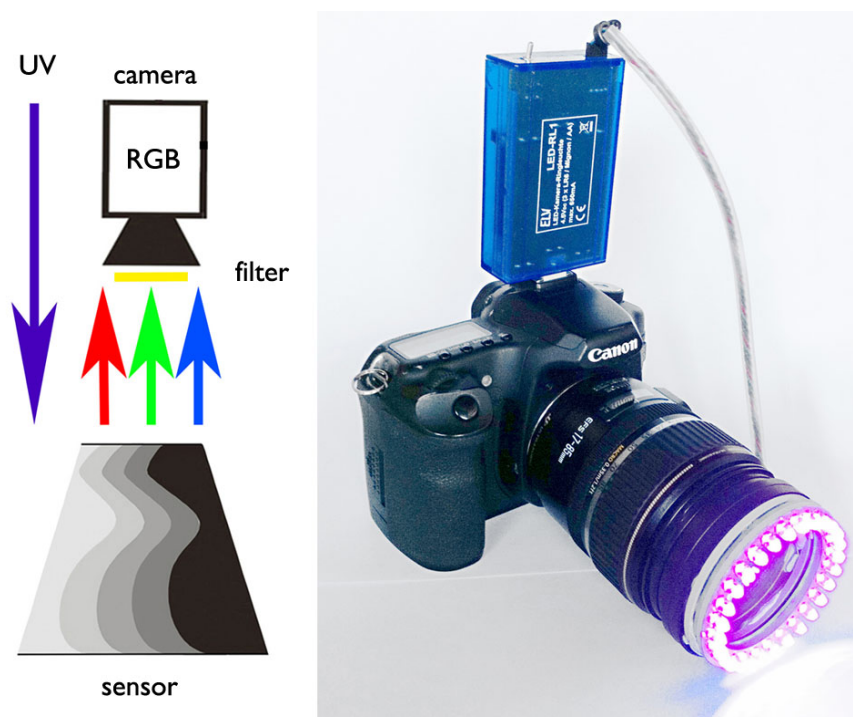


Figure 2.6 | *Left: Scheme of the RGB imaging setup. Right: a photo of the camera equipped with ring of UV-LEDs, filters and an electricity supply in the flash hotshoe (right).*

In this work either a Canon EOS model 50D (see **Fig 2.6**) or a model 550D (Canon Inc., Tokio, Japan; www.canon.com) are used for image acquisition. Both cameras allow for capturing images in RAW file type (.cr2) that offers a full 14 bit color depth. The model 550D even allows for recording RGB videos. The camera is equipped with a Canon EF-S 17-85 mm 1:4-5.6 IS USM or a EF-S 18-135 mm 1:3.5-5.6 IS standard canon zoom lens. The excitation source consists of a customized camera ring light (LED-RL 1, ELV Elektronik, Leer, Germany, www.elv.de). The white LEDs of the system were replaced by 28 UV-LEDs (UV5TZ-405-15, BIVAR Inc., Irvine, CA, USA, www.bivar.com) with a peak wavelength of 405 nm. The LEDs are battery operated using three 1.5 V mignon batteries. The viewing angle of the LEDs is 15°, which offers a virtually homogeneous light field in approximately 20 cm distance. The minimal focal distance of the lens is 30 cm. The minimal measurement distance is 20 cm if the camera is equipped with a +2 close-up lens. The electricity supply allows for wireless imaging with constant light intensity for more than 6 hours. The ring light is mounted on the lens via a 67 mm filter adapter. The filter adapter also includes the emission filter (Schott GG435 high pass filter) that blocks scattered light from the excitation light source.

2.7 References

- 1 Liebsch, G. Time-resolved luminescence lifetime imaging with optical chemical sensors: Set-up, controlling, concepts and applications *Ph.D. Thesis, University of Regensburg*, (2000).
- 2 Holst, G. & Grunwald, B. Luminescence lifetime imaging with transparent oxygen optodes. *Sensor Actuat B-Chem* **74**, 78-90, (2001).
- 3 Schröder, C. R. Luminescent planar single and dual optodes for time-resolved imaging of ph, pco₂ and po₂ in marine systems. *Ph.D. Thesis, University of Regensburg*, (2006).
- 4 Nagl, S. Fluorescent multiple chemical sensing using time-domain fluorescent lifetime imaging. *Ph.D. Thesis, University of Regensburg*, (2008).

3. 2D luminescence imaging of pH in vivo

Luminescence imaging of biological parameters is an emerging field in biomedical sciences. Tools to study two-dimensional (2D) pH distribution are needed to gain new insights into complex disease processes, such as wound healing and tumor metabolism. In recent years, luminescence-based methods for pH measurement have been developed. However, for in vivo applications, especially for studies on humans, biocompatibility and reliability under varying conditions have to be ensured. Here we present a referenced luminescent sensor for 2D high-resolution imaging of pH in vivo. The ratiometric sensing scheme is based on time-domain luminescence imaging of fluorescein isothiocyanate (FITC) and ruthenium(II)tris-(4,7-diphenyl-1,10-phenanthroline) [Ru(dpp)₃]. To create a biocompatible 2D sensor, these dyes were bound to or incorporated into microparticles (aminocellulose, polyacrylonitrile) and particles were immobilized in polyurethane hydrogel on transparent foils. We demonstrate sensor precision and validity by conducting in vitro and in vivo experiments, and show the versatility in imaging pH during physiological and chronic cutaneous wound healing in humans. Implementation of this technique may open new vistas in wound healing, tumor biology and other biomedical fields. (Proc Natl Acad Sci USA, 2011 vol. 108 no. 6 2432-2437).

3.1 Introduction

There is great interest in luminescence imaging of essential biological parameters, such as pH, pO₂, hydrogen peroxide (H₂O₂), and Ca²⁺ at the moment¹⁻⁶. Recently, luminescence-based methods for pH measurement have been developed^{7,8}. However, a method for *in vivo* studies on human subjects has not yet been realized. The major challenges for *in vivo* applications are that biocompatibility and reliability under varying conditions (illumination, oxygen, and temperature) have to be ensured. The standard tool for pH

measurement, the glass electrode⁹, is not approved for clinical use and only allows single-spot measurements, which make 2D imaging impossible.

Multiple methods for pH imaging exist: ratiometric luminescent pH detection is a straightforward and referenced approach, which has been used, for instance, to measure intracellular pH. In these works, either combinations of dextran-conjugated indicator and reference dyes (fluorescein/tetramethylrhodamine, pHrodo/rhodamine-green), or SNARF (seminaphtho-rhodafluor) derivatives have been used¹⁰⁻¹². However, to obtain 2D-images, either modifications of the optical system during measurements or the use of an image splitter are necessary to separate the signals. Ratiometric methods may suffer from Förster resonance energy transfer (FRET), and most importantly from differential photobleaching of indicator/reference dyes. The latter problem may be avoided by using intrinsically referenced luminescence lifetime imaging (LLI) of one single pH-indicator. LLI has been used for high-resolution 2D- and 3D-pH mapping in studies on cells, tissue samples, and artificial skin constructs^{13,14}. These techniques are, however, difficult to implement in studies on live human subjects, because of long scanning times, highly sophisticated measurements setups (confocal microscope, laser, etc.), and the necessity of a spatially fixed sample. Furthermore, most scanning techniques are invasive, as the luminophores have to be in direct contact with the sample¹⁵. Additionally, pH-imaging probes based on ¹H, ³¹P, and ¹³C have been developed for magnetic resonance spectroscopy (MRS) of tumor pH, but (i) the low sensitivity of spectroscopy, (ii) the oftentimes small pH-induced chemical shift of these agents, and (iii) the complex measurement system make it (i) hard to create high-resolution images with (ii) precise pH values at clinical magnetic field strengths in (iii) routine clinical settings¹⁶⁻¹⁸.

To date, no pH sensor exists that detects pH over a wide proton concentration range, allows for fast micro- and macroscopic 2D-pH imaging, is non-invasive and biocompatible for *in vivo* use on humans. We developed a 2D-pH sensor that meets these requirements. The prerequisites included (i) the use of a referenced method, since *in vivo* conditions are quite variable, (ii) non-toxic and easily applicable materials, (iii) a dynamic range of pH 3 to 9, and (iv) a non-invasive method, so to be suitable for clinical applications.

For *in vitro* characterization, we conducted calibration experiments under varying conditions (pO₂ and temperature changes) and studied the (spatio)temporal resolution. To evaluate the precision and validity *in vivo*, we measured the pH gradient in the *stratum corneum* (SC) after tape stripping of the SC on the volar forearm and compared the results with data obtained using the standard glass electrode. Additionally, we applied the sensor to a routine clinical problem, i.e. cutaneous wound healing, to demonstrate its potential and superiority in comparison to the glass electrode⁹. We used split-thickness skin graft donor sites as standardized cutaneous wounds and measured the pH over the time course of physiological healing. To accent the potential for 2D imaging, we visualized the pH distribution within a chronic cutaneous wound. We chose cutaneous wound healing as a first *in vivo* application for the luminescent pH sensor because the wound fluid¹⁹ and its varying pH are known to greatly affect healing²⁰⁻²². Despite the fact that there are numerous new findings in wound healing²³, knowledge on basic clinical parameters like pH is still missing in literature, which is obviously due to the lack of appropriate tools for 2D-pH imaging *in vivo*. The importance to study basic biological parameters in wound healing is highlighted by the fact that H₂O₂ gradients have recently been found to be essential for immediate leukocyte recruitment to the wound site after tissue injury⁵.

Additionally, pH has a major impact on the pathogenesis of chronic wounds, which often present an interdisciplinary treatment challenge. Apart from the impact on the quality of life of the patients affected, chronic wounds are a fundamental economic burden²⁴. About one third of the dermatological health budget in the United States is spent on the treatment of chronic wounds, more than for all oncological indications (melanoma, non-melanoma skin cancer) together²⁴. Therefore, *in vivo* studies of the pH distribution in tumor growth and metabolism are expected to be among the future applications for the luminescent 2D-pH sensor^{25,26}.

This article shows the development, *in vitro* characterization, *in vivo* validation, and clinical application of the first sensor for 2D luminescence imaging of pH in humans.

3.2 Results and Discussion

3.2.1 Luminescence imaging of pH

Imaging of pH is challenging as many of the pH-dependent luminophores exhibit luminescence lifetimes that are too short for LLI methods, which do not utilize microscopic scanning. To overcome this issue, we used time-domain dual lifetime referencing (tdDLR), a method previously described by our group⁸. Two simultaneously excitable luminophores with different lifetimes were chosen, fluorescein isothiocyanate (FITC, $\lambda_{\text{ex}} = 495 \text{ nm}$, $\lambda_{\text{em}} = 525 \text{ nm}$, singlet emission = fluorescence, $< 5 \text{ ns}$ lifetime) as the indicator and ruthenium(II)tris-(4,7-diphenyl-1,10-phenanthroline) [$\text{Ru}(\text{dpp})_3$, $\lambda_{\text{ex}} = 441 \text{ nm}$, $\lambda_{\text{em}} = 597 \text{ nm}$, triplet emission = phosphorescence, $\sim 6 \mu\text{s}$ lifetime] as the reference (Fig. 3.1).

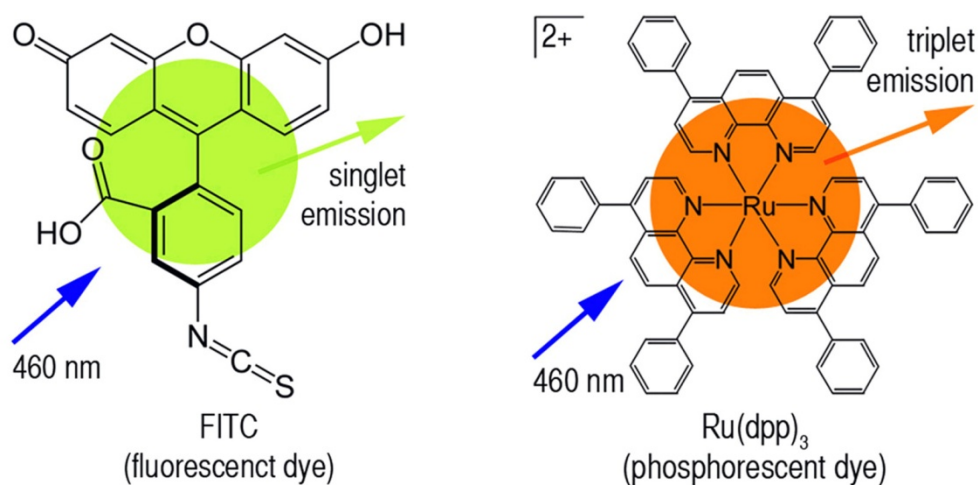


Figure 3.1 | Chemical structure of the indicator dye fluorescein isothiocyanate (FITC) and the reference dye ruthenium(II)tris-(4,7-diphenyl-1,10-phenanthroline) [$\text{Ru}(\text{dpp})_3$].

Both dyes can be excited at 460 nm with light emitting diodes (LED), which allows to image pH in one single excitation-emission cycle. Luminescence was recorded using a time-gated, charge-coupled device (CCD) camera with a 530 nm long-pass optical filter (Fig. 3.2).

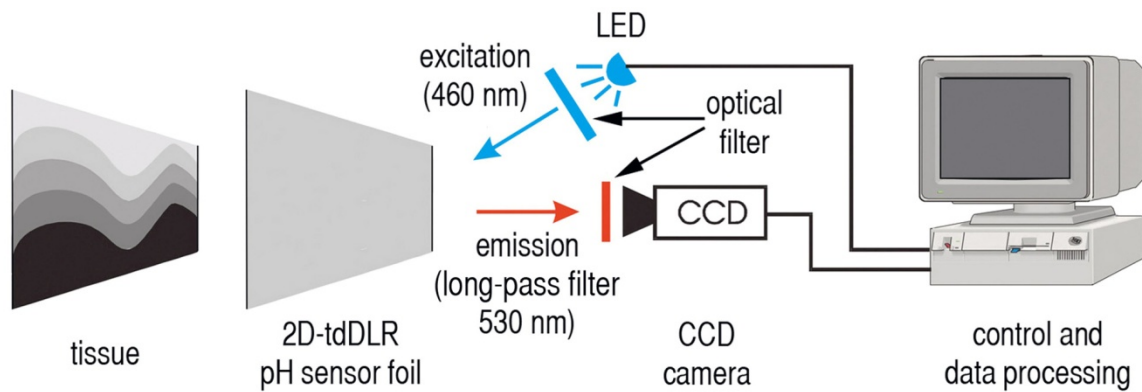


Figure 3.2 | The sensor foil is applied to the tissue, protons diffuse into the sensor and luminophores are excited (LED, $\lambda_{\text{ex}} = 460 \text{ nm}$). Time-gated luminescence intensities are recorded (530 nm long-pass optical filter) with a CCD camera, and subsequently data are processed.

The long-lasting phosphorescence of $\text{Ru}(\text{dpp})_3$ enables recording luminescence during the emission phase (LED off), whereas the combined luminescence of FITC and $\text{Ru}(\text{dpp})_3$ is detected during excitation (LED on). Thus, the pH-dependent FITC signal is referenced to the pH-independent $\text{Ru}(\text{dpp})_3$ signal. Luminescence intensity was integrated in two time gates: one during excitation (A_{ex}) and one during emission (A_{em}). Given the fact that during excitation the integrated signal intensity reflects the combination of FITC and $\text{Ru}(\text{dpp})_3$ signals, A_{ex} is $A_{\text{ex}}(\text{FITC}) + A_{\text{ex}}[\text{Ru}(\text{dpp})_3]$. However, 250 ns after turning the LED off, fluorescence of FITC has decayed, and only the phosphorescence signal of $\text{Ru}(\text{dpp})_3$ is detected, so that A_{em} is $A_{\text{em}}[\text{Ru}(\text{dpp})_3]$ (**Fig. 3.3**). The ratio R of $A_{\text{ex}}/A_{\text{em}}$ denotes a referenced integrated signal intensity⁸. Thus, little irregularities in particle distribution or illumination of the sensor do not alter the measured ratio R . This fact is a major advantage, especially if the density of the sensor particles differs locally, or if illumination cannot be controlled as precisely as in a laboratory setting.

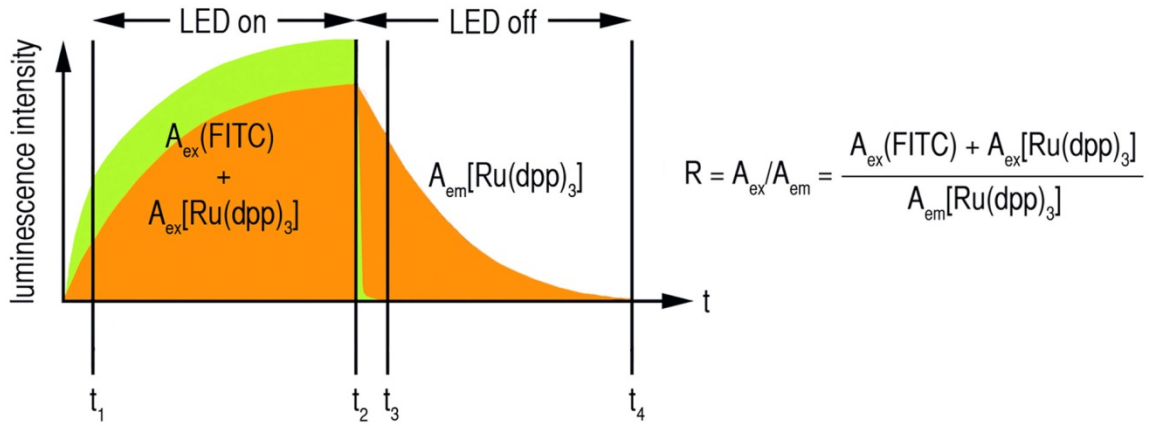


Figure 3.3 | *The sensor During excitation the combined luminescence intensity of FITC (green) and Ru(dpp)₃ (orange) is detected, whereas during the emission time gate only the luminescence intensity of Ru(dpp)₃ is detected. Luminescence intensity is recorded and integrated in two time gates, one during excitation (t₁-t₂, A_{ex}) and one during emission (t₃-t₄, A_{em}). A ratio R of A_{ex}/A_{em} allows to calculate pH from the respective five-parametric calibration curve obtained for each sensor (see Fig. 3.12).*

To calculate pH values based on the detected R , we calibrated each sensor and computed a five-parametric sigmoidal fit according to:

Equation (3.1):
$$R = \frac{a}{b + (c * e^{d * pH} + t)}$$

This enables the measurement of pH over a wide proton concentration range as not only the pseudo-linear part of the calibration curve is used. From the respective calibration curve, pH is calculated by solving the equation for pH:

Equation (3.2):
$$pH = \frac{\ln \left[\frac{b * (R + t) - a}{c * (t - R)} \right]}{d}$$

3.2.2 Material design

In contrast to other methods, our non-invasive approach ensures high biocompatibility for *in vivo* use. A three-step safety system was introduced: (i) luminophores were covalently bound to or encapsulated in biologically inert particles to prevent leaching of the luminophores, (ii) particles were immobilized in a biocompatible matrix on transparent foils to prevent particle leakage into tissues (**Fig. 3.4**), and (iii) particles were synthesized to have a minimal size of 0.5 μm in diameter to hamper or at least to slow down the process of possible cellular uptake.

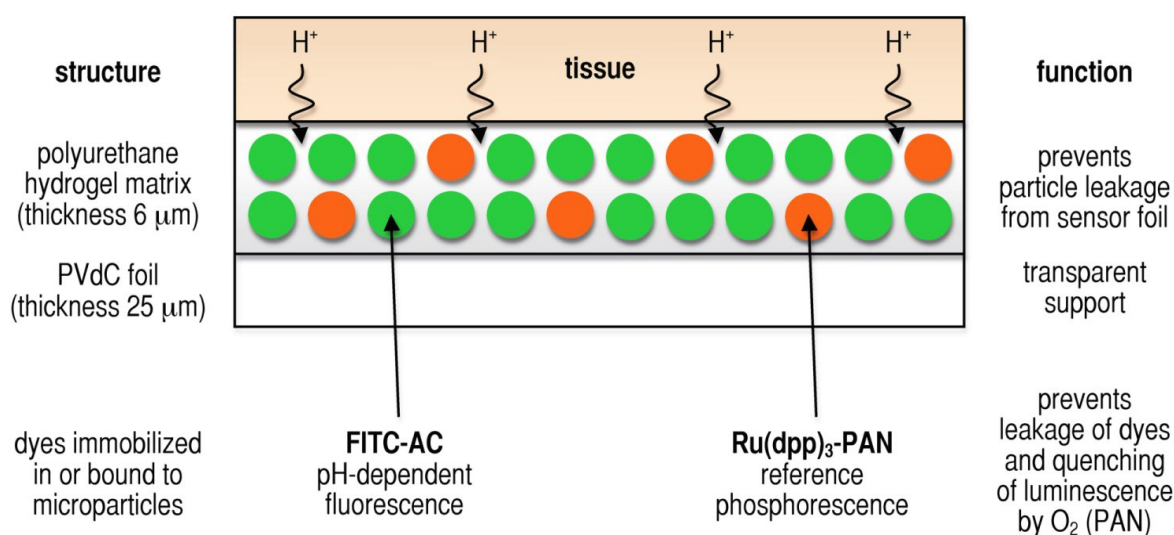


Figure 3.4 | A schematic view of a sensor foil is shown. Particles are embedded in a hydrogel matrix on transparent PVdC foils, thereby preventing particle leakage. Foils are applied to tissues with the hydrogel coated surface. Protons diffuse into the hydrogel matrix and towards the microparticles. The transparency of the foils allows simultaneously observing the underlying anatomic structures.

Therefore, FITC was covalently bound to aminocellulose (AC) particles (FITC-AC, 0.75 to 8 μm , **Fig. 3.5A**) and Ru(dpp)₃ was physically entrapped (hydrophobic interactions) in polyacrylonitrile particles [Ru(dpp)₃-PAN, 0.5 to 1 μm , **Fig. 3.5B**].

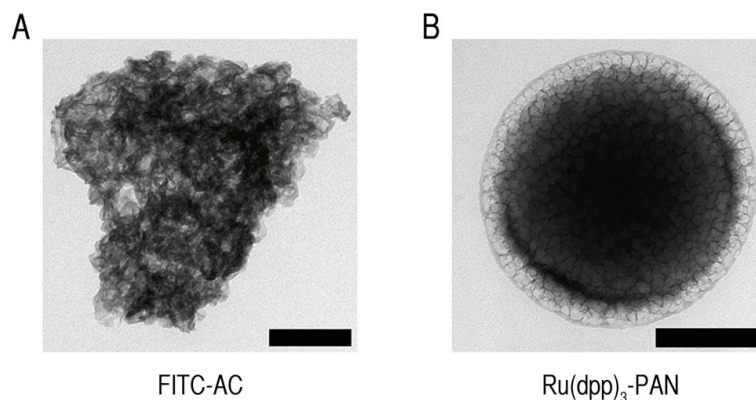


Figure 3.5 | Transmission electron microscopic (TEM) images of (A) fluorescein isothiocyanate bound to aminocellulose particles (FITC-AC) and (B) ruthenium(II)tris-(4,7-diphenyl-1,10-phenanthroline) incorporated into polyacrylonitrile particles [Ru(dpp)₃-PAN]. (Scale bars, 200 nm).

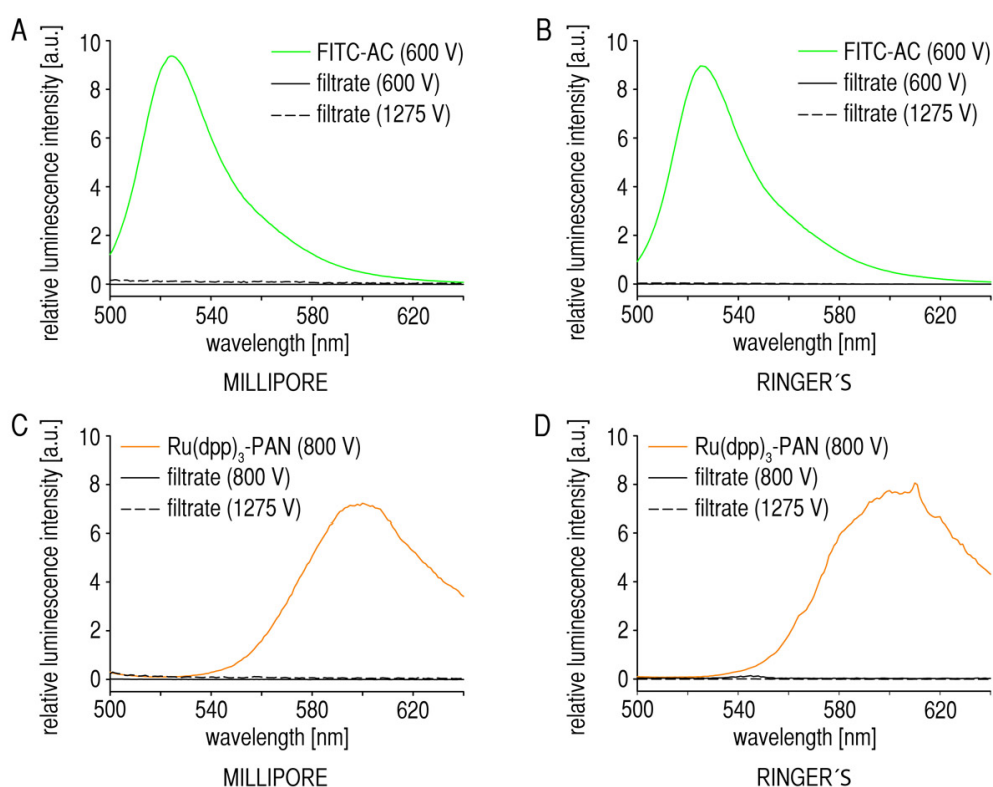


Figure 3.6 | Results of leaching experiments for both dyes in Millipore water (A,C) and Ringer's solution (B,D). Colored lines represent the spectra of the particle suspension; solid lines equal the spectra of the centrifuged and filtered solutions with constant detector gain. Dashed lines (full detector gain) show the lack of dye traces in filtered solutions. Thus, no leaching of dyes out of the particles occurred. (a.u. = arbitrary units).

Thus, leakage of dyes is prevented (**Fig. 3.6**). AC was chosen because it (i) offers amino groups to covalently bind FITC, (ii) is a hydrophilic polymer that allows fast proton diffusion for a quick sensor response, and because (iii) FITC exhibits a high singlet quantum yield in hydrophilic environments ($\phi_{\text{singlet}} = 0.97$ in H_2O)²⁷. The conjugation of FITC to AC shifts the pK_a of fluorescein from 6.8 to 5.9. Residual amino groups of AC were blocked with acetic anhydride to remove surface charges that may alter sensor response. PAN is a hydrophobic polymer which is impermeable to oxygen (oxygen diffusion coefficient P $0.00015 \cdot 10^{-13} \text{ cm}^2 \cdot \text{Pa} \cdot \text{s}^{-1}$)^{28,29}, thus preventing the quenching of reference luminescence and also the formation of reactive oxygen species (ROS), such as singlet oxygen (see below under biocompatibility). The encapsulation in PAN would also prevent FRET in case of a significant overlap between the luminescence spectra of certain dyes, but FRET is not an issue with the dyes used in this work. The spectra of the dyes immobilized in the particles are shown in **Fig. 3.7**.

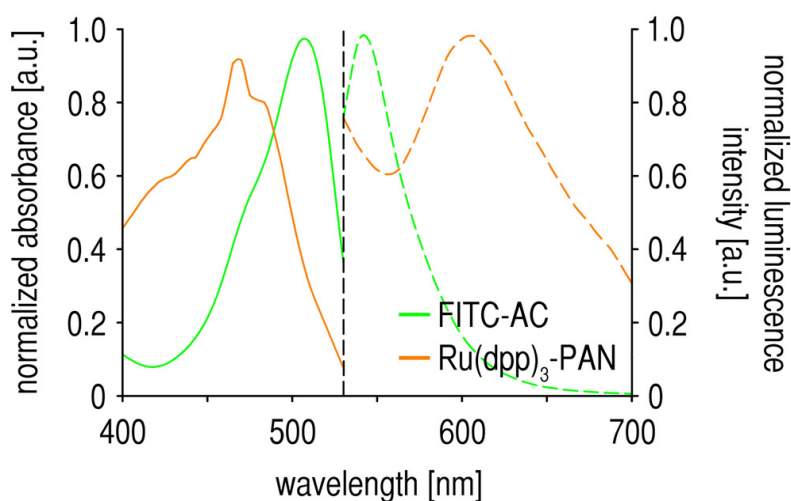


Figure 3.7 | Solid lines represent absorbance and dashed lines represent luminescence intensity. Luminescence intensity was measured with 460 nm excitation. The vertical dashed line symbolizes the 530 nm long-pass optical filter used for *in vitro* and *in vivo* luminescence intensity detection. (a.u. = arbitrary units).

FITC-AC and $\text{Ru}(\text{dpp})_3\text{-PAN}$ particles were subsequently immobilized in a polyurethane-hydrogel matrix (thickness $\sim 6 \mu\text{m}$) on a transparent poly(vinylidene-chloride) foil (PVdC, thickness $\sim 12 \mu\text{m}$) to prevent leakage of particles (**Fig. 3.8**) and to create a 2D sensor.

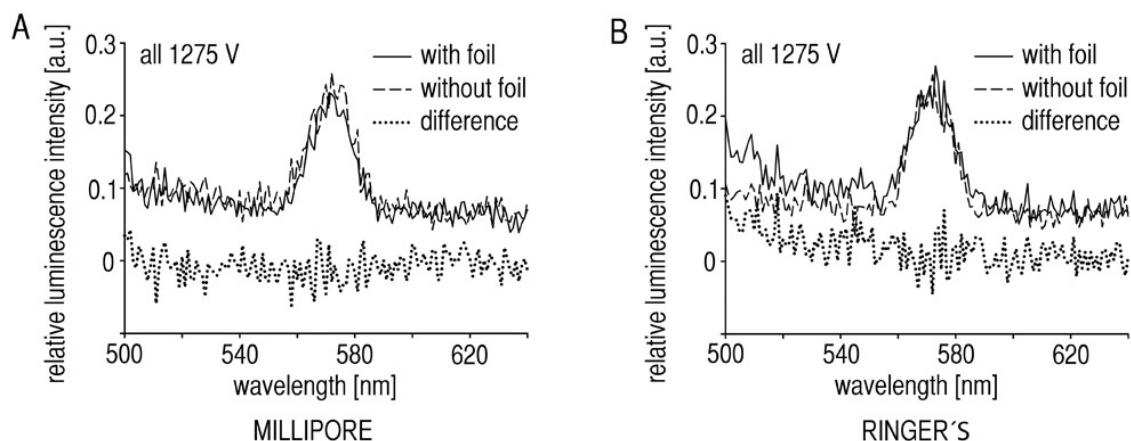
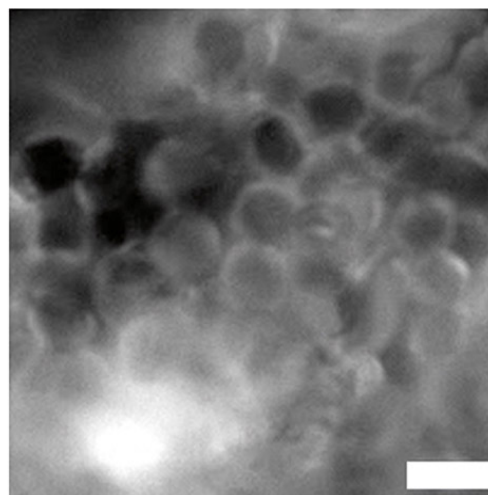


Figure 3.8 | Results of experiments on particle leakage out of the sensor. The spectra of the incubated solution (solid lines) and blank controls (dashed lines) are given. The peak at 570 nm results from an internal reflection in the instrument. The corrected spectra (dotted lines) indicate no leakage of FITC-AC and $\text{Ru}(\text{dpp})_3\text{-PAN}$ into both solutions. (a.u. = arbitrary units).

The sensors were sterilized during the fabrication process with ethanol in water (90% v/v) as the solvent for the hydrogel matrix. The PVdC support is transparent, inert and flexible to be applicable to uneven surfaces. The transparency of the foils allows the observation of the underlying anatomical structures and the creation of exact overlay pictures (photographic and luminescence image) (see **Fig. 3.4**). Prior to use, all sensor foils were inspected for gross irregularities or larger uncoated gaps by means of fluorescence microscopy (**Fig. 3.9**).

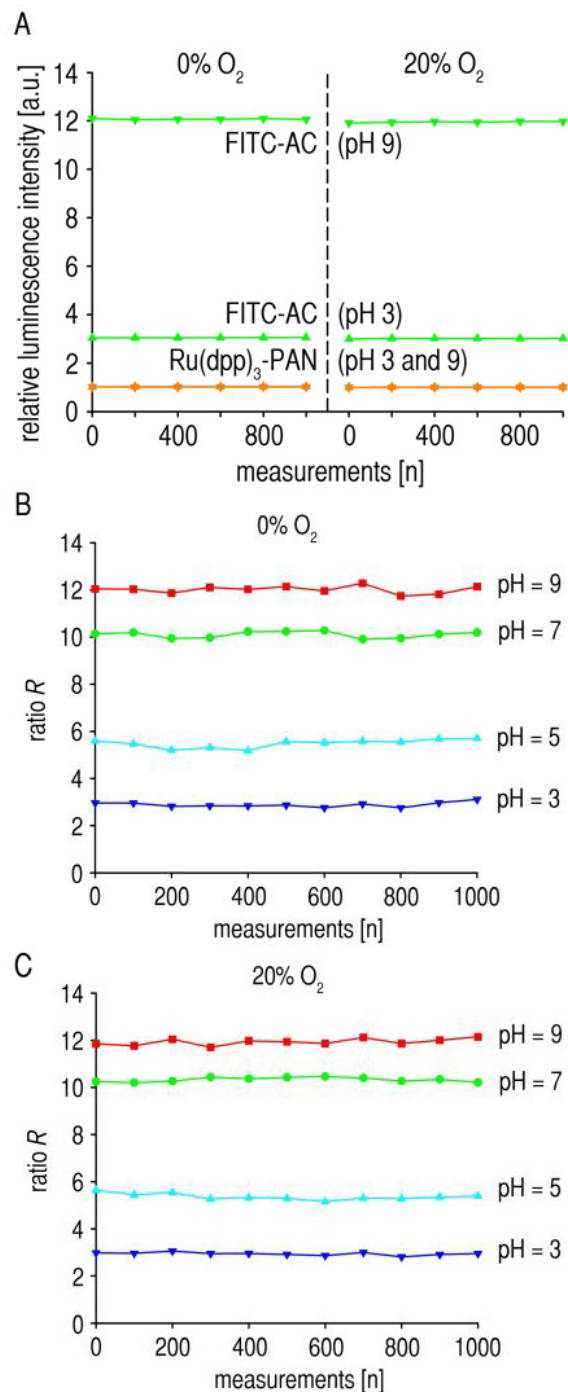
Figure 3.9 | Fluorescence microscopic image of a poly(vinylidene-chloride) (PVdC) foil coated with FITC-AC sensor particles and $\text{Ru}(\text{dpp})_3\text{-PAN}$ reference particles (e.g. in the lower left corner) embedded in a polyurethane-hydrogel matrix. (Scale bar, 1 μm).



3.2.3 *In vitro* characterization

A set of *in vitro* experiments served to characterize the sensor. For at least 1,000 measurement cycles, dyes show high photostability, even under different oxygen and pH conditions (Fig. 3.10A). Most importantly, the luminescence intensity ratio R remains almost unchanged (Fig. 3.10B and 3.10C).

Figure 3.10 | (A) Photostability: relative luminescence intensities of FITC-AC (green) and $Ru(dpp)_3$ -PAN (orange) during repeated measurements under varying oxygen and pH values. The vertical dashed line separates the experiments for 0 and 20% O_2 . Relative luminescence intensities of $Ru(dpp)_3$ -PAN are virtually identical for pH 3 and 9. (B, C) Luminescence intensity ratios at varying oxygen and pH values. The ratio R of the luminescence intensities of FITC and $Ru(dpp)_3$ is presented for 1,000 repetitive measurements under (B) 0 and (C) 20% oxygen. For each oxygen concentration, data on R are presented for varying pH values. There is virtually no change in R for each of the conditions studied.



Thus, the sensor produces reliable measurements even during continuous imaging. To extend the shelf time of the sensor, foils were stored in optically opaque envelopes until use. To determine the time necessary for accurate pH measurements (proton diffusion through hydrogel matrix to FITC-AC particles), we conducted timetrace studies that showed a 99% steady-state signal response after 56 ± 13 s (**Fig. 3.11**). Therefore, all subsequent measurements were done after 1.5 min.

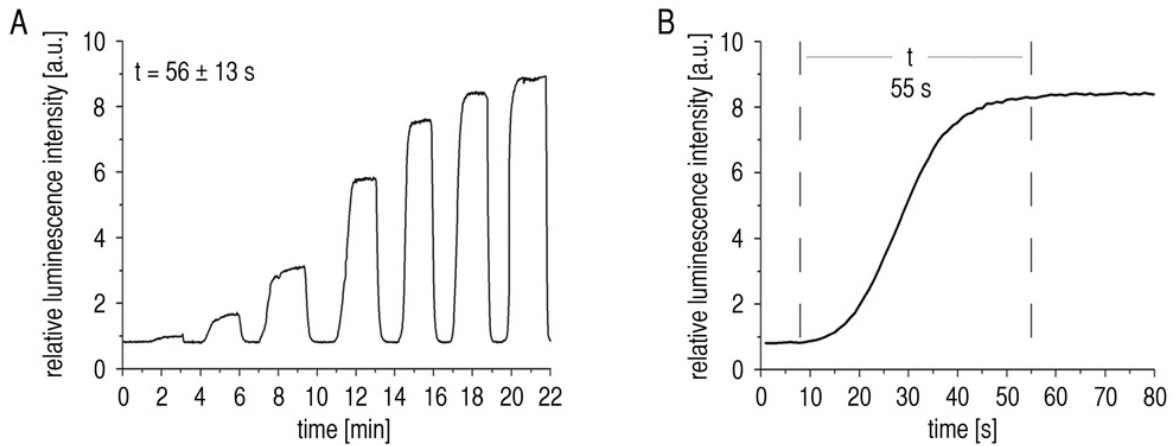
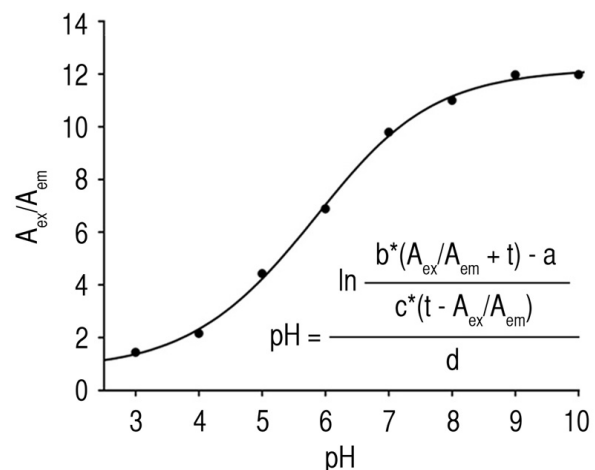


Figure 3.11 | Timetrace of sensor response (a.u. = arbitrary units) following defined pH variations (**A**) until 99 % steady-state conditions for pH measurements were achieved (t : time until steady-state = 56 ± 13 s, $n = 10$ sensors) and (**B**) a representative pH variation. (For t : mean \pm SD, $n = 10$).

Calibration showed sigmoidal curves and reliable pH measurements within the pH range of at least 3-9 (**Fig. 3.12**), which covers the range needed for clinical use.

Figure 3.12 | Sigmoidal calibration curve of the sensor. pH values may be calculated from the measured ratio R (A_{ex}/A_{em}) of integrated signal intensities during excitation (LED on; A_{ex}) and emission (LED off; A_{em}) by means of a five parametric sigmoidal equation. The pK_a of the sensor is 5.9.



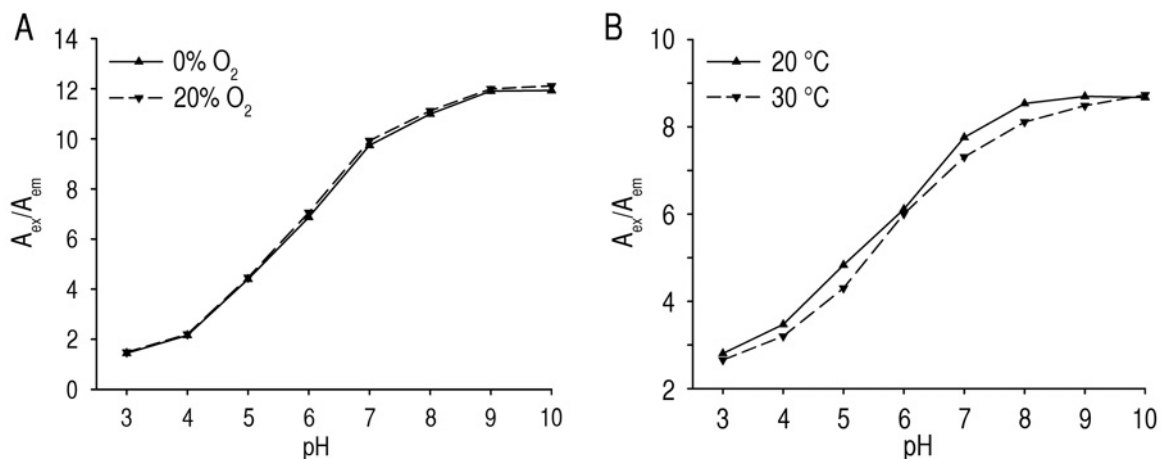
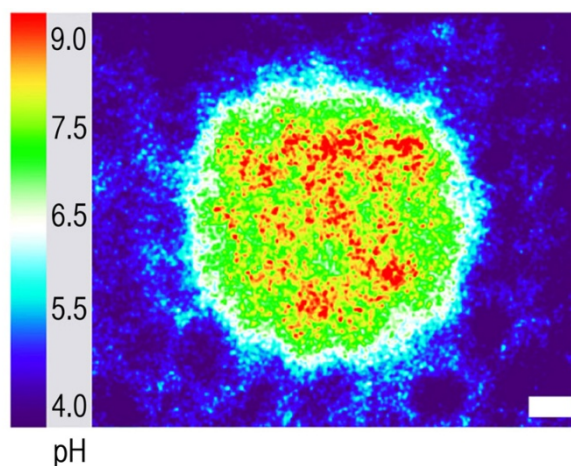


Figure 3.13 | A representative sensor calibration shows neither oxygen (A) nor crucial temperature dependency (B).

The sensor is independent of oxygen tension over a wide range (Fig. 3.13A). This independence is important as O_2 is known to be a quencher of luminescence and may vary in clinical settings. Additionally, the response is virtually unaffected by temperature changes in the range encountered in clinical settings (Fig. 3.13B).

Figure 3.14 | A Spatial resolution shown by a representative visualization of a drop (pH 8) on a sensor foil impregnated in a solution of pH 4 after connecting the CCD camera to a microscope (see Video IV.1). (Scale bar, 10 μm).



The spatial resolution of the sensor foils was studied by coupling the CCD camera to a microscope. Using our setup, we found that differences in pH may be detected with a resolution of $< 5 \mu\text{m}$ (Fig. 3.14). Continuous imaging showed that hardly any horizontal proton diffusion occurs in hydrogel, which would alter the resolution (Video IV.1 on enclosed CD). However, other microscopic imaging systems may allow higher resolution³⁰.

3.2.4 Biocompatibility

Dyes were bound to or encapsulated in inert polymer particles, and sensor particles were immobilized on PVdC-foils (see above and in methods), thus preventing dye and particle leakage into tissues. However, prior to use in an *in vivo* setting, potential cytotoxic effects were studied by exposure of human epidermal keratinocytes (HEK) and L929 fibroblasts to sensor particles. Cell viability was assessed with the 3-(4,5-dimethyl-2-thiazolyl)-2,5-diphenyl-tetrazolium-bromide (MTT) assay. Both particle types show no cytotoxicity (**Figs. 3.15 and 3.16**).

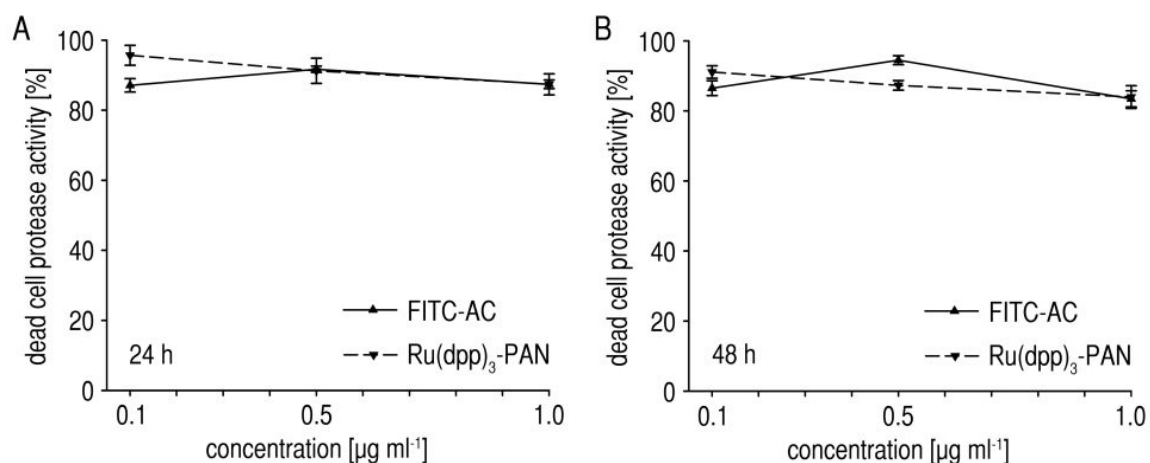


Figure 3.15 | No increase in dead cell protease release from L929 was observed after (A) 24 h and (B) 48 h, indicating that particles exhibit no cytotoxic potential. Dead cell protease activity is given as percentage of untreated controls (counts s⁻¹ of controls: 4687 ± 207 after 24 h, 4820 ± 50 after 48 h). (mean ± SEM, triplicate samples).

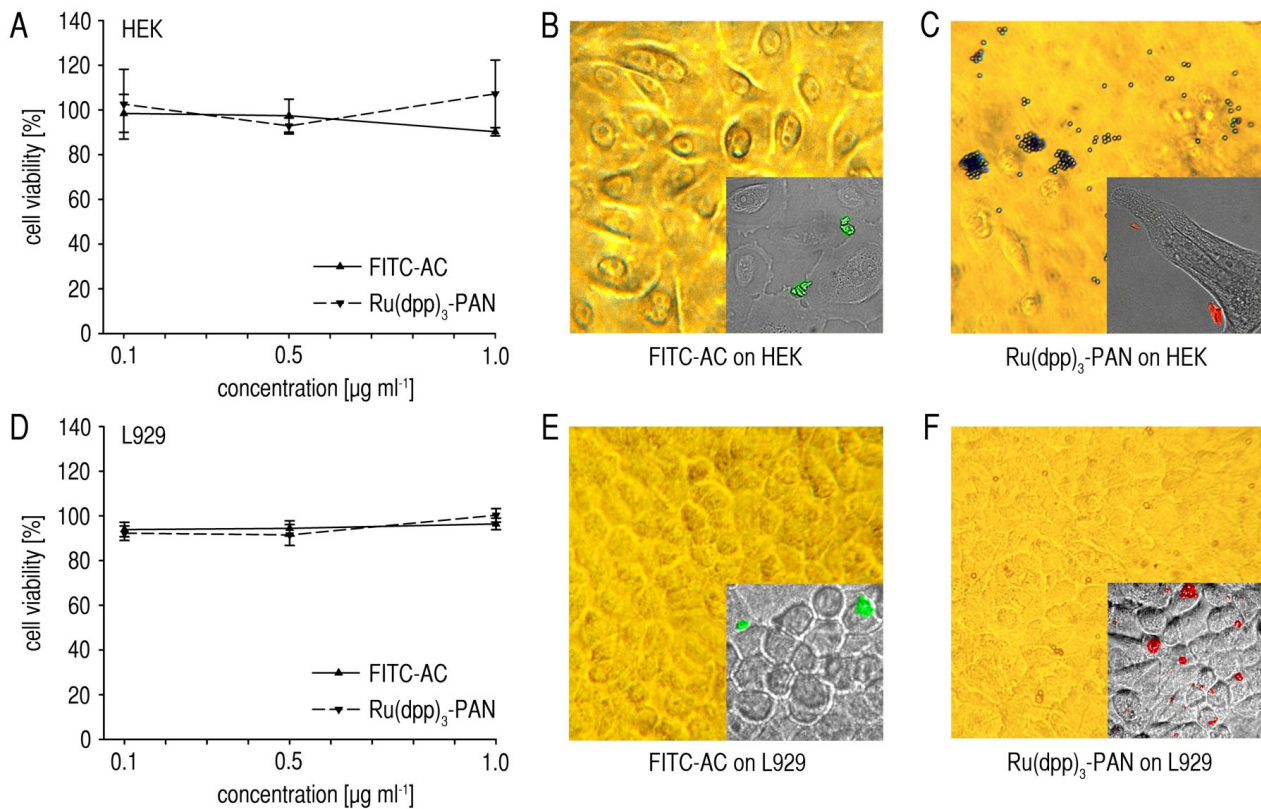


Figure 3.16 | (A,D) No cytotoxicity of FITC-AC and $\text{Ru(dpp)}_3\text{-PAN}$ towards (A) human epidermal keratinocytes (HEK) and (D) L929 fibroblasts was observed as quantified by MTT assays. Cell viability is expressed as the percentage of viable cells compared to controls. (mean \pm SEM, triplicate samples). (B,E) FITC-AC particles are only visible using fluorescence microscopy (green in overlay picture insets). (C,F) Inverted and fluorescence microscopy shows the exposure of HEK/L929 towards $\text{Ru(dpp)}_3\text{-PAN}$ particles (dark colored circles, red in overlay picture insets). As seen in the picture insets, both particle types tend to agglomerate and are not taken up by live HEK/L929. Also see **Figs. 3.16, 3.17** and **Videos IV.2-5** on the enclosed CD.

The results from the cellular uptake experiments revealed that the particles are not taken up by live cells within a period of 24 h (**Fig. 3.17** and respective **Videos IV.2-5**, **Fig. 3.18**).

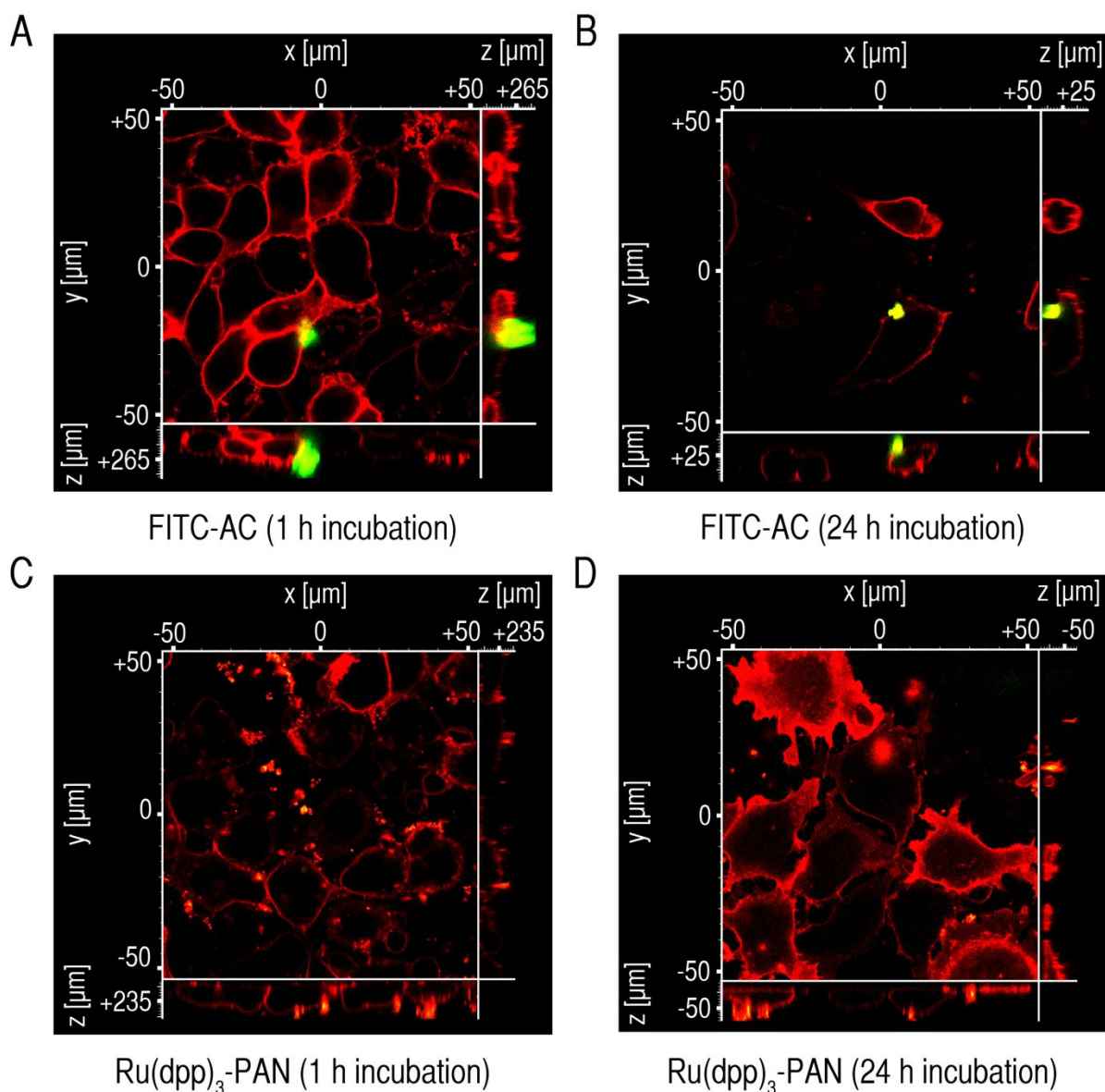


Figure 3.17 | Confocal microscopic analysis of cellular particle uptake: **(A-D)** Neither FITC-AC nor Ru(dpp)₃-PAN particles (both 1.0 $\mu\text{g ml}^{-1}$ in supernatants) are taken up by live L929 fibroblasts after **(A,C)** 1 h and **(B,D)** 24 h incubation. **(A,B)** FITC-AC are seen (green) as particle agglomerates on the cell surface. **(C,D)** Multiple Ru(dpp)₃-PAN are seen (yellow to orange) on the surface of various cells. For better visualization, see confocal microscopic image stacks in **Videos IV.2-5** on the enclosed CD.

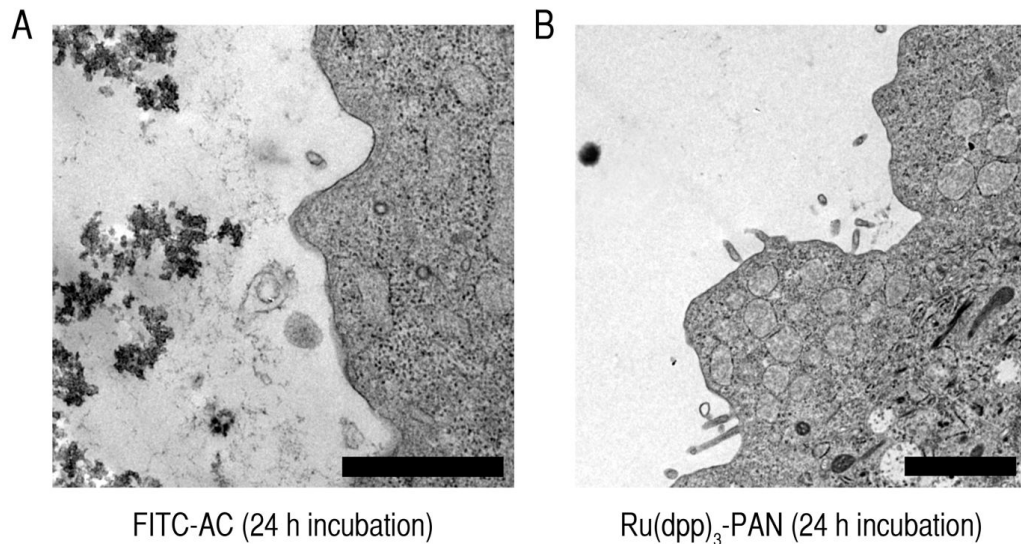


Figure 3.18 | Electron microscopic analysis of cellular particle uptake: Neither FITC-AC (**A**) nor $\text{Ru(dpp)}_3\text{-PAN}$ (**B**) are taken up by live human epidermal keratinocytes (HEK). (**A**) FITC-AC agglomerates are seen in the left part of the image in close proximity to HEK. No FITC-AC could be found inside HEK. (**B**) A single $\text{Ru(dpp)}_3\text{-PAN}$ particle is shown outside live HEK in the left part of the image. $\text{Ru(dpp)}_3\text{-PAN}$ was not found inside HEK.

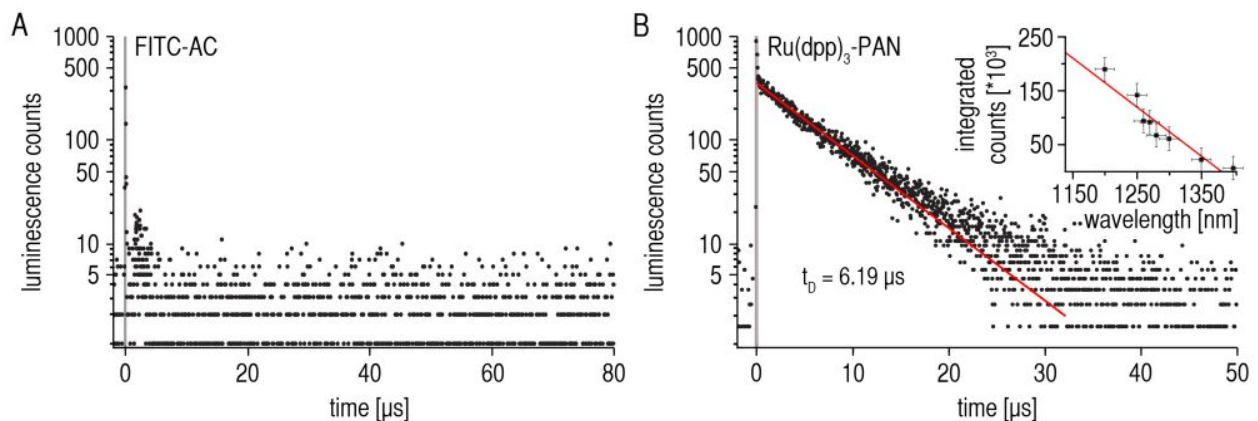


Figure 3.19 | Singlet oxygen detection: Neither (**A**) FITC-AC nor (**B**) $\text{Ru(dpp)}_3\text{-PAN}$ led to the formation of singlet oxygen. (**A,B**) $0 \mu\text{s}$ denotes the start of excitation (vertical grey lines). (**B**) The red line shows the exponential decay of luminescence ($t_D =$ decay time), representing the phosphorescence signal of $\text{Ru(dpp)}_3\text{-PAN}$. The picture inset shows the integrated luminescence signal at certain wavelengths (fit shown as red line).

Additionally, we showed that both types of microparticles do not lead to the formation of cytotoxic singlet oxygen, a member of the reactive oxygen species (ROS) family (**Fig. 3.19**). FITC does not effectively create singlet oxygen because it is a poor triplet emitter ($\phi_{\text{triplet}} =$

0.03 in H₂O)²⁷, and Ru(dpp)₃ may not create singlet oxygen as it is shielded by oxygen-impermeable PAN. The method described herein prevents direct exposure of tissues towards the agents. In terms of safety, it has to be mentioned that fluorescein conjugates are routinely used in medical diagnostics, even as injectables, e.g. in fluorescence angiography^{31,32}.

3.2.5 *In vivo* validation

For luminescence imaging *in vivo*, sensor foils only remained on tissues for the duration of measurements (< 5 min from application to image). To validate our method *in vivo*, we measured the pH gradient in the *stratum corneum* (SC) by tape stripping of the SC on the volar forearm³³. A set of experiments on 10 volunteers served to evaluate the precision and validity of the sensor *in vivo*.

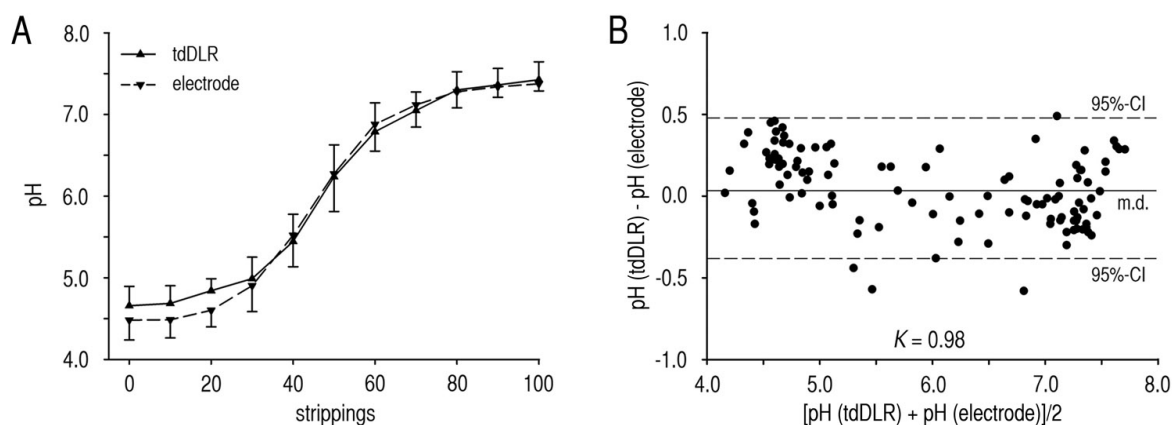


Figure 3.20 | *Stratum corneum* pH gradient (A) on the volar forearm measured with luminescent pH sensors and a pH glass electrode. Relative standard deviation (RSD) amounted to $4.32 \pm 1.35\%$ for the sensor and to $4.53 \pm 2.04\%$ for the glass electrode. (mean \pm SD, $n = 10$). The respective Bland-Altman-md-plot (B) shows 96% of measurements within the 95% confidence interval (CI), and the Krippendorff coefficient amounted to $K = 0.98$. m.d. = mean difference.

Therefore, pH measurements were compared with data obtained with the glass electrode⁹. The SC was gradually removed by multiple tape strippings and a trans-SC pH gradient was found with luminescence imaging and electrodes (**Fig. 3.20A**). No significant

differences in pH values were found between the two methods. A high level of precision was achieved for an *in vivo* setting, and the precision was similar for both methods (relative standard deviation: $RSD_{\text{tdDLR}} = 4.32 \pm 1.35\%$, $RSD_{\text{electrode}} = 4.53 \pm 2.04\%$). A Bland-Altman-md-plot³⁴ (**Fig. 3.20B**) was created for method comparison, showing excellent concordance (96% of the measurements within the 95% confidence interval; Krippendorff coefficient $K = 0.98$). Hereby, we have proven that the pH sensor can be reliably used in an *in vivo* setting.

3.2.6 Luminescence imaging of pH in cutaneous wound healing

The sensor was then applied to a routine clinical problem, i.e. cutaneous wound healing, to show its potential and superiority in comparison to the glass electrode. We used split-thickness skin graft donor sites on the thighs of 10 patients as standardized cutaneous wounds because of the potential of pH to act as a diagnostic for healing. Basically, cutaneous wound healing comprises three major overlapping phases: inflammation, proliferation (tissue formation), and tissue remodeling^{22,35}.

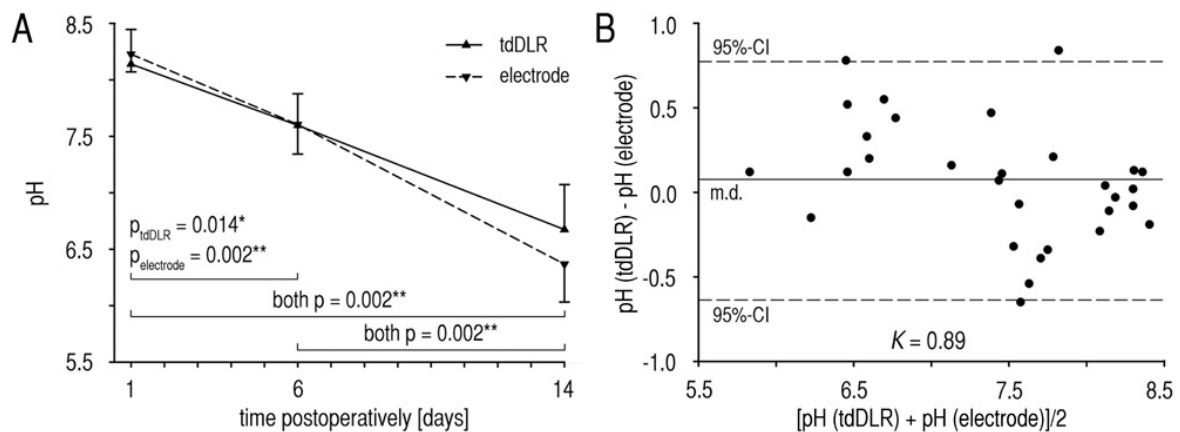


Figure 3.21 | pH during physiological wound healing of split-thickness ($\sim 400 \mu\text{m}$) skin graft donor sites on the thigh (**A**) using luminescence imaging of pH and a pH glass electrode. pH gradually declined over the time course of physiological cutaneous wound healing, reflecting the re-establishment of the epidermal barrier. The respective Bland-Altman-md-plot (**B**) shows 93% of the measurements within the 95%-CI, and the Krippendorff coefficient amounted to $K = 0.89$. m.d. = mean difference. (mean \pm SD, $n = 10$, $*p < 0.05$, $**p < 0.01$).

We found that pH continuously decreased during physiological healing and that no significant differences existed between the two methods (**Fig. 3.21 A and B**). Thereby, we were able to prove that the sensor is reliably applicable in a clinical setting, showing great promise as a tool to monitor pH in clinical routine.

The major advantage, however, is the capability of the sensor to yield 2D-pH images, which is mandatory for the evaluation of spatially heterogeneous processes like wound healing or tumor biology. Representative photographs of split-skin donor site wounds are presented for day 1 (inflammation), 6 (granulation = fibroblast proliferation) and 14 (re-epithelialization = keratinocyte migration and proliferation) after split-skin harvesting (**Fig. 3.22 A-C**). The pseudocolor images (**Fig. 3.22 D-F**) show local differences in pH during the wound healing stages, and the transparency of the sensor foils enables the correlation of clinical and pseudocolor 2D-pH images.

In chronic wound healing, a sustained inflammatory phase is supposed to prevent this stepwise process of wound closure^{22,35}. To accent the potential for 2D-pH imaging, the heterogeneity of pH within a chronic venous ulcer was visualized (**Fig. 3.23 A and B**). Within this chronic wound, extensive areas with pH values as detected in the inflammatory phase (red to yellow) are seen, thus indicating a sustained inflammatory phase. The intact surrounding skin (**Fig. 3.23 A and B**, e.g. upper left and right corners) is clearly demarcated by lower pH values.

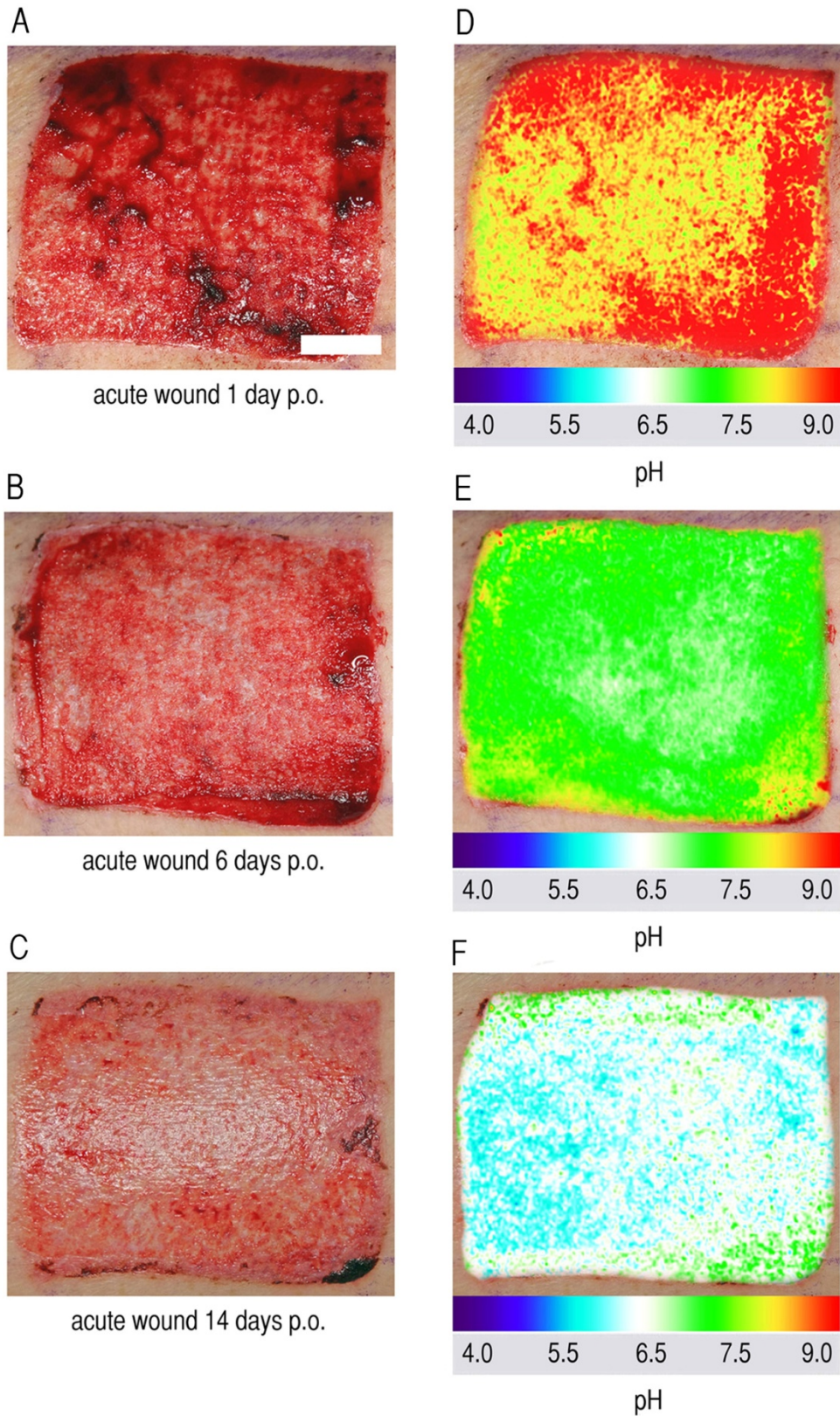


Figure 3.22 | Luminescence imaging of pH during cutaneous wound healing: (A-C) Wound healing of split-thickness ($\sim 400 \mu\text{m}$) skin graft donor sites on (A) day 1 (inflammation), (B) day 6 (granulation) and (C) day 14 (reepithelialization) after split-skin harvesting. (D-F) Respective pseudocolor images created with optical 2D-pH sensors. Wound healing is reflected by decreasing pH values. p.o. = post-operatively. (Scale bars, 1 cm).

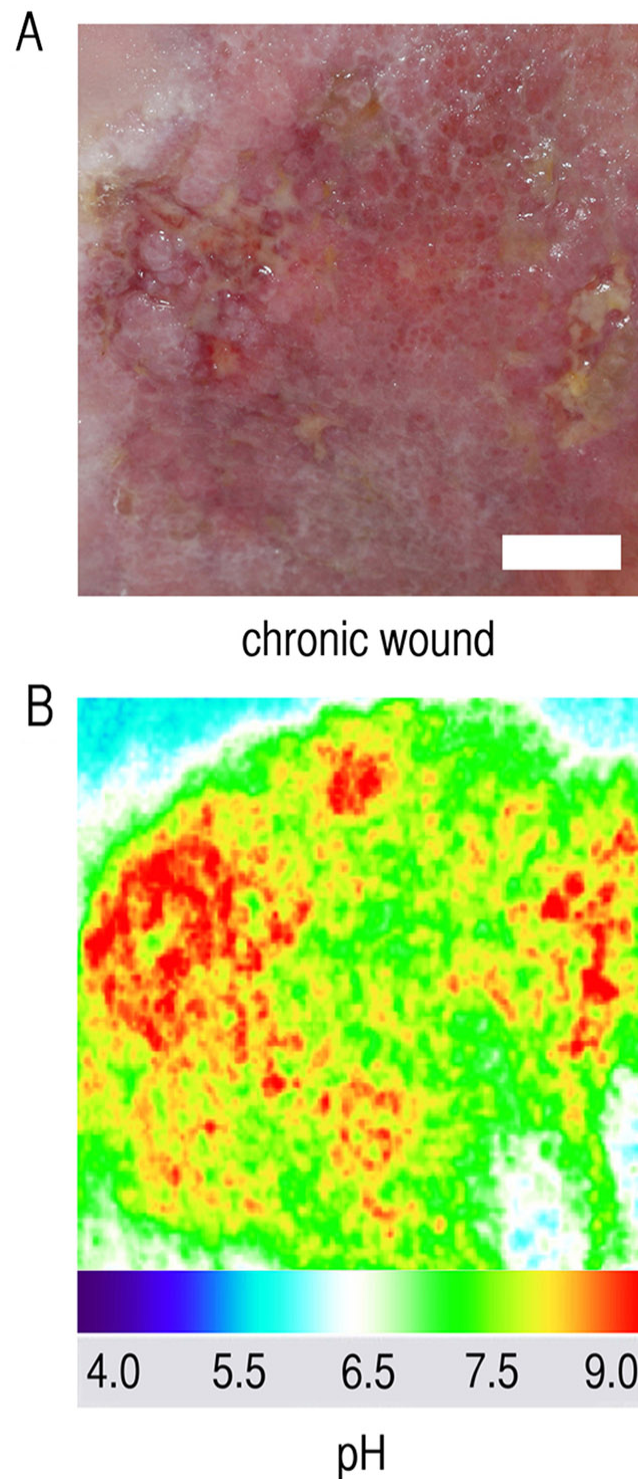


Figure 3.23 | Chronic venous ulcer (A) on the medial ankle and the respective pH distribution (B). Different stages of healing within this wound (inflammation, granulation) and surrounding intact skin (e.g. upper left and right corners) are visualized. The colors allow an easy correlation with the wound healing phases as shown for physiological healing (see Fig 3.22). (Scale bars, 1 cm).

3.3 Materials and methods

3.3.1 Microparticle preparation

10 mg (2% w/w) FITC (Sigma-Aldrich Chemie GmbH, Talkirchen, Germany) was covalently conjugated to 500 mg aminocellulose particles (AC, Presens, Regensburg, Germany) in 18 ml sodium bicarbonate buffer (50 mM, pH 9) to form FITC-AC particles (reaction time 2h). Residual amino groups on the particles were blocked with acetic anhydride (Ac_2O , Sigma-Aldrich). 100 mg AC reacted with 200 mg Ac_2O in 10 ml ethanol for 12 h. Particles were washed (eight times with distilled water) and additionally filtered via centrifugation (10 min, 3500 rpm, EDA12, Hettich, Tuttlingen, Germany) after each washing step. Reference particles were synthesized by incorporating (2% w/w) ruthenium(II)tris-(4,7-diphenyl-1,10-phenanthroline) $[\text{Ru}(\text{dpp})_3]$, Sigma-Aldrich in polyacrylonitrile (PAN, Sigma-Aldrich) to form $\text{Ru}(\text{dpp})_3$ -PAN particles³⁶. We obtained particles by precipitating 250 mg PAN dissolved in 50 ml dimethylformamide with 70 ml distilled water (dropwise addition, 1 ml s^{-1}) and subsequent addition of 20 ml Brine. Particles were washed (eight times with distilled water, four times with ethanol) and subsequently filtered via centrifugation (10 min, 3500 rpm) after each washing step. Reactions were conducted at room temperature and particles were freeze-dried (Modulyo, IMA Edwards, Dongen, Netherlands) for storage. Particle size was assessed with a LEO912 AB transmission electron microscope (Carl Zeiss AG, Jena, Germany).

3.3.2 Preparation of sensor foils

150 mg FITC-AC and 50 mg $\text{Ru}(\text{dpp})_3$ -PAN were mixed with 20 ml of a solution (5% w/v) consisting of polyurethane-hydrogel (type D4, Cardiotech International Inc., Wilmington, MA, USA) in ethanol/water (90/10 v/v). This mixture was spread on a transparent poly(vinylidene-chloride) (PVdC) foil (Saran plastic wrap, Dow Chemicals, Midland, MI, USA) with a K Control Coater model 101 knife coating device (RK Print-Coat Instruments Ltd., Litlington, UK) to form a 120 μm thick film³⁷⁻³⁹. After drying, the sensor layer was 6

μm thick. We controlled particle distribution on the foils by means of fluorescence microscopy (Axiotech, Carl Zeiss AG).

3.3.3 Time response, spectra and photostability

Timetraces ($\lambda_{\text{ex}} = 460 \text{ nm}$, $\lambda_{\text{em}} = 530 \text{ nm}$, 8 nm slits) of multiple defined pH variations (pH 1-10, single pH steps) were acquired on an Aminco-Bowman AB2 luminescence spectrometer (Thermo Spectronic, Rochester, NY, USA). Response time was defined as the time interval between the change of the buffer solution until a steady-state result was achieved. We used Britton Robinson buffers (50 mM, composed of: 0.04 M H_3BO_3 0.04 M H_3PO_4 and 0.04 M acetic acid in distilled water). Absorbance and luminescence ($\lambda_{\text{ex}} = 460 \text{ nm}$, 4 nm slits) spectra were obtained using the same setup. We processed data with LOESS (locally weighted scatterplot smoothing). Photostability experiments were carried out on sensor foils with either FITC-AC or $\text{Ru}(\text{dpp})_3\text{-PAN}$ using the imaging setup described in the main text. Relative luminescence intensities of both dyes were examined (1,000 measurement cycles) under varying pH (50 mM Britton Robinson buffers, pH 3 and 9) and oxygen (0 and 20%) values in a calibration chamber at 30 °C. Additional experiments on the operational time of the pH sensor foils were carried out by determining the luminescence intensity ratio R over 1,000 measurements for 0, 10 and 20% oxygen at pH 3, 5, 7, and 9, respectively.

3.3.4 Luminescence measurement and calibration

The camera was combined with a light emitting 460 nm LED array (Luxeon V Star LXHL-LB5C, 5W, Lumileds Lighting Company, San Jose, CA, USA). To image 2D-pH distribution, tdDLR measurements⁸ were performed by means of an ImageX Time-gated Imaging system (TGI, Photonic Research Systems, Salford, UK) with an integrated 12 bit CCD chip (640*480 pixels). Parameters were set as: subtract background, 5 μs gate width, 0.25 μs delay time, 6 μs lamp pulse, 400 Hz recording frequency, and 100 ms integration time.

We used a 530 nm long-pass OG530 glass filter (Schott, Mainz, Germany) as an emission filter. Calculations and pseudocolor image processing were done with ImageX software (Microsoft Corporation, Redmond, WA, USA) and ImageJ (<http://rsbweb.nih.gov/ij/>). Sensor calibration (pH 3-10, single pH steps) was performed at 20-40 °C (5 °C steps) with varying oxygen concentrations (0-20% oxygen in argon, 5% steps).

3.3.5 Dye leaching and particle leakage

To investigate dye leaching out of particles, 5 mg of FITC-AC and Ru(dpp)₃-PAN, respectively, were suspended in 5 ml Millipore water (MembraPure Astacus, Bodenheim, Germany) and Ringer's solution (B. Braun AG, Melsungen, Germany) each. Suspensions were continuously shaken for 24 h. 2 ml of the suspension were centrifuged (10 min, 10*10³ rpm). Supernatants were additionally filtered (200 nm cut-off syringe filter, Whatman, Dessel, Germany) to separate potentially leached dye molecules and particles. We studied both the original particle suspensions and the filtered supernatants in an Aminco-Bowman AB2 luminescence spectrometer (Thermo Spectronic). Spectra of the supernatants were recorded twice, once with the same gain as used to record spectra of the suspensions (600/800 V) and secondly with full detector gain (1,275 V) to detect traces of dyes in the solutions.

Leakage of particles out of the sensor foil was investigated by incubating pH-sensor foils in Ringer's solution and Millipore water, respectively. Sensor foils (surface 2 cm²) were placed in 2 ml of the respective liquids and were shaken for 24 h. The sensors were removed and the solutions were investigated in the luminescence spectrometer (full detector gain 1,275 V). Pure Ringer's solution and Millipore water served as blank controls.

3.3.6 Cytotoxicity

Human epidermal keratinocytes (HEK, Invitrogen, Karlsruhe, Germany) were cultured until confluence in keratinocyte growth medium with supplement (kGMS). HEK were detached using collagenase type 2 (0.1 U ml^{-1} , Roche Diagnostics, Basel, Switzerland) and resuspended in kGMS. HEK (passage 3) in kGMS were seeded (2.5×10^3 cells well⁻¹) in 96-well flat-bottom microtiter plates (Costar Inc., Pleasanton, CA, USA) and cultured ($37 \text{ }^\circ\text{C}$, 95% humidity, 5% CO_2) for three days. kGMS was renewed or replaced with FITC-AC or $\text{Ru(dpp)}_3\text{-PAN}$ in kGMS ($0.1, 0.5, 1.0 \text{ } \mu\text{g ml}^{-1}$) and HEK were incubated for 48 h. For fluorescence microscopy, we seeded HEK (passage 5) in 6-well flat-bottom microtiter plates (Costar Inc.).

Fibroblast growth medium with supplement (fGMS) for L929 fibroblasts (American Type Culture Collection CCL I fibroblast, NCTC clone 929, Manassas, VA, USA) consisted of DMEM supplemented with 5% v/v fetal bovine serum, 2 mM L-glutamine, 2.2 mg ml⁻¹ sodium bicarbonate, penicillin, and streptomycin (Lonza, Basel, Switzerland). L929 (passage 4) were cultured until confluence on 75 cm^2 culture flasks, detached by 2.5%/1% trypsin/EDTA (BioWhittaker Inc., Walkersville, MD, USA), resuspended in fGMS, seeded (passage 5, 10×10^3 cells well⁻¹) in 96-well flat-bottom microtiter plates, and cultured until confluence as described for HEK. fGMS was renewed or replaced with FITC-AC or $\text{Ru(dpp)}_3\text{-PAN}$ in fGMS ($0.1, 0.5, 1.0 \text{ } \mu\text{g ml}^{-1}$), and L929 were incubated for 48 h. Additionally, L929 (passage 5) were seeded on Thermanox slides (Nunc GmbH & Co. KG, Langensfeld, Germany) in 24-well plates for (fluorescence) microscopic imaging.

HEK/L929 in 96-well plates were washed twice with kGMS/fGMS, and cytotoxicity was evaluated with the 3-(4,5-dimethyl-2-thiazolyl)-2,5-diphenyl-tetrazoliumbromide (MTT) assay. Supernatants were replaced by kGMS/fGMS supplemented with 16% MTT solution and incubated for 1-4 hours (depending on absorbance). Reaction was stopped with 2% sodium dodecyl sulfate (SDS), and triplet samples of absorbance were measured at 490 nm (reference wavelength 650 nm, 96-well plate reader, MWG-Biotech AG, Ebersberg, Germany). Cell viability was expressed as the percentage of viable cells compared to controls (kGMS/fGMS only).

Supernatants of L929 on 96-well plates after 24 and 48 h exposure to microparticles were analyzed for dead cell protease activity with CytoTox-Glo assays (Promega GmbH, Mannheim, Germany) according to manufacturer's instructions. Luminescence counts were measured using a Victor³ multilabel reader (PerkinElmer, Rodgau, Germany).

We examined the morphology of live HEK/L929 monolayers (96-well plates) as well as particle exposure (96-, 24-, and 6-well plates) with an inverted (Labovert FS, Leica Microsystems GmbH, Wetzlar, Germany) and a fluorescence microscope (Axiostar Plus, Carl Zeiss AG, Jena, Germany). For fluorescence microscopy, we used a 475/40 nm band-pass excitation filter and a 545/35 nm band-pass emission filter (both: Omega Optical, Brattleboro, VT, USA).

3.3.7 Cellular uptake

For confocal microscopic imaging, L929 (passage 5, 50×10^3 cells well⁻¹) were seeded on 4-well Lab-Tek chamber slides (Nunc GmbH & Co. KG) and cultured until confluence. fGMS was replaced with microparticles in fGMS ($1.0 \mu\text{g ml}^{-1}$) and L929 were incubated for 1 and 24 h, respectively. Supernatants were removed, cells were embedded in paraformaldehyde (4%, 4°C) for fixation, and stored for 24 h until analysis. Subsequently, paraformaldehyde was removed, cells were washed three times with phosphate buffered saline plus Ca^{2+} plus Mg^{2+} (PBS), and membranes were stained with DiC₁₈(3) ($2 \mu\text{g ml}^{-1}$ in PBS, 1 h incubation; Invitrogen, Darmstadt, Germany). Supernatants were removed, cells were washed three times with PBS, and confocal microscopy was done with a Nikon Eclipse C-1/90i (Nikon Instruments Inc., Melville, NY, USA) and a 488 nm laser (30 μm pinhole).

For electron microscopic analysis of the cellular uptake of microparticles, HEK (passage 6) were grown until confluence on 25 cm² culture flasks. kGMS was replaced with microparticles in kGMS ($1.0 \mu\text{g ml}^{-1}$), and HEK were incubated for 24 h. HEK were detached (see above), re-suspended in kGMS, and transferred to falcon tubes (BD Biosciences, Heidelberg, Germany). Supernatants were removed from the cell pellets, and

cells exposed to microparticles were embedded in Karnovsky's fixative for electron microscopy.

3.3.8 Singlet oxygen detection

Particle suspensions (Millipore water, 1 mg ml^{-1}) were excited with a frequency-doubled Nd:YAG laser (532 nm, 100×10^3 pulses, 70 ns pulse duration, 100 mW, 20 s irradiation time, 8 mm spot size, 2.0 kHz repetition rate; PhotonEnergy, Ottensos, Germany). Suspensions were magnetically stirred. We investigated singlet-oxygen luminescence with an IR-sensitive photomultiplier (R5509-42, Hamamatsu Photonics Deutschland GmbH, Herrsching, Germany). The luminescence signal was detected by means of a 950 nm cut-off filter (Omega Optical) and a 1,270 nm bandpass filter with a full width of half-maximum (FWHM) of 10 nm (LOT-Oriel, Darmstadt, Germany). To analyze data, we used Mathematica 5.2 (Wolfram Research, Berlin, Germany).

3.3.9 Study subjects

All participants were provided with verbal and written information on the study and signed informed consent was obtained from each participant. The local ethics committee had given approval (No. 06/171: 2007) and all experiments were conducted in full accordance with the sixth revision (Seoul, Korea, 2008) of the Declaration of Helsinki (1964). For the *stratum corneum* (SC) tape stripping experiments, male volunteers ($n = 10$, 27.7 ± 4.0 years) were included. None of the volunteers had any history of skin disorders, had suffered from a skin condition or had been subject to dermatological treatment on the volar forearm in the past or at the time of measurement. Volunteers did not exercise, wash, or apply topical formulations on the volar forearm for 24 hours prior to the measurements. Split-skin grafts (thickness $400 \mu\text{m}$, $n = 10$, 4/6 female/male, 65.10 ± 20.23 years) were harvested from the left or right thigh to cover tissue defects at

different body sites after excision of skin tumors. A chronic venous ulcer on the medial right ankle of a female patient (66 years) was visualized.

3.3.10 *In vivo* luminescence imaging

Sensor foils were gently applied to the skin or the wound surface (starting from one margin), and were allowed to slowly adapt to tissue surfaces due to adhesion forces. This technique prevents the inclusion of air bubbles underneath the foils during application, thereby ensuring uniform contact between sensors and tissues. No pressure was applied to the foils during measurements. For SC pH-gradient measurements³³, we removed the SC from the volar forearm with 100 tape strippings. 3M Scotch Ruban adhesive tape (4 cm², 3M Deutschland GmbH, Neuss, Germany) was pressed firmly against the skin for 3 seconds, then swiftly pulled away. The SC was removed down to the *stratum granulosum*, which appeared as a glistening layer³³. Temperature and humidity were kept constant. We recorded pH after every 10 strippings and we measured pH in split-skin donor site wounds after 1, 6, and 14 days following split-skin harvesting. For the first 6 days, Tielle® (in case of extensive exsudation Tielle-Plus®, both: Johnson & Johnson, Langhorne, PA, USA) was used as wound dressing and subsequently replaced by Mepilex® (Mölnlycke Healthcare GmbH, Erkrath, Germany) which remained on the donor site from day 6 to 14 postoperatively. We recorded pH using the 2D sensor foils covering the entire wound surface (time from application to removal of foils < 5 min). For measurements [distance from camera to stripping site 8 cm (SC-gradient) or 30 cm (split-skin wounds), focus-controlled] we used data from standard-sized squares (100*100 pixels) from the exact spot where the glass electrode had been placed to measure pH. 2D pseudocolor pH images of the entire wounds were also obtained. No residual luminescence was detected after removal of the sensor foils, confirming that there was no leakage of sensor particles.

3.3.11 Statistics

We used Sigma Plot 11.0 (Systat Software Inc., Chicago, IL, USA) for all analyses. Data are given as mean \pm standard deviation (SD) except otherwise denoted. Normality testing was passed and paired t-tests were done to analyze differences between pH values during the time course of split-skin donor site healing. We conducted t-tests to check for differences between the measurements obtained by luminescence imaging and glass electrodes. We considered a p-value below 0.05 as significant and a p-value below 0.01 as highly significant. Results were marked with one or two asterisks within the graphs. To assess the precision of the methods, we calculated the relative standard deviation (RSD) of measurements as $(SD \text{ mean}^{-1}) * 100\%$. For method comparisons, we created Bland-Altman-md-plots for pH measurements and calculated the respective Krippendorff coefficients K .

3.4 Conclusion

In this work, we developed an optical pH sensor *in vitro*, which was validated *in vivo*, and we showed for the first time a non-invasive method for 2D and potential real-time pH imaging *in vivo*. We also present the first images of pH distribution during acute and chronic wound healing in literature. Extensive areas within a chronic wound showed similar pH values to those during the initial phase after wounding. Using the respective color code, the pseudocolor 2D-pH images allow the easy correlation of pH with the heterogeneous morphology of chronic wounds. Further studies of the 2D-pH distribution in heterogeneous chronic wounds²⁴ aim at the development of a pattern recognition model^{40,41} to predict the course of cutaneous healing. Furthermore, the biocompatible sensor holds great potential for various clinical and laboratory applications, such as tumor biology (tumor microenvironment)^{25,26}, the study of pH in dermatological conditions (e.g. epidermal barrier dysfunction in atopic dermatitis)⁴², microbiology (e.g. imaging bacterial cultures) and food technology⁴³⁻⁴⁵, and monitoring industrial production processes.

3.5 Additional studies using the pH sensor

(submitted, 2011)

An additional *in vivo* study was conducted for validation of the pH sensor. The effect of 10 % alpha hydroxyl acid (AHA, Dr. August Wolff GmbH & Co. KG, Bielefeld, Germany; www.wolf-arzneimittel.de) emulsion on human skin pH was investigated using both, the pH sensor and the glass electrode. The AHA-emulsion was applied to volar forearm skin of healthy male volunteers ($n = 12$, 25.42 ± 3.58 yrs). 4 cm² of the skin were treated according to the package insert. The formulation was wiped off 10 minutes after application. The pH was measured prior to the treatment and over the following three hours after application (see **figure 3.24**).

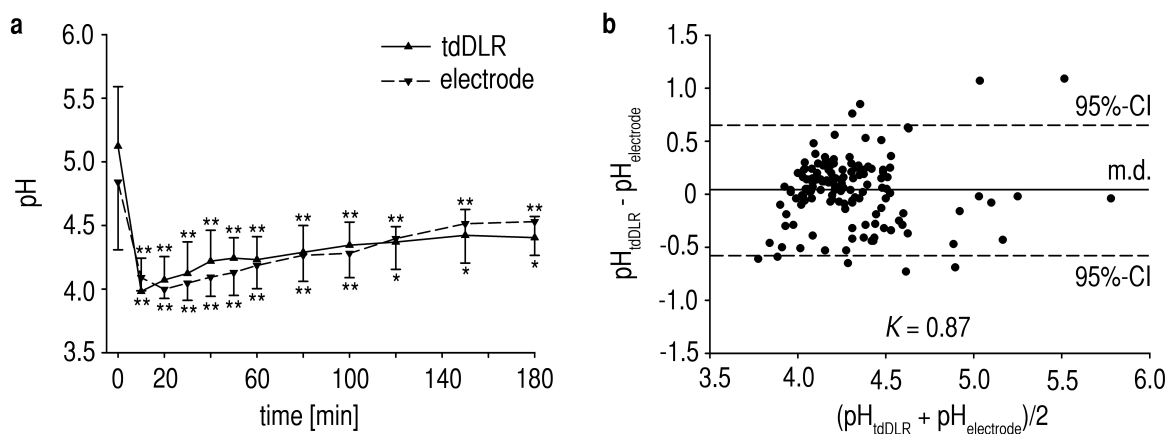


Figure 3.24 | Skin surface pH after topical treatment with 10 % AHA-emulsion. **a** shows the skin surface pH before and a time course during three hours subsequent to application. pH significantly decreases after treatment. Throughout the entire time course the pH remains significantly reduced. **b** depicts the respective Bland-Altman-md-plot for comparison of the results obtained with the sensor and those from the glass electrode. 94.45 % of the results lie within the 95 % confidence interval.

Besides the time course of the induced skin pH alteration, the depth of penetration of pH changes was studied using the pH sensor. A tape-stripping study (see section 3.3.10) was performed on female volunteers ($n = 5$, 21.32 ± 4.34 yrs).

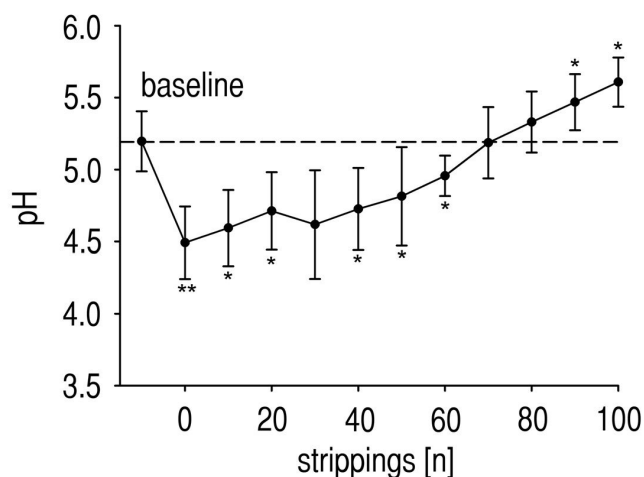


Figure 3.24 | *Stratum corneum pH before (baseline) after cream application (0 strippings). pH significantly reduces. pH increases with advancing of the stripping experiment.*

During stratum corneum stripping, pH was markedly reduced (compared to pH values in section 3.2.5). This indicated that the fruity acid effects even deeper layers of skin (at least stratum corneum). The results in **figure 3.24** and **figure 3.25** again show the reliability of the tdDLR pH sensor.

3.6 References

- 1 Lee, D. *et al.* In vivo imaging of hydrogen peroxide with chemiluminescent nanoparticles. *Nat Mater* **6**, 765-769, (2007).
- 2 Nagai, T., Sawano, A., Park, E. S. & Miyawaki, A. Circularly permuted green fluorescent proteins engineered to sense Ca^{2+} . *Proc Natl Acad Sci U S A* **98**, 3197-3202, (2001).
- 3 Nagai, T., Yamada, S., Tominaga, T., Ichikawa, M. & Miyawaki, A. Expanded dynamic range of fluorescent indicators for Ca^{2+} by circularly permuted yellow fluorescent proteins. *Proc Natl Acad Sci U S A* **101**, 10554-10559, (2004).
- 4 Nakai, J., Ohkura, M. & Imoto, K. A high signal-to-noise Ca^{2+} probe composed of a single green fluorescent protein. *Nat Biotechnol* **19**, 137-141, (2001).
- 5 Niethammer, P., Grabher, C., Look, A. T. & Mitchison, T. J. A tissue-scale gradient of hydrogen peroxide mediates rapid wound detection in zebrafish. *Nature* **459**, 996-999, (2009).
- 6 Zhang, G., Palmer, G. M., Dewhirst, M. W. & Fraser, C. L. A dual-emissive-materials design concept enables tumour hypoxia imaging. *Nat Mater* **8**, 747-751, (2009).
- 7 Bowyer, W. J., Xu, W. & Demas, J. N. Determining proton diffusion in polymer films by lifetimes of luminescent complexes measured in the frequency domain. *Anal Chem* **81**, 378-384, (2009).
- 8 Liebsch, G., Klimant, I., Krause, C. & Wolfbeis, O. S. Fluorescent imaging of pH with optical sensors using time domain dual lifetime referencing. *Anal Chem* **73**, 4354-4363, (2001).
- 9 Walpole, G. S. An improved hydrogen electrode. *Biochem J* **8**, 131-133, (1914).
- 10 Bassnett, S., Reinisch, L. & Beebe, D. C. Intracellular pH measurement using single excitation-dual emission fluorescence ratios. *Am J Physiol* **258**, C171-178, (1990).

- 11 Chen, Y. & Arriaga, E. A. Individual acidic organelle pH measurements by capillary electrophoresis. *Anal Chem* **78**, 820-826, (2006).
- 12 Deriy, L. V. *et al.* Disease-causing mutations in the cystic fibrosis transmembrane conductance regulator determine the functional responses of alveolar macrophages. *J Biol Chem* **284**, 35926-35938, (2009).
- 13 Behne, M. J. *et al.* Nhe1 regulates the stratum corneum permeability barrier homeostasis. Microenvironment acidification assessed with fluorescence lifetime imaging. *J Biol Chem* **277**, 47399-47406, (2002).
- 14 Carlsson, K. & Liljeborg, A. Simultaneous confocal lifetime imaging of multiple fluorophores using the intensity-modulated multiple-wavelength scanning (ims) technique. *J Microsc* **191**, 119-127, (1998).
- 15 Niesner, R. *et al.* 3d-resolved investigation of the pH gradient in artificial skin constructs by means of fluorescence lifetime imaging. *Pharm Res* **22**, 1079-1087, (2005).
- 16 Gallagher, F. A. *et al.* Magnetic resonance imaging of pH in vivo using hyperpolarized ¹³C-labelled bicarbonate. *Nature* **453**, 940-943, (2008).
- 17 Gillies, R. J., Liu, Z. & Bhujwalla, Z. ³¹P-mrs measurements of extracellular pH of tumors using 3-aminopropylphosphonate. *Am J Physiol* **267**, C195-203, (1994).
- 18 van Sluis, R. *et al.* In vivo imaging of extracellular pH using ¹H mrsi. *Magn Reson Med* **41**, 743-750, (1999).
- 19 Winter, G. D. Formation of the scab and the rate of epithelization of superficial wounds in the skin of the young domestic pig. *Nature* **193**, 293-294, (1962).
- 20 Hunt, T. K., Twomey, P., Zederfeldt, B. & Dunphy, J. E. Respiratory gas tensions and pH in healing wounds. *Am J Surg* **114**, 302-307, (1967).
- 21 Schreml, S. *et al.* The impact of the pH value on skin integrity and cutaneous wound healing. *Journal of the European Academy of Dermatology and Venereology* **24**, 373-378, (2009).
- 22 Singer, A. J. & Clark, R. A. Cutaneous wound healing. *N Engl J Med* **341**, 738-746, (1999).
- 23 Schreml, S., Szeimies, R.-M., Prantl, L., Landthaler, M. & Babilas, P. Wound healing in the 21st century. *J Am Acad Dermatol* [Epub ahead of print], (2010).
- 24 Bickers, D. R. *et al.* The burden of skin diseases: 2004 a joint project of the american academy of dermatology association and the society for investigative dermatology. *J Am Acad Dermatol* **55**, 490-500, (2006).
- 25 N.N. Tumour pH. *Lancet* **340**, 342-343, (1992).
- 26 Vaupel, P., Kallinowski, F. & Okunieff, P. Blood flow, oxygen and nutrient supply, and metabolic microenvironment of human tumors: A review. *Cancer Res* **49**, 6449-6465, (1989).
- 27 Devanathan, S., Dahl, T. A., Midden, W. R. & Neckers, D. C. Readily available fluorescein isothiocyanate-conjugated antibodies can be easily converted into targeted phototoxic agents for antibacterial, antiviral, and anticancer therapy. *Proc Natl Acad Sci U S A* **87**, 2980-2984, (1990).
- 28 Brandrup, J., Immergut, E. H. & Grulke, E. A. Polymer handbook. *Wiley-VCH New-York* (1999).
- 29 Borisov, S. M. *et al.* Springer series on fluorescence, vol. 4: Fluorescence of supermolecules, polymers, and nanosystems *Springer, Berlin, Heidelberg*, (2008).
- 30 Barretto, R. P., Messerschmidt, B. & Schnitzer, M. J. In vivo fluorescence imaging with high-resolution microlenses. *Nat Methods* **6**, 511-512, (2009).
- 31 Kwan, A. S., Barry, C., McAllister, I. L. & Constable, I. Fluorescein angiography and adverse drug reactions revisited: The lions eye experience. *Clin Experiment Ophthalmol* **34**, 33-38, (2006).
- 32 Yannuzzi, L. A. *et al.* Fluorescein angiography complication survey. *Ophthalmology* **93**, 611-617, (1986).

- 33 Ohman, H. & Vahlquist, A. In vivo studies concerning a pH gradient in human stratum corneum and upper epidermis. *Acta Derm Venereol* **74**, 375-379, (1994).
- 34 Bland, J. M. & Altman, D. G. Statistical methods for assessing agreement between two methods of clinical measurement. *Lancet* **1**, 307-310, (1986).
- 35 Gurtner, G. C., Werner, S., Barrandon, Y. & Longaker, M. T. Wound repair and regeneration. *Nature* **453**, 314-321, (2008).
- 36 Kurner, J. *et al.* Inert phosphorescent nanospheres as markers for optical assays. *Bioconjugate Chemistry* **12**, 883-889, (2001).
- 37 Borisov, S., Vasylevska, A., Krause, C. & Wolfbeis, O. Composite luminescent material for dual sensing of oxygen and temperature. *Advanced Functional Materials* **16**, 1536-1542, (2006).
- 38 Wolfbeis, O. S. Sensor paints. *Advanced Materials* **20**, 3759-3763, (2008).
- 39 Stich, M. I. J., Fischer, L. H. & Wolfbeis, O. S. Multiple fluorescent chemical sensing and imaging. *Chem Soc Rev* **39**, 3102-3114, (2010).
- 40 Schugart, R. C., Friedman, A., Zhao, R. & Sen, C. K. Wound angiogenesis as a function of tissue oxygen tension: A mathematical model. *Proc Natl Acad Sci U S A* **105**, 2628-2633, (2008).
- 41 Xue, C., Friedman, A. & Sen, C. K. A mathematical model of ischemic cutaneous wounds. *Proc Natl Acad Sci U S A* **106**, 16782-16787, (2009).
- 42 Cork, M. J. *et al.* Epidermal barrier dysfunction in atopic dermatitis. *J Invest Dermatol* **129**, 1892-1908, (2009).
- 43 Davey, K. R. Modelling the combined effect of temperature and pH on the rate coefficient for bacterial growth. *Int J Food Microbiol* **23**, 295-303, (1994).
- 44 Olson, E. R. Influence of pH on bacterial gene expression. *Mol Microbiol* **8**, 5-14, (1993).
- 45 Tolba, M. K. & Saleh, A. M. Correlation between pH-value of tomato tissue and its susceptibility to attack by two fusaria. *Nature* **173**, 87, (1954).

4. 2D luminescent pO₂ sensor for *in vivo* imaging in physiological wound oxygenation

In this chapter, a 2D in vivo sensor for imaging of physiological wound oxygenation is described. The sensor is based on two-dimensional luminescence lifetime imaging (2D-LLI) of dynamic oxygen quenching of the dye Palladium(II)-meso-tetraphenyl-tetrabenzoporphyrin (Pd-TPTBP). The dye is incorporated in partially oxygen blocking polystyrene-co-acrylonitrile (PSAN) particles to precisely control its sensitivity for oxygen measurements in the physiological relevant range of 0 to 160 mmHg. Particles were immobilized in a hydrogel film on transparent foils to allow simultaneous observation of the underlying structures. Skin graft donor sites were investigated as a standardized model for physiological wound healing. The oxygen partial pressure (pO₂) of the wound surface was measured at 1, 6, and 14 days after split-skin harvesting. In a second experiment, the upper skin layer (stratum corneum) was completely removed by tape strippings to study the impact of the stratum corneum on the epidermal oxygen barrier. (Exp Dermatol, 2011, in press DOI: 10.1111/j.1600-0625.2011.01263.x)

4.1 Introduction

There still is a lack of understanding in the role of oxygen in wound healing. In this context, the stratum corneum (SC) is supposed to be a major part of the epidermal oxygen barrier but unfortunately, precise data is still missing in the literature. Cutaneous wound healing is basically divided into three major phases: the initial inflammatory phase (cytokines, chemokines, etc.), the proliferative phase (neangiogenesis, fibroblast proliferation, reepithelialization), and the final tissue remodeling phase (extracellular matrix reorganization).¹ These phases overlap during healing. Although, there are numerous publications on the molecular and cellular events during cutaneous wound

healing² the basic clinical parameters like pO₂ and pH are not completely unveiled in this context. pO₂ has a major impact on cutaneous wound healing³. The standard technique for oxygen measurements, the Clark electrode, comprises technical problems within clinical routine⁴ (also see *chapter 1*). Thus, precise studies on wound pO₂ were not possible for decades.

During the last decades, new and promising tools for *in vivo* pO₂ measurements based on optical read-out were developed⁵⁻¹⁶. Many of the problems associated with the use of glass electrodes have been overcome with these more or less non-invasive techniques: (i) heating of the skin is no longer required, (ii) no analyte consumption with the use of luminescent sensors, and further (iii) 2D images rather than only single spot measurement can be obtained.

Rumsey⁵, Wilson^{6,9}, and Intaglietta⁸ have established minimal invasive 2D imaging methods for oxygen in tissue at the end of the last century. These methods include intravenous injection of the luminescence indicator dyes accompanied by the risk of toxicity. The invasive character limits this technique to animal experiments and thus is not applicable in clinical routine. Itoh *et al.*⁷ applied probes absorbed in silica gel to prevent direct contact. However, these non-referenced luminescence intensity measurements⁵⁻⁷ require time-consuming recalibration and careful data interpretation, since neither indicator movement nor distribution can be controlled precisely.

Stücker, Hartman, and Lübbers^{10,11,14} embedded oxygen sensitive ruthenium complexes in polymer matrices to form first non-invasive planar optical sensors for pO₂ measurements on human skin. The sensors can be read out via referenced 2D-LLI. The methods were used to measure pO₂ in tissue of intact human skin or in malignant melanoma on skin. Babilas *et al.*^{12,15,16} used platinum(II)-octaethyl-porphyrines in planar polystyrene films for tumor imaging in animals and blood microcirculation in human skin. However, these sensors only allow for application in either intact skin or animal experiments. Further, these planar sensors impede application on uneven surfaces (e.g. cutaneous wound surfaces) due to the use of relatively non-flexible sensor supports.

To date, no sensor exists that allows for *in vivo* 2D pO₂ imaging in cutaneous wounds of humans. The prerequisites to create such a sensor include (i) the use of a

referenced method, since *in vivo* conditions are quite variable, (ii) non-toxic materials, (iii) convenient application on wound surfaces, (iv) a dynamic range of 0 to 100 mmHg (physiological relevant range), and (v) a completely non-invasive method, in order to be applicable under clinical conditions. In this chapter, the development of such an optical pO₂ sensor including *in vitro* characterization, *in vivo* validation, and clinical application of the sensor is described.

4.2 Results and Discussion

4.2.1 Material design and *in vitro* characterization

As a additional prerequisite the oxygen sensitive indicator should be combinable with the pH sensor¹⁷ described in the previous chapter to form an optical dual sensor for pH and pO₂. The dye Palladium(II)-meso-tetraphenyl-tetrabenzoporphyrin (Pd-TPTBP; Sigma-Aldrich) (**Fig. 4.1**) was chosen as oxygen indicator.

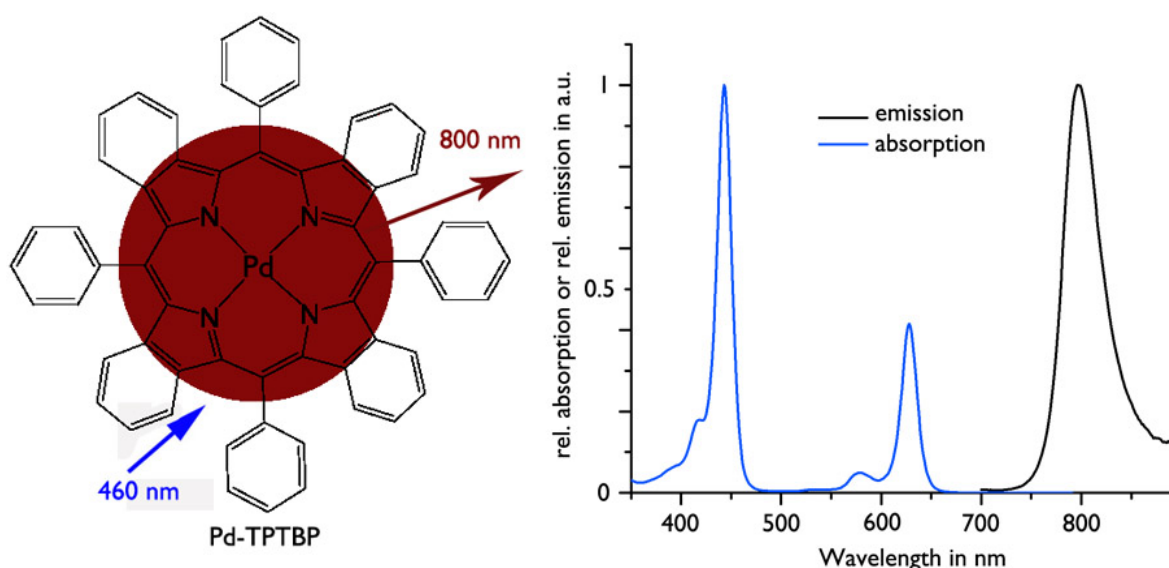


Figure 4.1 | Chemical structure (left) and spectral properties (right) of the *indicator dye Palladium(II)-meso-tetraphenyl-tetrabenzoporphyrin*.

The metalloporphyrin has four benzene rings, each attached to one of the four pyrrole subunits. During the last two decades those metalloporphyrins gained popularity due to superior quantum yield and photostability, and their red shift in the absorbance and emission spectra compared to the precursor porphyrins^{18,19}. Due to their high oxygen sensitivity, they were applied in numerous oxygen sensors¹⁹⁻²³.

The Pd-TPTBP offers excellent spectral properties. The Soret band of the Pd-TPTBP at 444 nm is excitable with the 460 nm LED of the time-gated imaging setup (described in *chapter 2.5*). The dye offers a huge Stokes shift. Further, the emission peak at 796 nm is separated from the emission peaks of FITC and Ru(dpp)₃ from the pH sensor.

The phosphorescence decay time for Pd-TPTBP is 40 to 300 μs depending on the oxygen concentration. Collisional luminescence quenching by oxygen can be described by a Stern–Volmer relationship:

$$\text{(Equation 4.1):} \quad \tau_0/\tau = 1 + K_{SV} * pO_2 = I_0/I$$

Where τ_0 represents the luminescence decay time at 0 mmHg pO₂ and K_{SV} is the Stern–Volmer constant reflecting the sensor sensitivity^{24,25}.

A more complex but also more correct way to describe non-monoexponential decays is the two-site model²⁶⁻²⁸. The two-site model accounts for different chemical and physical microenvironments such as polymer matrices or particles.

$$\text{(Equation 4.2):} \quad \tau_0/\tau = I_0/I = f_1/(1 + K_{SV}^1 * pO_2) + f_2/(1 + K_{SV}^2 * pO_2)$$

f_1 and f_2 represent the fraction of the molecules located in the different environments with different Stern-Volmer constants.

The decay time of the Pd-TPTBP and thus pO₂ can be determined using 2D-LLI and rapid lifetime determination with the time-gated imaging system described in *chapter*

2.5. For imaging pO₂ the camera was equipped with an 800 nm bandpass filter with 60 nm half width to exclusively record the light emitted by the oxygen probe.

The strategy to from an *in vivo* sensor for imaging pO₂ in human wounds was quite similar to the strategy in *chapter 3*: The luminescent optical sensor film consists of polymer particles doped with indicator dye molecules in hydrogel matrix layers which were prepared by spreading a liquid particle/matrix-polymer cocktail onto a transparent polyester support (the foil)²⁹⁻³¹. A hydrogel type D4 (Cardiotech International Inc) was used as matrix material on poly(vinylidene chloride) (PVdC) (Saran food barrier wrap, Dow Chemicals) sensor support foils to hinder direct contact of particles and tissue. Particle size should exceed 500 nm to hinder possible cellular uptake. The scheme of the foil is described in **Fig. 4.2**.

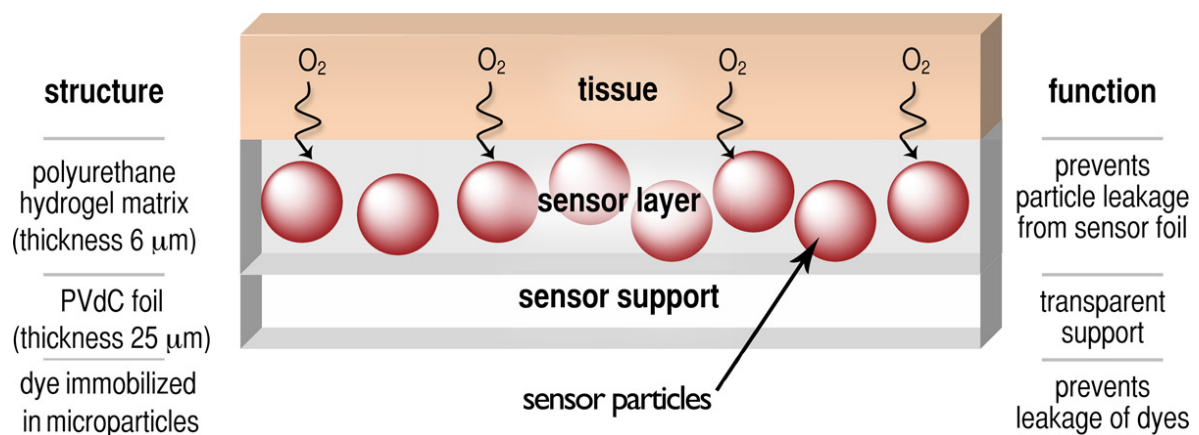


Figure 4.2 | A schematic view of a sensor foil is shown. Particles are embedded in a hydrogel matrix on a transparent PVdC foil, thereby preventing particle leakage. Foils are applied to tissues with the hydrogel coated surface. Oxygen diffuses into the hydrogel matrix and towards the microparticles. The transparency of the foils allows simultaneous observing of the underlying anatomic structures.

In a first approach, the dye Pd-TPTBP was embedded in polystyrene (PS) microparticles. PS possesses a high oxygen permeability coefficient P of $1.9 \cdot 10^{-13} \text{ cm}^2 \cdot \text{Pa} \cdot \text{s}^{-1}$ ^{32,33}. The particles had a size of 800 nm and were incorporated in the D4 matrix. The responding

characteristics towards oxygen partial pressure in the range of 0 to 160 mmHg were investigated (**Fig.4.3**).

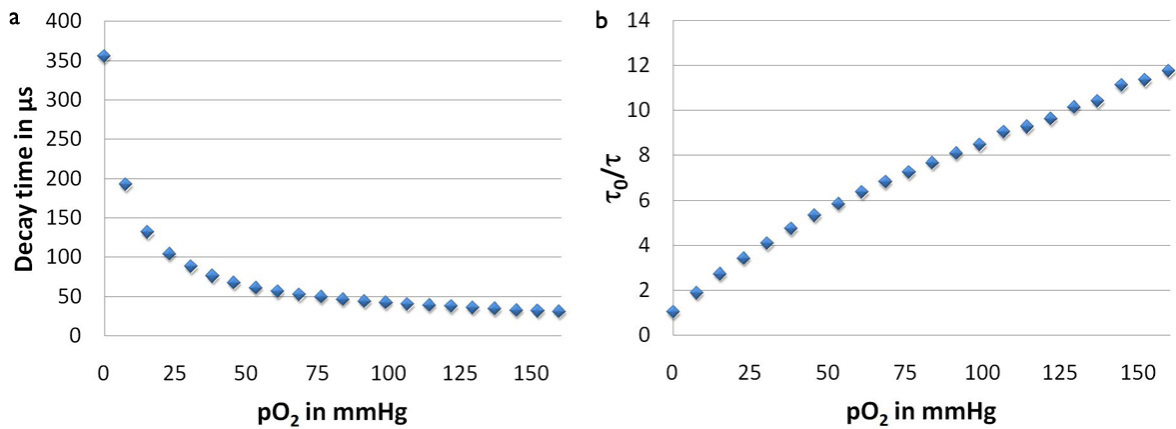


Figure 4.3 | (a) Responding behavior of the phosphorescence decay time of Pd-TPTBP in PS microparticles in a D4 hydrogel film towards oxygen and (b) respective Stern-Volmer plot.

The luminescence decay time decreased from 350 μs (0 mmHg) to 40 μs (in case of 160 mmHg). 90% of the decrease was reached with 50 mmHg pO₂. The sensitivity of the sensor is too high for application in tissue. A sensor for pO₂ measurements in tissue should cover at least a range of 0 to 100 mmHg. The Stern Volmer K_{sv} constant for a linear plot of the range of 0 to 50 mmHg was found to be 0.0985/mmHg.

The material of the microspheres had to be changed. A polymer that is more impermeable for oxygen lowers the sensitivity of the oxygen indicator Pd-TPTBP and thus increases the effective dynamic range of the sensor. The co-polymer (poly(styrene-co-acrylonitrile) (PSAN) with 30 wt% acrylonitrile content was chosen due to its moderate gas permeability. The oxygen permeability coefficient P was $3.5 \cdot 10^{-14} \text{ cm}^2 \cdot \text{Pa} \cdot \text{s}^{-1}$ ^{34,35}. Therefore, the polymer retards the rapid quenching of both luminescence intensity and lifetime of Pd-TPTBP by oxygen.

The graphs in **Figure 4.4** show that the PSAN microparticles extend the dynamic range up to 160 mmHg. The range of 0 to 100 mmHg for tissue measurements can be described by a linear Stern-Volmer plot with a K_{sv} of 0.0336/mmHg (see fit line in **Fig 4.4**).

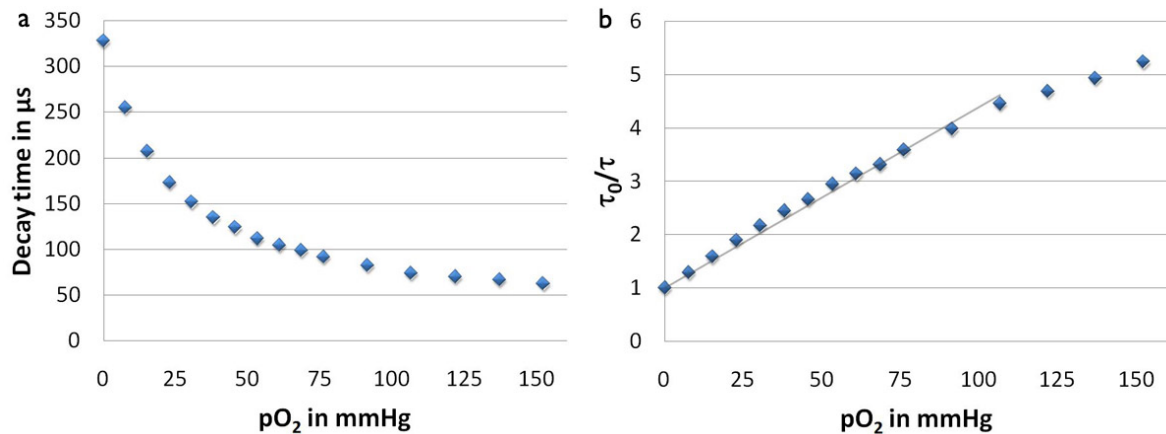


Figure 4.4 | (a) Response of the phosphorescence decay time of Pd-TPTBP in PSAN microparticles in a D4 hydrogel film towards oxygen and (b) respective Stern-Volmer plot including a line of best fit for the range of 0 to 100 mmHg.

The sensor shows a slight response towards temperature upon changing from 20 to 37°C (see **Fig. 4.5**). During physiological pO₂ determination, the temperature ranges from approximately 25 to 35 °C depending on the measurement site. Thus temperature is not an interfering factor. Photobleaching of the dyes is also not an issue using this sensor since lifetime measurements operate with intrinsically referenced signals.

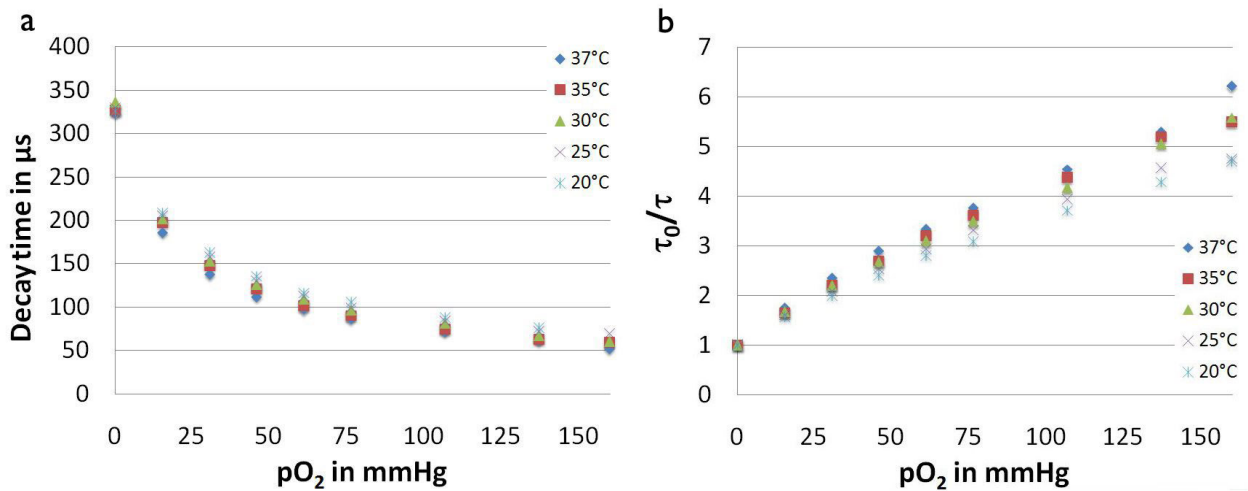


Figure 4.5 | Temperature sensitivity of the decay time (a) in the range of 20 to 37°C and the respective Stern-Volmer plot (b).

The oxygen sensitive microspheres had minimum dimensions of 0.5 to 1 μm in diameter (see Fig. 4.6a) to hamper cellular uptake and particle leakage. A fluorescence microscopic analysis of a sensor film ensured homogeneous allocation of the particles in the sensor matrix layer (Fig. 4.6b). There were no gross irregularities or larger uncoated gaps in the sensor foil that may cause erroneous pO₂ distribution results.

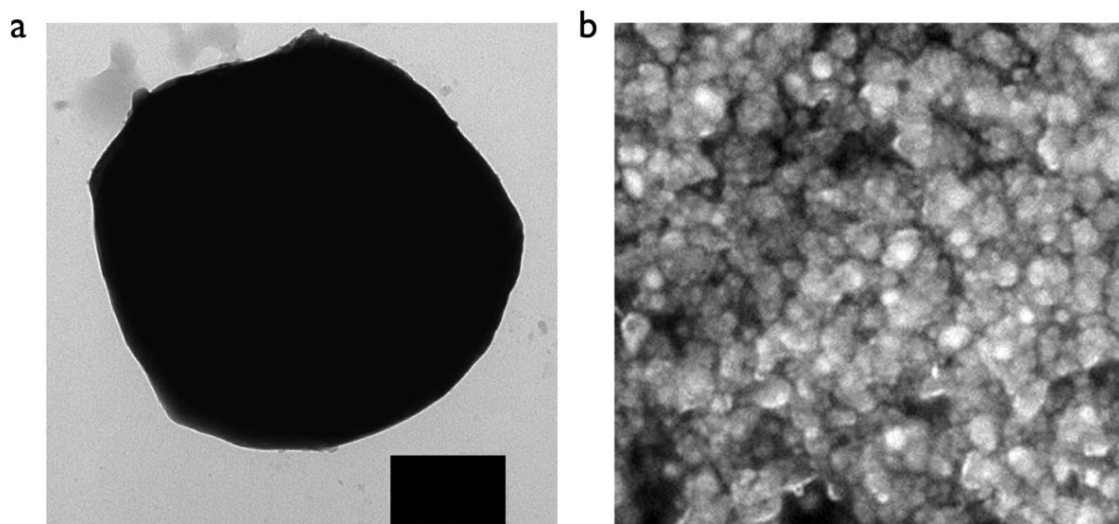


Figure 4.6 | (a) Particle size ranged from 0.5 to about 1 μm as seen by transmission electron microscopy. The representative Pd-TPTBP-PSAN sensor-particle is 0.7 μm . Black bar is 0.2 μm . (b) The fluorescence microscopic image shows the Pd-TPTBP-PSAN sensor-particles immobilized in D4-hydrogel on transparent PVdC-foils. 20-fold magnification.

4.2.2 Biocompatibility

The use in human wounds requires a highly biocompatible sensor. The matrix material used (hydrogel type D4) is medical grade and approved for medical applications. The sensor support foil (SARAN) is chemically inert. Although the particles are well retained by the hydrogel matrix and direct contact of cells (on the wound surface or skin) is prevented, cytotoxicity had to be excluded. A two-parametric test was conducted. No cytotoxicity of these microparticles was observed in a concentration range of 0.1 to 10 µg/ml as seen by MTT assays (**Fig. 4.8a**). In addition, particles were exposed to keratinocyte cultures and visualized by means of inverted microscopy (**Fig. 4.8b**). Even if keratinocytes were exposed to a low number of particles, cytotoxic effects were excluded.

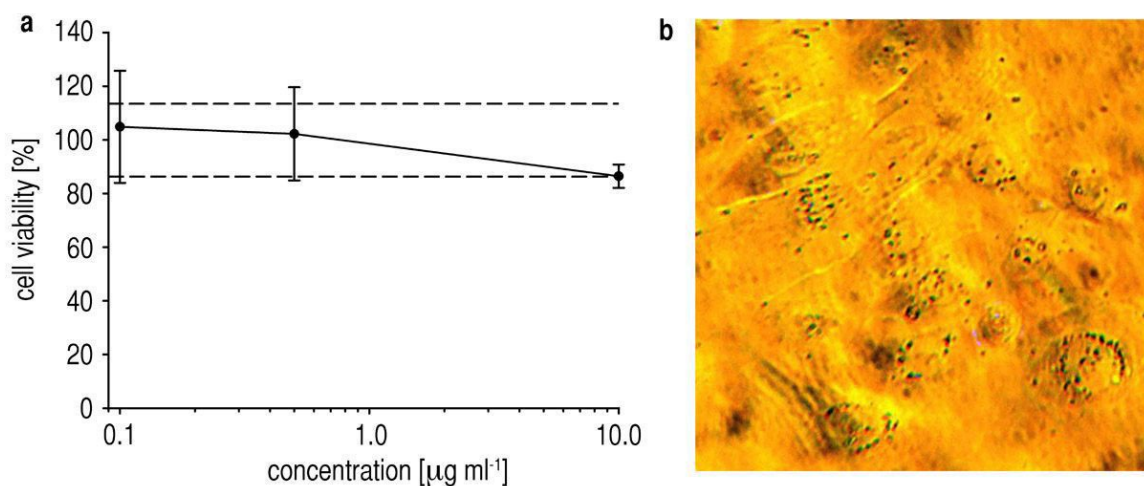


Figure 4.8 | **(a)** MTT assays showed no cytotoxic impact of Pd-TPTBP-PSAN particles towards keratinocytes (48 h incubation). Dashed lines represent the range of controls ± 2 SD. Mean \pm SD, quadruplicate samples. **(b)** Exposure of keratinocytes towards particles (10 µg/ml) was confirmed by microscopic imaging of particles on keratinocyte monolayers. 40-fold magnification.

4.2.3 In vivo imaging of wound healing

Skin graft donor sites were investigated as a standardized model for physiological wound healing. The pO₂ of the wound surface (p_{ws}O₂) of 12 patients was observed 1, 6, and 14 days, respectively, after skin harvesting. Over 14 days the p_{ws}O₂ decreased continuously (Fig. 4.9).

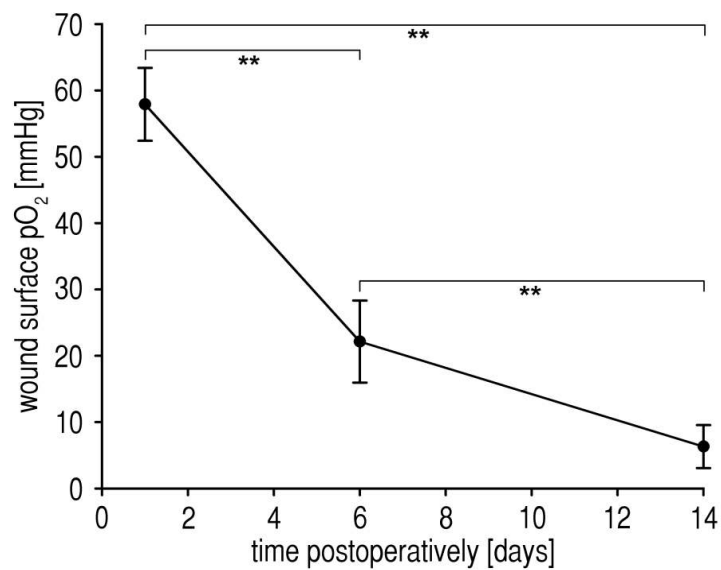


Figure 4.9 | p_{ws}O₂ during the time course of physiological wound healing of split-skin donor sites: p_{ws}O₂ decreased significantly from day 1 to 6 postoperatively, and again from day 6 to day 14. The decrease in p_{ws}O₂ represents the re-establishment of the epidermal oxygen barrier function during wound healing. Mean ± SD, n = 12, triplicate samples, **P < 0.001.

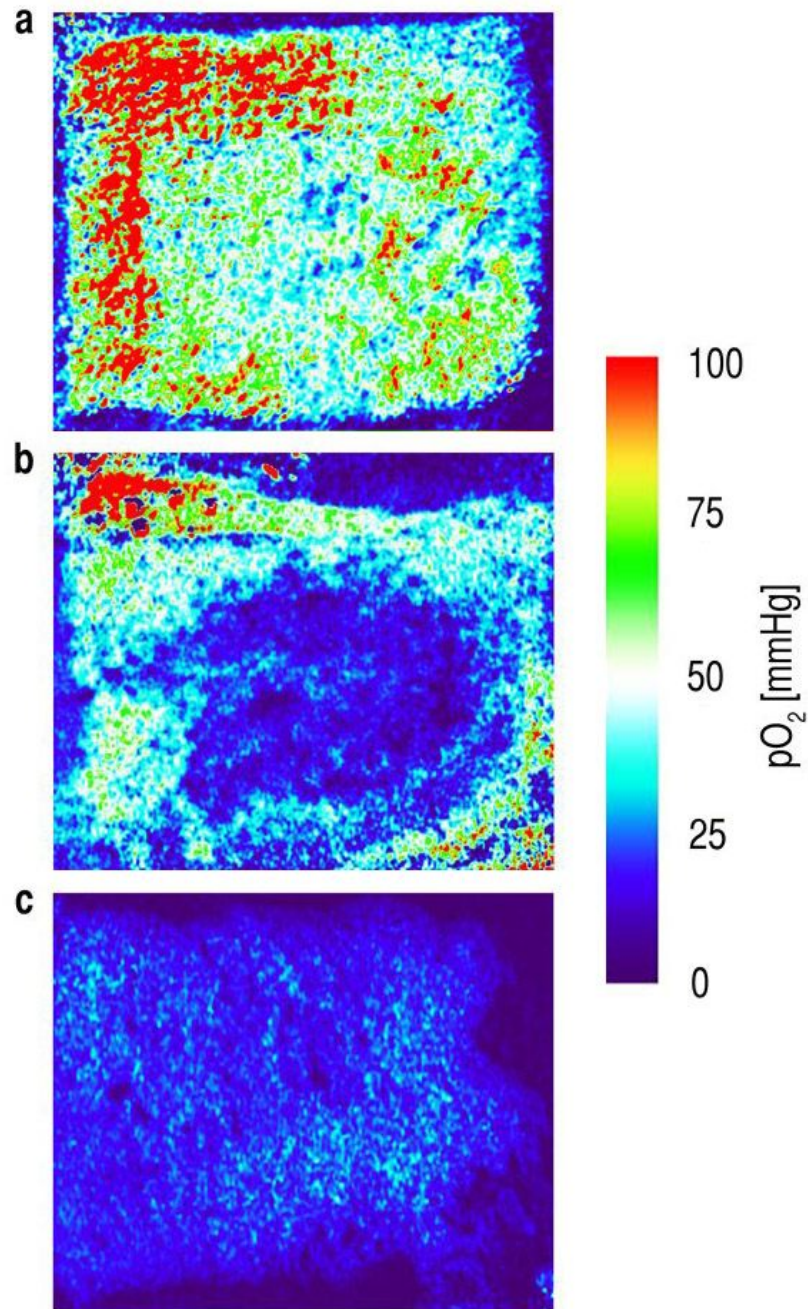


Figure 4.10 | Visualization of wound surface oxygenation at split-skin donor sites: Representative pseudocolor images of spatial $p_{ws}O_2$ distribution produced with 2D-LLI. (a) One day after split-thickness skin graft harvesting, the wound was rather inhomogeneous, and vast areas lacked a significant epidermal oxygen barrier, visible by the brighter orange to red areas. Other areas showed beginning epidermal regeneration as seen by the green to blue colors. (b) After 6 days, large areas within the donor site wounds were partially re-epithelialized as noticeable by the lower $p_{ws}O_2$ values, represented by the darker colors. (c) 14 days postoperatively, most of the donor site wound was re-epithelialized (dark blue or violet areas), and $p_{ws}O_2$ was between 0 and about 10 mmHg.

On day one postoperatively, $p_{ws}O_2$ was assessed to be 57.90 ± 5.49 mmHg. After 6 days the $p_{ws}O_2$ was decreased with high significance ($P < 0.001$) to 22.14 ± 6.18 mmHg. The wound started re-epithelialization. Fourteen days after skin harvesting, $p_{ws}O_2$ of the wound surface further decreases to 6.32 ± 3.24 mmHg. Again, the decrease between day 6 and 14 after surgery was highly significant ($P < 0.001$). All wound surfaces showed marked re-epithelialization. For the first time in literature, the spatially heterogeneous process of healing – as seen by the respective $p_{ws}O_2$ decrease – was visualized with 2D-LLI. A visualization of pO_2 over the course of the healing process of a representative wound can be seen in **Fig. 4.10**.

4.2.4 *In vivo* imaging of skin during stratum corneum removal

In a second *in vivo* experiment, the SC was removed by tape strippings to investigate if the epidermal oxygen barrier is located inside the SC or deeper in skin. In literature, the SC is thought to be a significant barrier for oxygen diffusion through skin^{11,36-39}. The hypothesis was that pO_2 of the skin surface ($p_{ss}O_2$) should increase after SC removal because of the vanishing SC oxygen barrier.

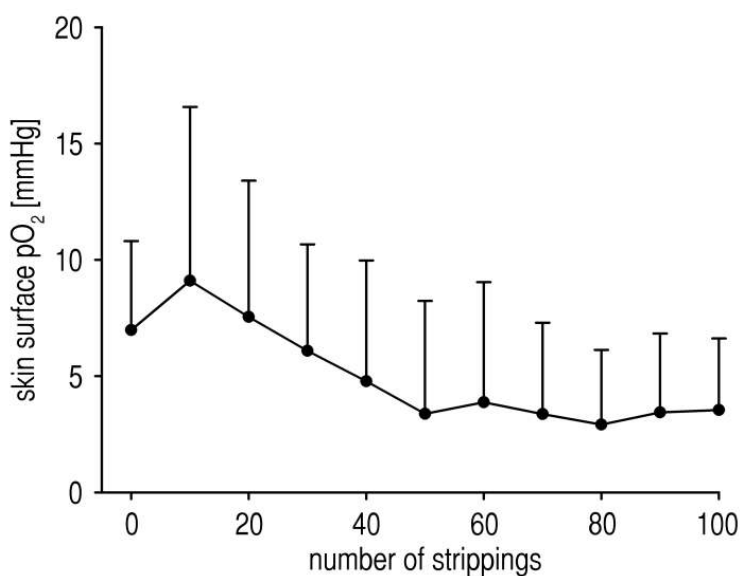


Figure 4.11 | $p_{ss}O_2$ during tape stripping of the SC did not significantly alter as measured with 2D-LLI. Even after complete SC removal following 100 tape strippings, no significant change in $p_{ss}O_2$ was observed compared with values obtained before stripping. Mean \pm SD, $n = 10$, triple samples.

The average $p_{ss}O_2$ on healthy skin of 10 patients (triple measurements) was calculated to be 6.98 ± 3.83 mmHg. The SC was removed via 100 tape strippings. The $p_{ss}O_2$ did not show any significant change. $p_{ss}O_2$ was 3.54 ± 3.08 mmHg after 100 strippings and no significant difference ($P = 0.051$) was observed compared with starting $p_{ss}O_2$ (**Fig.4.11**).

These results indicate that the SC is no major barrier for oxygen diffusion in the epidermis. The major oxygen barrier is suggested to be deeper in skin (stratum granulosum, stratum spinosum, ect.).

4.3 Materials and Methods

4.3.1 Microparticle preparation

Chemicals were purchased from Sigma-Aldrich and all the reactions were conducted at room temperature unless otherwise specified.

The polystyrene microspheres stained with Pd-TPTBP were synthesized by a “soaking” method^{40,41}. The synthetic procedure is customized and optimized to the properties of the used compounds. 50 mg of the PS particles (1 μ m, Polyscience, Niles, USA; www.polyscience.com) were mixed with 5 ml of distilled water and 2.5 ml THF, sonicated (Bandelin Sonorex RK 52) for 30 min to swell the PS microspheres and simultaneously treated with 1 ml of a 1.0 mg ml⁻¹ solution of Pd-TPTBP in THF that was added to the drop wise suspension with a speed of 0.2 ml s⁻¹. The mixture was sonicated for another 20 min. The THF was evaporated using a rotary evaporator. The resulting oxygen sensitive PS particles in the residual water suspension were separated under centrifugation, washed with ethanol and water (four times each). Particles were freeze-dried (Modulyo) for storage.

The PSAN oxygen sensor beads with Pd-TPTBP were prepared using a precipitation method according to literature⁴²⁻⁴⁴. The method was slightly modified to result in particles with a minimum size of 500 nm. 250 mg of (poly(styrene-co-acrylonitrile) (30 wt% acrylonitrile content, 185,000 M_w) was dissolved in 30 ml DMF at 60°C. 5 mg (2% w/w) of

Pd-TPTBP was added to the solution after cooling to room temperature. The solution was slowly but fairly stirred at approximately 350 rpm. 80 ml doubly distilled water was slowly added with approximately 1 drop per second. The solution was stirred for further 30 minutes after water addition. The resulting oxygen sensitive PSAN particles were separated under centrifugation and washed with ethanol for six times to remove the DMF. Particles were stored as ethanolic suspension to prevent agglomeration. Particle sizes were determined with a LEO912 AB transmission electron microscope (Carl Zeiss).

4.3.2 Preparation of the sensor foils

20 mg of the respective oxygen sensitive particles were mixed with a 1 ml of a 9:1 (v/v) ethanol/water solution containing 5% (w/v) of the polyurethane hydrogel (type D4). The particle/matrix cocktail was stirred for at least 12 h and then was spread on a transparent PVdC (Saran food barrier wrap) or polyethyleneterephlate (MYLAR[®], Dr. D. Müller, Ahlhorn, Germany; www.mueller-ahlhorn.com) foils using a K Control Coater model 101 knife coating device (see *chapter 2*) to form a wet 120 µm thick film⁴⁵⁻⁴⁷. Drying of the film resulted in a 6 µm thick sensor layer. Particle distribution inside the sensor foils was investigated using fluorescence microscopy (Axiotech, Carl Zeiss) prior to use.

4.3.3 Luminescence imaging of pO₂ and calibrations

The pO₂ images were recorded using the time-gated imaging setup described in *chapter 2.5*. The recording frequency of the camera was set to 400 Hz. Lifetime was acquired with 70 µs gate width. Luminescence window 1 was recorded with a delay of 1 µs after the excitation pulse (50 µs) to eliminate background fluorescence, while window 2 started after 36 µs. The images were background corrected versus dark images without previous excitation. Triplicates of each image were collected in every measurement cycle. A 800/60 nm bandpass filter (Omega Optical, Brattleboro, VT, USA; www.omegafilters.com) served to separate emitted luminescence from background. The sensors were calibrated in a

calibration chamber (see *chapter 2.4*) from 0 to 160 mmHg pO₂ via mixing oxygen and nitrogen gasses (Linde). Calibrations were repeated at temperatures varying from 20 to 37°C.

4.3.4 Cytotoxicity

Primary human epidermal keratinocytes (HKs) from our laboratory were cultured until confluence in keratinocyte growth medium with supplement (kGMS). HKs were detached using collagenase type 2 (0.1 U/ml, Roche Diagnostics, Basel, Switzerland) and resuspended in kGMS. HKs (passage 3) in kGMS were seeded ($2.5 \cdot 10^3$ cells /well) in 96-well flat-bottom microtiter plates (Costar Inc., Pleasanton, CA, USA) and cultured for 3 days. kGMS was renewed or replaced with FITC-AC and Ru(dpp)₃-PAN in kGMS (0.1-10 µg/ml) and HKs were incubated for 48 h. Cells were washed twice with kGMS and cytotoxicity was evaluated using the 3-(4,5-dimethyl-2-thiazolyl)-2,5-diphenyl-tetrazoliumbromide (MTT) assay. Supernatants were replaced by kGMS supplemented with 16% MTT solution, incubated for 4 h, reaction was stopped with 2% SDS, and quadruplicate samples of absorbance were measured at 540 nm (96-well plate reader; MWG-Biotech AG, Ebersberg, Germany). Cell viability was expressed as the percentage of viable cells compared with controls (kGMS only). Morphology of live cells was examined using an optical microscope (Carl Zeiss).

4.3.5 *In vivo* luminescence imaging

Sensor foils were applied to the skin or the wound surface as described in section 3.3.10. Temperature and humidity were kept constant during measurements. We recorded pO₂ using the 2D sensor foils covering the entire wound surface. The time from application to removal of foils was less than 5 min. No residual luminescence was detected after removal of the sensor foils, confirming that there was no leakage of sensor particles.

4.3.6 Study participants

Male volunteers (n = 10) with a mean age of 27.7 ± 4.0 (SD) years were included in the study on tape stripping. None of the volunteers had any history of skin disorders and none suffered from a skin condition or were subject to dermatological treatment on the volar forearm in the past or at the time of measurement.

The st-SG (thickness set to 400 μm) patients (n = 12, 3 female, 9 male) had a mean age of 67.1 ± 18.8 (SD) years. st-SG were harvested from the left or right ventral thigh to cover tissue defects at different body sites after excision of melanomas and non-melanoma skin cancers. All patients were provided with verbal as well as written information on the study and signed informed consent was obtained from each patient prior to the measurements. The local ethics committee has given approval (No. 06/171: 2007). All experiments and investigations were conducted in full accordance with the Somerset amendment (South Africa, 1996) of the Declaration of Helsinki (1964).

4.3.7 Assessment of the pO₂ on wound surface

The pO₂ values of the skin graft donor sites were assessed by calculating mean values of the pO₂ from all measurement points (i.e. pixels) located within the wound surface. pO₂ values were determined 1, 6, and 14 days after skin harvesting via recording triple samples each. The distance between camera and sample was focus controlled between 25 and 35 cm.

4.3.8 Measurement of the epidermal oxygen barrier pO₂

SC removal for assessing SC pO₂ was conducted according to a method for investigation of SC-pH gradient from Ohman *et al.*⁴⁸ (see also *chapter 3*). The SC was removed on the volar forearm via 100 tape strippings using 3M Scotch Ruban adhesive tape (3M Europe,

Diegem, Belgium; www.3M.com). The tape was firmly pressed against the skin and pulled away uninterrupted. pO₂ triple measurements were carried out after each 10 strippings. The measurements were recorded in 8 cm focal distance using an additional +3 diopter close up lens. Data is assessed from size-standardized squares of 100 x 100 pixels.

4.3.9 Statistics

Sigma Plot 11.0 (Systat Software Inc., Chicago, IL, USA) was used for all analyses. Data are given as mean \pm SD except otherwise denoted. After normality testing, we did a paired t-test to analyze differences between mean pO₂ values obtained from the wound surfaces (n = 12, triple samples) at different time points of healing. Differences in pO₂ values obtained from stripping experiments (n = 10, triplicate samples) were analyzed with one way analysis of variance (ANOVA) on ranks and multiple pair wise comparisons according to Dunn's method. Differences before and after stripping were also analyzed by paired t-testing. Throughout the results, P < 0.05 was considered significant and P < 0.001 was considered highly significant. Significant results were marked with asterisks within the graphs.

4.4 Conclusion

In summary, a first total non-invasive approach for a clinical planar optical oxygen sensor is developed. Intrinsically referenced read out is achieved by 2D-LLI. The sensitivity and dynamic range of the oxygen sensitive dye Pd-TPTBP was controlled to match the physiological range of 0 to 100 mmHg by incorporation in fairly oxygen blocking PSAN microparticles. Further, the particles prevent direct contact of probes and tissue. Biocompatibility of the materials for use in a clinical setup on life human subjects was tested and ensured. The sensor was used for a set of *in vivo* experiments. The first 2D images of the pO₂ distribution during cutaneous wound healing were obtained using this

sensor. Further, two studies on the epidermal oxygen barrier function were carried out. New insights of the location of that barrier were gained and data from literature was rebutted.

4.5 References

- 1 Singer, A. J. & Clark, R. A. Cutaneous wound healing. *N Engl J Med* **341**, 738-746, (1999).
- 2 Schreml, S., Szeimies, R. M., Prantl, L., Landthaler, M. & Babilas, P. What the new millenium taught us about cutaneous wound healing. *J Am Acad Dermatol*, (2009, in press).
- 3 Schreml, S. *et al.* The role of oxygen in wound healing and chronic wound pathogenesis. *J Am Acad Dermatol*, (2009, in press).
- 4 Clark, L. C., Jr., Wolf, R., Granger, D. & Taylor, Z. Continuous recording of blood oxygen tensions by polarography. *J Appl Physiol* **6**, 189-193, (1953).
- 5 Rumsey, W. L., Vanderkooi, J. M. & Wilson, D. F. Imaging of phosphorescence - a novel method for measuring oxygen distribution in perfused tissue. *Science* **241**, 1649-1651, (1988).
- 6 Wilson, D. F. & Cerniglia, G. J. Localization of tumors and evaluation of their state of oxygenation by phosphorescence imaging. *Cancer Res* **52**, 3988-3993, (1992).
- 7 Itoh, T., Yaegashi, K., Kosaka, T., Kinoshita, T. & Morimoto, T. In-vivo visualization of oxygen-transport in microvascular network. *Am J Physiol-Heart C* **267**, 2068-2078, (1994).
- 8 Kerger, H., Torres, I. P., Rivas, M., Winslow, R. M. & Intaglietta, M. Systemic and subcutaneous microvascular oxygen-tension in conscious syrian golden-hamsters. *Am J Physiol-Heart C* **268**, 802-810, (1995).
- 9 Vinogradov, S. A. *et al.* Noninvasive imaging of the distribution in oxygen in tissue in vivo using near-infrared phosphors. *Biophys J* **70**, 1609-1617, (1996).
- 10 Hartmann, P., Ziegler, W., Holst, G. & Lubbers, D. W. Oxygen flux fluorescence lifetime imaging. *Sensor Actuat B-Chem* **38**, 110-115, (1997).
- 11 Stücker, M. *et al.* Flim of luminescent oxygen sensors: Clinical applications and results. *Sensors and Actuators B: Chemical* **51**, 171-175, (1998).
- 12 Babilas, P. *et al.* In vivo phosphorescence imaging of po(2) using planar oxygen sensors. *Microcirculation* **12**, 477-487, (2005).
- 13 Lochmann, C., Hansel, T., Haupl, T. & Beuthan, J. An oxygen imaging system for medical applications: Preliminary results. *Biomed Tech* **51**, 111-115, (2006).
- 14 Smolle, J. *et al.* Non-invasive imaging of tissue po₂ in malignant melanoma of the skin. *Melanoma Research* **16**, 479-486, (2006).
- 15 Babilas, P. *et al.* Transcutaneous po₂ imaging during tourniquet-induced forearm ischemia using planar optical oxygen sensors. *Exp Dermatol* **17**, 265-265, (2008).
- 16 Geis, S. *et al.* Transcutaneous po₂ measurement during tourniquet-induced venous occlusion using dynamic phosphorescence imaging. *Clin Hemorheol Microcirc* **40**, 249-258, (2008).
- 17 Schreml, S. *et al.* Two-dimensional luminescence imaging of ph in vivo. *Exp Dermatol* **20**, 208-208, (2011).

- 18 Rogers, J. E. *et al.* Observation and interpretation of annulated porphyrins: Studies on the photophysical properties of meso-tetraphenylmetalporphyrins. *J Phys Chem A* **107**, 11331-11339, (2003).
- 19 Vinogradov, S. A. & Wilson, D. F. Metallotetrabenzoporphyrins - new phosphorescent probes for oxygen measurements. *J Chem Soc Perk T 2*, 103-111, (1995).
- 20 Vinogradov, S. A. & Wilson, D. F. Extended porphyrins - new ir phosphors for oxygen measurements. *Oxygen Transport to Tissue Xviii* **411**, 597-603, (1997).
- 21 Lee, S. K. & Okura, I. Photoluminescent determination of oxygen using metalloporphyrin-polymer sensing systems. *Spectrochim Acta A* **54**, 91-100, (1998).
- 22 Papkovsky, D. B., Ponomarev, G. V., Trettnak, W. & Oleary, P. Phosphorescent complexes of porphyrin ketones - optical-properties and application to oxygen sensing. *Analytical Chemistry* **67**, 4112-4117, (1995).
- 23 Borisov, S. M., Nuss, G. & Klimant, I. Red light-excitable oxygen sensing materials based on platinum(ii) and palladium(ii) benzoporphyrins. *Analytical Chemistry* **80**, 9435-9442, (2008).
- 24 Stern, O. & Volmer, M. Über die abklingungszeit der fluoreszenz. *Physikalische Zeitschrift*, 183-188, (1919).
- 25 Liebsch, G., Klimant, I., Frank, B., Holst, G. & Wolfbeis, O. S. Luminescence lifetime imaging of oxygen, ph, and carbon dioxide distribution using optical sensors. *Appl Spectrosc* **54**, 548-559, (2000).
- 26 Carraway, E. R., Demas, J. N. & Degraff, B. A. Photophysics and oxygen quenching of transition-metal complexes on fumed silica. *Langmuir* **7**, 2991-2998, (1991).
- 27 Draxler, S. & Lippitsch, M. E. Lifetime-based sensing: Influence of the microenvironment. *Analytical Chemistry* **68**, 753-757, (1996).
- 28 Lu, X. & Winnik, M. A. Luminescence quenching in polymer/filler nanocomposite films used in oxygen sensors. *Chem Mater* **13**, 3449-3463, (2001).
- 29 Wolfbeis, O. S. Materials for fluorescence-based optical chemical sensors. *J Mater Chem* **15**, 2657-2669, (2005).
- 30 Schreml, S. *et al.* 2d luminescence imaging of ph in vivo. *Proc Natl Acad Sci U S A* **108**, 2432-2437, (2011).
- 31 Wolfbeis, O. S. Sensor paints. *Adv Mater* **20**, 3759-3763, (2008).
- 32 Asai, K., Amao, Y., Iijima, Y., Okura, I. & Nishide, H. Novel pressure-sensitive paint for cryogenic and unsteady wind-tunnel testing. *J Thermophys Heat Tr* **16**, 109-115, (2002).
- 33 Gouin, S. & Gouterman, M. Ideality of pressure-sensitive paint. Iii. Effect of the base-coat permeability on the luminescence behavior of the sensing layer. *J Appl Polym Sci* **77**, 2815-2823, (2000).
- 34 Brandrup, J., Immergut, E. H. & Grulke, E. A. Polymer handbook. *Wiley-VCH New-York* (1999).
- 35 Borisov, S. M. *et al.* Springer series on fluorescence, vol. 4: Fluorescence of supermolecules, polymers, and nanosystems *Springer, Berlin, Heidelberg*, (2008).
- 36 Berardesca, E. & Maibach, H. Transcutaneous co₂ and o₂ diffusion. *Skin Pharmacol* **6**, 3-9, (1993).
- 37 Heise, H. M., Lampen, P. & Stucker, M. Reflectance spectroscopy can quantify cutaneous haemoglobin oxygenation by oxygen uptake from the atmosphere after epidermal barrier disruption. *Skin Res Technol* **9**, 295-298, (2003).
- 38 Stucker, M., Moll, C. & Altmeyer, P. [cutaneous oxygen supply. With special consideration of skin uptake of oxygen from the atmosphere]. *Hautarzt* **55**, 273-279, (2004).
- 39 Stucker, M. *et al.* The cutaneous uptake of atmospheric oxygen contributes significantly to the oxygen supply of human dermis and epidermis. *J Physiol* **538**, 985-994, (2002).
- 40 Zhang, Z. L., Long, Y., Pan, J. B. & Yan, X. M. Preparation of fluorescence-encoded microspheres in a core-shell structure for suspension arrays. *J Mater Chem* **20**, 1179-1185, (2010).

- 41 Behnke, T. *et al.* Encapsulation of hydrophobic dyes in polystyrene micro- and nanoparticles via swelling procedures. *J Fluoresc*, epub ahead of print, (2010).
- 42 Borisov, S. M. *et al.* Precipitation as a simple and versatile method for preparation of optical nanochemosensors. *Talanta* **79**, 1322-1330, (2009).
- 43 Borisov, S. M., Vasylevska, A. S., Krause, C. & Wolfbeis, O. S. Composite luminescent material for dual sensing of oxygen and temperature. *Adv Funct Mater* **16**, 1536-1542, (2006).
- 44 Kurner, J. *et al.* Inert phosphorescent nanospheres as markers for optical assays. *Bioconjugate Chem* **12**, 883-889, (2001).
- 45 Borisov, S., Vasylevska, A., Krause, C. & Wolfbeis, O. S. Composite luminescent material for dual sensing of oxygen and temperature. *Advanced Functional Materials* **16**, 1536-1542, (2006).
- 46 Wolfbeis, O. S. Sensor paints. *Advanced Materials* **20**, 3759-3763, (2008).
- 47 Stich, M. I. J., Fischer, L. H. & Wolfbeis, O. S. Multiple fluorescent chemical sensing and imaging. *Chem Soc Rev* **39**, 3102-3114, (2010).
- 48 Ohman, H. & Vahlquist, A. In vivo studies concerning a pH gradient in human stratum corneum and upper epidermis. *Acta Derm Venereol* **74**, 375-379, (1994).

5. Dual sensor for pO₂ and pH *in vivo* using a time-gated approach

A 2D in vivo sensor for simultaneous imaging of physiological wound pH and oxygenation is described in this chapter. The sensor is based on the two different time-gated imaging techniques described in chapter 3 and 4. The tdDLR and the pO₂ sensor particles were simultaneously embedded in a hydrogel matrix and thus combined in one resulting dual sensor layer. Different emission filter sets separate the sensor responses of pO₂ and pH. Cross sensitivities and temperature dependency of the hybrid sensor were studied. The sensor served in two in vivo studies: one on physiological wound healing of skin graft wounds and one on chronic wounds with vasculitic or venous etiopathogenesis. (manuscript in preparation, 2011)

5.1 Introduction

Optical sensors, so called optodes (indicators) or optrodes (the whole sensors) gained large popularity during the last decades¹⁻⁶. Optodes for chemical species are sensitive, non-toxic, and non-invasive and enable spatially resolved analyte detection^{2,7}. Especially imaging of biologically relevant parameters, such as pH, pO₂, hydrogen peroxide (H₂O₂), and Ca²⁺ are of great interest for researchers at the moment⁸⁻¹⁷. A large number of optrodes allow for visualization of only one single parameter, but optical sensing and imaging also paves the way for simultaneous detection of multiple parameters^{7,18,19}. Several dual sensors were reported, mainly for pO₂/temperature, pCO₂/temperature (temperature compensated oxygen or carbon dioxide optrodes), pCO₂/pO₂, and pH/pO₂^{7,19-24}. Stich *et al.* even reported a triple sensor for simultaneous determination of pH, oxygen, and temperature²⁵.

Two concepts for multiple analyte sensor membranes were established: a double-layer concept^{20,21} and a monolayer concept^{7,26,27}. In the double-layer sensors, the sensor

chemistry for each analyte is located in a different layer. Generally, a second layer covers a first that is directly immobilized on a sensor support. Problems during fabrication may occur. The first layer may be destroyed by applying the second layer. The monolayer sensor type overcomes those problems. It contains all sensor materials in one matrix layer. This sensor format is a more straightforward approach, the fabrication process is less tedious and the response times of the sensors are faster due to limited diffusion distances.

Referencing optode signals is always a major concern most notably for *in vivo* measurements. Oxygen or temperature signals are referenced in the majority of cases intrinsically via lifetime determination^{2,18,19,28-30}. Concerning dual sensors, lifetime signals were separated either via RLD and separation of emission wavelengths or via dual lifetime determination (DLD)^{21,26,30,31} using luminophores exhibiting largely different lifetimes. pH or pCO₂ sensing and imaging is mostly based on fluorescent indicators with luminescence lifetimes that are too short to be imaged with fluorescent lifetime imaging^{17,32,33}. Only few exceptions allow for RLD of pH indicators³⁴. Measurement schemes such as tdDLR are used to reference luminescent signals with short lifetimes (see *chapter 1 and 3*)³⁵.

Simultaneous observation of multiple parameters is of special interest for researchers to correlate different analyte distributions in inhomogeneous samples. Regarding dermatological issues and especially wound healing processes, the correlation of pH values and wound oxygenation is still not completely revealed³⁶⁻³⁹. Hitherto, a few dual sensors for simultaneous sensing^{23,40,41} and imaging²⁴ of pH/pO₂ exist. The dual imaging technique for pH/pO₂ from Schröder *et al.*²⁴ offers dual referenced read-out. This scheme enables the detection of pO₂ via RLD and pH measurement as modified tdDLR signals which refers the pH dependent fluorescence signals to the oxygen indicator signal. Unfortunately, the procedure requires tedious mathematical processing and the sensor is very sensitive towards temperature. Further, the sensor does not allow for *in vivo* imaging.

5.2 Results and Discussion

5.2.1 General sensor concept

The two imaging schemes of the pH sensor⁴² (see *chapter 3*) and the pO₂ sensor¹⁷ (described in *chapter 4*) were combined to create a dually referenced *in vivo* pH/pO₂ sensor. The combination of these concepts allows for simultaneous and referenced read-out with a one layer sensor concept. FITC-AC particles (indicator beads) and inert Ru(dpp)₃ PAN particles as reference beads were used for independently referenced tdDLR pH measurements. pO₂ is imaged via RLD of PdTPTBP in PSAN particles. The particles were embedded in a hydrogel matrix which was then deposited on a PVdC sensor support foil (**Fig.5.1**).

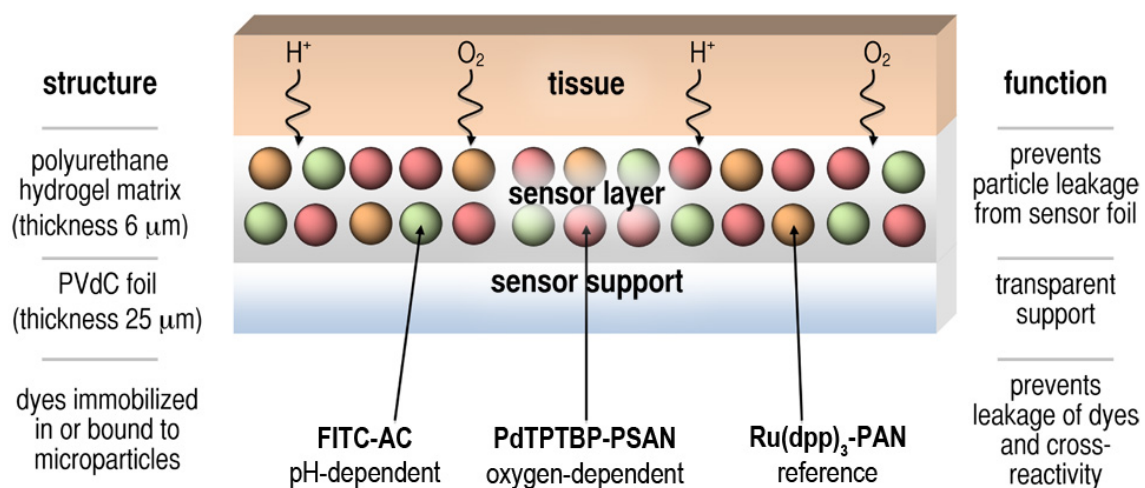
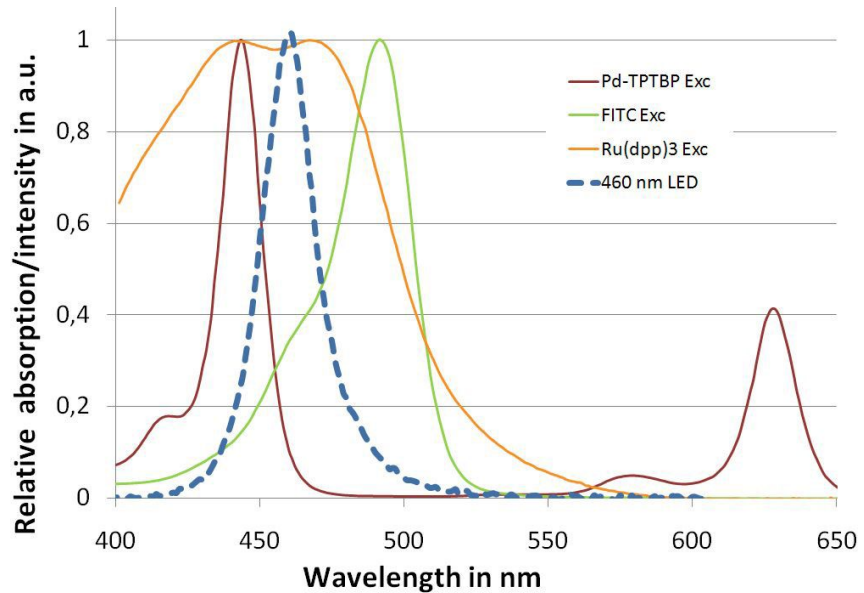


Figure 5.1 | *Sensor foil scheme: Dyes are immobilized in particles to prevent leaching of dyes. The particles are embedded in a proton and oxygen permeable hydrogel matrix to hinder particle leakage out of the sensor. The transparent sensor support allows for localization of underlying structures.*

All three dyes can be photoexcited with the 460 nm LED of the time-gated imaging device (see *chapter 2.5*). The excitation spectra of the dyes and the emission spectra of the LED are shown in **Figure 5.2**. Besides the Soret-Band, the oxygen sensitive PdTPTBP has an additional Q-Band excitation peak at 630 nm^{43,44}. This band may cause FRET or internal reabsorption of emitted light. FRET is prevented by the use of microparticles. The

particles have a minimum size of 500 nm which is much larger than the maximal distance for partners in a FRET (approximately 10 nm)^{45,46}. Internal reabsorption does not effectively disturb the pH/pO₂ measurements since the process of collisional quenching (with oxygen) only affects the excited state but not the absorption process⁴⁶.

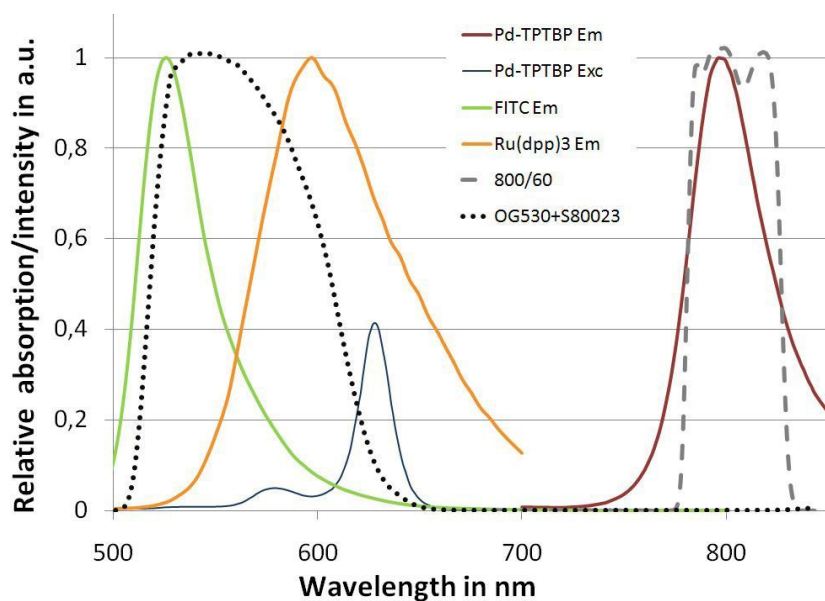
Figure 5.2 | Excitation spectra of the dual sensor particles including the spectrum of the 460 nm LED (dashed blue line).



5.2.2 Signal separation

The signals of the dual sensor can to be separated using optical filters (see **Fig. 5.3**).

Figure 5.3 | Separation of the emitted luminescence signals of the dual sensor. A bandpass filter (dashed grey line) separates the oxygen sensor response, and pH signals were collected using a filter combination (dotted blue line) of an OG530 and a S80023 glass filter.



The pO₂ sensitive luminescence is separated from the pH signals via an 800/60 nm bandpass filter that is exclusively passed by luminescence of the probe PdTPTBP. The luminescent signals of the pH sensor part are on the one hand cut off of excitation light by an OG530 highpass filter. On the other hand, a S80023 bandpass filter closes the spectral window for the pH measurement to block disturbing signals of the oxygen indicator.

5.2.3 *In vitro* characterization

The sensor was calibrated in the range of pH 3 to 10 and 0 to 160 mmHg, respectively (**Fig. 5.4**). The pH sensor showed a pK_a of 5.9. The total sensor response in the range of 0 to 160 mmHg can be described using a more complicated modified Stern-Volmer plot, the two-site model^{29,47,48}. Fortunately, the calibration curve in desired range of 0 to 100 mmHg is sufficiently described by a simple linear Stern-Volmer plot. A K_{sv} of 0.0337/mmHg was found.

Further, the cross sensitivity of the pH signal towards different pO₂ ranging from 0 to 160 mmHg was investigated. The pH dependent signal R (= A_{ex}/A_{em}) is independent from oxygen tension (**Fig. 5.5**). The intensity of the FITC-AC particles is virtually not affected by oxygen. Photoexcited FITC in hydrophilic environments almost exclusively results in a singlet emission ($\phi_{\text{singlet}} = 0.97$ in H₂O) and thus cannot be quenched by oxygen⁴⁹. The reference dye indeed emits from its excited triplet state and thus could be quenched by oxygen, but it is shielded by oxygen impermeable PAN particles.

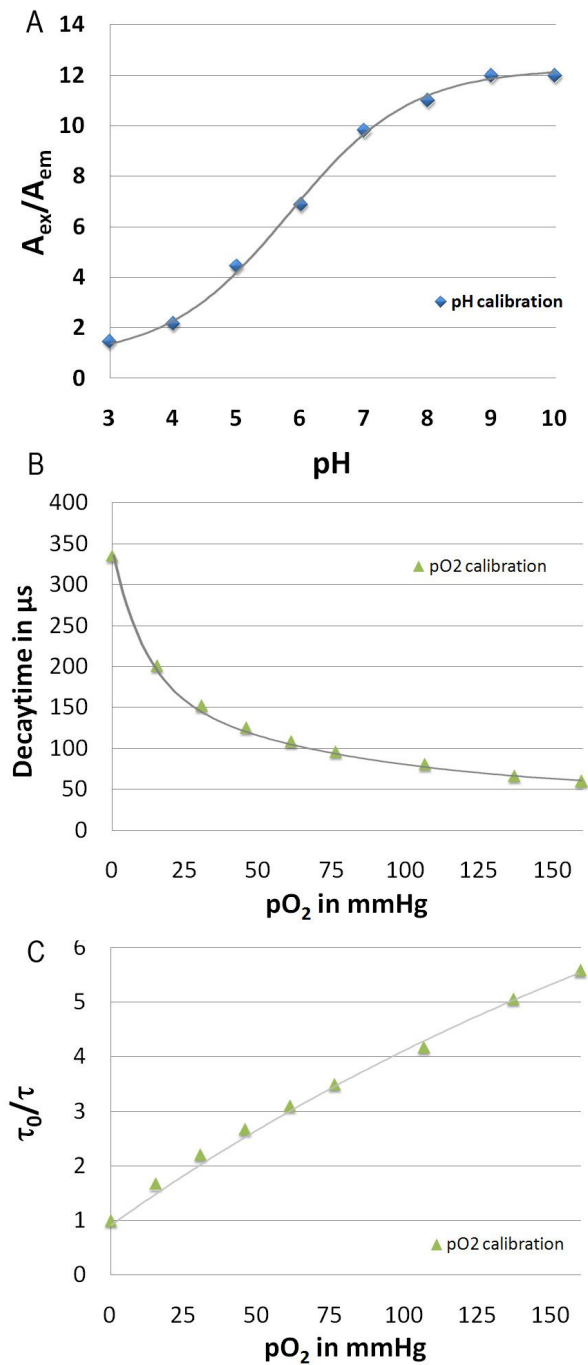
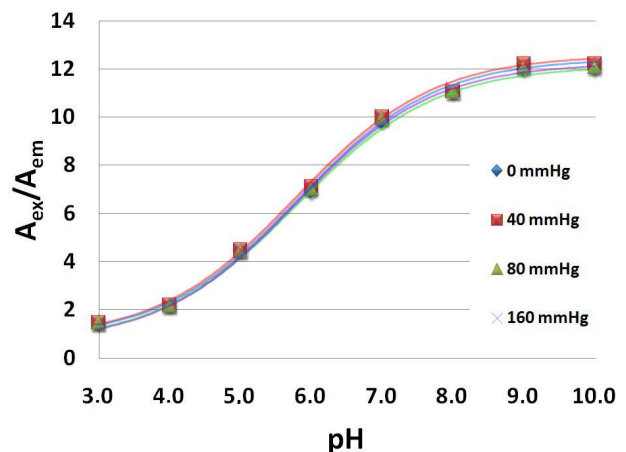


Figure 5.4 | Calibration graphs of the dual sensor: response of the pH dependent signal $R (= A_{ex}/A_{em})$ towards different buffer solutions (**A**) results in a sigmoidal behavior in the range of pH 3 to 9. The response of the phosphorescence decay time (**B**) of Pd-TPTBP in PSAN microparticles towards oxygen gives biexponential decay. **C** shows the respective Stern-Volmer plot. All calibrations were carried out at 30°C.

Figure 5.5 | pH titration plots at various partial pressures of oxygen. No cross sensitivity of the pH signal towards oxygen was found for the range of 0 to 160 mmHg.



The oxygen response of the dual sensor also showed no cross sensitivity (**Fig.5.6**). The oxygen sensitive probe is incorporated in PSAN particles. PSAN is a hydrophobic polymer which inhibits protons or water from diffusing into the particles towards the sensor molecules and cause collisional quenching.

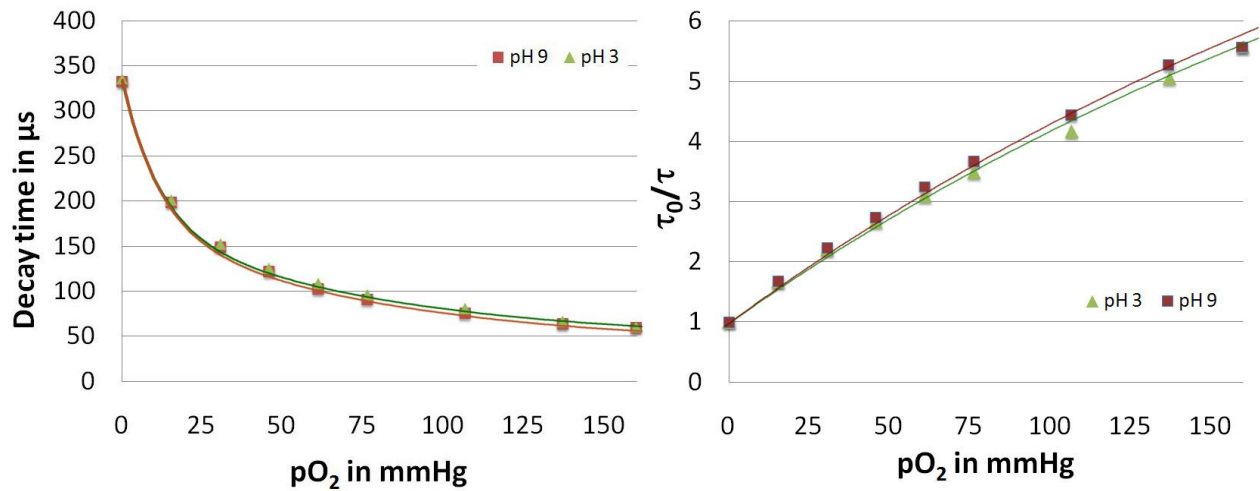


Figure 5.6 | Calibration plots at varying pH values. No cross sensitivity of the pO_2 signal towards pH solutions was found. Decay times for oxygen calibrations at pH 3 and pH 9 were virtually identical.

Neither pH signals (**Fig.5.7**) nor pO_2 measurements (**Fig.5.8**) showed critical temperature sensitivity in the range of 20 to 37 °C.

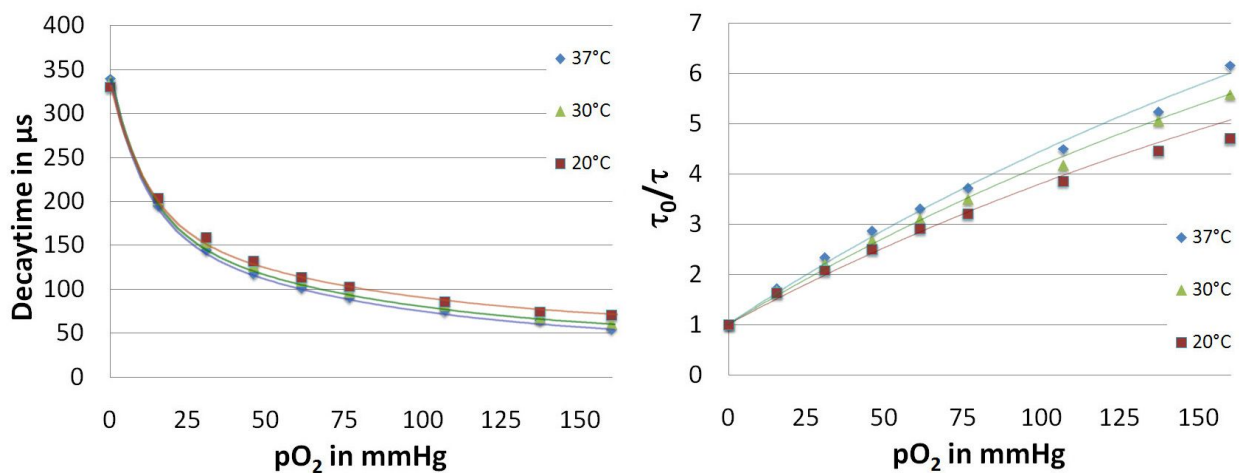
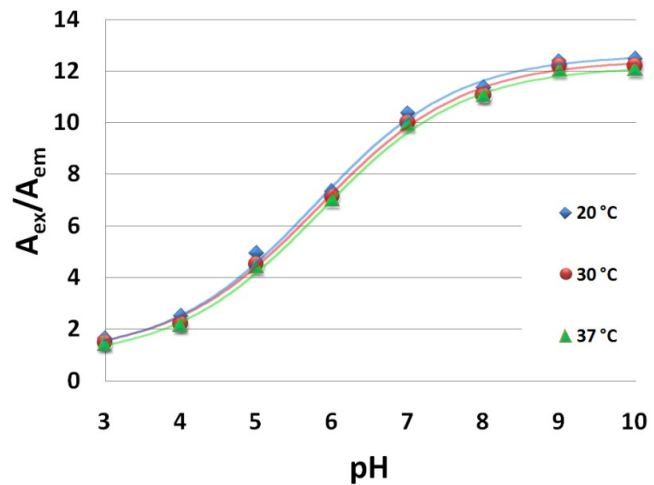


Figure 5.7 | Calibration plots towards pO_2 at varying temperatures. The oxygen response of the sensor showed no exceeding temperature sensitivity from 20 to 37 °C.

Figure 5.8 | pH titration plots at varying temperatures. No substantial temperature sensitivity of the pH dependent signal $R (= A_{ex}/A_{em})$ of the sensor was found from 20 to 37 °C.



Particle sizes, photobleaching and biocompatibility issues of the particles used in the time-gated dual sensor were already discussed in the previous chapters. The response times of the dual sensor were identical to those of the single parameter sensors (*chapter 3 and 4*).

5.2.4 Imaging of a skin graft donor site

In a first experiment, physiological wound healing of skin graft wounds was simultaneously visualized with the pH/pO₂ dual sensor as described in *chapter 3 and 4* for the single sensors. The pH and the pO₂ of the wound surface of 3 patients were observed 1, 6, and 14 days postoperatively (**Fig. 5.9**). Both, pH and pO₂ results of the dual sensor matched the data observed by the use of the single sensors. pH values decreased from pH 7 to 8.5 on day 1 to approximately pH 6 on day 14 due to the re-establishment of the epidermal pH barrier. Concomitant, the wound oxygenation decreased from approximately 80 mmHg to low range pO₂ values of 5 to 20 mmHg.

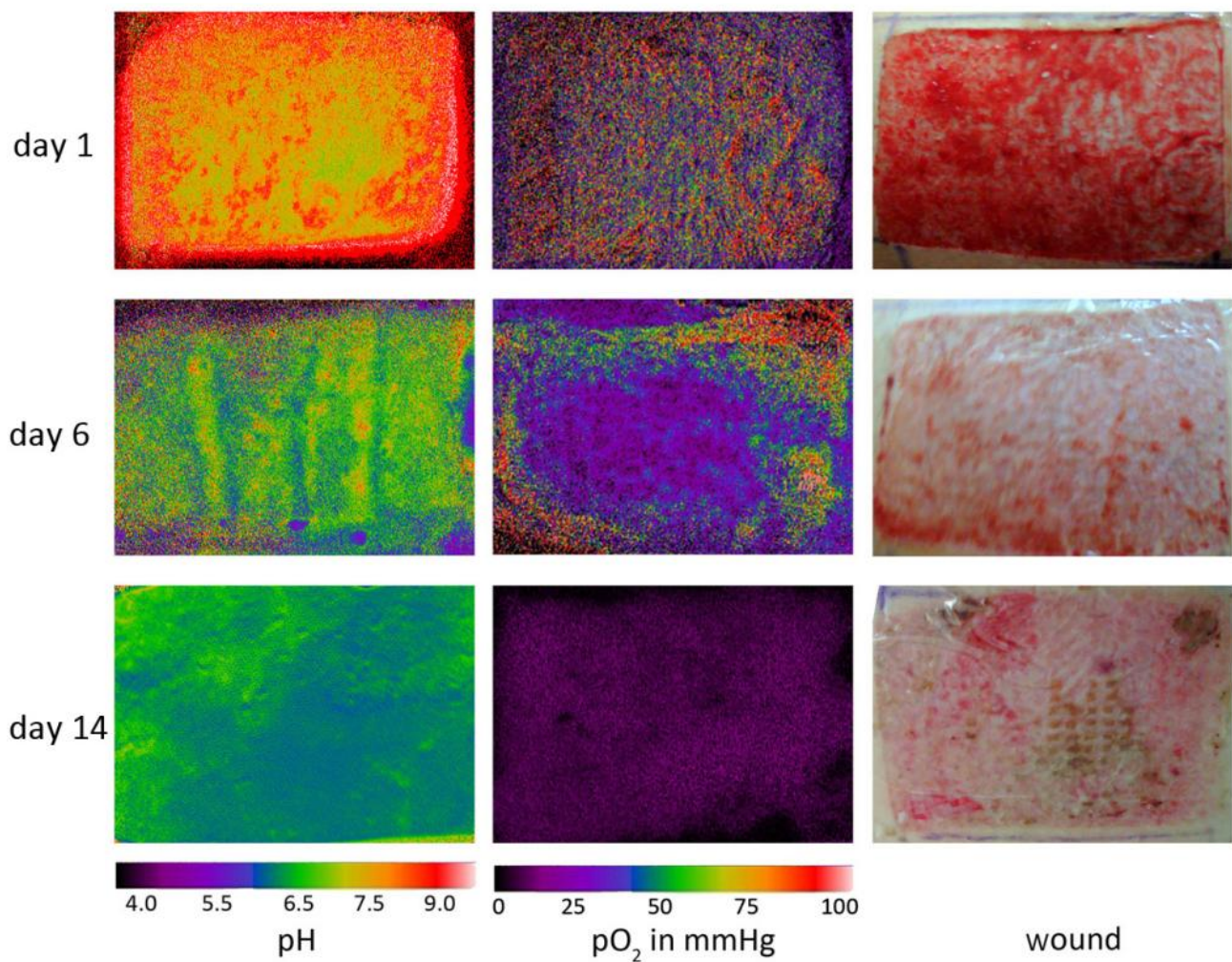


Figure 5.9 | Visualization of pH and pO₂ distributions (displayed in pseudocolor) during physiological wound healing of a representative split skin harvest donor site on day 1, 6, and 14 respectively. pH and pO₂ values decrease with progressive re-establishment of the epidermal barriers in skin. Scale: 8.5 x 13 cm.

5.2.5 Imaging of chronic ulcers

In a second *in vivo* experiment, chronic wounds (ulcers) caused by vasculitis or with venous etiopathogenesis were investigated. **Figure 5.10** exemplarily shows a vasculitic ulcer and the respective pH and oxygen distributions. The relatively small ulcer was had a size of 5 x 2.5 cm and was located on the lower left leg.

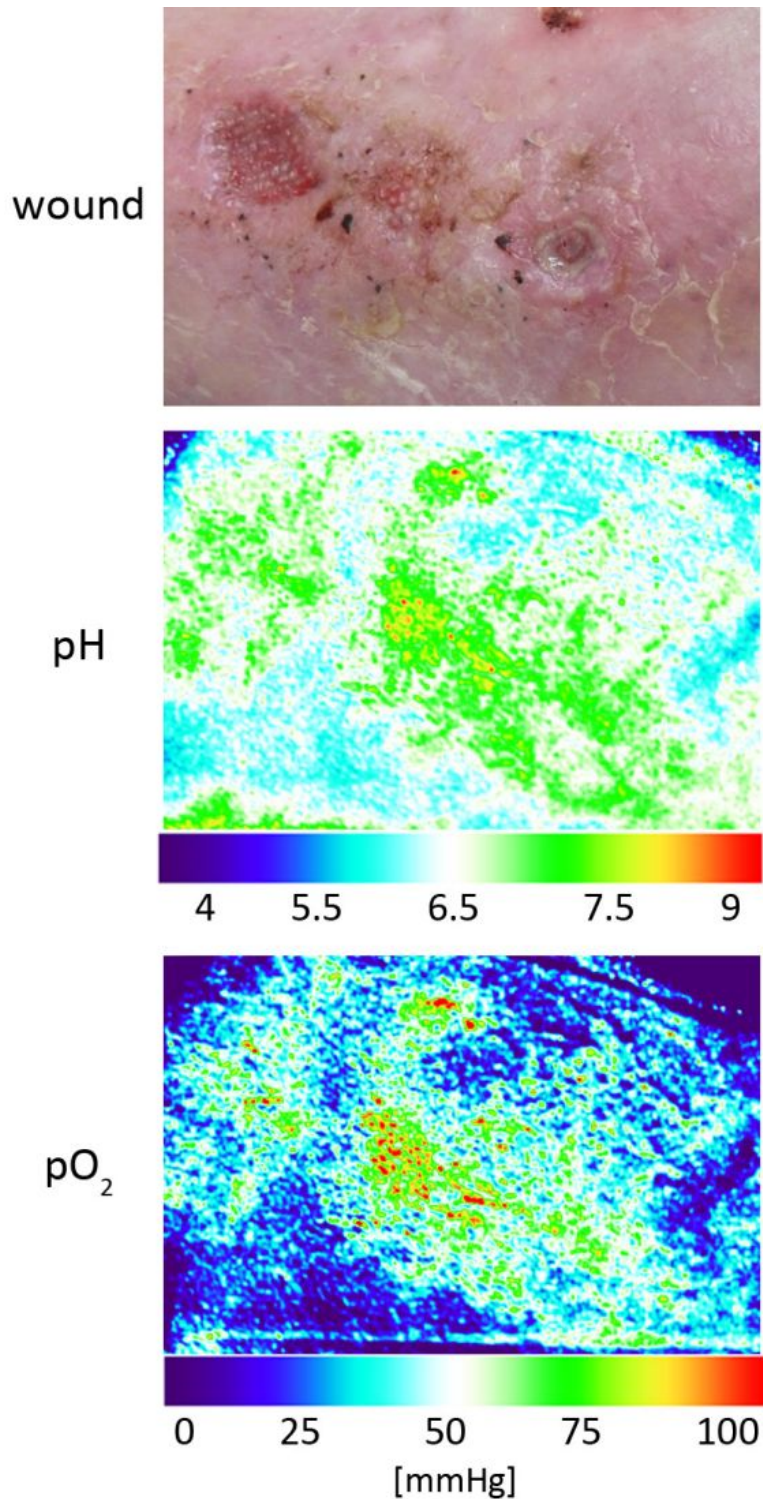


Figure 5.10 | Visualization of the pH and pO₂ distribution of a chronic vasculitic ulcer on the left foot of a patient. The real color picture (top) shows the heterogeneous wound surface including three parts with defective skin. pH and pO₂ values (middle and bottom) inside and in surrounding environments of the defective skin parts were found to be moderately increased (pH 6.8 – 8 and 70 – 90 mmHg). The lower left side of the respective analyte distribution images shows more intact skin with pH values of approximately pH 6 and low oxygenation levels (5 – 30 mmHg). Scale: 4.2 x 7 cm.

Besides vasculitic ulcers, the study also included venous ulcers. **Figure 5.11** depicts a venous ulcer with a larger and deep skin defect, and the respective analyte distributions. The venous ulcer was sized 4 x 10 cm.

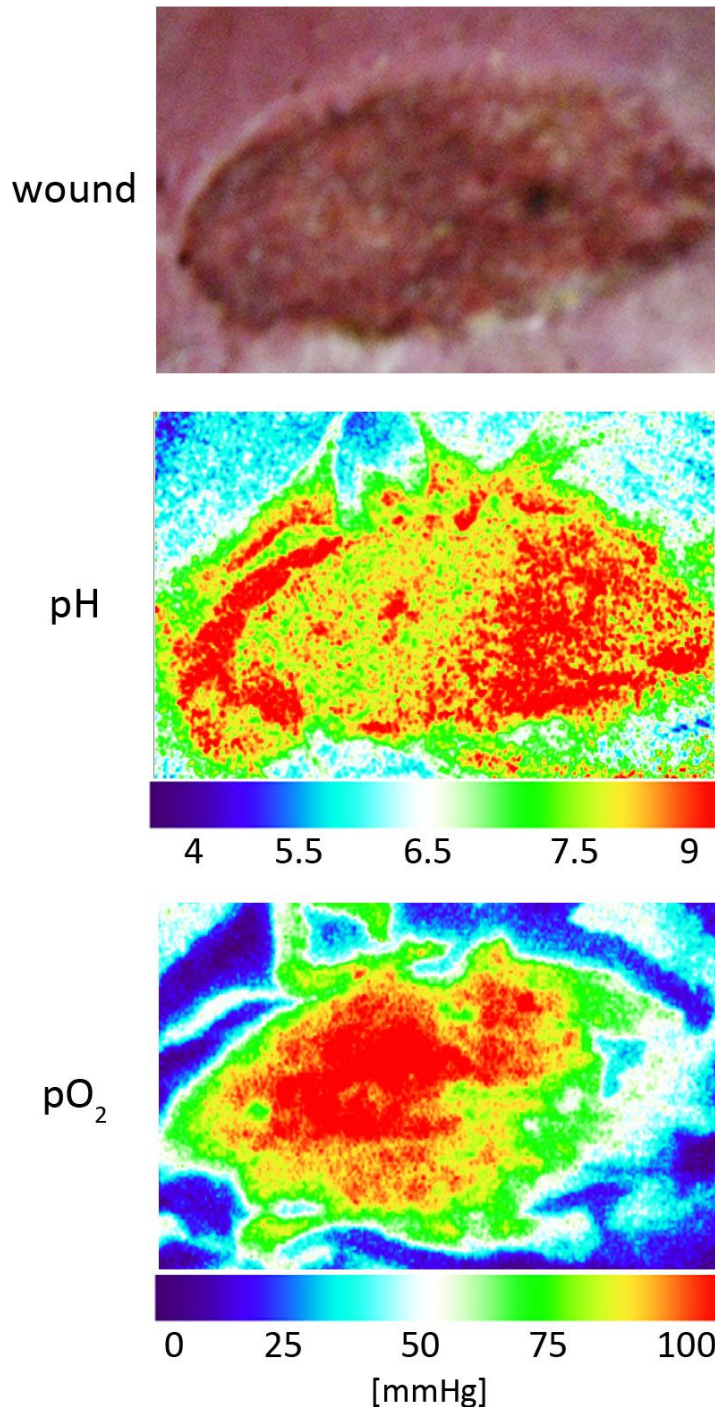


Figure 5.11 | Visualization of the pH and pO₂ distribution of a chronic venous ulcer on a left leg. The real color picture shows the wound surface with one large area of defective skin. pH and pO₂ values (middle and bottom) inside defective skin were found to be highly increased (pH 8 - 9 and up to 90 mmHg). The surrounding tissue shows relatively normal to slight increased pH and pO₂ values (pH 6 and 5 - 30 mmHg pO₂). Scale: 6 x 10 cm.

Other ulcers in the study were sized up to 18 x 10 cm. They had either to be visualized with one big sensor foil to generate an overview or were visualized in parts to get more detailed information on analyte distributions.

5.3 Materials and methods

5.3.1 Microparticle preparation

The preparation of the pH sensitive FITC-AC and the Ru(dpp)₃-PAN reference particles is described in section 3.3.1. The oxygen sensor beads were prepared according to section 4.3.1.

5.3.2 Preparation of sensor foils

150 mg FITC-AC, 50 mg Ru(dpp)₃-PAN and 100 mg of Pd-TPTBP-PSAN were mixed with 20 ml of a solution consisting of 5% (w/v) of polyurethane-hydrogel (type D4, Cardiotech International Inc.) in ethanol/water (90/10 v/v). This mixture was spread on a transparent poly(vinylidene-chloride) (PVdC) foil (Saran[®] plastic wrap) with a knife coating device to result in a 120 μm thick wet film^{18,19,21}. After drying, the sensor layer was 6 μm thick.

5.3.3 Luminescence imaging of pH/pO₂ and calibrations

The pH/pO₂ images were recorded using the time-gated imaging setup described in *chapter 2.5*. For all measurements, the recording frequency of the camera was set to 400 Hz. For pH measurements camera parameters were set as follows: subtract background, 5 μs gate width, 0.25 μs delay time, 6 μs lamp pulse, and 100 ms integration time. An optical filter combination of a 530 nm long-pass OG530 glass filter and a S80023 bandpass filter (both obtained from Schott) served to filter emission light.

Oxygen sensitive lifetime of Pd-TPTBP was acquired with 70 μ s gate width. Luminescence window 1 was recorded with a delay of 1 μ s after the excitation pulse (50 μ s) to eliminate background fluorescence. Window 2 started after 36 μ s. Dark images were subtracted to correct the background. An 800/60 nm bandpass filter (Omega Optical) separated the oxygen signal from background and pH sensor luminescence.

Triple samples were collected in every measurement cycle. Each depicted pH/pO₂ distribution reflects a mean of three measurements. The sensors were calibrated in a calibration chamber (see *chapter 2.4*) from 0 to 160 mmHg pO₂ via mixing oxygen and nitrogen gasses (Linde) and from pH 3-10 in single pH steps using 50 mM Britton Robinson buffers (consisting of 0.04 M H₃BO₃, 0.04 M H₃PO₄ and 0.04 M CH₃COOH in distilled H₂O). Calibrations were repeated at temperatures varying from 20 to 37°C.

Measurements, calibrations, calculations, and pseudocolor image processing were accomplished with ImageX software (Microsoft). Additional pseudocolor image processing for visualization of chronic wounds was performed with ImageJ (<http://rsbweb.nih.gov/ij/>).

5.3.4 Study participants

All participants were provided with verbal and written information on the study and signed informed consent was obtained from each participant. The local ethics committee had given approval (No. 06/171: 2007) and all experiments were conducted in full accordance with the sixth revision (Seoul, Korea, 2008) of the Declaration of Helsinki (1964). Split-skin graft (thickness 400 μ m, female, 68 years) was harvested from the left thigh to cover a tissue defect after excision of skin tumors. The donor site was investigated. Further, a chronic venous ulcer on the lower left leg (lateral, since 3 years) of a female patient (74 years) and a chronic vasculitic ulcer (since 5 years) on the left foot of a female patient (70 years) were imaged.

5.3.5 *In vivo* luminescence imaging

Sensor foils were gently applied to the skin or the wound surface as described in section 3.3.10. Temperature and humidity were kept constant throughout the measurements. pH and pO₂ were imaged on a split-skin donor site wound after 1, 6, and 14 days following split-skin harvesting. Chronic wounds were visualized subsequent to removal of the wound dressing. pH/pO₂ was recorded using 2D dual sensor foils covering the entire wound surface. The time from application to removal of the foils did not exceed 8 min. The distance between camera and tissue sample was focus controlled between 25 and 35 cm.

5.4 Conclusion

In summary, the first total non-invasive *in vivo* sensor for dual imaging of pH and pO₂ in human tissue is developed. The sensor offers independently referenced read-out for each of the two species. Imaging of pH is referenced via td-DLR. Oxygen measurements are intrinsically referenced via 2D-LLI and RLD. The signal for pH and pO₂ are separated via emission filters. The dual sensor offers a dynamic range that covers the physiological range for wound healing and skin investigations. The signals neither show cross sensitivity nor significant temperature dependency. The optode was used *in vivo* to obtain the first simultaneously recorded images of pH/pO₂ distributions during cutaneous wound healing. A split skin donor site and chronic ulcers were studied.

5.5 References

- 1 Vurek, G. G. *In vivo* optical chemical sensors. *P Soc Photo-Opt Inst* **494**, 2-6, (1984).
- 2 McDonagh, C., Burke, C. S. & MacCraith, B. D. Optical chemical sensors. *Chem Rev* **108**, 400-422, (2008).
- 3 Wolfbeis, O. S. Materials for fluorescence-based optical chemical sensors. *J Mater Chem* **15**, 2657, (2005).
- 4 Wolfbeis, O. S. Optical sensors: Industrial, environmental and diagnostic applications (springer series on chemical sensors and biosensors). *Springer, Berlin*, 1 - 34, (2003).
- 5 Wolfbeis, O. S. Proceedings of the 1st european conference on optical chemical sensors and biosensors - europt(r)ode-1 - graz, austria april 12-15, 1992 - preface. *Sensor Actuat B-Chem* **11**, R10-R10, (1993).
- 6 Borisov, S. M. & Wolfbeis, O. S. Optical biosensors. *Chem Rev* **108**, 423-461, (2008).

- 7 Nagl, S. & Wolfbeis, O. S. Optical multiple chemical sensing: Status and current challenges. *The Analyst* **132**, 507 (2007).
- 8 Lee, D. *et al.* In vivo imaging of hydrogen peroxide with chemiluminescent nanoparticles. *Nat Mater* **6**, 765-769, (2007).
- 9 Nagai, T., Sawano, A., Park, E. S. & Miyawaki, A. Circularly permuted green fluorescent proteins engineered to sense ca²⁺. *Proc Natl Acad Sci U S A* **98**, 3197-3202, (2001).
- 10 Nagai, T., Yamada, S., Tominaga, T., Ichikawa, M. & Miyawaki, A. Expanded dynamic range of fluorescent indicators for ca²⁺ by circularly permuted yellow fluorescent proteins. *Proc Natl Acad Sci U S A* **101**, 10554-10559, (2004).
- 11 Nakai, J., Ohkura, M. & Imoto, K. A high signal-to-noise ca²⁺ probe composed of a single green fluorescent protein. *Nat Biotechnol* **19**, 137-141, (2001).
- 12 Niethammer, P., Grabher, C., Look, A. T. & Mitchison, T. J. A tissue-scale gradient of hydrogen peroxide mediates rapid wound detection in zebrafish. *Nature* **459**, 996-999, (2009).
- 13 Zhang, G., Palmer, G. M., Dewhirst, M. W. & Fraser, C. L. A dual-emissive-materials design concept enables tumour hypoxia imaging. *Nat Mater* **8**, 747-751, (2009).
- 14 Lochmann, C., Hansel, T., Haupl, T. & Beuthan, J. An oxygen imaging system for medical applications: Preliminary results. *Biomed Tech* **51**, 111-115, (2006).
- 15 Smolle, J. *et al.* Non-invasive imaging of tissue po₂ in malignant melanoma of the skin. *Melanoma Research* **16**, 479-486, (2006).
- 16 Geis, S. *et al.* Transcutaneous po₂ measurement during tourniquet-induced venous occlusion using dynamic phosphorescence imaging. *Clin Hemorheol Microcirc* **40**, 249-258, (2008).
- 17 Schreml, S. *et al.* 2d luminescence imaging of ph in vivo. *Proc Natl Acad Sci U S A* **108**, 2432-2437, (2011).
- 18 Wolfbeis, O. S. Sensor paints. *Adv Mater* **20**, 3759-3763, (2008).
- 19 Stich, M. I. J., Fischer, L. H. & Wolfbeis, O. S. Multiple fluorescent chemical sensing and imaging. *Chem Soc Rev* **39**, 3102-3114, (2010).
- 20 Wolfbeis, O. S., Weis, L. J., Leiner, M. J. P. & Ziegler, W. E. Fiber-optic fluorosensor for oxygen and carbon-dioxide. *Analytical Chemistry* **60**, 2028-2030, (1988).
- 21 Borisov, S. M., Vasylevska, A. S., Krause, C. & Wolfbeis, O. S. Composite luminescent material for dual sensing of oxygen and temperature. *Adv Funct Mater* **16**, 1536-1542, (2006).
- 22 Borisov, S. M., Neurauter, G., Schroeder, C., Klimant, I. & Wolfbeis, O. S. Modified dual lifetime referencing method for simultaneous optical determination and sensing of two analytes. *Appl Spectrosc* **60**, 1167-1173, (2006).
- 23 Vasylevska, G. S., Borisov, S. M., Krause, C. & Wolfbeis, O. S. Indicator-loaded permeation-selective microbeads for use in fiber optic simultaneous sensing of ph and dissolved oxygen. *Chem Mater* **18**, 4609-4616, (2006).
- 24 Schroder, C. R., Polerecky, L. & Klimant, I. Time-resolved ph/po₂ mapping with luminescent hybrid sensors. *Analytical Chemistry* **79**, 60-70, (2007).
- 25 Stich, M. I. J., Schaeferling, M. & Wolfbeis, O. S. Multicolor fluorescent and permeation-selective microbeads enable simultaneous sensing of ph, oxygen, and temperature. *Adv Mater* **21**, 2216, (2009).
- 26 Hradil, J., Davis, C., Mongey, K., McDonagh, C. & MacCraith, B. D. Temperature-corrected pressure-sensitive paint measurements using a single camera and a dual-lifetime approach. *Meas Sci Technol* **13**, 1552-1557, (2002).
- 27 Nagl, S., Stich, M. I. J., Schäferling, M. & Wolfbeis, O. S. Method for simultaneous luminescence sensing of two species using optical probes of different decay time, and its application to an enzymatic reaction at varying temperature. *Anal Bioanal Chem* **393**, 1199-1207, (2008).

- 28 Amao, Y. Probes and polymers for optical sensing of oxygen. *Microchim Acta* **143**, 1-12, (2003).
- 29 Draxler, S. & Lippitsch, M. E. Lifetime-based sensing: Influence of the microenvironment. *Analytical Chemistry* **68**, 753-757, (1996).
- 30 Rai, V. K. Temperature sensors and optical sensors. *Applied Physics B* **88**, 297-303, (2007).
- 31 Stich, M. I. J., Nagl, S., Wolfbeis, O. S., Henne, U. & Schaeferling, M. A dual luminescent sensor material for simultaneous imaging of pressure and temperature on surfaces. *Adv Funct Mater* **18**, 1399-1406, (2008).
- 32 Weidgans, B. M. New fluorescent optical pH sensors with minimal effects of ionic strength. *Ph.D. Thesis, University of Regensburg*, 15, (2004).
- 33 Han, J. & Burgess, K. Fluorescent indicators for intracellular pH. *Chem Rev* **110**, 2709-2728, (2010).
- 34 Wang, Y. *et al.* Phosphorescent pH sensors and switches with substitutionally tunable response range based on photo-induced electron transfer. *Luminescence* **20**, 339-346, (2005).
- 35 Liebsch, G., Klimant, I., Krause, C. & Wolfbeis, O. S. Fluorescent imaging of pH with optical sensors using time domain dual lifetime referencing. *Analytical Chemistry* **73**, 4354-4363, (2001).
- 36 Allen, D. B. *et al.* Wound hypoxia and acidosis limit neutrophil bacterial killing mechanisms. *Arch Surg-Chicago* **132**, 991-996, (1997).
- 37 Schreml, S., Szeimies, R.-M., Prantl, L., Landthaler, M. & Babilas, P. Wound healing in the 21st century. *J Am Acad Dermatol* **63**, 866-881, (2010).
- 38 Singer, A. J. & Clark, R. A. Cutaneous wound healing. *N Engl J Med* **341**, 738-746, (1999).
- 39 Schreml, S. *et al.* The impact of the pH value on skin integrity and cutaneous wound healing. *J Eur Acad Dermatol* **24**, 373-378, (2009).
- 40 Kocincová, A. S. *et al.* Multiplex bacterial growth monitoring in 24-well microplates using a dual optical sensor for dissolved oxygen and pH. *Biotechnol Bioeng* **100**, 430-438, (2008).
- 41 Kocincova, A. S., Borisov, S. M., Krause, C. & Wolfbeis, O. S. Fiber-optic microsensors for simultaneous sensing of oxygen and pH, and of oxygen and temperature. *Analytical Chemistry* **79**, 8486-8493, (2007).
- 42 Schreml, S. *et al.* Two-dimensional luminescence imaging of pH in vivo. *Exp Dermatol* **20**, 208-208, (2011).
- 43 Soret, J.-L. Analyse spectrale: Sur le spectre d'absorption du sang dans la partie violette et ultra-violette. *Comptes rendus de l'Académie des sciences*, 1269-1270, (1883).
- 44 Borisov, S. M. *et al.* Photophysical properties of the new phosphorescent platinum(ii) and palladium(ii) complexes of benzoporphyrins and chlorins. *J Photoch Photobio A* **206**, 87-92, (2009).
- 45 Förster, T. Zwischenmolekulare energiewanderung und fluoreszenz. *Annalen der Physik* **437**, 55-75, (1948).
- 46 Lakowicz, J. R. Principles of fluorescence spectroscopy 2nd edition. *Springer, Berlin*, (1999).
- 47 Carraway, E. R., Demas, J. N. & Degraff, B. A. Photophysics and oxygen quenching of transition-metal complexes on fumed silica. *Langmuir* **7**, 2991-2998, (1991).
- 48 Lu, X. & Winnik, M. A. Luminescence quenching in polymer/filler nanocomposite films used in oxygen sensors. *Chem Mater* **13**, 3449-3463, (2001).
- 49 Devanathan, S., Dahl, T. A., Midden, W. R. & Neckers, D. C. Readily available fluorescein isothiocyanate-conjugated antibodies can be easily converted into targeted phototoxic agents for antibacterial, antiviral, and anticancer therapy. *Proc Natl Acad Sci U S A* **87**, 2980-2984, (1990).

6. Ratiometric RGB imaging

This chapter describes a novel and straightforward luminescence concept for ratiometric read-out. Most notably, the concept makes use of a standard digital photographic camera that serves as a rudimentary "spectrometer" for wavelength separation. The method is based on the fact that digital pictures are composed of three virtually independent (viz. a red, green, and blue) pictures that are separately stored in digital cameras (the so-called RGB technique). Such cameras are quite affordable which is of particular significance with respect to clinical (routine) applications. Analyte distributions can be calculated by dividing the data contained in the analyte channel by those of the reference channel. The RGB technique offers remarkable improvement and simplification in fluorescence ratiometric imaging (FRIM). First, this chapter introduces the general RGB concept on the basis of a simple oxygen sensor membrane. Furthermore, different applications using the RGB method are described. The methods include a pH as well as a CO₂ sensor membrane.

6.1 Photographing oxygen distribution

The spatial distribution of oxygen can be imaged with a standard digital camera by making use of a specially designed sensor film and by exploiting the specific RGB option of digital photography. This resulted in the simplest method ever described for sensing and imaging this important species. (Angewandte Chemie International Edition, 2010 vol. 49 no 29 4907-4909)

6.1.1 Introduction

Oxygen is one of the most fundamental chemical species for life on earth. Consequently, determining of oxygen concentrations is essential in various areas such as medicine^{1,2} and

physiology³, biology^{4,5}, biotechnology⁶⁻⁸, clinical diagnosis^{1,2}, cancer research^{9,10}, the chemical industry^{8,11}, environmental sciences¹², and in less obvious areas such as coal mines¹³, food packaging¹⁴, or marine research¹⁵. Oxygen also is the species that is sensed in so-called pressure-sensitive paints (PSPs)¹⁶⁻¹⁸. PSPs are indispensable tools in automotive and aerodynamic research. Further, oxygen plays an important role in biosensors based on enzyme-associated reactions during which oxygen is consumed, for example in biosensors for glucose¹⁹. Oxygen sensors are based on measurement of either (gas) pressure²⁰, electrical current (e.g. Clark electrode)²¹, or of signals of appropriate optical (usually luminescent) indicators²². They are fabricated in large numbers and widely applied nowadays. Optical oxygen sensors have become a subject of particular research in recent years^{22,23} in view of their distinct advantages over other kinds of sensors (see *chapter 1*), and because they enable chemical species to be detected remotely or invasively if combined with optical fiber technology^{24,25} or in nanometer dimensions^{26,27}. Quite recently, oxygen has been detected via dual-color systems rather than with single emitting probes²⁸⁻³². Such methods enable semi-quantitative colorimetric determination of oxygen via visual read-out. However, sophisticated instrumentation is required for quantitative sensing and imaging, and this represents a substantial drawback.

A recent trend in sensor technology was started by Suslick et al.³³⁻³⁵ and Filipini et al.^{36,37} involving the use of devices such as computer screens or mobile phone cameras to monitor chemical targets. This can substantially reduce the costs and time that is needed for development of diagnostic instrumentation. Moreover, such devices are affordable and familiar to potential users. In this section the combination of 2-color digital photographic cameras (another "familiar" device) and 2-color sensor technology is shown as a simple method for sensing and imaging of oxygen that may replace more complex systems³⁸.

6.1.2 Results and discussion

Practically all digital photographic cameras are based on the use of metal oxide semiconductor (CMOS) chips containing so-called RGB channels (see **Fig. 6.1**) that are

sensitive to the red, green and blue part of the visible spectrum. A Bayer matrix of filter elements is arranged on the CMOS chip to split the picture into three colors. The RGB chips contain the double amount of green pixels compared to red and blue pixels, which mimics the wavelength sensitivity of the human eye. The final color picture seen by the user is composed of the three virtually independent RGB data sets.

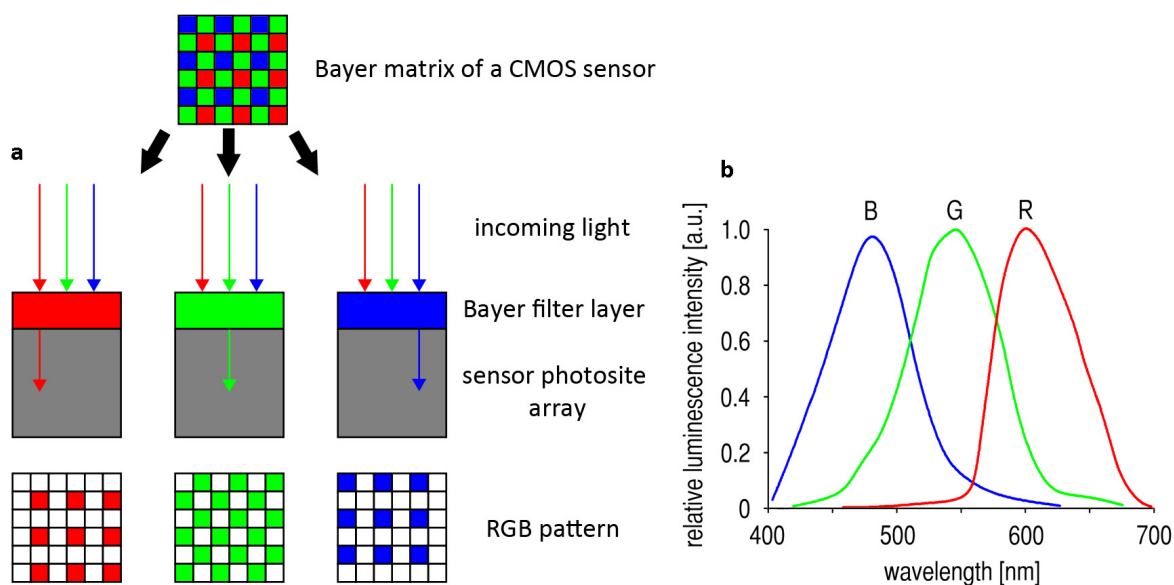


Figure 6.1 | (a) Schematic drawing of a CMOS chip with a Bayer filter matrix and (b) the spectral response of the three color channels.

Histograms reflect the distribution of brightness of the three colors that is recorded in the respective color channel. This paves the way to a quantitative read-out in dual-color based optical chemical sensing which is particularly useful in case of oxygen sensing where fluorometry is the method of choice.

To achieve this goal, a sensor layer for oxygen was designed that employs two dyes that spectrally match the red and the green channels, respectively, of an RGB chip. The known platinum(II) *meso*-tetrakis-(pentafluorophenyl)porphinato complex³⁹ (PtTPFPP) has a red luminescence and was chosen as the probe for oxygen. PtTPFPP can be efficiently excited at 409 nm (which is close to the peak of the strong Soret band) to give a fairly narrow red emission band peaking at 650 nm. Thus, it perfectly matches the red channel of the RGB chips as shown in **Fig. 6.2**. The search for a reference dye that is

also excitable at 405 nm but displays green emission led to the fluorophore N-(5-carboxypentyl)-4-piperidino-1,8-naphthalimide with its fairly narrow fluorescence band peaking at 510 nm (in the polymeric solvent used in the present work). The green emission is only detected by the green and the blue channel. The latter is omitted for this oxygen sensor. The dyes are excited with blue LED (409 nm) that may interfere with the measurement and require additional optical filters.

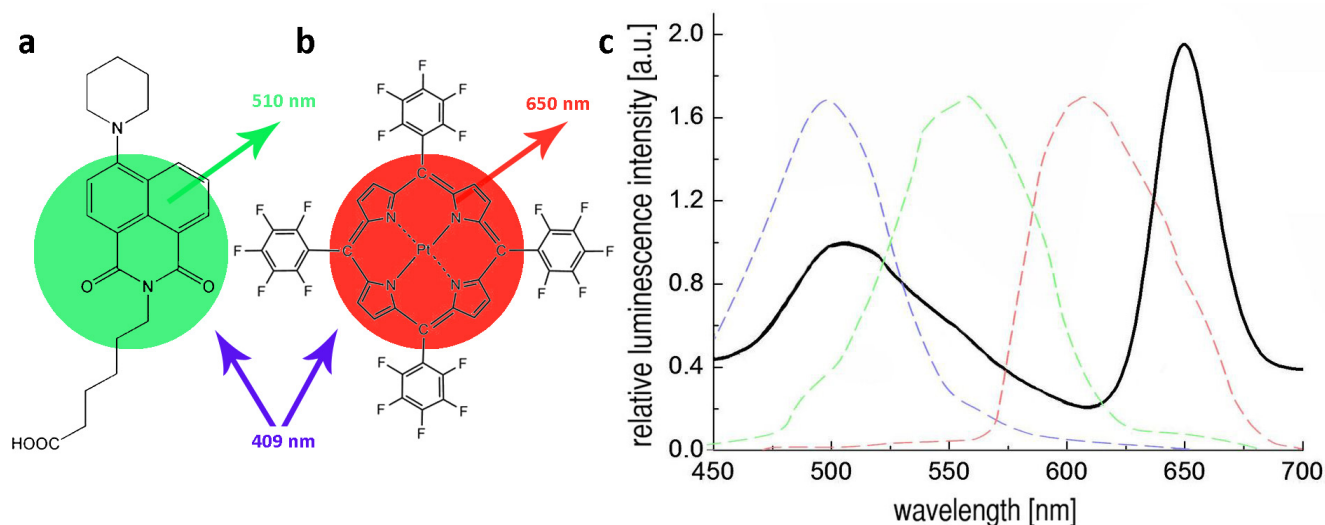


Figure 6.2 | Chemical structures of (a) the reference dye N-(5-carboxypentyl)-4-piperidino-1,8-naphthalimide and (b) the indicator dye platinum(II) meso-tetrakis-(pentafluorophenyl)porphyrin (under ambient conditions). (c) The black line represents the emission spectra of the sensor. The oxygen indicator (peak at 650 nm) is located within the spectra of the red channel (dashed red line) and the reference dye (broad peak at 510 nm) emits within the spectral response of the green and blue channels (dashed green and blue line).

A commercially available and highly biocompatible polyurethane hydrogel was chosen as the polymer matrix ("solvent") to host the two dyes. This polymer is a good solvent for the two dyes and possesses excellent oxygen permeability. Polymer and dyes were dissolved in an ethanol/water mixture and this "paint"¹⁷ was spread via knife coating onto a transparent polyester support to result in a 6- μm thick sensor film after solvent evaporation.

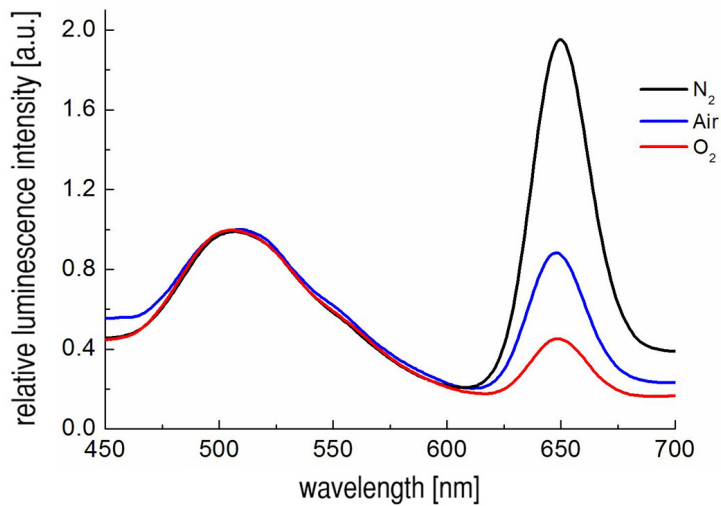


Figure 6.3 | Spectral sensor response towards nitrogen gas (black line), ambient air (blue line), and oxygen (red line).

The fluorescence of the red dye is dynamically quenched by oxygen (**Fig. 6.3**). This does not spectrally shift the red emission, but the brightness of the red pixels varies strongly with changing oxygen content in the atmosphere. The emission of the naphthalimide fluorophore, in contrast, is not measurably quenched by oxygen so that the brightness of the pixels does not change. Rather, the green dye acts as an optical contrast and also gives a reference (fluorescence) signal in the RGB channel system.

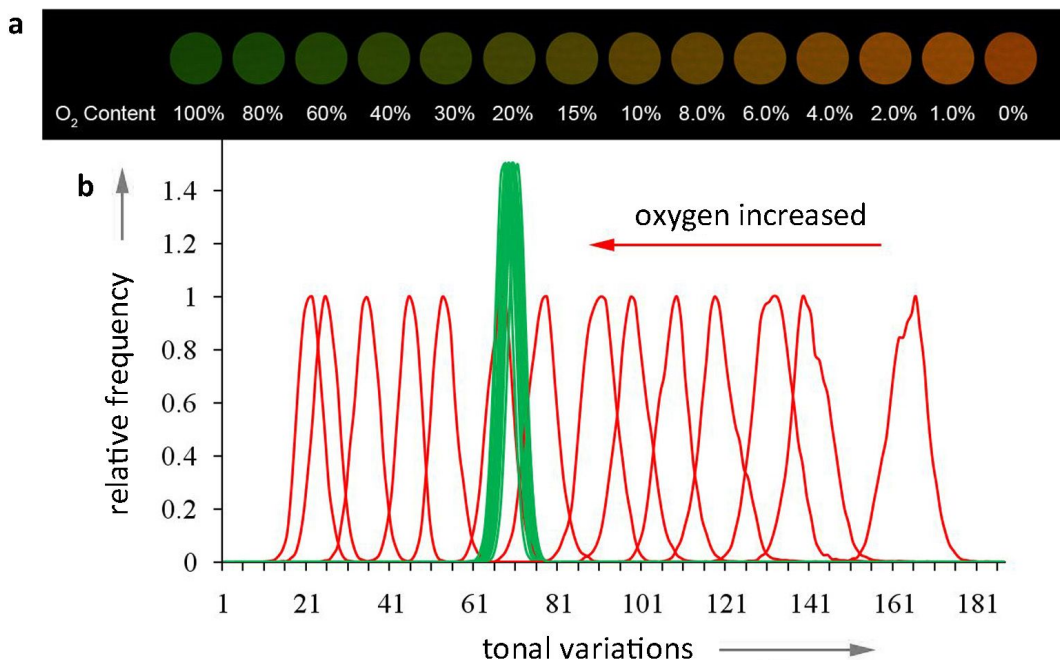


Figure 6.4 | Apparent colors of the sensor layer at different concentrations of oxygen (**a**) and the corresponding image histograms of the red and green channels (**b**). The relative frequency represents the relative number of pixels for each tonal value.

Fig. 6.4a shows that the response of the sensor layer to partial pressure of oxygen can be both visually seen and imaged via RGB camera. **Fig. 6.4b** displays the green and red channel histograms corresponding to these colorimetric pictures (ROI: 200 x 200 pixels). The peaks of the histograms of the green channel are displayed in green color, and those of the red channel in red. The green peaks obviously are not shifted when changing oxygen concentrations, whilst the red peaks move to lower values with increasing concentration of oxygen.

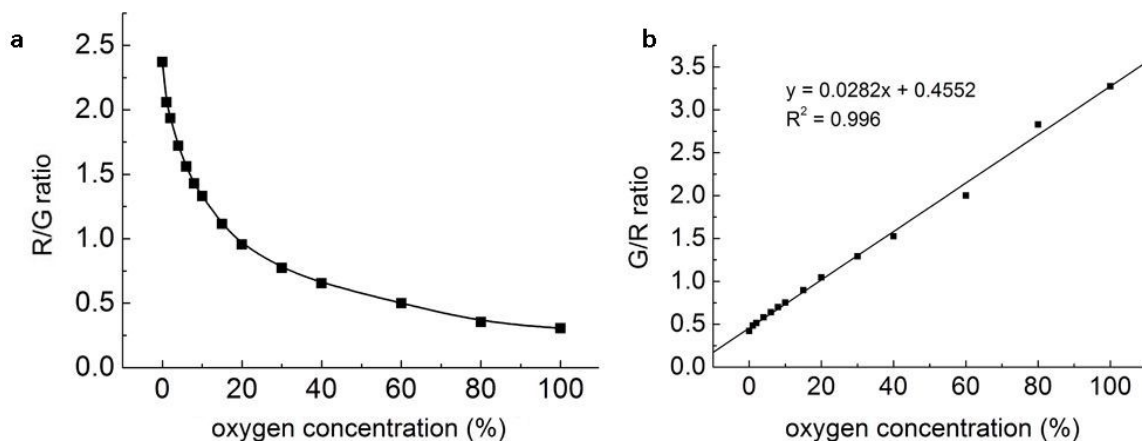


Figure 6.5 | (a) Plot of the ratio R/G as a function of oxygen concentration in nitrogen gas at a pressure of 1 atm. R/G represents the intensity of the red channel divided by the intensity of the green channel. **(b)** An inverse plot reveals a linear relationship of the G/R ratio and oxygen concentration.

An exponential quenching curve is obtained by dividing the data of red channel by those of the green channel (the so-called R/G ratio) as can be seen in **Fig. 6.5a**. The reciprocal value of the R/G ratio (the G/R ratio) is linearly related ($y = 0.0282x + 0.4452$, $R^2 = 0.9960$) to oxygen concentration (see **Fig. 6.5b**). Hence, it can be used for precise quantitative determination of oxygen at single spots but of course also enables imaging of spatial oxygen distributions. The visible color change of the sensor layer, in turn, results from changes in the ratio of the intensities of the red and green luminescence (**Fig. 6.3** and **Fig. 6.4a**). Most notably, this ratio is independent of the intensity of the purple LED used for photoexcitation.

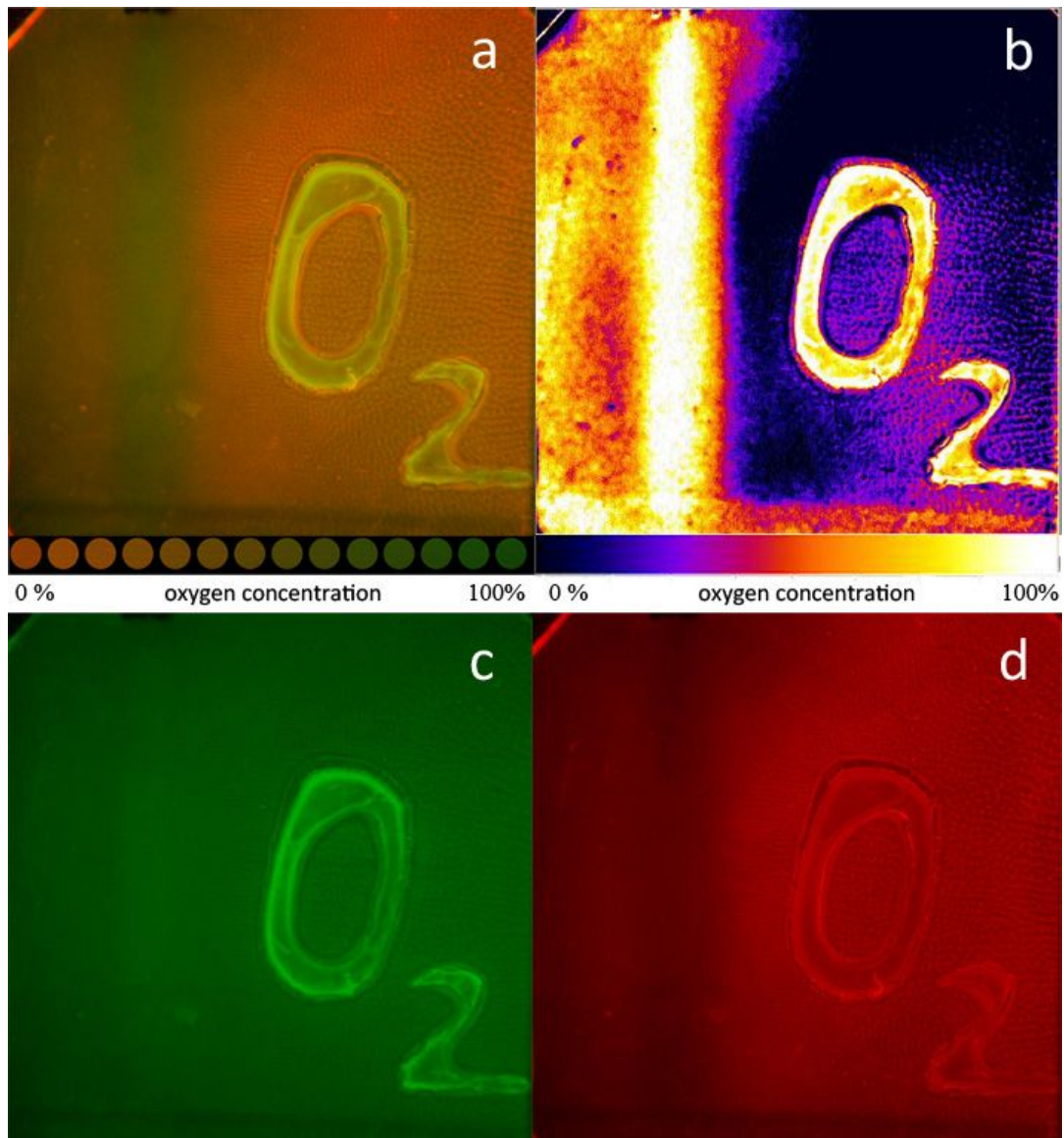


Figure 6.6 | *Photographing spatial oxygen distribution: (a) A regular photo (14 bit color-depth per channel) obtained either for direct colorimetric read-out or for RGB read-out. The color channels of the photo are split and a pseudo color image (b) of the G/R ratio can be calculated with data of the green channel (c) and the red channel (d). Image size: 5 x 5 cm.*

Fig. 6.6 demonstrates the future potential of the RGB technique and photographing oxygen distribution. The image was obtained by photographing the sensor layer described before. The characters "O₂" were written onto the sensor layer using a solution of the block-copolymer poly(acrylamide-co-acrylonitrile) which is impermeable to oxygen. The sensor layer with the characters O₂ painted onto its surface was first placed in an

atmosphere of nitrogen, then exposed to a flow of pure oxygen, and then photographed under illumination with the 409-nm LED. The characters "O₂" and the flow of oxygen are easily visible in the "normal" photographic picture (**Fig. 6.6a**). However, the processed picture (**Fig. 6.6b**) exhibits better contrast and reveals a more detailed image of the distribution of oxygen. Digital processing of the two channels (R and G) was performed by using the free software ImageJ. In future, the processing step may be directly integrated in a camera firmware.

It was noted that the color depth is affected by several camera settings, i.e. by aperture, ISO, and shutter speed. Therefore, the effects of these parameters were more systematically investigated. (**Fig. 6.7**). However, their effects on color depth can be eliminated by comparing relative peak positions in the RGB method and by calculating (and normalizing) the R/G ratio. Results also reveal that the photographic method allows read-out of rather dark images which is difficult in case of conventional colorimetric methods. Another crucial point is photobleaching. **Figure 6.8** depicts that the dyes used in this sensor are quite photostable. Further, differential photostability is kept to a minimum with this combination (< 3 % per hour of continuous illumination).

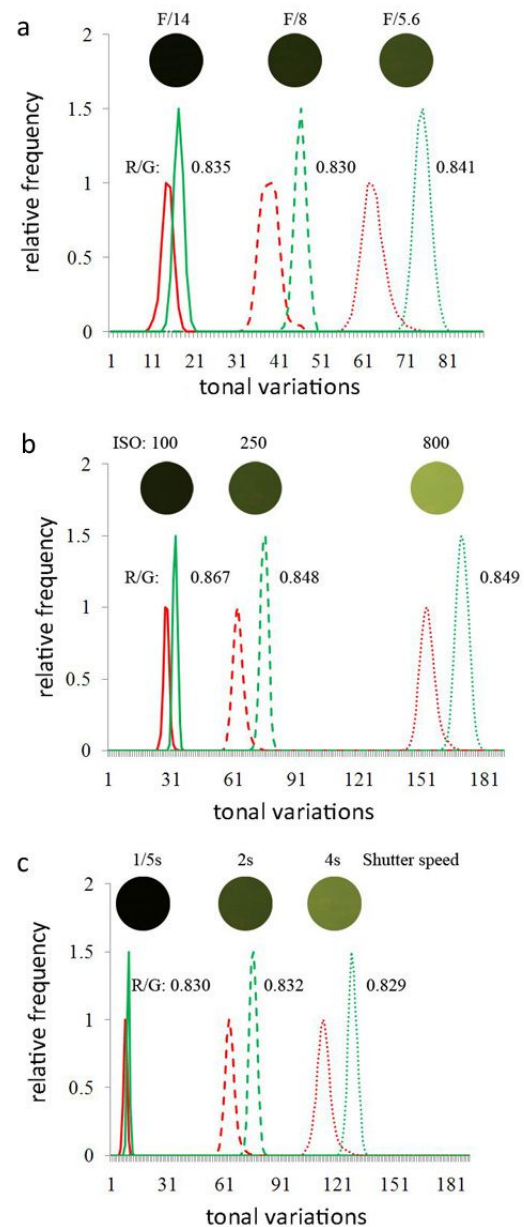


Figure 6.7 | Aperture size (a), ISO (b), and shutter speed (c) induced changes in color depth, corresponding histograms and R/G ratios.

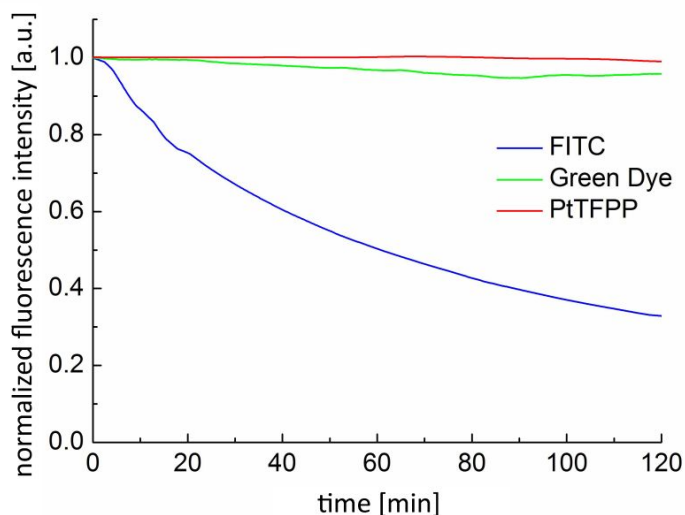


Figure 6.8 | Photostability of the indicator (red line) and the reference (green line) compared to FITC.

6.1.3 Methods and materials

6.1.3.1 Preparation of the oxygen-sensing layer

90 μl of a solution containing 2 mg mL^{-1} of N-(5-carboxypentyl)-4-piperidino-1,8-naphthalimide in ethanol and 110 μl of a solution of 2 mg mL^{-1} PtTPFP in ethanol were mixed with 500 μl of a hydrogel solution (5.0 % (w/w) of D4 hydrogel in 90/10 (v/v) ethanol/water). This “cocktail” was stirred for at least 4 h and then was spread on a transparent poly(ethylene terephthalate) (Mylar®) using the self-built knife-coating device (*chapter 2.2*) to form a wet 120 μm thick film⁴⁰. Drying of the film resulted in a 6 μm thick sensor layer. The word “O₂” was written with a solution of 30 μl of a solution containing 2 mg mL^{-1} of N-(5-carboxypentyl)-4-piperidino-1,8-naphthalimide in ethanol and 35 μl of a solution of 2 mg mL^{-1} PtTPFP in ethanol mixed with 100 μl of a poly(acrylamide-co-acrylonitrile) solution (5.0 % (w/w) in DMF).

6.1.3.2 Imaging and data processing

The oxygen distribution herein was imaged using an earlier stage of the imaging system mentioned in *chapter 2.6*. The setup consists of a standard digital camera (Canon EOS model 50D and a Canon EF-S 17-85 mm 1:4-5.6 IS USM lens) and an ultra-bright 409-nm

LED (LD-405-200; Roithner Lasertechnik; www.roithner-laser.com) for photo-excitation. Camera parameters were set as follows: Raw+jpg; aperture 1:5.6; ISO sensitivity 160; shutter speed 1/8 s. The Raw image data were processed using Adobe Camera Raw plugin for Adobe Photoshop (both from Adobe Systems Software Ireland Ltd., Dublin, Ireland; www.adobe.com). White balance was set to 2450 K. Pictures were stored as 16 bit TIF files and further processed with ImageJ software (<http://rsbweb.nih.gov/ij/>).^{41,42} Data were processed using following steps: run("Split Channels"); imageCalculator("Divide create 32-bit", "C3-all.tif", "C2-all.tif"); run("Interactive 3D Surface Plot").

6.1.3.3 Characterization of the sensor

The sensor was calibrated in the calibration chamber described in *chapter 2.4* with nitrogen and oxygen gas from Linde. The photostability experiments were conducted using the time trace function of an AB2 spectrofluorimeter ($\lambda_{\text{ex}} = 409 \text{ nm}$; $\lambda_{\text{em1}} = 510 \text{ nm}$; $\lambda_{\text{em2}} = 650 \text{ nm}$; 4 nm slits).

6.1.4 Discussion

The method presented here offers attractive features. In terms of sensing, it is characterized by high colorimetric resolution, precision (calculated to be +/- 0.2 % at air oxygen level), 14-bit color depth per channel in the photographic read-out, broad operational range, and applicability under ambient conditions. It is noted that the materials used in this sensor are easily accessible and environmentally friendly. The use of potentially toxic quantum dots⁴³ is not necessary, sensors can be fabricated in a single step, sensing films are highly uniform, and the application of an established hydrogel makes the sensor highly biocompatible. The analytical range may be fine-tuned by incorporating the indicator probes into polymers of appropriate permeability for oxygen. The dyes used here are quite photostable and no leaching of the dyes is observed (notwithstanding the option of covalently immobilizing the green fluorophore in a matrix

via its carboxy group). In terms of features of the optical system we note that a conventional digital camera can be used along with a commercial purple LED flashlight. While not used in this work, the blue channel of the RGB chip may be used for gaining additional spectral information in context with multiple sensing⁴⁴ (see chapter 7). We therefore believe that this approach, due to its simplicity and versatility, is of interest whenever oxygen is to be sensed, and potentially can be extended to other species if appropriate probes are available.

6.2 Absorbance- and emission-based RGB imaging of CO₂

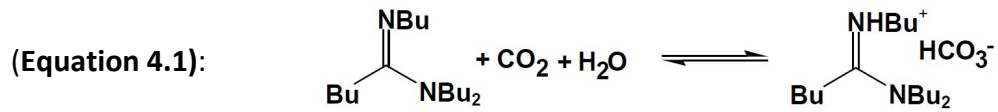
(Analytical Chemistry, 2011, vol. 8 no. 83, 2846-2851)

6.2.1 Imaging of CO₂

The RGB read-out technique described in this chapter was also used to image carbon dioxide. Generally, optical carbon dioxide sensors are based on two different concepts, i.e. a “wet” and a “dry” concept. The wet CO₂ sensors are based on an internal carbonate buffer solution that is embedded in a hydrophobic polymer matrix along with a pH indicator dye in its base form⁴⁵⁻⁴⁷. This sensor type is also referred as Severinghaus-type sensors^{48,49}. Hydrophobic polymers are used that are permeable to CO₂ (or gases) but prevent proton diffusion. Thus, the internal pH is independent from external pH variations and the generated optical signal solely relies on the external pCO₂. The dry type of CO₂ sensors, also so called plastic sensors, were developed by Raemer⁵⁰, Mills^{47,51,52} and Weigl⁵³. Commonly, pH indicators in their base form with lipophilic quaternary ammonium counter ions are immobilized in hydrophobic polymers along with lipophilic organic bases. The organic base replaces the aqueous buffer system that is used in the wet sensor type.

The CO₂ sensor herein works with a different principle. It makes use of a solvatochromic dye along with an additive that possesses switchable hydrophobicity. Substituted amidines of fatty acids were reported to have a great impact on the hydrophobicity of their microenvironment^{54,55}. N,N,N'-tributylpentanamidine⁵⁶ (TB-PAM)

largely changes the hydrophilicity on binding CO_2 . The process of binding CO_2 is completely reversible as visible in following equation:



The additive TB-PAM and the solvatochromic probe Nile Red (NR) are embedded in a matrix of ethyl cellulose. Ethyl cellulose is gas permeable but impermeable for protons. NR undergoes a strong solvatochromic shift both in color (from brick red to magenta, see **Fig. 6.10** RGB image row) and in fluorescence (orange to red, see **Fig. 6.12** RGB image row) by changing the polarity of its microenvironment. Both color changes can be read out via the RGB imaging technique.

First, the color change is imaged via absorbance based (more correctly reflectometric based) RGB imaging. A spectral shift towards the red spectrum occurs with increasing CO_2 . The color of the sensor film in the absence of CO_2 is red, with an absorption band that fairly well matches the sensitivity of the blue channel. With increasing concentrations of dissolved CO_2 ($d\text{CO}_2$), the color is shifted toward magenta tone, thus better matching the green channel. The spectral overlap of the absorptions and the RGB channels is represented in **Fig. 6.9**.

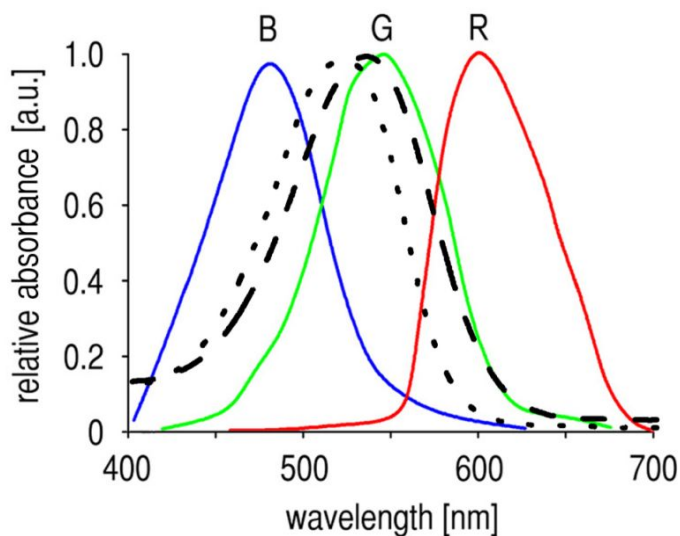


Figure 6.9 | Spectral overlap of the RGB spectrum and the absorption of NR in presence (1 M $d\text{CO}_2$; dashed line) and in absence (0 M $d\text{CO}_2$; dotted line) of CO_2 .

Photographic images of the sensor layers were acquired (**Fig. 6.10**), and processed as described before. The red channel does not contain any information for use in

reflectometric pictures and was discarded. Next, the blue channel image was referenced to the green channel image, and the ratiometric images were then generated in pseudocolors (**Fig. 6.10** row 4).

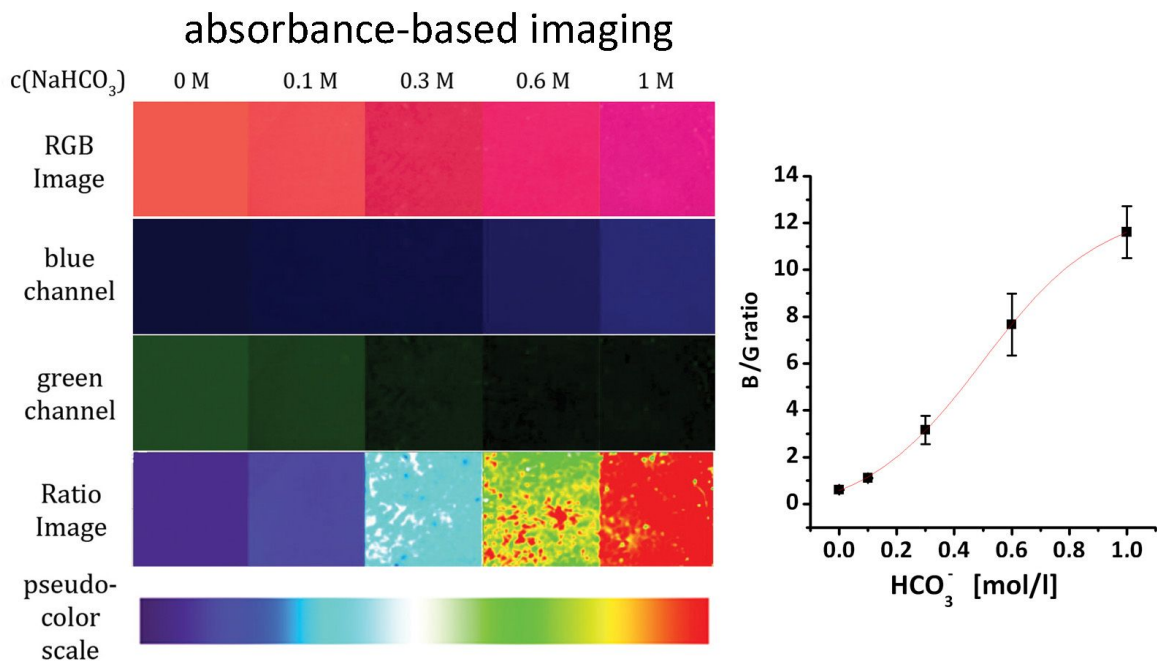


Figure 6.10 | Schematic and calibration of the reflectometric RGB read-out of the CO_2 sensor. Row 1 gives the conventional RGB images in presence of various concentrations of bicarbonate ($d\text{CO}_2$). Rows 2 and 3 depict the colors of the blue and green channel. The ratiometric images in row 4 reflect the concentration of $d\text{CO}_2$ (in pseudo-colors). The right side represents the obtained calibration curve from 0 to 1M of $d\text{CO}_2$.

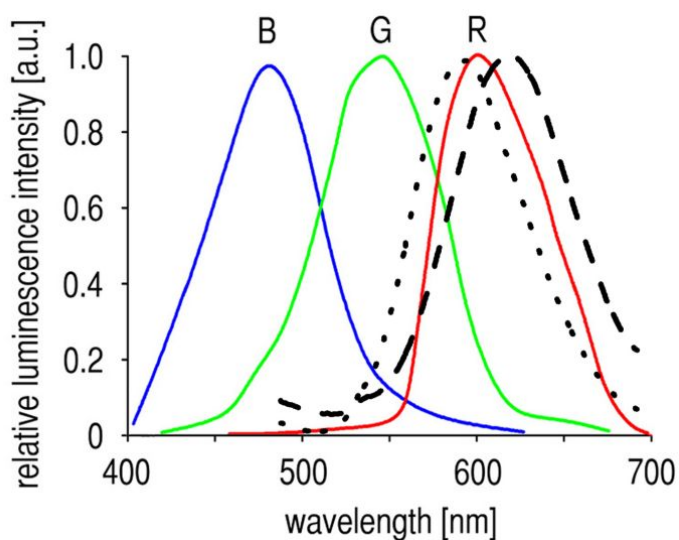


Figure 6.11 | Spectral overlap of the RGB spectrum and the emission of NR in absence (0 M $d\text{CO}_2$; dotted line) and in presence (1 M $d\text{CO}_2$; dashed line) of CO_2 .

The sensing scheme for imaging fluorescence is similar, except that the data of the green and red channel is used, and the blue channel is omitted. It is based on the shift that is observed in the fluorescence spectra of the sensor films on increasing the concentration of dissolved CO_2 . The spectral change and the resulting changes on the overlap with the RGB channels are shown in **Fig. 6.11**. The R/G ratio of the fluorescence signals increases with increasing level of dCO_2 (**Fig. 6.12**).

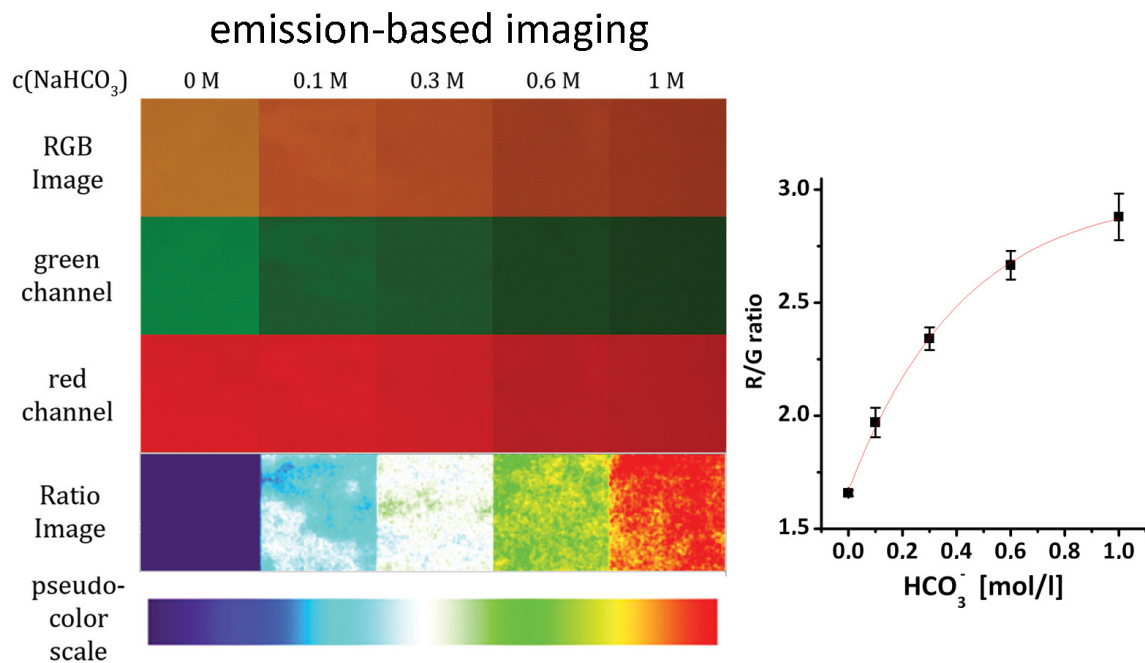


Figure 6.12 | Schematic and calibration of the emission based RGB read-out of the CO_2 sensor. Row 1 depicts the RGB images, rows 2 and 3 the colors of the blue and green channel, and row 4 the ratiometric images dependent on dCO_2 concentration. The right graph represents the calibration curve obtained from 0 to 1 M of dCO_2 .

The reflectometric (absorption-based) as well as the fluorimetric (emission-based) method enable direct and quantitative imaging of dCO_2 via an intrinsically referenced RGB read-out. The methods are not influenced by fluctuations of the light sources, non-uniform illumination, dye concentration, and dye leaching. This intrinsically referenced method is even independent of photobleaching. The reflectometric technique (the “poor scientist's imager”) is straightforward and requires a minimum of instrumentation to read the sensor layer. Only a digital camera and a sheet of white paper as background are

needed. Nevertheless, a stable and fairly pure color temperature of the ambient light is required to avoid chromatic aberrations. Chromatic aberrations would result in errors in the rationed intensities. The fluorimetric read-out also is simple but it additionally requires an external excitation light source (LEDs, for example) and optical filters (separation of emitted light from excitation).

6.2.2 Methods and materials

6.2.2.1 Preparation of the sensor membrane

0.5 mg of NR was mixed with 150 μ l of TB-PAM and 1 ml of a 5 % solution of ethyl cellulose (50 mg ethyl cellulose in 1 ml of an 80/20 (v/v) toluene/ethanol mixture). The cocktail was spread onto a polyester (MYLAR®) foil using a self-built knife coating device (see section 2.2). The film was dried under ambient conditions resulting in a 12 μ m thick sensor layer.

6.2.2.2 Imaging setup, data read-out, and calibrations

A digital camera (type EOS 50D) was used in the RGB readout techniques. Reflectometric imaging was performed with sensor films placed on a sheet of white paper (of ISO 9001 quality; Evolve; www.evolve-paper.com) that serves both as a neutral background and as a white reference. White balance depends on ambient light and has to be set to neutral white. Camera parameters were set as follows: white balance 2700 K; aperture 5.6; ISO sensitivity 100; shutter speed 0.02 s.

Fluorescence images were obtained following photoexcitation with an array of twelve 470-nm LEDs (type L-7113PBC-A; Kingbright; www.conrad.de). Light was passed through a BG12 color glass filter that – in essence – is permeable to light of wavelengths between 450 and 480 nm only before hitting the sensor. Emitted light was passed through an OG510 long-pass filter (both from Schott, Germany; www.schott.com).

Camera parameters were set as follows: white balance 3000 K; aperture 5.6; ISO sensitivity 200; shutter speed 0.2 s.

Split color and rationed pseudocolor images were obtained in both methods (reflectance and fluorescence) using the ImageJ software. The absorbance-based RGB read-out was conducted as follows: The R, G, and B channels were separated using Image>Color>Split channels. The red channel contains no relevant absorption (better: reflectometric) data and was discarded. The blue and the green channel were rationed via Process>Image calculator>Green divided by red image>Create 32 bit float result. Pseudo-color pictures were obtained by Plugins>3D>Interactive 3D surface plot.

In case of fluorescence imaging, the R, G, and B channels were separated as described above. In this case, the blue channel does not contain any relevant data and is disposed. The red and green channel were rationed via Process>Image calculator>Green divided by red image>Create 32 bit float result and multiplied by 100 for better image contrast via Process>Math>Multiply>100. Pseudo-color pictures were obtained via Plugins>3D>Interactive 3D surface plot.

The sensor films were exposed to different concentrations of $d\text{CO}_2$ for 30 min and subsequently photographed. Solutions for calibration were prepared as follows: Standards for dissolved CO_2 levels were prepared freshly prior to the measurement by dissolving sodium hydrogen carbonate in distilled and carbon dioxide free water to yield a 1 M solution of NaHCO_3 . This solution was subsequently diluted with CO_2 -free water to cover the desired range of concentrations. CO_2 -free water was prepared by boiling doubly distilled water (to remove any dissolved CO_2), followed by purging with nitrogen gas.

6.3 RGB imaging of pH

6.3.1 Material design

At least, the proof of principle for a sensor membrane for ratiometric RGB imaging of pH distributions is presented. The sensor concept is based on the use of one indicator dye and one reference dye. The sensor comprises the pH-sensitive FITC-AC particles that were already introduced in *chapter 3*. PtTPFPP in oxygen- and water-impermeable poly(methacrylonitril-co-divinylbenzene-co-acrylic acid) (PD) nanoparticles⁵⁷ (referred to as PtTPFPP-PD) served as reference signal and optical contrast. The polymer PD is used because the oxygen-blocking PAN is not suitable for certain kinds of dyes. PD, in contrast to PAN, can incorporate a sufficient amount of metalloporphyrin molecules. PD is synthesized via a co-polymerization of acrylic acid, divinylbenzene and methacrylonitril. Both particle types were embedded in a proton permeable hydrogel (type D4) as the sensor matrix layer.

The sensor can be excited using a standard 366 nm UV lamp. The pH dependent (green to yellow) emission of FITC-AC is recorded in the green channel of the RGB camera. The red emission of the reference particles is separately recorded in the red channel (see **Fig. 6.13**). The blue channel contains no relevant information and is discarded.

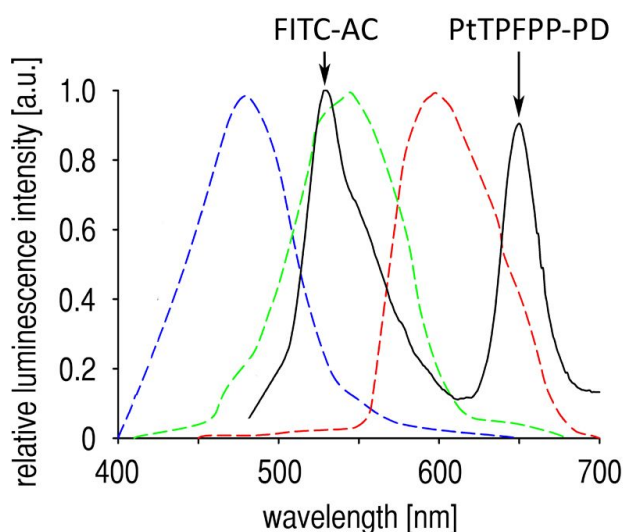


Figure 6.13 | Spectral overlap of the RGB spectrum from the camera (dashed colored lines) and the emitted light from the sensor.

The reference particles show no dependency on pH as can be seen in **Fig.6.14**.

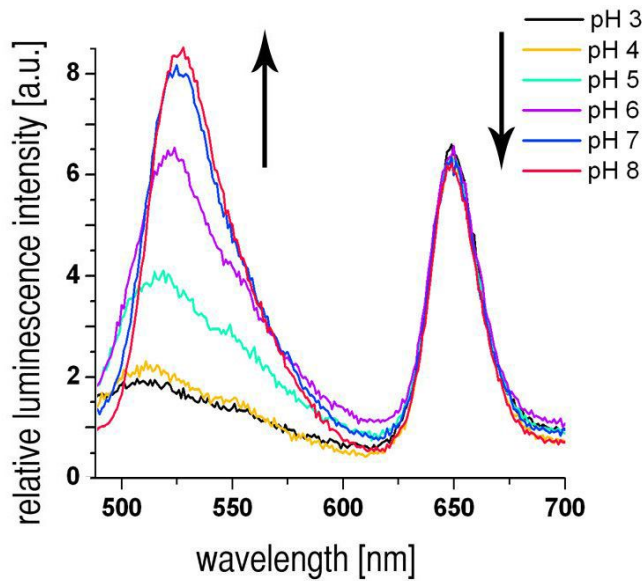


Figure 6.14 | Spectral response of the sensor for various pH. The peak at 650 nm from the reference is not affected while the FITC-AC peak at 525 nm increases with increasing pH.

The sensor can be read out by visual colorimetry (**Fig. 6.15** top row) via comparison to a color scale or by using the RGB technique (**Fig. 6.15**).

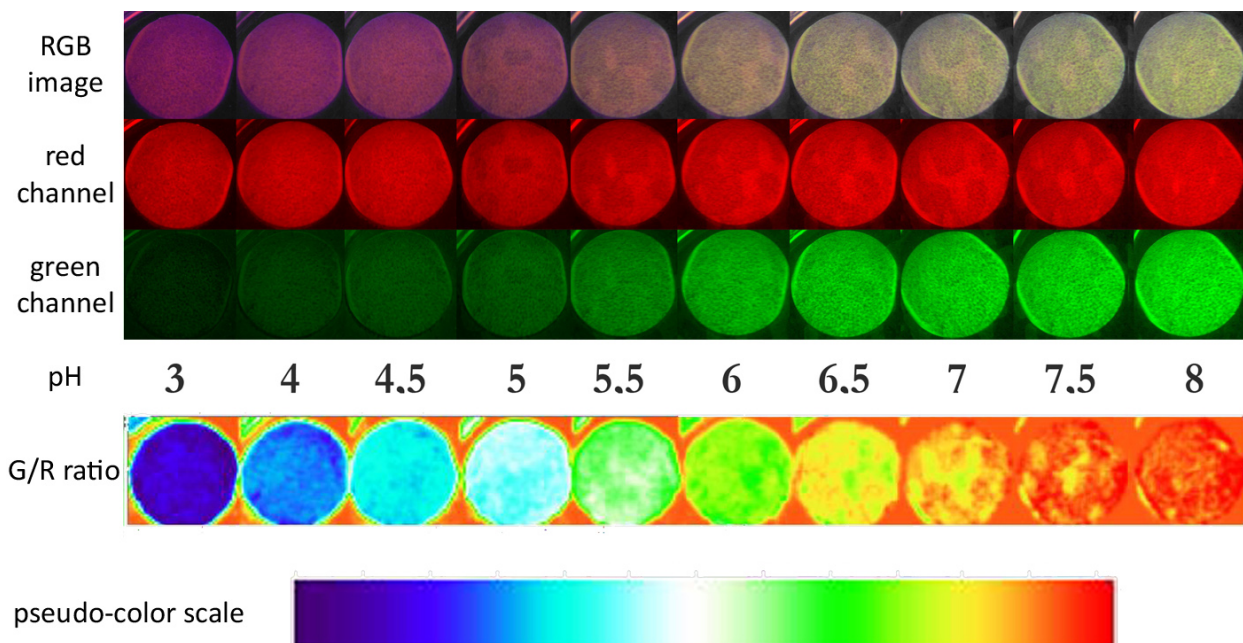


Figure 6.15 | RGB read-out of the pH sensor. Row 1 gives the conventional RGB images of the sensor using buffers with varying pH. Rows 2 and 3 depict the colors of the red and green channel. The red luminescence of the reference particles remains constant while the green luminescence increases with increasing pH. The ratiometric images in row 4 reflect the pH values in pseudo-colors.

The G/R ratio of the green and red channel response shows sigmoidal behavior towards pH in the physiological range of pH 3 to pH 8 (Fig. 6.16). The response times were similar to those determined in *chapter 3*.

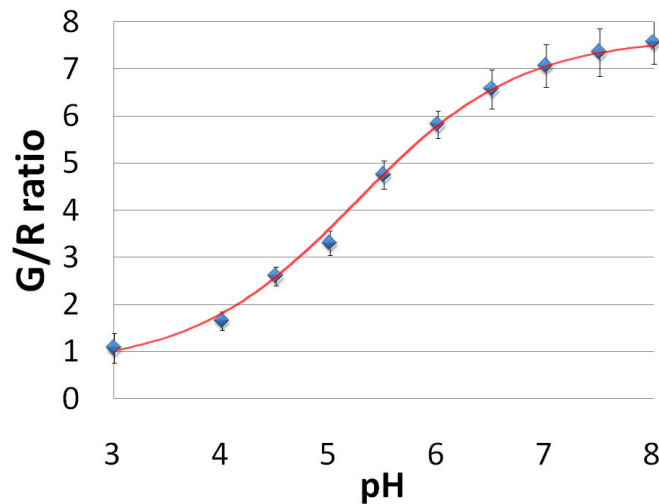


Figure 6.16 | Sigmoidal response of the G/R ratio towards pH. The pK_a is 5.4.

6.3.2 Materials and methods

6.3.2.1 Microparticle and sensor membrane preparation

The preparation of FITC-AC is described in section 3.3.1. A threefold rather than a double excess of acetic anhydride is used for endcapping of the particles used in this section. The synthesis and staining of PtTPFPP-PD reference particles was previously described by Nagl⁵⁷. PD was obtained as pre-synthesized polymer (PD-Optosense, PMAN-3) from PreSens GmbH (www.presens.de). 100 mg of PD, 1 mg PtTPFPP and 40 mg SDS were dissolved in 40 mL of acetone. The solution was stirred for 1 h. 80 mL of 1 mM NaOH was added dropwise via a dropping funnel (over 3 hours). The dispersion was neutralized by adding 100 mM HCl. Subsequently the dispersion was filtrated 4 times using a 100 nm cellulose nitrate filter. Particles were freeze-dried for storage.

The sensor cocktail contained 10 mg of FITC-AC and 20 mg of PtTPFPP-DP suspended in 1 ml of a 5 % (w/v) solution of the polyurethane hydrogel (type D4) in 9:1 (v/v) ethanol/water. The “cocktail” was stirred for at least 48 h and then was spread on a transparent Mylar® foil using a self built knife coating device to form a wet 200 µm thick film. Drying of the film at ambient conditions resulted in a 10 µm thick sensor layer.

6.3.2.2 Imaging setup, data read-out, and calibrations

A digital camera (type EOS 50D) was used for RGB read-out. Fluorescence images were obtained during photoexcitation with a commercially available UV light source (366 nm; VWR, Germany, www.vwr.com) Emitted light passed a GG435 long-pass filter (Schott) prior to collection via the CMOS chip of the camera. Camera parameters were set as follows: white balance 4500 K; aperture 5.6; ISO sensitivity 200; shutter speed 0.2 s. Data were processed using imageJ with following processing steps: run("Split Channels"); imageCalculator("Divide create 32-bit", "C3-all.tif","C2-all.tif"); run("Interactive 3D Surface Plot").

50 mM Britton-Robinson buffers⁵⁸ (consisting of 0.04 M H₃BO₃, 0.04 M H₃PO₄ and 0.04 M CH₃COOH in distilled H₂O) were used for sensor calibration. Sensors were equilibrated with respective buffer solutions for 1 minute in a flow through cell prior to photographing.

6.4 References

- 1 Hung, M. C., Mills, G. B. & Yu, D. H. Oxygen sensor boosts growth factor signaling. *Nat Med* **15**, 246-247, (2009).
- 2 Bruick, R. K. & McKnight, S. L. Transcription - oxygen sensing gets a second wind. *Science* **295**, 807-808, (2002).
- 3 Webster, J. G. Encyclopedia of medical devices and instrumentation. *Wiley, New York* **Vol. 6** (2006).
- 4 Epstein, R. J. Human molecular biology: An introduction to the molecular basis of health. *Cambridge Univ. Press, Cambridge, UK*, (2003).

- 5 Periasamy, A., Clegg, R. M. Flim microscopy in biology and medicine. *CRC Press, Boca Raton, FL*, (2009).
- 6 Ge, X. D. *et al.* Validation of an optical sensor-based high-throughput bioreactor system for mammalian cell culture. *J Biotechnol* **122**, 293-306, (2006).
- 7 Kocincova, A. S. *et al.* Multiplex bacterial growth monitoring in 24-well microplates using a dual optical sensor for dissolved oxygen and ph. *Biotechnol Bioeng* **100**, 430-438, (2008).
- 8 Riegel, E. R., Kent, J. A. Riegel's handbook of industrial chemistry. *Springer, Berlin*, (2003).
- 9 Babilas, P. *et al.* Transcutaneous po₂ imaging during tourniquet-induced forearm ischemia using planar optical oxygen sensors. *Exp Dermatol* **17**, 265-265, (2008).
- 10 Zhang, G. Q., Palmer, G. M., Dewhirst, M. & Fraser, C. L. A dual-emissive-materials design concept enables tumour hypoxia imaging. *Nat Mater* **8**, 747-751, (2009).
- 11 Narayanaswamy, R., Wolfbeis, O.S. Optical sensors for industrial, environmental and clinical applications. *Springer, Berlin*, (2003).
- 12 Girard, J. Principles of environmental chemistry. *Jones & Bartlett, Boston*, (2009).
- 13 Bergman, I. Rapid-response atmospheric oxygen monitor based on fluorescence quenching. *Nature* **218**, 396, (1968).
- 14 Mills, A. Oxygen indicators and intelligent inks for packaging food. *Chem Soc Rev* **34**, 1003-1011, (2005).
- 15 Moore, T. S. *et al.* Marine chemical technology and sensors for marine waters: Potentials and limits. *Annu Rev Mar Sci* **1**, 91-115, (2009).
- 16 Stich, M. I. J. & Wolfbeis, O. S. Pressure sensitive paints: Standardization in fluorometry: State-of-the art and future challenges. *Springer, Berlin*, chapter 20, (2007).
- 17 Wolfbeis, O. S. Sensor paints. *Adv Mater* **20**, 3759-3763, (2008).
- 18 Liu, T., Sullivan, J.P. Pressure and temperature sensitive paints. *Springer, Berlin*, (2005).
- 19 Borisov, S. M. & Wolfbeis, O. S. Optical biosensors. *Chem Rev* **108**, 423-461, (2008).
- 20 Maier, R. R. J., Barton, J. S., Jones, J. D. C., McCulloch, S. & Burnell, G. Dual-fibre bragg grating sensor for barometric pressure measurement. *Meas Sci Technol* **14**, 2015-2020, (2003).
- 21 Severinghaus, J. W. & Astrup, P. B. History of blood gas analysis. Iv. Leland clark's oxygen electrode. *Journal of Clinical Monitoring* **2**, 125-139, (1986).
- 22 McDonagh, C., Burke, C. S. & MacCraith, B. D. Optical chemical sensors. *Chem Rev* **108**, 400-422, (2008).
- 23 Hoshi, T. & Lahiri, S. Oxygen sensing: It's a gas! *Science* **306**, 2050-2051, (2004).
- 24 Flusberg, B. A. *et al.* Fiber-optic fluorescence imaging. *Nat Methods* **2**, 941-950, (2005).
- 25 Wolfbeis, O. S. Fiber-optic chemical sensors and biosensors. *Analytical Chemistry* **76**, 3269-3284, (2004).
- 26 Chojnacki, P., Mistlberger, G. & Klimant, I. Separable magnetic sensors for the optical determination of oxygen. *Angew Chem Int Edit* **46**, 8850-8853, (2007).
- 27 Wu, C. F., Bull, B., Christensen, K. & McNeill, J. Ratiometric single-nanoparticle oxygen sensors for biological imaging. *Angew Chem Int Edit* **48**, 2741-2745, (2009).
- 28 Evans, R. C. & Douglas, P. Controlling the color space response of colorimetric luminescent oxygen sensors. *Analytical Chemistry* **78**, 5645-5652, (2006).
- 29 Evans, R. C. & Douglas, P. Design and color response of colorimetric multilumophore oxygen sensors. *Acs Appl Mater Inter* **1**, 1023-1030, (2009).
- 30 Wang, X. D., Chen, H. X., Zhao, Y., Chen, X. & Wang, X. R. Optical oxygen sensors move towards colorimetric determination. *Trac-Trend Anal Chem* **29**, 319-338, (2010).
- 31 Wang, X. D., Chen, X., Xie, Z. X. & Wang, X. R. Reversible optical sensor strip for oxygen. *Angew Chem Int Edit* **47**, 7450-7453, (2008).
- 32 Pfister, A., Zhang, G., Zareno, J., Horwitz, A. F. & Fraser, C. L. Boron polylactide nanoparticles exhibiting fluorescence and phosphorescence in aqueous medium. *Acs Nano* **2**, 1252-1258, (2008).

- 33 Feng, L., Musto, C. J., Kemling, J. W., Lim, S. H. & Suslick, K. S. A colorimetric sensor array for identification of toxic gases below permissible exposure limits. *Chem Commun* **46**, 2037-2039, (2010).
- 34 Lim, S. H., Feng, L., Kemling, J. W., Musto, C. J. & Suslick, K. S. An optoelectronic nose for the detection of toxic gases. *Nat Chem* **1**, 562-567, (2009).
- 35 Rakow, N. A. & Suslick, K. S. A colorimetric sensor array for odour visualization. *Nature* **406**, 710-713, (2000).
- 36 Alimelli, A. *et al.* Fish freshness detection by a computer screen photoassisted based gas sensor array. *Anal Chim Acta* **582**, 320-328, (2007).
- 37 Filippini, D. *et al.* Chemical sensing with familiar devices. *Angew Chem Int Edit* **45**, 3800-3803, (2006).
- 38 Nuiachristos, V. Fluorescence molecular imaging. *Annu Rev Biomed Eng* **8**, 1-33, (2006).
- 39 McGraw, C. M., Shroff, H., Khalil, G. & Callis, J. B. The phosphorescence microphone: A device for testing oxygen sensors and films. *Rev Sci Instrum* **74**, 5260-5266, (2003).
- 40 Borisov, S. M., Vasylevska, A. S., Krause, C. & Wolfbeis, O. S. Composite luminescent material for dual sensing of oxygen and temperature. *Adv Funct Mater* **16**, 1536-1542, (2006).
- 41 Wang, X. D., Meier, R. J., Link, M. & Wolfbeis, O. S. Photographing oxygen distribution. *Angew Chem Int Edit* **49**, 4907-4909, (2010).
- 42 Steiner, M.-S., Meier, R. J., Duerkop, A. & Wolfbeis, O. S. Chromogenic sensing of biogenic amines using a chameleon probe and the red-green-blue readout of digital camera images. *Analytical Chemistry* **82**, 8402-8405, (2010).
- 43 Resch-Genger, U., Grabolle, M., Cavaliere-Jaricot, S., Nitschke, R. & Nann, T. Quantum dots versus organic dyes as fluorescent labels. *Nat Methods* **5**, 763-775, (2008).
- 44 Burns, A., Ow, H. & Wiesner, U. Fluorescent core-shell silica nanoparticles: Towards "lab on a particle" architectures for nanobiotechnology. *Chem Soc Rev* **35**, 1028-1042, (2006).
- 45 Oter, O., Ertekin, K., Topkaya, D. & Alp, S. Room temperature ionic liquids as optical sensor matrix materials for gaseous and dissolved co₂. *Sensor Actuat B-Chem* **117**, 295-301, (2006).
- 46 Severinghaus, J. W. Whats new with co₂. *Acta Anaesth Scand* **34**, 13-17, (1990).
- 47 Mills, A. & Skinner, G. A. Water-based colourimetric optical indicators for the detection of carbon dioxide. *Analyst* **135**, 1912-1917, (2010).
- 48 Severinghaus, J. W. & Bradley, A. F. Electrodes for blood po₂ and pco₂ determination. *J Appl Physiol* **13**, 515-520, (1958).
- 49 Severinghaus, J. W. History of measuring o₂ and co₂ responses. *Adv Exp Med Biol* **605**, 3-8, (2008).
- 50 Raemer, D. B., Walt, D. R. & Munkholm, C. *US Patent 5.005.572*, (1991).
- 51 Mills, A., Chang, Q. & McMurray, N. Equilibrium studies on colorimetric plastic film sensors for carbon-dioxide. *Analytical Chemistry* **64**, 1383-1389, (1992).
- 52 Mills, A. & Chang, Q. Fluorescence plastic thin-film sensor for carbon-dioxide. *Analyst* **118**, 839-843, (1993).
- 53 Weigl, B. H. & Wolfbeis, O. S. Sensitivity studies on optical carbon-dioxide sensors based on ion-pairing. *Sensor Actuat B-Chem* **28**, 151-156, (1995).
- 54 Jessop, P. G., Heldebrant, D. J., Li, X. W., Eckert, C. A. & Liotta, C. L. Green chemistry - reversible nonpolar-to-polar solvent. *Nature* **436**, 1102-1102, (2005).
- 55 Phan, L. & Jessop, P. G. Switching the hydrophilicity of a solute. *Green Chem* **11**, 307-308, (2009).
- 56 Sackett, D. L. & Wolff, J. Nile red as a polarity-sensitive fluorescent-probe of hydrophobic protein surfaces. *Anal Biochem* **167**, 228-234, (1987).
- 57 Nagl, S. Fluorescent multiple chemical sensing using time-domain fluorescent lifetime imaging. *Ph.D. Thesis, University of Regensburg*, (2008).

- 58 Mongay, C. & Cerda, V. A britton–robinson buffer of known ionic strength. *Ann Chim*, 409, (1974).

7. Dual RGB imaging of oxygen and pH in vivo

Simplification of luminescence imaging techniques is desirable for the study of numerous kinds of biomedical processes. Current approaches are based on varying read-out frequencies¹, time-gating², or ratiometric schemes³. We present a material that enables referenced real-time and simultaneous visualization of two biologically important parameters in vivo: oxygen and pH. We used luminophores with emission peaks that correspond to the RGB spectrum of a commercial digital camera. To create a biocompatible material for 2D sensing, we immobilized microparticles loaded with platinum(II)-5,10,15,20-tetrakis-(2,3,4,5,6-pentafluorophenyl)-porphyrin (red channel; oxygen sensitive probe), fluorescein-isothiocyanate (green channel; pH probe), and diphenyl-anthracene (blue channel; reference dye), respectively, on transparent foils. The sensor material was characterized in vitro, and used to image oxygen and pH in acute and chronic human wounds. The material and method presented herein can be adapted to visualize various important biomedical parameters, and they may simplify biomedical imaging (e.g. of tumor metabolism) to a large extent. (submitted, 2011)

7.1 Introduction

Biologically relevant parameters such as pH, Ca(II), or oxygen can be visualized via luminescence-based read-out techniques¹, e.g. intensity measurements⁴⁻⁶, time-gated fluorescence lifetime imaging (FLIM)^{2,7} and dual lifetime referencing (DLR)^{2,8}, or ratiometric measurements⁹ based on wavelength separation. These schemes have various shortcomings such as being non-referenced in case of intensity-based imaging, or the necessity to acquire multiple images for referencing. FLIM and DLR require time-gated camera systems and need indicators or reference signals with decay times in the μs range. Imaging of parameters such as CO_2 ², H_2O_2 ^{10,11}, oxygen^{12,13}, Ca(II)¹⁴, and pH⁸ *in vivo* is an emerging field for research and diagnostics. The parameters oxygen and pH

particularly affect wound healing: oxygen supply alters the synthesis and release of growth factors, cytokines and chemokines (especially in the inflammatory phase)^{15,16}. Oxygen and pH affect cell proliferation and migration (new tissue formation phase)^{15,17}. Additionally, pH regulates cell differentiation and the activity of essential enzymes, e.g. matrix-metalloproteinases¹⁷⁻¹⁹. Here we introduce a material for a luminescence-based concept for simultaneous continuous imaging of oxygen and pH, using a conventional digital camera and LED excitation. The material was specifically applied for *in vivo* imaging of acute and chronic cutaneous healing of humans. This concept may have numerous other applications, such as biomedical sciences (e.g. tumor metabolism), food technology, and marine sciences.

7.2 Main text

Oxygen and pH can be directly visualized by luminescence-based methods but probes usually have to be in direct contact with the sample (tissue)^{4,5,20}. However, there is always the associated risk of toxicity. Dyes that are firmly bound to or incorporated in a sensor film do not suffer from this disadvantage. Concerning (luminescence) read-out, it is almost mandatory to use referenced methods to enable quantitative *in vivo* imaging and to prevent interferences caused by variations in the concentrations and distribution of probes. Intensity measurements are non-referenced, FLIM utilizes lifetime for intrinsic referencing. DLR uses a reference signal with long luminescence lifetime, and ratiometric measurements refer to a second analytical wavelength in the excitation or emission spectrum. Actually, ratiometric methods are straightforward but tedious because of the need to change filters or light sources. This also implies that images are created whereas data have not been acquired at the same time.

Previously, we presented luminescent single sensors for oxygen (based on FLIM, see *chapter 4*)²¹ and pH (based on DLR; *chapter 3*)⁸, and sensors for multiple analyte imaging¹ (see *chapter 5*), all based on rather complex instrumentation. Yet, there is a need for more simplified imaging techniques that (i) allow simultaneously acquiring

information on oxygen and pH, (ii) permit the use of affordable instrumental setups, and (iii) give referenced quantitative rather than just qualitative information.

7.2.1 RGB dual imaging and material design

In this work, we use ratiometric luminescence imaging with one excitation source and multiple wavelength read-out. We exploit the channel separation option of digital cameras to separate and reference signals^{22,23} (see *chapter 6*). Digital photographic cameras utilize metal oxide semiconductor (CMOS) chips with red, green, and blue (RGB) channels. These record the respective part of the visible spectrum (**Fig. 7.1**). Thus, one single color picture is composed of three virtually independent data sets. Digital cameras are comparably cheap, have a large dynamic range (14 bit in RAW mode), can be miniaturized, and offer easy handling compared to other setups. The use of such photographic systems combined with appropriate sensor materials instantly allows for simultaneous continuous imaging (even recording videos) of two different parameters.

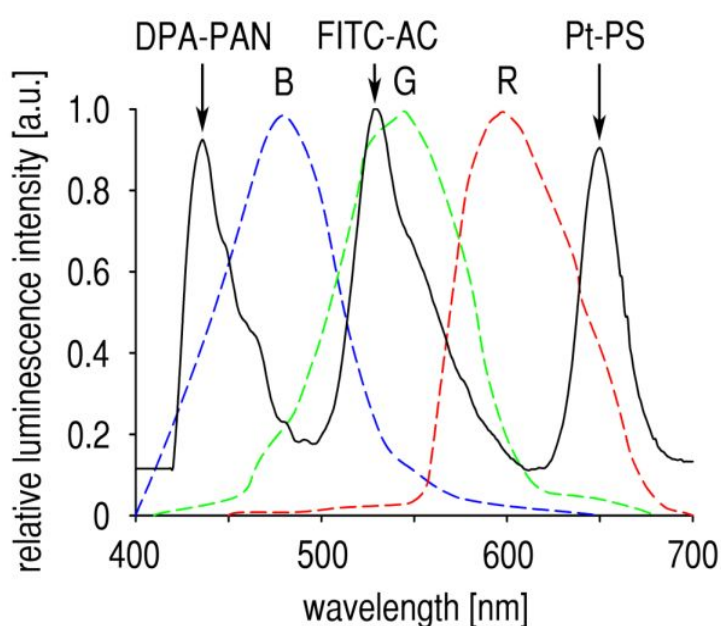
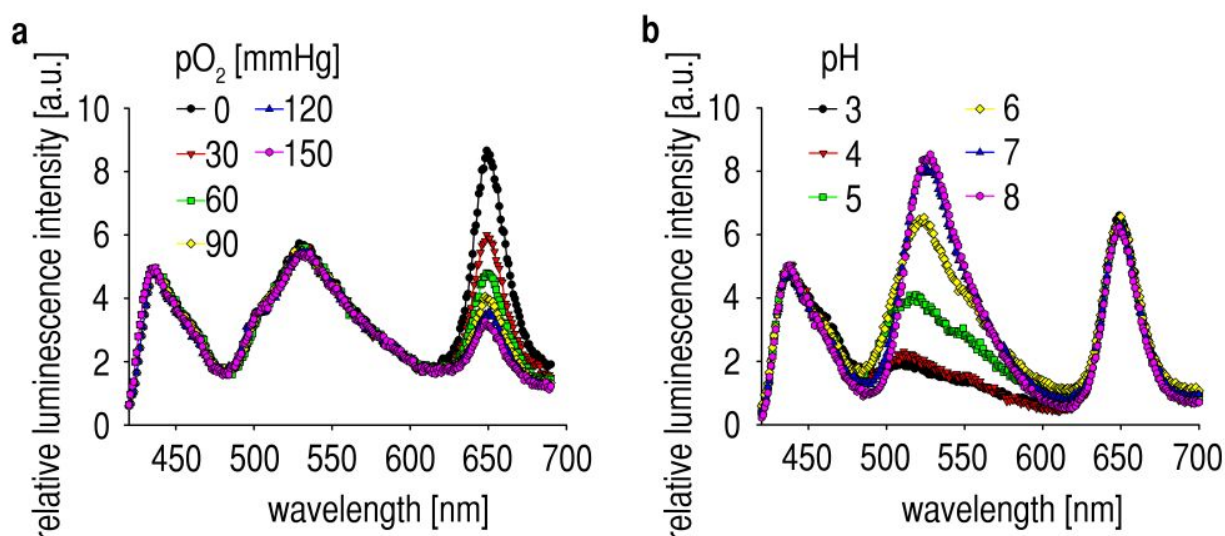


Figure 7.1 | Luminescence Emission spectrum of the sensor material and matching with the sensitivity of the RGB-channels of the digital camera: The dashed red, green, and blue lines (R, G, B) represent the spectral response of each respective color channel of the CMOS chip in the used camera. The black line gives the emission of the sensor material and clearly shows the three peaks of the three types of particles.

We designed a proper material for imaging oxygen and pH in vivo using this RGB read-out technique. Three dyes with emission peaks matching the three color channels of a digital

photographic camera (**Fig. 7.1**) were chosen: platinum(II)-5,10,15,20-tetrakis-(2,3,4,5,6-pentafluorophenyl)-porphyrin (Pt-TPFPP, λ_{em} 650 nm, red channel, oxygen-indicator), fluorescein-isothiocyanate (FITC, λ_{em} 530 nm, green channel, pH indicator), and diphenylanthracene (DPA, λ_{em} 440 nm, blue channel, reference fluorophore). All three are simultaneously excited with a ring of 28 UV-LEDs (emission peak: 405 nm) mounted on the camera lens. A photo of the imaging system is given in **Fig. 2.6 in chapter 2**. Red, green, and blue luminescence emitted by the sensor film is recorded with a standard digital camera equipped with a 435 nm long-pass optical filter to separate scattered blue excitation light from the recorded image.

Figure 7.2 | Emission spectra of the dual sensor in **(a)** an argon atmosphere containing 0



to 150 mmHg pO_2 at pH 5.5 and **(b)** at pHs between 3 and 8 at 15 mmHg of pO_2 .

To visualize analyte distributions, a real color RGB image of the sensor film is recorded (**Fig. 7.3b**), and is then split into the R, G, and B color channels (**Fig. 7.3c**). The intensity of the red luminescence of Pt-TPFPP decreases with increasing pO_2 , the green fluorescence

of FITC increases with increasing pH values, and the blue signal of the reference dye remains unaffected by both oxygen and pH (**Fig. 7.2**). In order to ratiometrically reference the signals, the intensity values of each pixel of the respective picture (R or B channel) are divided by the intensity values of the respective pixel in the blue reference channel. Thus, the red/blue ratio (R/B) of each pixel represents the referenced response to oxygen, and the green/blue ratio (G/B) is a referenced pH response (**Fig. 7.3d**). Oxygen response (R/B) follows exponential decay, whereas the pH signal (G/B) shows sigmoidal response, obviously because pH is a logarithmic parameter (**Fig. 7.3e**).

The main criteria in the design of the sensor material included (i) the compatibility with the RGB technique, (ii) the lack of dye leaching, and (iii) the biocompatibility of the materials, so to make the sensor applicable for *in vivo* use (**Fig. 7.4**). The three dyes were either covalently bound to, or incorporated in, inert polymer microparticles to prevent leaching of dyes. Next, the particles were immobilized in a biocompatible hydrogel matrix to prevent particle leakage. In view of the specific use of this sensor to study human wound healing, the microparticles have sizes between 0.5 and 8 μm to prevent possible cellular uptake. Another advantage of using microparticles is that fluorescence resonance energy transfer (FRET) between the various dyes cannot occur because the average distance of the partners in a FRET is much larger than 10 nm (upper limit for FRET)^{24,25}. Conceivably, sensor nanoparticles may be used as well but these exhibit a higher risk of leakage and cellular uptake.

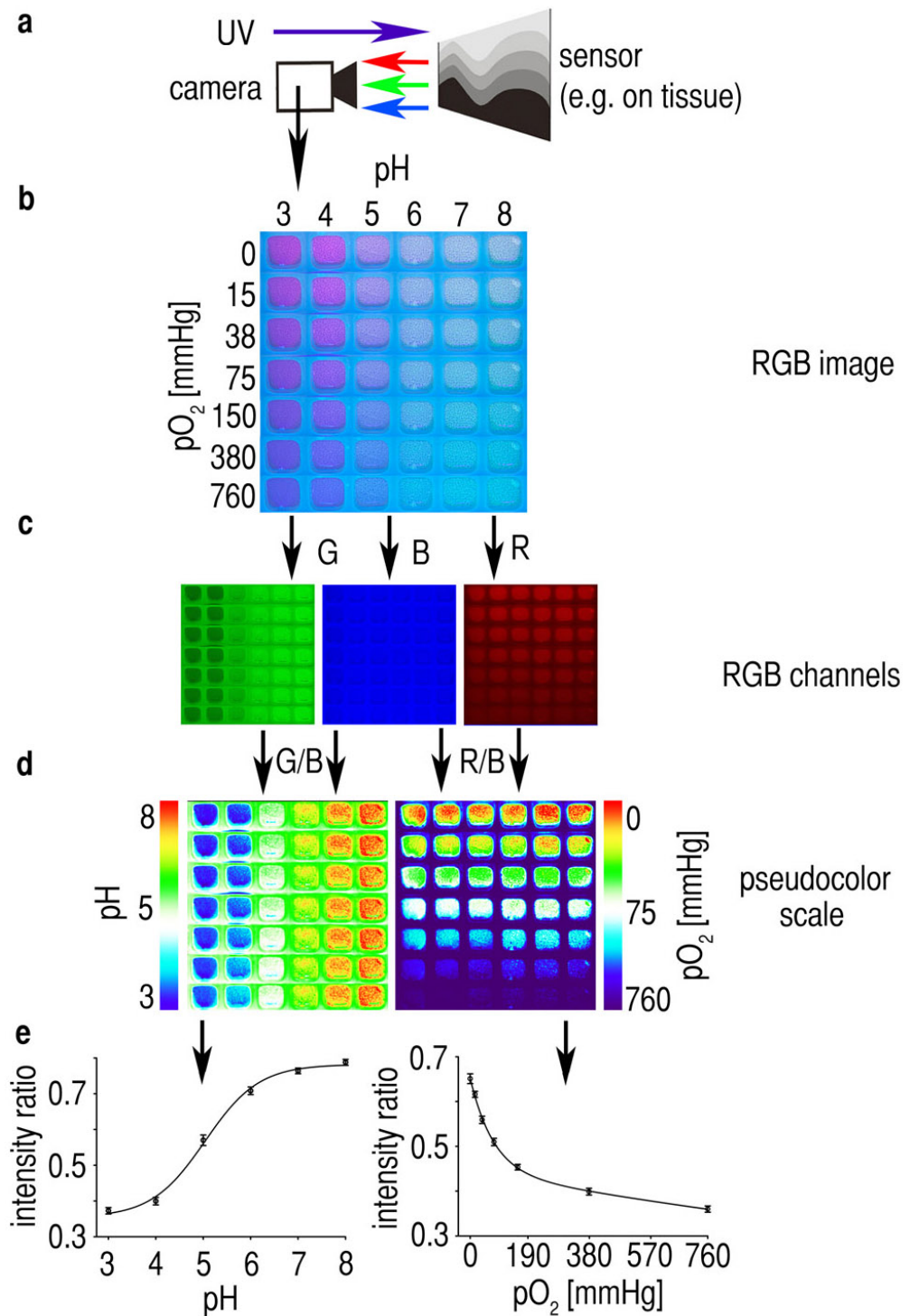


Figure 7.3 | Sensing scheme and calibration plots: **(a)** The sensor film is applied to a surface (e.g. wound tissue) and illuminated with UV light. The three dyes in the sensor layer emit red (R), green (G), and blue (B) light that is collected via a CMOS camera: **(b)** Real color picture (RGB image) of a calibration array with different pH values and oxygen concentrations. **(c)** The RGB image is split into three independent color channel pictures. **(d)** The ratio of red to blue channel pictures (R/B; displayed in pseudocolors) represents the oxygen response and shows the lack of cross-reactivity to pH. The ratio of green to blue channel pictures (G/B) reflects the response to pH and also demonstrates the lack of cross-reactivity to oxygen. **(e)** Respective calibration plots for oxygen (biexponential decay fit) and pH (sigmoidal fit).

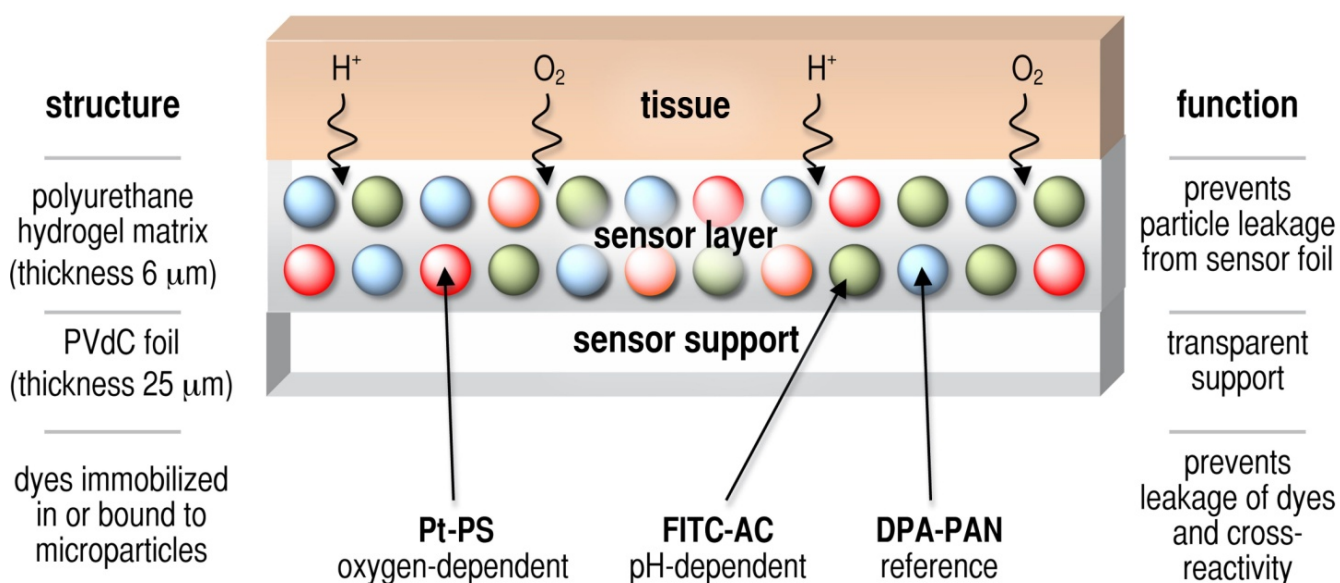


Figure 7.4 | *Sensor foil scheme: Dyes are immobilized or bound to microparticles to prevent leaching or cross-reactivity of the dual-sensor response. The particles are incorporated into a hydrogel matrix foil to prevent particle leakage. A transparent PVdC foil is used as sensor support. The sensor is placed on skin or wound surface, upon which oxygen and protons diffuse into the hydrogel matrix and to the microparticles where they modulate the emission of the respective beads.*

Pt-TPFPP was incorporated in polystyrene particles (Pt-PS, 1 to 3 μm , **Fig. 7.5a**) and DPA was embedded in polyacrylonitrile particles (DPA-PAN, 0.5 to 1 μm **Fig. 7.5c**). Both are well retained due to hydrophobic interactions and their complete insolubility in water. FITC was covalently attached to aminocellulose particles (FITC-AC, 2 – 8 μm , **Fig. 7.5b**). As a result, dyes do not leach out of the particles (**Fig. 7.6**). PS was chosen as the material for the oxygen sensitive particles due to its excellent gas permeability and hydrophobicity which renders it permeable to oxygen, but not for water and protons. In contrast, AC possesses amino groups for covalent immobilization of FITC, is hydrophilic and rapidly penetrated by protons. The pK_a of fluorescein shifts from 6.8 to 5 upon conjugation of FITC to AC. This is beneficial in terms of sensing pH in tissue. Residual amino groups of AC were blocked with acetic anhydride to remove excess charges that may act as local buffer and slow down sensor response. PAN, a hydrophobic polymer that is virtually

impermeable to oxygen and ions, was used to fabricate completely inert reference particles.

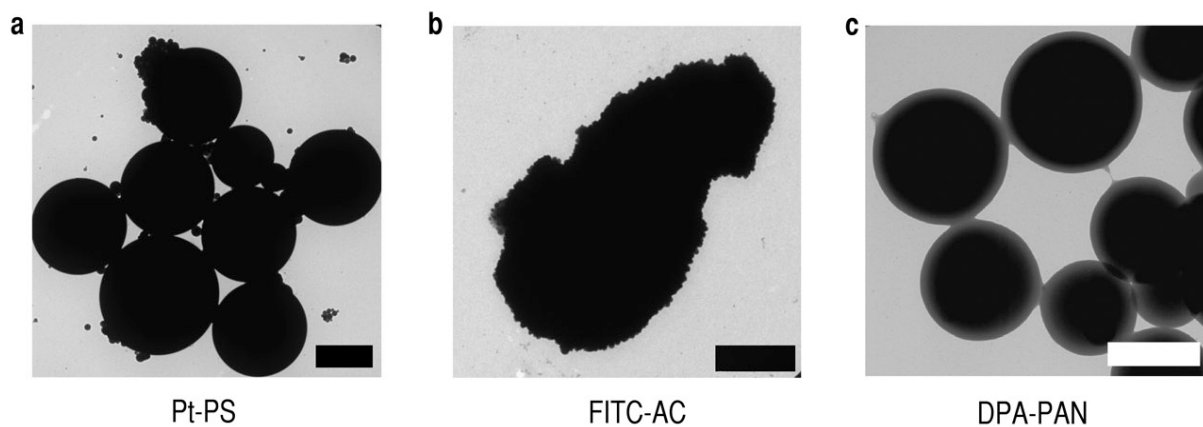


Figure 7.5 | Transmission electron microscopy (TEM) images: **(a)** platinum(II)-5,10,15,20-tetrakis-(2,3,4,5,6-pentafluorophenyl)-porphyrin embedded in polystyrene particles (Pt-PS; scale bar 2 μm). **(b)** fluorescein isothiocyanate bound to aminocellulose particles (FITC-AC; scale bar 2 μm). **(c)** 9,10-diphenylanthracene incorporated in polyacrylonitrile particles (DPA-PAN; scale bar 0.5 μm).

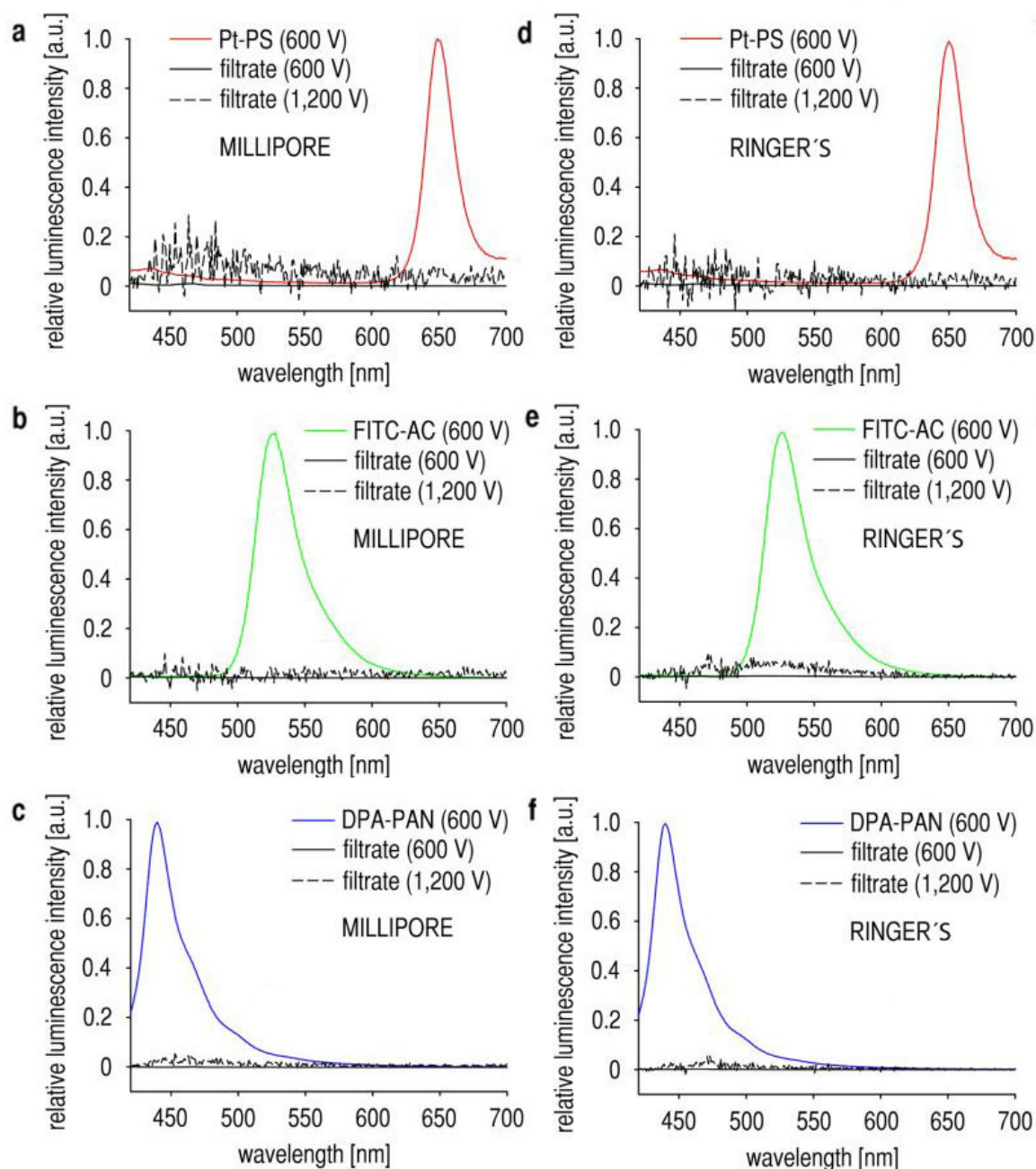


Figure 7.6 | *Leaching of dyes: Results of the leaching experiments for all three sorts of particles in Millipore water (a-c) and Ringer's solution (d-f). Colored lines represent the luminescence spectra of particle suspensions. Solid black lines are the spectra of the centrifuged and filtered solutions with identical detector gain (600V each). Dashed lines (full detector gain) show the lack of traces of dyes in filtered solutions.*

The three kinds of microparticles were added to a solution of polyurethane hydrogel in 90% (v/v) ethanol in water. This “cocktail” was then knife-coated onto a transparent 25- μm poly(vinylidene chloride) (PVdC) foil to create a 2D sensor foil (**Fig 7.7**)^{8,26}.

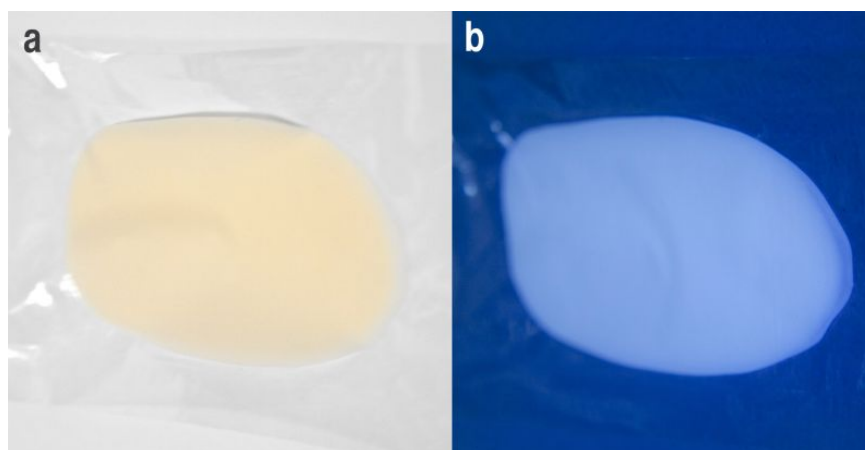


Figure 7.7 | Picture of a sensor film: (a) A daylight real color picture of a 6 μm thick yellowish sensor layer on the transparent support. (b) The sensor under photoexcitation.

Thus, particle leakage is prevented (**Fig. 7.8**). The sensor layer had a thickness of 6 μm after solvent evaporation. Sensors were sterilized during fabrication using ethanol as solvent. The PVdC-support is biologically inert, transparent, and flexible for application to uneven surfaces (e.g. wound surface). Sensors were examined by fluorescence microscopy to ensure homogeneous particle distribution (**Fig. 7.9**).

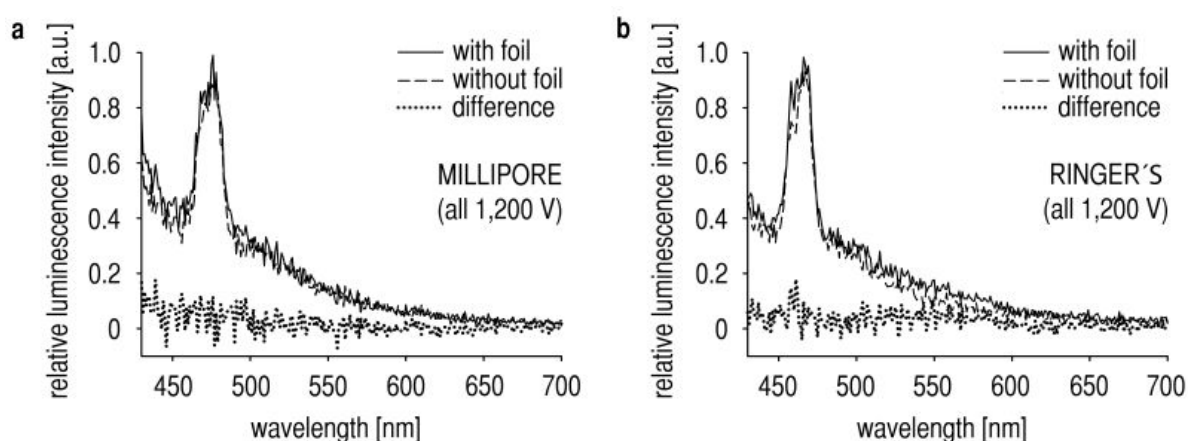
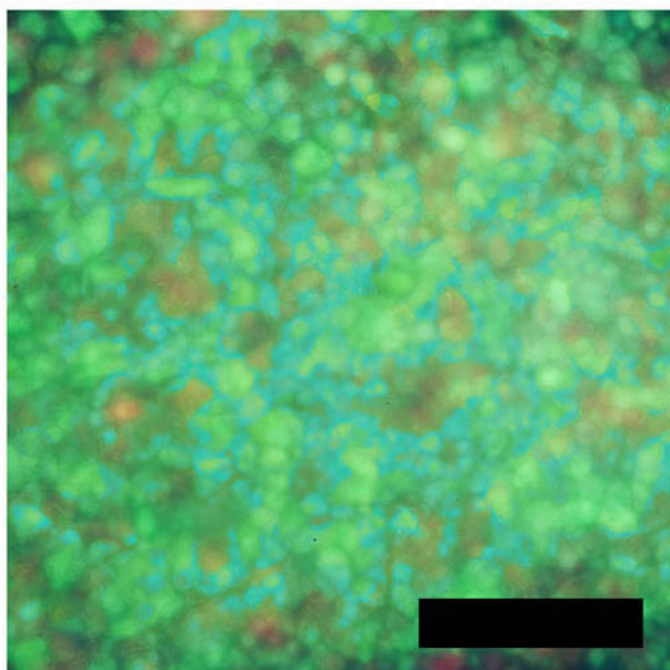


Figure 7.8 | Leakage of particles: Results of experiments on particle leakage out of the sensor foil. The spectra of the incubated solutions (solid lines) and blank controls (dashed lines) are given. The peak at 470 nm results from an internal reflection in the instrument. The corrected spectra (dotted lines) indicate the absence of leakage of Pt-PS, FITC-AC, and DPA-PAN into both solutions. (a.u. = arbitrary units).



foil surface

Figure 7.9 | *Fluorescence microscopic image of a poly(vinylidene-chloride) (PVdC) foil coated with sensor particles (Pt-PS, FITC-AC, and DPA-PAN) in a polyurethane hydrogel matrix (scale bar 50 μm).*

7.2.2 Cytotoxicity

The immobilization of microparticles in hydrogel prevents direct contact with tissue. Nevertheless, potential cytotoxicity was studied prior to use on human subjects. A three-parametric test was conducted by exposing human epidermal keratinocytes (HKs) and L929 fibroblasts to such particles, and assessing cell viability using the 3-(4,5-dimethyl-2-thiazolyl)-2,5-diphenyl-tetrazolium-bromide (MTT) assay. In addition, dead cell protease assays were performed. The results reveal that particles do not exhibit cytotoxicity (**Fig 7.10** and **Fig. 7.11**) and are not taken up by live cells (**Fig 7.12** and respective **Video VII.1-2**). Cellular uptake of FITC-AC was already excluded in a previous work⁸ (see *chapter 2*).

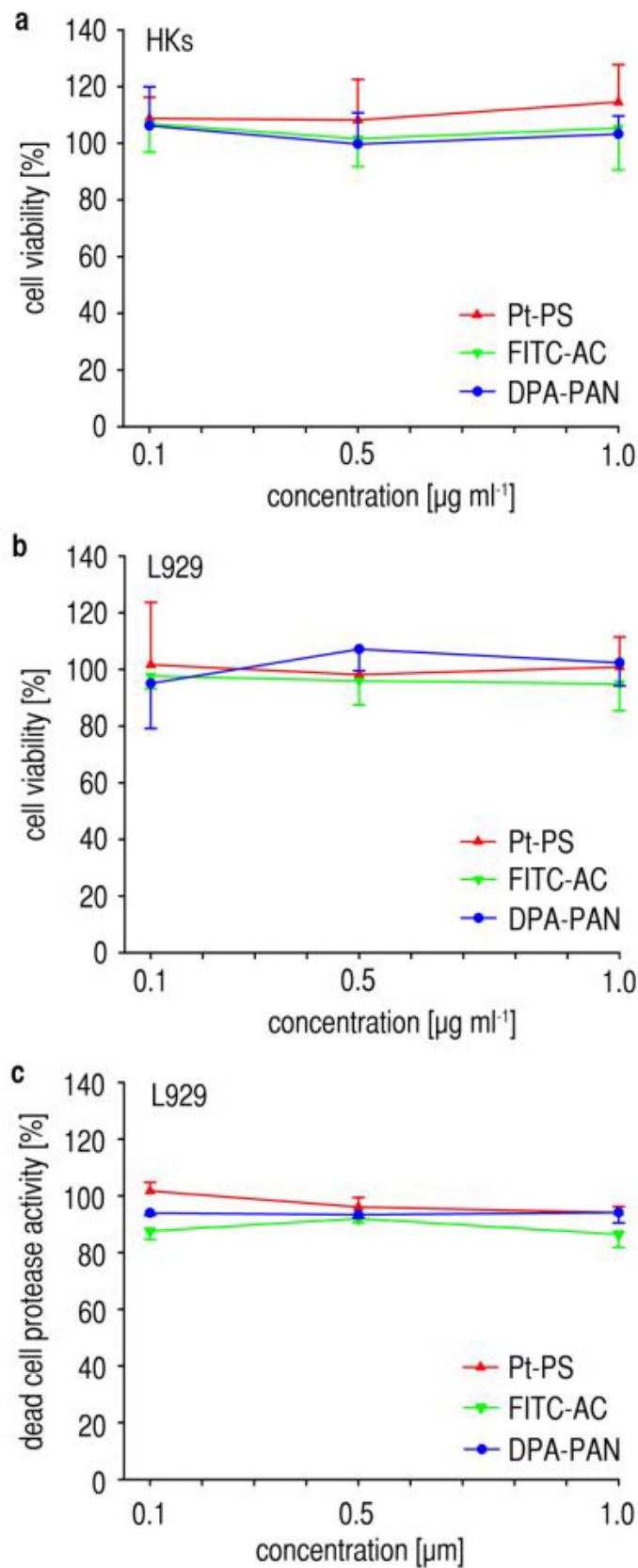


Figure 7.10 | Cytotoxicity, particle exposure and MTT assays part 1: (a-c) No cytotoxicity can be detected for Pt-PS, FITC-AC and DPA-PAN towards (a) human epidermal keratinocytes (HKs) and (b) L929 fibroblasts. Cell viability in the MTT assays is expressed as the percentage of viable cells compared to controls. (mean \pm SD, quadruplicate samples). The release of dead cell protease from L929 was not increased after 24 h of incubation with microparticles, (c) indicating that particles exhibit no cytotoxic potential. Dead cell protease activity is given as the percentage of untreated controls (mean \pm SD, quadruplicate samples).

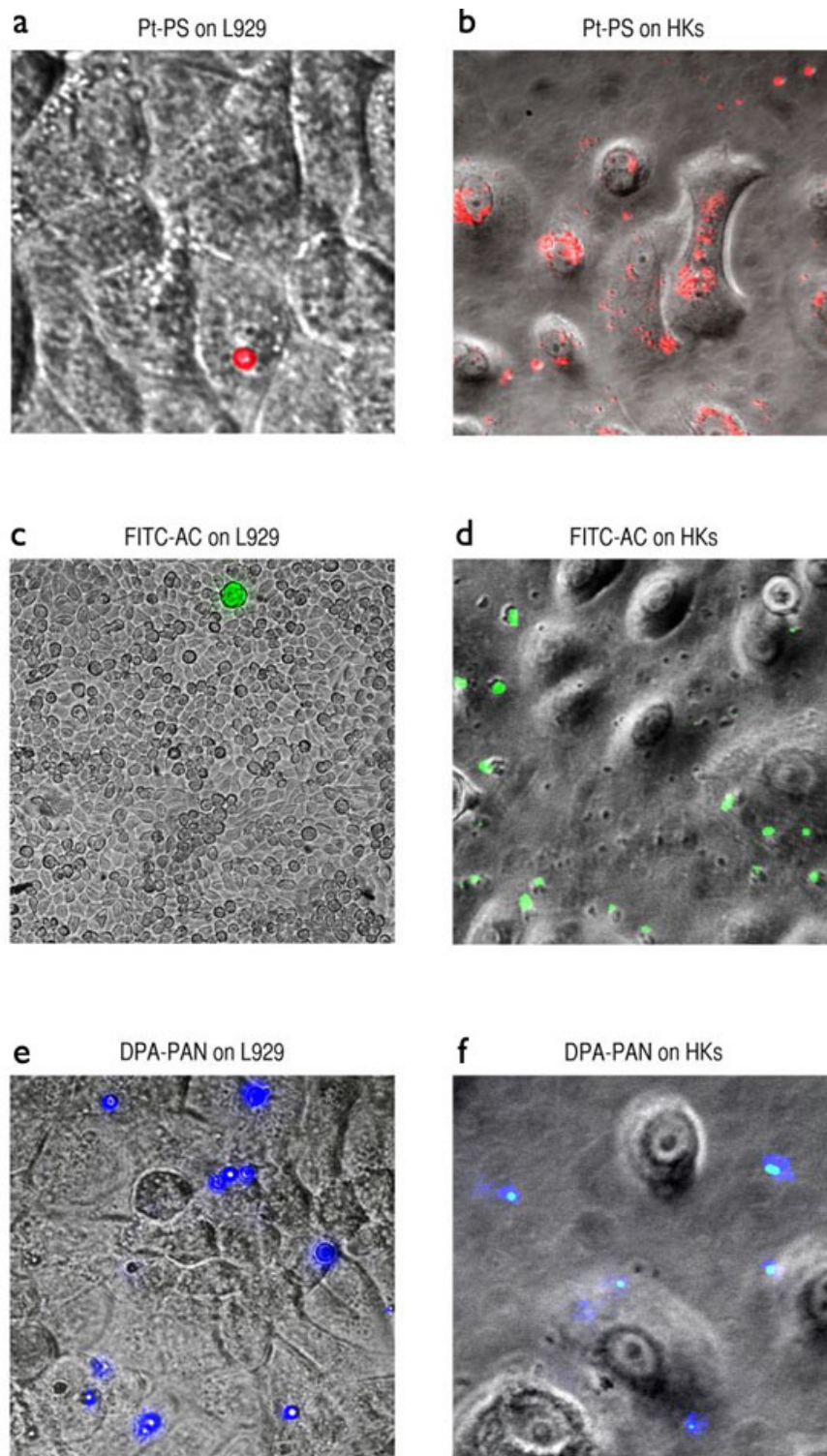


Figure 7.11 | Cytotoxicity, particle exposure and MTT assays part 2: Inverted and fluorescence microscopy shows the exposure of (**a**, **c**, and **d**) L929 and (**b**, **d**, and **f**) HKs towards (**a**, **b**) Pt-PS, (**c**, **d**) FITC-AC and (**e**, **f**) DPA-PAN particles (red, green and blue in overlays). As seen in the pictures, particles tend to agglomerate and are not taken up by live HKs/L929.

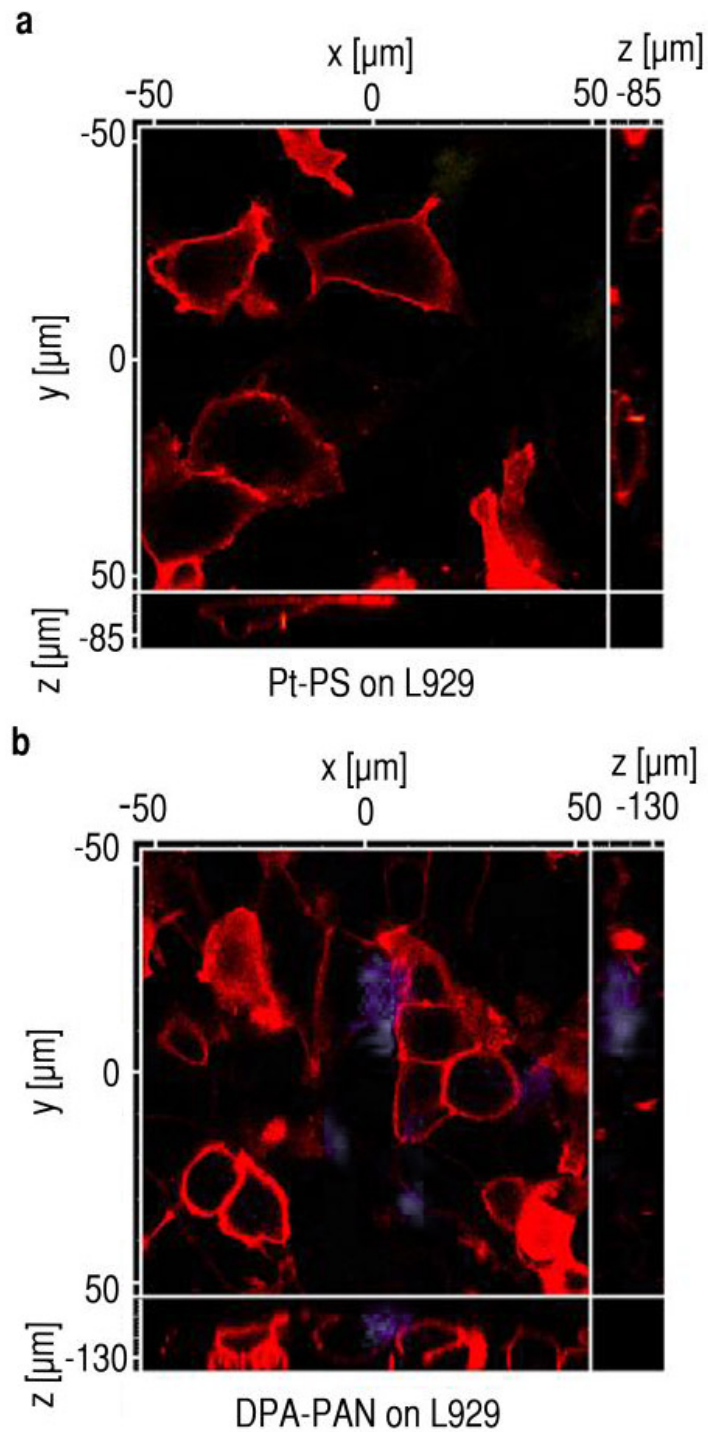


Figure 7.12 | Confocal microscopic analysis of cellular particle uptake: Live L929 fibroblasts do not internalize DPA-PAN (a) or Pt-PS (b) particles (both $1.0 \mu\text{g ml}^{-1}$ in supernatants) within 24 h of incubation. (a) Multiple Pt-PS particles are seen (orange to red spots) on the surface of various cells. (b) DPA-PAN (blue) can be seen as agglomerates on the cell surface (displayed in red). For better visualization of particles and their location, see the confocal microscopic image stacks in **Videos SV3** and **SV4** on the enclodes CD.

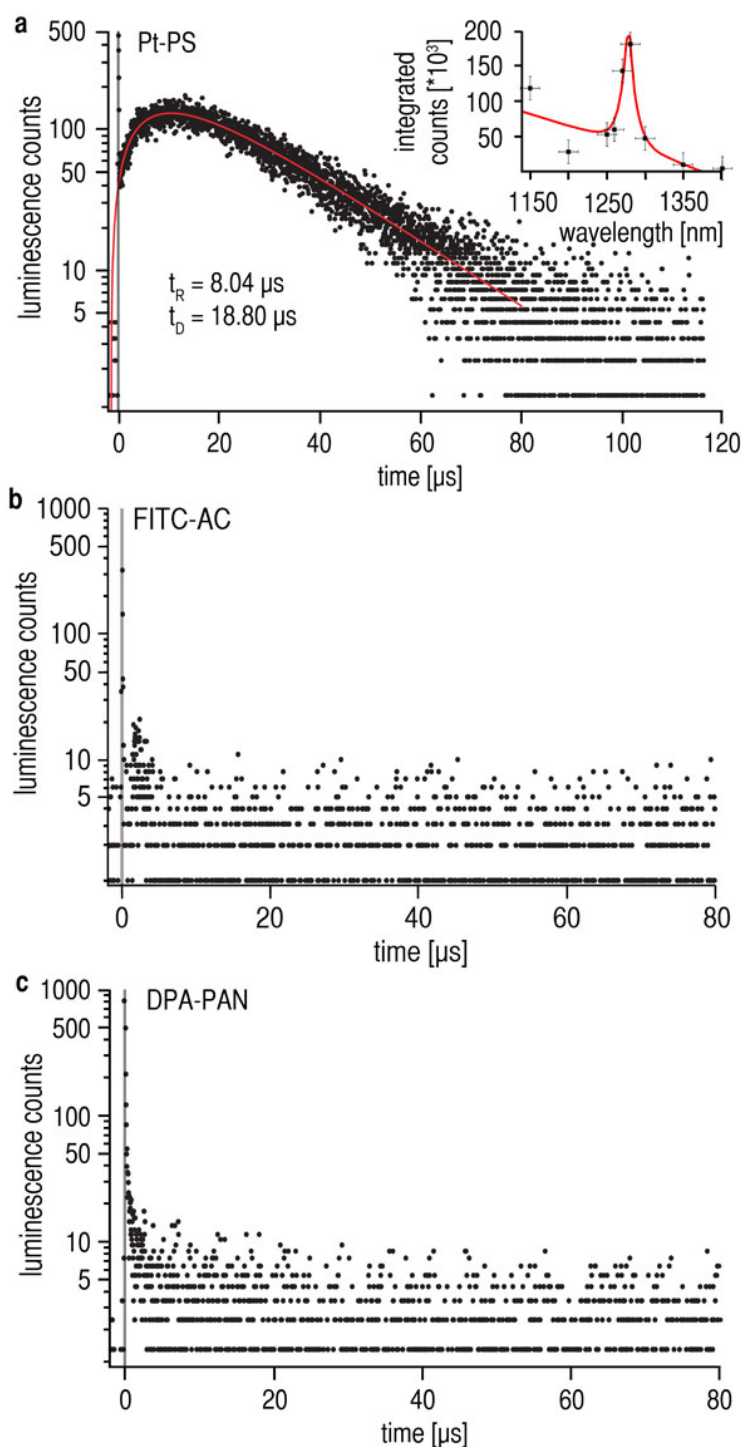


Figure 7.13 | Singlet oxygen detection: (a) Pt-PS leads to the production of singlet oxygen. The red curve shows the singlet oxygen signal of Pt-PS (t_R = rise time, t_D = decay time). The inset shows the integrated luminescence signal at certain wavelengths (fit shown as red curve). Neither FITC-AC (b) nor DPA-PAN (c) led to the formation of singlet oxygen. (a-c) Time zero denotes the start of excitation (vertical grey lines).

We also studied the generation of singlet oxygen (1O_2), a member of the reactive oxygen species. Laser excitation of Pt-PS indeed lead to the production of 1O_2 but in negligible quantity as indicated in **Fig. 7.13a**. Since the dual sensors described here are photoexcited by LED (rather than with strong lasers) we conclude that formation of 1O_2 does not present a risk here. Secondly, the lifetime of 1O_2 is rather short.²⁷ This prevents diffusion of 1O_2 out of the sensor. There was no generation of 1O_2 by FITC-AC and DPA-PAN (**Fig. 7.13b-c**).

7.2.3 In vitro characterization

The sensor was then characterized in a set of *in vitro* experiments. Calibration plots were established, by recording the R/B ratio as a function of oxygen in the range of 0 to 760 mmHg. The function follows a four-parametric biexponential decay fit (**Fig. 7.3e**), and a three-parametric monoexponential decay fit matches the physiologically relevant range (0 to 160 mmHg pO₂). The unit mmHg (SI unit 1 Pa = 7.5006 · 10⁻³ mmHg) for pO₂ is used in this paper as it is widely used in biomedical sciences. Oxygen content in mmHg can be calculated by solving the equation in **Fig. 7.14a** for pO₂. The calibration for G/B follows a four-parametric sigmoidal fit. pH values can be calculated via the equation in **Fig. 7.14b**.

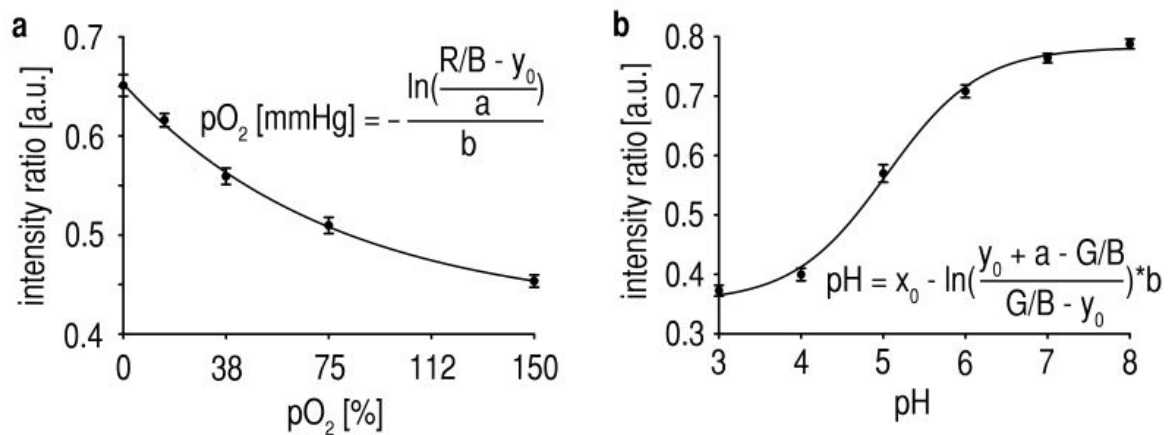


Figure 7.14 | Calibration curves and fit equations for pH and oxygen: **(a)** Plot of the intensity ratios of the red and blue channels (R/B) of the sensor layer as a function of physiologically relevant oxygen concentrations in argon gas at atmospheric pressure. The equation represents the inverse function of an exponential fit for O₂ content calculation. **(b)** Calibration plot of green and blue channel ratios (G/B) for varying pH. The equation for calculating pH is the inverse function of a four-parametric sigmoidal fit.

Photobleaching is a major concern in ratiometric measurements, particularly if dyes bleach at different rates. A respective study under varying oxygen and pH conditions revealed that there is virtually no decrease in luminescence emission over time even after more than 40 min of continuous illumination (**Fig. 7.15**). Sensors were, however, stored protected from light until use.

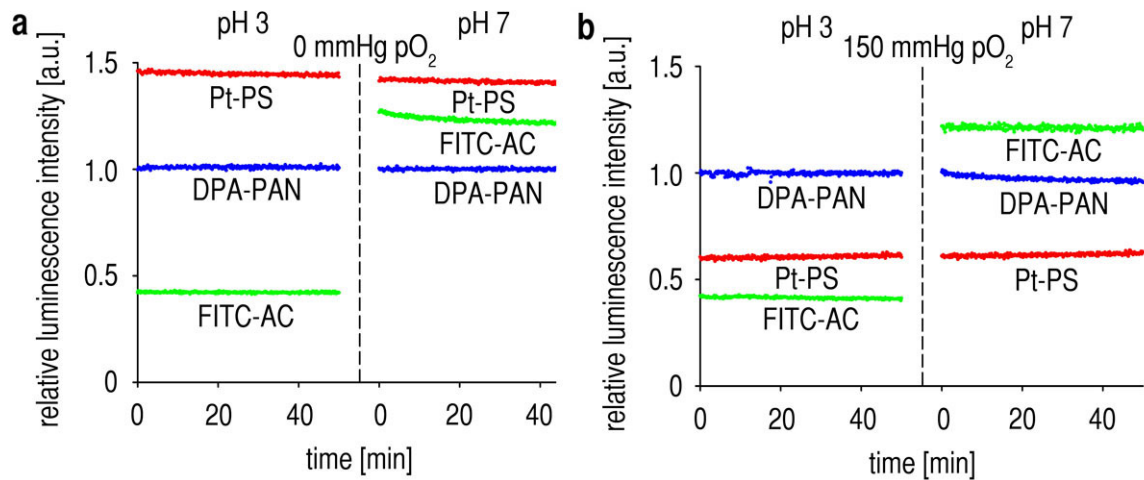


Figure 7.15 | Photostability of the luminescence signals: Pt-PS (red lines, 650 nm), FITC-AC (green, 530 nm), and DPA-PAN (blue, 440 nm) under continuous illumination. The graphs show virtually constant luminescence intensities even under varying conditions ((a) pH 3 and pH 7 at 0 mmHg; (b) pH 3 and 7 at 150 mmHg; 30 °C).

The response times (99% signal changes) towards oxygen and pH (**Fig. 7.16** and **supplementary Video VII3-4** on the enclosed CD) are 30 s (from oxygen to argon), 9 s (from argon to oxygen), and 25 s for pH changes (6 to 8). The different response times for oxygen result from the known differential gas diffusion rates of oxygen and argon in polystyrene²⁸. Consequently, all measurements started 1 min after sensor application.

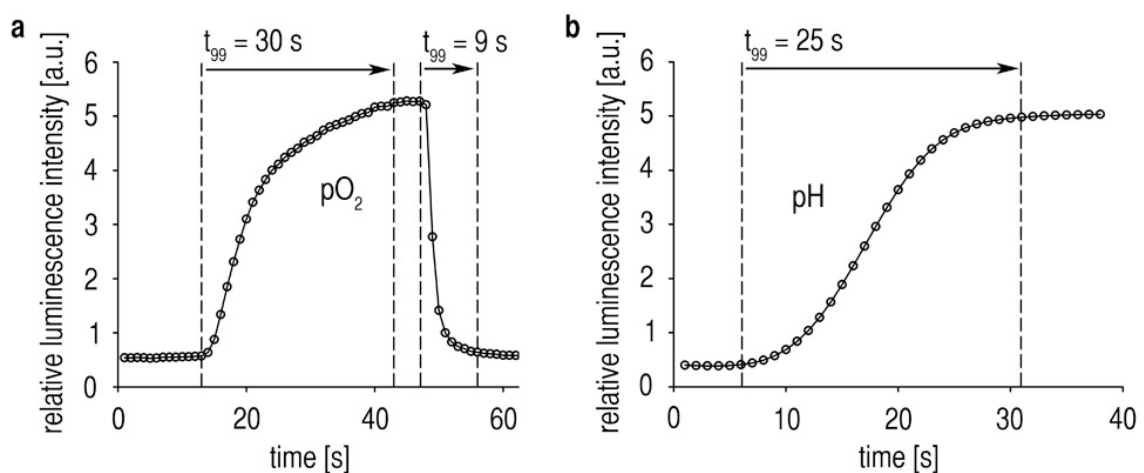


Figure 7.16 | Time traces of sensor response with luminescence intensities at 650 nm (a) following pO_2 variations from 0 to 760 mmHg ($t_{99} = 30$ s towards argon, $t_{99} = 9$ s towards oxygen) and at 530 nm (b) for pH variation from pH 3 to 8 ($t_{99} = 25$ s), until 99 % of the steady-state signal (t_{99}) was reached.

The sensor responds to oxygen from 0 to 760 mmHg (**Fig. 7.3e**), with the highest sensitivity in the physiological range (**Fig. 7.14a**). pH sensitivity is from 3 to 8 (**Fig. 7.14b**), thus covering the clinically relevant range. Neither oxygen- nor pH-signals show relevant cross-sensitivity (**Fig. 7.17**) or temperature dependency (20 to 40 °C, **7.18**).

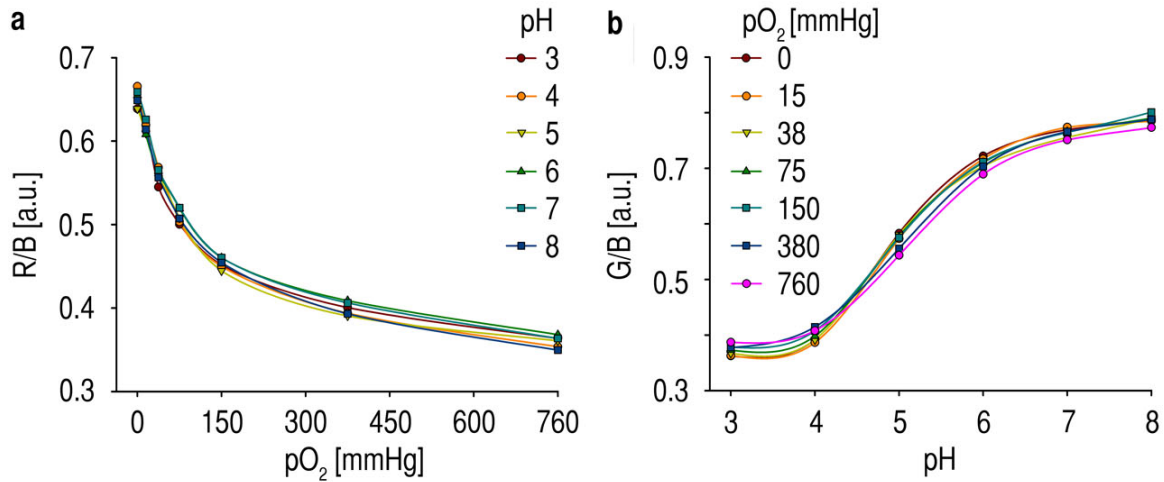


Figure 7.17 | *Cross-sensitivities: The R/B oxygen signal (a) with varying pH from 3 to 8 in single steps and the G/B pH signal (b) with varying oxygen concentrations. Neither pH nor oxygen signals showed cross-sensitivity for the respective other parameter.*

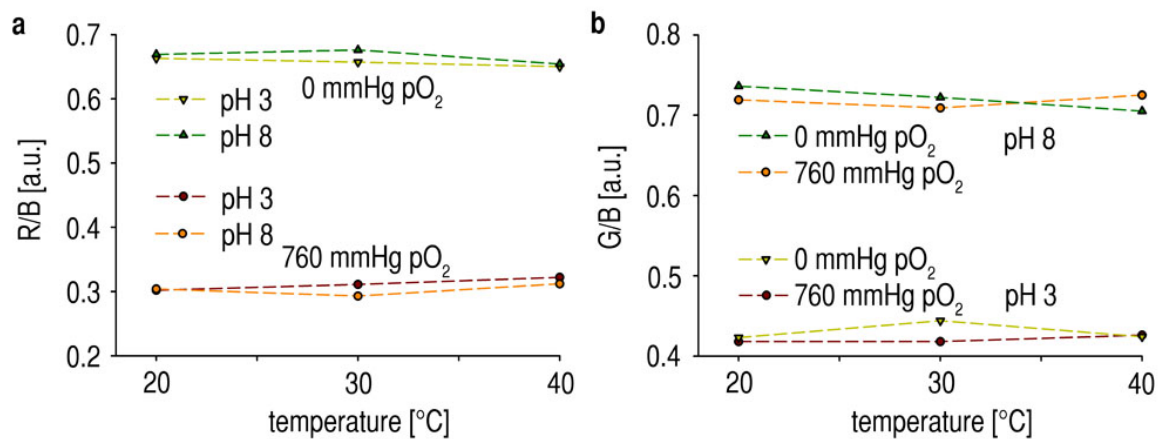


Figure 7.18 | *Temperature insensitivity of the sensor: No significant temperature sensitivity of the sensor between 20 and 40 °C was found by comparing the R/B ratio for oxygen (a) and the G/B ratio for pH (b) at 0 and 760 mmHg pO₂ at different pH.*

7.2.4 In vivo imaging

The sensor material was applied to simultaneously image oxygen and pH in tissue (see Supplementary Information). Imaging of intact skin (volar forearm) showed virtually homogeneous distributions of oxygen and pH (**Fig. 7.19**). The epidermis is known to prevent diffusion of oxygen through skin, thus resulting in very low pO_2 on the skin surface. The results herein confirm experiments²¹ obtained by luminescence lifetime imaging of pO_2 (see *chapter 4*). The pH of the skin surface was found to be around pH 4.5 to 5.5 using the RGB sensor.

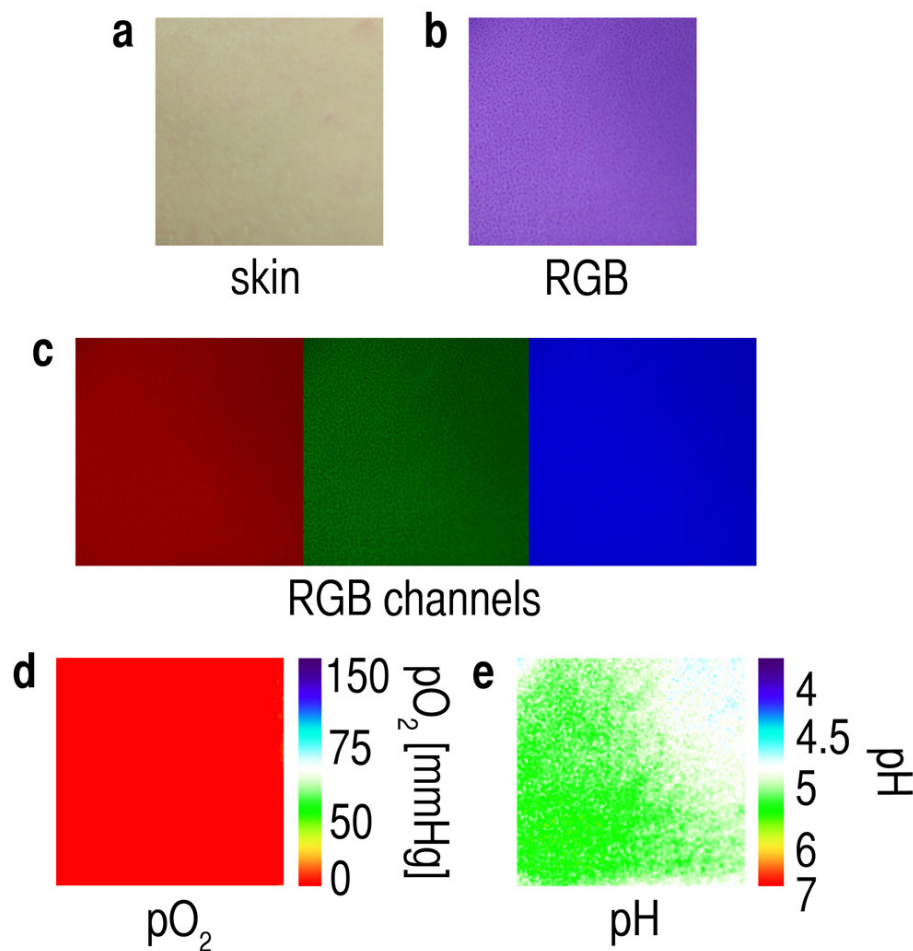


Figure 7.19 | In vivo application of the dual sensor on plain and healthy skin surface of a volar forearm: (a) shows a picture of the skin surface. (b) depicts the RGB image of the skin with an overlaying sensor. The picture is split into the three respective color channels (c). The R/B ratio in (d) shows the response of the oxygen sensor. The G/B ratio shows the pH distribution on the surface of skin and wound (e). For scaling, see the calibration plots in **Fig. 7.14**. Image sizes: 5 x 5 cm.

Imaging of a skin graft donor site (postoperative day 5) indicated more heterogeneous analyte distributions (**Fig. 7.20**). Wound healing is indicated by decreasing oxygen and pH values as previously shown by our group^{8,21} (see *chapter 3 and 4*). The different regions of the donor site wound can be attributed to (i) either the phase of new tissue formation (partially re-epithelialized areas in upper left part of the acute wound), or (ii) to earlier stages of healing (inflammatory areas in lower right part of the wound). Obviously, the full barrier function of the superficial skin layers was not yet regenerated.

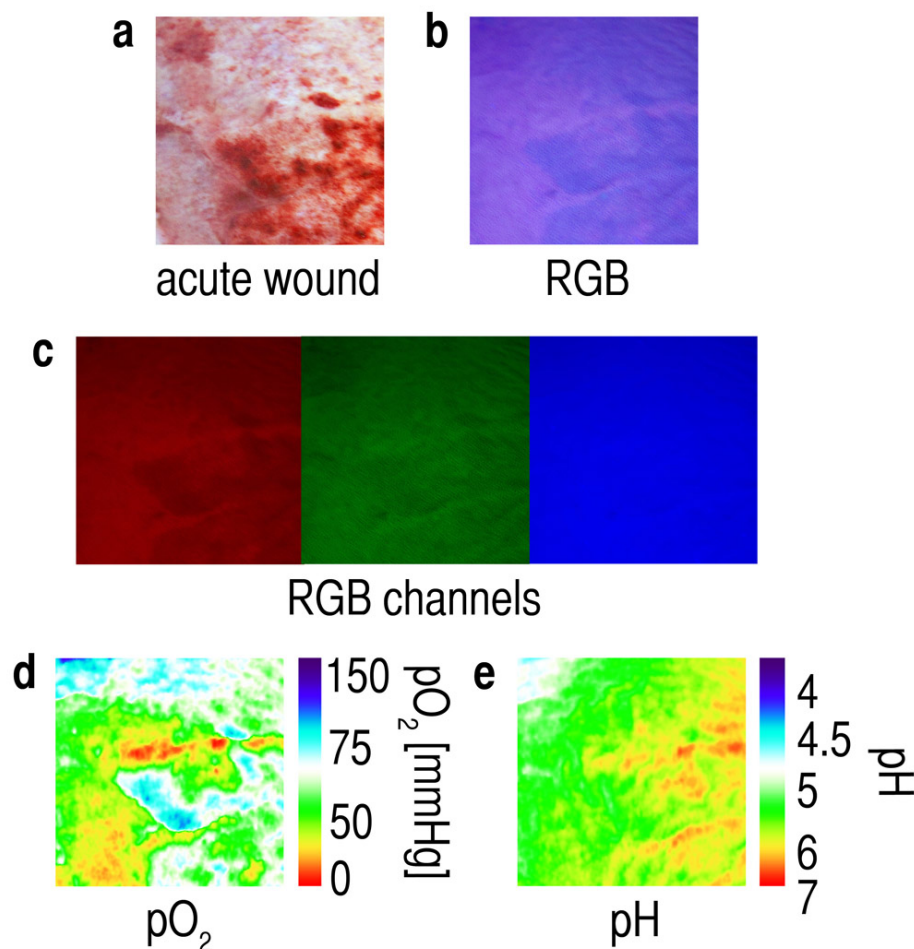


Figure 7.20 | In vivo application of the dual sensor on a skin graft donor site (postoperative day 5) as a model for acute wound healing: (a) shows a picture of the wound surface. (b) depicts the RGB image of the skin with an overlaying sensor. The picture is split into the three respective color channels (c). The R/B ratio in (d) shows the response of the oxygen sensor. The G/B ratio shows the pH distribution on the surface of skin and wound (e). Image sizes: 5 x 5 cm.

To demonstrate the potential for 2D imaging, the heterogeneous relief of a chronic wound was visualized (**Fig. 7.21**). Oxygen and pH values are indicative of a sustained inflammatory phase, especially the high pH values in the upper left part of the wound. This area is also quite hypoxic, which is probably due to the high oxygen demand during inflammation and tissue formation in wound healing. However, further studies are required to study oxygen and pH in chronic healing.

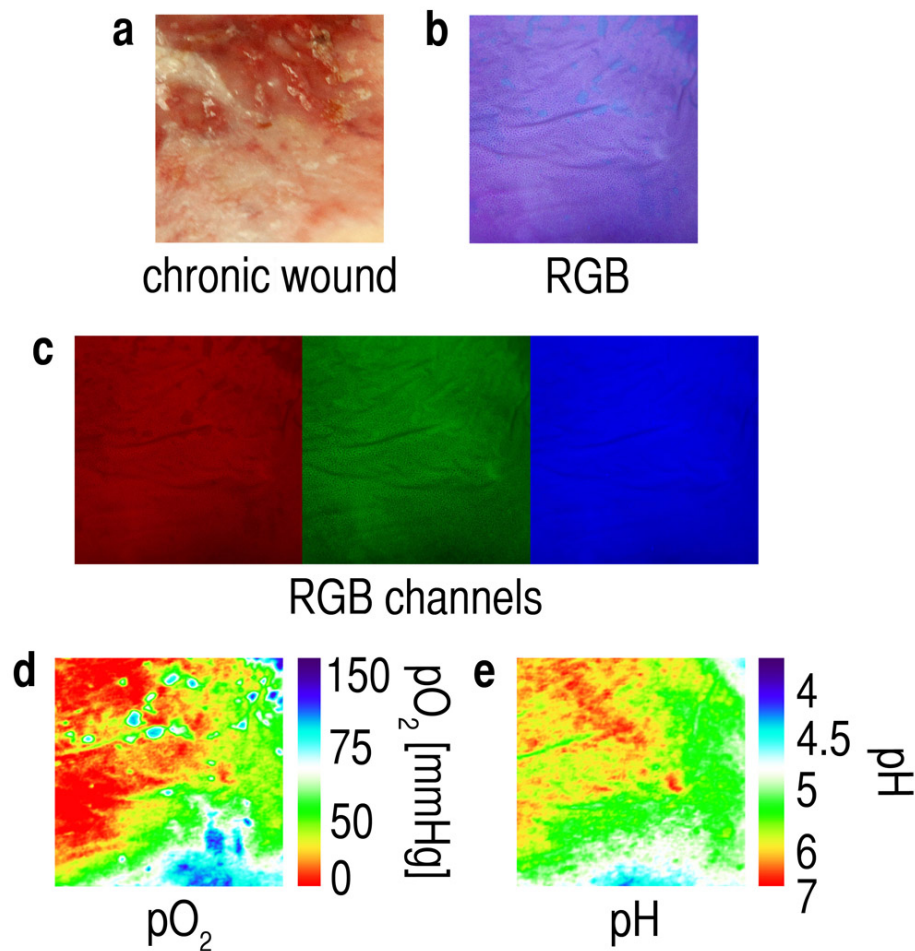


Figure 7.21 | In vivo application of the dual sensor on a chronic wound: (a) shows a picture of the chronic wound surface. (b) represents the RGB image of the skin with an overlaying sensor. The picture is split into the three respective color channels (c). The R/B ratio in (d) shows the response of the oxygen sensor. The G/B ratio shows the pH distribution on the surface of skin and wound (e). Image sizes: 5 x 5 cm.

7.3 Materials and Methods

7.3.1 Microparticle preparation

Chemicals were purchased from Sigma-Aldrich (Steinheim, Germany; www.sigmaaldrich.com) unless otherwise specified. The oxygen sensitive sensor particles were prepared by dissolving α,α' -azoisobutyronitrile (62.5 mg) in a mixture of styrene (7.0 ml) and methacrylic acid (60 μ l) and mixing the solution with ethanol (25 ml) containing dissolved poly(vinyl pyrrolidone) (0.188 g; type K-30). The solution was deoxygenated by purging it with nitrogen, and polymerization for 24 h at 70 °C. The resulting particles were centrifuged (10 min at 1,030 g, EDA12; Hettich, Tuttlingen, Germany; www.hettichlab.com) and washed three times with ethanol after cooling to 25 °C. 300 mg of the PS particles were mixed with distilled water (20 ml) and tetrahydrofuran (THF) (15 ml), sonicated (Bandelin Sonorex RK 52, Berlin, Germany; www.bandelin.com) for 30 min to swell the PS beads and simultaneously treated with 5 ml of a 1.0 mg ml⁻¹ solution of Pt-TPFPP in THF which was added dropwise (0.2 ml s⁻¹) to the suspension. The mixture was sonicated for another 20 min to ensure that virtually all the dye molecules were inside the hydrophobic PS particles. The THF was then evaporated using a rotary evaporator. The Pt-PS particles in the residual water suspension were separated under centrifugation, washed with ethanol and water (four times each).^{29,30}

The FITC-AC particles were prepared by reacting FITC (10 mg) with AC particles (Presens, Regensburg, Germany; www.presens.de) (500 mg) in sodium bicarbonate buffer (18 ml, 50 mM, pH 9) for 2 h. Residual amino groups on the particles were blocked by reacting AC (100 mg) with acetic anhydride (200 mg) in ethanol (10 ml) for 12 h. Particles were washed (eight times with distilled water) and filtered via centrifugation (10 min at 1,030 × g) after each washing step.

Reference particles were synthesized by incorporating (10% wt/wt) DPA in PAN to form DPA-PAN particles. These precipitate from a solution of DPA (30 mg) and PAN (300 mg) in dimethylformamide (30 ml) upon slow addition of distilled water (70 ml; drop-wise addition at 1 ml s⁻¹) and subsequent addition of brine (20 ml). Particles were washed

(four times with ethanol and four times using distilled water) and subsequently filtered via centrifugation (10 min at $1,030 \times g$) after each washing step.³¹

All the reactions were conducted at room temperature unless otherwise specified, and particles were freeze-dried (Modulyo; IMA Life S.r.l, Bologna, Italy; www.ima.it) before storage. Particle sizes were determined with a LEO912 AB transmission electron microscope (Carl Zeiss, Jena, Germany; www.zeiss.com).

7.3.2 Preparation of the sensor foils

Pt-PS (50 mg), FITC-AC (70 mg), and DPA-PAN (20 mg) were mixed with an ethanol/water (4 ml; 9:1; v/v) solution containing 5% (w/v) of the polyurethane hydrogel (type D4; Cardiotech Intl. Inc., Wilmington, USA; www.cardiotech-inc.com). The “cocktail” was stirred for at least 48 h and then was spread on a transparent PVdC foil (Saran food barrier wrap, Dow Chemicals, Midland, MI, USA) using a K Control Coater model 101 knife coating device (R K Print-Coat Instruments Ltd., Litlington, UK) to form a wet 120 μm thick film²⁸. Drying of the film resulted in a 6 μm thick sensor layer. Particle distribution inside the sensor foils was investigated using fluorescence microscopy (AxioTech, Carl Zeiss AG, Jena, Germany, www.zeiss.de) prior to use. A representative sample in is shown in **Fig. 7.9**.

7.3.3 Imaging and data processing

The RGB imaging setup consists of a standard digital camera and a modified ring light (LED-RL 1, ELV Elektronik, Leer, Germany, www.elv.de) (see *chapter 2.6*). A Canon EOS model 50D was used for image acquisition and model 550D was used for filming. A Canon EF-S 17-85 mm 1:4-5.6 IS USM lens is used throughout. The LEDs of the ringlight were replaced by 28 LEDs (405 nm peak wavelength; UV5TZ-405-15, BIVAR Inc., Irvine, CA, USA, www.bivar.com). A Schott GG435 high pass filter (Schott, Mainz, Germany, www.schott.com) was placed in front of the lens to act as emission filter.

Camera parameters were set as follows: Raw+jpg; aperture 1:5.6; ISO sensitivity 160; shutter speed 1/8 s. Excessive ambient light is to be avoided. The Raw image data were processed using Adobe Camera Raw plugin for Adobe Photoshop (both from Adobe Systems Software Ireland Ltd., Dublin, Ireland; www.adobe.com). White balance was set to 2450 K. Pictures were stored as 16 bit TIF files and further processed with ImageJ software (<http://rsbweb.nih.gov/ij/>).^{22,23} Data were processed using a self programmed macro file (see **appendix 12.2** for details and source code).

7.3.4 Dye leaching and particle leaching

5 mg of each of the microparticles Pt-PS, FITC-AC, and DPA-PAN, respectively, were suspended in 5 ml of Millipore water (Membrapure Astacus, Bodenheim, Germany; www.membrapure.de) and Ringer solution (B. Braun AG, Melsungen, Germany; www.bbraun.com). The suspensions were continuously shaken for 24 h and subsequently divided in two parts. One part was centrifuged at $1,030 \times g$ for 10 min and the supernatant additionally filtered via a syringe filter (white label, Whatman, Dessel, Germany; www.whatman.com) to separate the particles from the solution containing leached dye. Both solutions (two solutions per kind of particles and solvent) were submitted to fluorometry to detect leached probes. The filtered and centrifuged solutions were recorded twice, at identical detector voltages as the original particle suspensions (600 V) and at full detector gain (1200 V).

For investigation of particle leakage, two cm² of the dual sensor foil were incubated with 2 ml of Millipore or 2 ml of Ringer solution. The solutions were shaken for 24 h, the sensor removed, and the liquids analyzed by fluorometry (full detector gain, 1200 V, pure liquids served as blank control).

7.3.5 Cytotoxicity

Human epidermal keratinocytes (HKs, Invitrogen, Karlsruhe, Germany; www.invitrogen.com) were cultured until confluence in keratinocyte growth medium with supplement (kGMS). HKs were detached using collagenase type 2 (0.1 U ml^{-1} , Roche Diagnostics, Basel, Switzerland; www.roche.com) and resuspended in kGMS. HKs (passage 3) in kGMS were seeded ($2.5 \times 10^3 \text{ cells well}^{-1}$) in 96-well flat-bottom microtiter plates (Costar Inc., Pleasanton, CA, USA; www.costar.com) and cultured ($37 \text{ }^\circ\text{C}$, 95% humidity, 5% CO_2) for three days. kGMS was renewed or replaced with Pt-PS, FITC-AC, DPA-PAN in kGMS (0.1 , 0.5 , $1.0 \text{ } \mu\text{g ml}^{-1}$) and HKs were incubated for 48 h. For fluorescence microscopy, HKs (passage 5) were seeded in 6-well flat-bottom microtiter plates (Costar Inc.).

Fibroblast growth medium with supplement (fGMS) for L929 fibroblasts (American Type Culture Collection CCL I fibroblast, NCTC clone 929, Manassas, VA, USA; www.atcc.org) consisted of DMEM supplemented with 5% v/v fetal bovine serum, 2 mM L-glutamine, 2.2 mg ml^{-1} sodium bicarbonate, penicillin, and streptomycin (Lonza, Basel, Switzerland; www.lonza.com). L929 (passage 4) were cultured until confluence on 75 cm^2 culture flasks, detached by 2.5%/1% trypsin/EDTA (BioWhittaker Inc., Walkersville, MD, USA; www.lonza.com), resuspended in fGMS, seeded (passage 5, $10 \times 10^3 \text{ cells well}^{-1}$) in 96-well flat-bottom microtiter plates, and cultured until confluence as described for HKs. fGMS was renewed or replaced with Pt-PS, FITC-AC or DPA-PAN in fGMS (0.1 , 0.5 , $1.0 \text{ } \mu\text{g ml}^{-1}$), and L929 were incubated for 48 h. Additionally, L929 (passage 5) were seeded on Thermanox slides (Nunc GmbH & Co. KG, Langenselbold, Germany, www.nalgenunc.com) in 24-well plates for (fluorescence) microscopic imaging.

HKs/L929 in 96-well plates were washed twice with kGMS/fGMS, and cytotoxicity was evaluated with the 3-(4,5-dimethyl-2-thiazolyl)-2,5-diphenyl-tetrazoliumbromide (MTT) assay. Supernatants were replaced by kGMS/fGMS supplemented with 16% MTT solution and incubated for 1-4 h (depending on absorbance). Reaction was stopped with 2% sodium dodecyl sulfate (SDS), and quadruplicate samples of absorbance were measured at 490 nm (reference wavelength 650 nm, 96-well plate reader, MWG-Biotech

AG, Ebersberg, Germany, www.mwg-biotech.com). Cell viability was expressed as the percentage of viable cells compared to controls (kGMS/fGMS only).

Supernatants of L929 on 96-well plates after 24 h of exposure to microparticles were analyzed for dead cell protease activity with CytoTox-Glo assays (Promega GmbH, Mannheim, Germany; www.promega.com) according to the manufacturer's instructions. Luminescence counts were measured using a Victor3 multilabel reader (PerkinElmer, Rodgau, Germany; www.perkinelmer.com).

The morphology of live HKs/L929 monolayers (96-well plates) as well as particle exposure (96-, 24-, and 6-well plates) was examined with an inverted microscope (Labovert FS, Leica Microsystems GmbH, Wetzlar, Germany; www.leica-microsystems.com) and a fluorescence microscope (Axiostar Plus, Carl Zeiss AG, Jena, Germany; www.zeiss.de). In case of fluorescence microscopy, a FITC filter set for FITC-AC, a Cy5 emission filter for Pt-PS and XF02 set for DPA-PAN (all from Omega Optical, Brattleboro, VT, USA; www.omegafilters.com) were introduced.

7.3.6 Cellular uptake

For confocal microscopic imaging, L929 (passage 5; 50,000 cells well⁻¹) were seeded on 4-well Lab-Tek chamber slides (Nunc). Cells were cultured until confluence. fGMS was replaced with microparticles in fGMS (1.0 µg ml⁻¹ each) and L929 were incubated for 24 h, respectively. Supernatants were removed from the chambers and a 4% solution of paraformaldehyde (4°C) was added to the cells for fixation. Fixed cells were stored for 24 h until analysis. Prior to microscopy, paraformaldehyde was removed by centrifugation, cells were washed three times with phosphate buffered saline plus Ca plus Mg (PBS), and membranes were stained with DiC₁₈(3) (Invitrogen) (2 µg mL⁻¹ in PBS; 1 h incubation). Supernatants were removed, cells washed three times with PBS, and then submitted to confocal microscopy using a Nikon Eclipse C-1. (Nikon Instruments, Tokio, Japan; www.nikoninstruments.com) and a 488nm laser light source (30-µm pinhole).

7.3.7 Singlet oxygen detection

Particle suspensions (Millipore water, 1 mg ml^{-1}) were photoexcited with a frequency-doubled Nd:YAG laser (532 nm, $100 \cdot 10^3$ pulses, 70 ns pulse duration, 100 mW, 20 s irradiation time, 8 mm spot size, 2.0 kHz repetition rate; PhotonEnergy, Ottensooos, Germany; www.photon-energy.de). Suspensions were magnetically stirred. Singlet oxygen luminescence was detected with an IR-sensitive photomultiplier (R5509-42, Hamamatsu Photonics Deutschland GmbH, Herrsching, Germany; www.hamamatsu.com). After having passed a 950nm cut-off filter (Omega Opticals) and a 1,270nm bandpass filter with a full width of half-maximum of 10 nm (LOT-Oriel, Darmstadt, Germany, www.lot-oriel.com). Data were analyzed with Mathematica 5.2 (Wolfram Research, Berlin, Germany; www.wolfram.com).

7.3.8 *In vitro* sensor characterization

The emission spectra of the particles and the sensor were acquired on an Aminco-Bowman AB2 luminescence spectrometer (Thermo Spectronic, Rochester, NY, USA; www.thermo.com) at an excitation wavelength of 405 nm with a slit width of 4 nm. 50 mM Britton Robinson buffers (consisting of 0.04 M H_3BO_3 , 0.04 M H_3PO_4 and 0.04 M CH_3COOH in distilled H_2O) were used throughout to obtain buffers of defined pH. Argon and oxygen (Linde, Pullach, Germany; www.linde-gas.de) and a gas-mixing device (MKS, Andover, MA, USA; www.mksinst.com) were used to generate defined oxygen partial pressures. Calibration and cross sensitivity experiments were performed using buffer solutions of pH 3 to 8 in single steps at pO_2 of 0, 15, 38, 75, 150, 380 and 760 mmHg each, at atmospheric pressure and at 30 °C.

Photostability experiments were conducted using the ring of LEDs of the imaging setup in a focal distance of 30 cm as excitation source and gathering emitted light using an AB2 luminescence spectrometer in the time trace mode. Photostability was investigated at pH 3 and 8, and 0 or 150 mmHg pO_2 respectively, at room temperature and constant illumination over 40 minutes. The response times were determined by

recording the time traces of the emission peaks at 650 nm (oxygen) and 525 nm (pH), respectively. Response time was defined as the period of time, starting with changing buffer solutions (pH 3 to pH 8) or oxygen concentrations (0 to 760 mmHg pO₂ and back to 0) until 99% of a steady-state signal (t_{99}) was reached. The sensitivity of the dual sensor to temperature was studied at pH 3, pH 8, 0 and 150 mmHg pO₂, respectively, for 20 °C, 30 °C, and 40°C (temperature range in tissue).

7.3.9 Study on human subjects

All participants were provided with verbal and written information on the study and signed consent was obtained from each participant. The local ethics committee had given approval (No. 06/171: 2007) and all experiments were conducted in full accordance with the sixth revision (Seoul, Korea, 2008) of the Declaration of Helsinki (1964). The male volunteer (28 years) for intact skin imaging had no history of skin disorders, and had not suffered from a skin condition or had been subject to dermatological treatment on the volar forearm in the past or at the time of measurement. He did not exercise, wash, or apply topical formulations on the volar forearm for 24 hours prior to the measurement. A split-skin graft (thickness 400 μm) was harvested from a female patient (84 years) from the left ventral thigh to cover a tissue defect on the head after excision of a skin tumor. The according donor site was imaged. A chronic skin wound, resulting from a pyoderma gangraenosum, on the right lower leg of a male patient (73 years) was visualized.

7.3.10 Sensor application *in vivo*

Sensor foils were deposited on tissue or wound surfaces by gently applying the foil starting from one wound margin. Bubbles can be avoided by starting on one end of the sensor and allowing the foil slowly adapt to the surface due to adhesion forces. Thus, uniform contact to tissue is assured, false measurements are prevented, and no physical

pressure was exerted on the sensor foil or to the wound thereafter. In total, *in vivo* experiments do not exceed 5 minutes from application time on tissue to foil removal.

7.3.11 Statistics

We used Sigma Plot 11.0 (Systat Software Inc., Chicago, IL, USA, www.systat.com) for all analyses. Data are given as mean \pm standard deviation (SD) unless otherwise noted. Normality testing was passed and t-tests were done to analyze differences in cell viability (MTT vs. controls; dead cell protease activity) after microparticle exposure. We considered a p-value below 0.05 as significant and a p-value below 0.01 as highly significant.

7.4 Conclusion

In summary, we present a sensor material that shows great promise for simplification of optical imaging techniques. It can be read out by a ratiometric method based on the RGB option of digital cameras we refer as RGB photographing. The biocompatible material was characterized *in vitro*, and applied to visualize human wound healing *in vivo*. We believe that the new material and method can further the understanding of the role of oxygen and local pH in biomedical sciences (e.g. wound healing, tumor metabolism and metastasis, medical treatment efficacy, tissue transplantation), but also in marine sciences, and in numerous bio(techno)logical processes where dual imaging can provide essential knowledge. The material design combined with the novel imaging technique also paves the way for various other multiple analyte sensing approaches with other sensitivity ranges or for different analyte combinations. Modified camera firmware with integrated mathematical processing even allows for recording movies and real-time simultaneous viewing of temporal variations in the 2D-distributions of two parameters.

7.5 References

- 1 Stich, M. I. J., Fischer, L. H. & Wolfbeis, O. S. Multiple fluorescent chemical sensing and imaging. *Chem Soc Rev* **39**, 3102-3114, (2010).
- 2 Liebsch, G., Klimant, I., Frank, B., Holst, G. & Wolfbeis, O. S. Luminescence lifetime imaging of oxygen, ph, and carbon dioxide distribution using optical sensors. *Appl Spectrosc* **54**, 548-559, (2000).
- 3 Bassnett, S. Intracellular ph regulation in the embryonic chicken lens epithelium. *J Physiol-London* **431**, 445-464, (1990).
- 4 Rumsey, W. L., Vanderkooi, J. M. & Wilson, D. F. Imaging of phosphorescence - a novel method for measuring oxygen distribution in perfused tissue. *Science* **241**, 1649-1651, (1988).
- 5 Wilson, D. F. & Cerniglia, G. J. Localization of tumors and evaluation of their state of oxygenation by phosphorescence imaging. *Cancer Res* **52**, 3988-3993, (1992).
- 6 Vinogradov, S. A. *et al.* Noninvasive imaging of the distribution in oxygen in tissue in vivo using near-infrared phosphors. *Biophys J* **70**, 1609-1617, (1996).
- 7 Babilas, P. *et al.* In vivo phosphorescence imaging of po(2) using planar oxygen sensors. *Microcirculation* **12**, 477-487, (2005).
- 8 Schreml, S. *et al.* 2d luminescence imaging of ph in vivo. *Proc Natl Acad Sci U S A* **108**, 2432-2437, (2011).
- 9 Bassnett, S., Reinisch, L. & Beebe, D. C. Intracellular ph measurement using single excitation-dual emission fluorescence ratios. *Am J Physiol* **258**, C171-C178, (1990).
- 10 Lee, D. *et al.* In vivo imaging of hydrogen peroxide with chemiluminescent nanoparticles. *Nat Mater* **6**, 765-769, (2007).
- 11 Niethammer, P., Grabher, C., Look, A. T. & Mitchison, T. J. A tissue-scale gradient of hydrogen peroxide mediates rapid wound detection in zebrafish. *Nature* **459**, 996-999, (2009).
- 12 Sakadzic, S. *et al.* Two-photon high-resolution measurement of partial pressure of oxygen in cerebral vasculature and tissue. *Nat Methods* **7**, 755-759, (2010).
- 13 Zhang, G. Q., Palmer, G. M., Dewhirst, M. & Fraser, C. L. A dual-emissive-materials design concept enables tumour hypoxia imaging. *Nat Mater* **8**, 747-751, (2009).
- 14 Grewe, B. F., Langer, D., Kasper, H., Kampa, B. M. & Helmchen, F. High-speed in vivo calcium imaging reveals neuronal network activity with near-millisecond precision. *Nat Methods* **7**, 399-405, (2010).
- 15 Schreml, S. *et al.* Oxygen in acute and chronic wound healing. *Br J Dermatol* **163**, 257-268, (2010).
- 16 Gurtner, G. C., Werner, S., Barrandon, Y. & Longaker, M. T. Wound repair and regeneration. *Nature* **453**, 314-321, (2008).
- 17 Sharpe, J. R., Harris, K. L., Jubin, K., Bainbridge, N. J. & Jordan, N. R. The effect of ph in modulating skin cell behaviour. *Brit J Dermatol* **161**, 671-673, (2009).
- 18 Schreml, S. *et al.* The impact of the ph value on skin integrity and cutaneous wound healing. *J Eur Acad Dermatol* **24**, 373-378, (2010).
- 19 [Anon]. Tumor ph. *Lancet* **340**, 342-343, (1992).
- 20 Niesner, R. *et al.* 3d-resolved investigation of the ph gradient in artificial skin constructs by means of fluorescence lifetime imaging. *Pharm Res-Dord* **22**, 1079-1087, (2005).
- 21 Schreml, S. *et al.* 2d luminescence imaging of physiological wound oxygenation. *Exp Dermatol*, (2011).
- 22 Steiner, M.-S., Meier, R. J., Duerkop, A. & Wolfbeis, O. S. Chromogenic sensing of biogenic amines using a chameleon probe and the red-green-blue readout of digital camera images. *Analytical Chemistry* **82**, 8402-8405, (2010).

- 23 Wang, X. D., Meier, R. J., Link, M. & Wolfbeis, O. S. Photographing oxygen distribution. *Angew Chem Int Edit* **49**, 4907-4909, (2010).
- 24 Förster, T. Zwischenmolekulare Energiewanderung und Fluoreszenz. *Annalen der Physik* **437**, 55–75, (1948).
- 25 Lakowicz, J. R. Principles of fluorescence spectroscopy 2nd edition. *Springer, Berlin*, (1999).
- 26 Wolfbeis, O. S. Sensor paints. *Adv Mater* **20**, 3759-3763, (2008).
- 27 Wilkinson, F., Helman, W. P. & Ross, A. B. Rate constants for the decay and reactions of the lowest electronically excited singlet-state of molecular-oxygen in solution - an expanded and revised compilation. *J Phys Chem Ref Data* **24**, 663-1021, (1995).
- 28 Borisov, S. M., Vasylevska, A. S., Krause, C. & Wolfbeis, O. S. Composite luminescent material for dual sensing of oxygen and temperature. *Adv Funct Mater* **16**, 1536-1542, (2006).
- 29 Behnke, T. *et al.* Encapsulation of hydrophobic dyes in polystyrene micro- and nanoparticles via swelling procedures. *J Fluoresc*, epub ahead of print, (2010).
- 30 Zhang, Z. L., Long, Y., Pan, J. B. & Yan, X. M. Preparation of fluorescence-encoded microspheres in a core-shell structure for suspension arrays. *J Mater Chem* **20**, 1179-1185, (2010).
- 31 Kurner, J. M. *et al.* Inert phosphorescent nanospheres as markers for optical assays. *Bioconjugate Chem* **12**, 883-889, (2001).

8. Summary

This thesis describes the development and characterization of novel optical sensor materials for clinical *in vivo* applications. At first, biocompatible single- and dual sensors for the clinically important parameters pH and pO₂ were realized using a time-resolved read-out. For the first time, spatial pH and/or pO₂ distributions in cutaneous and chronic wounds of humans were visualized. Further, a novel read-out technique for Fluorescence Ratiometric Imaging (FRIM) is presented. Planar sensor membranes for photographing of oxygen-, pH-, or CO₂ distributions were designed. Finally, a biocompatible *in vivo* sensor for simultaneous and continuous read-out of pH/pO₂ based on the new technique is demonstrated.

Chapter 1 gives a short introduction on the importance of pH and pO₂ especially in dermatology. Further, a brief overview on measurement techniques for oxygen and pH, and optical sensor techniques is presented. Chapter 2 describes the instruments that are applied in this thesis.

In chapter 3, a referenced luminescent sensor for 2D high-resolution imaging of pH *in vivo* is described. The time-resolved sensing scheme is based on time-domain luminescence imaging of FITC and using a ruthenium complex as reference. The biocompatibility of this sensor is warranted via a three step safety mechanism. First, the dyes were covalently bound to, or incorporated in microparticles. Second, the size of the microparticles hampers or at least slows down cellular uptake. Finally, the particles were immobilized in a hydrogel to prevent particle leakage. A set of *in vitro* experiments served to characterize the sensor. It covers the physiologically relevant range of pH 3 to pH 9. The biocompatibility of the sensor was tested by conducting experiments on cytotoxicity, cellular uptake, and singlet oxygen production. Several *in vivo* studies on human tissue pH comparing sensor and pH electrode signals served to validate the sensor. Next, spatial and temporal pH distributions during cutaneous wound healing were imaged via the sensor. The visualization of heterogenic pH distribution in a chronic ulcer demonstrates the potential of the sensor.

An *in vivo* sensor to image physiological wound oxygenation is presented in chapter 4. The sensor is based on luminescence lifetime imaging of an oxygen sensitive palladium porphyrin. The dye was incorporated in a partially oxygen blocking polymer in order to extend the sensitivity matching the physiological range of 0 to 100 mmHg. Studies on split-skin harvest sites and the oxygen gradient of the stratum corneum were accomplished.

The pH sensor particles of chapter 3 and the pO_2 sensitive particles (chapter 4) were combined to form one dual sensor layer for simultaneous *in vivo* imaging of pH/ pO_2 . The sensor is described in detail in chapter 5. The signals of the hybrid sensor were separated using different emission filter sets. The sensor served to visualize analyte distributions on split skin donor sites and chronic venous as well as vasculitic ulcers.

Chapter 6 deals with a novel and straightforward concept for ratiometric imaging read-out referred to as RGB imaging or photographing. The technique relies on fluorescence ratiometric imaging and makes use of the fact that digital pictures are composed of three virtually independent (viz. a red, green, and blue) pictures that are separately stored in digital cameras. The camera serves as a rudimentary "spectrometer" for wavelength separation. The imaging concept is illustrated with the help of a specially designed oxygen sensor membrane, and a sensor for intrinsically referenced imaging of CO_2 with RGB read-out is described. Moreover, the proof of principle of a RGB pH sensor membrane is demonstrated.

Finally, chapter 7 describes a referenced dual sensor for pO_2 /pH based on the RGB technique including its transfer from the lab bench to clinical application. The novel material uses all three color channels of the RGB camera. It comprises the utilization of an inert reference fluorophore in the blue channel, a pH dependent signal in the green channel, and an oxygen dependent signal in the red channel. The biocompatibility of the materials was studied and ensured. The sensor material was characterized in detail *in vitro*, and applied *in vivo* to simultaneously visualize pH and pO_2 distributions in human tissue on intact skin and during cutaneous and chronic wound healing.

9. Zusammenfassung

Diese Dissertation beschreibt die Entwicklung und Charakterisierung neuartiger optischer Sensormaterialien für klinische *in vivo*-Anwendungen. Zunächst wurden zeitaufgelöst auslesbare Einzel- und Dual-Sensoren für die klinisch relevanten Parameter pH und pO₂ entwickelt. Durch diese Sensoren konnte zum ersten Mal die räumliche Verteilung der pH- und/oder Sauerstoff-Werte in kutanen und chronischen Wunden visualisiert werden. Desweiteren beschreibt diese Arbeit eine neue Auslesetechnik für ratiometrische Fluoreszenzbildgebungsverfahren. Hierfür wurden zweidimensionale Sensormembranen zur Darstellung der Verteilung von Sauerstoff-, CO₂- oder pH-Werten designt. Zuletzt gelang es, einen auf der neuen Auslesetechnik basierenden Sensor zur zeitgleichen und kontinuierlichen Bestimmung von pH/pO₂ in menschlichem Gewebe zu realisieren.

Im ersten Kapitel wird kurz die Relevanz der Parameter pH und pO₂ geschildert. Hierbei wird speziell auf deren Einfluss auf dermatologische Fragestellungen eingegangen. Bestehende Messtechniken zur Bestimmung von pH-Werten und Sauerstoffkonzentrationen werden vorgestellt. Ein Hauptaugenmerk liegt hier speziell auf den optischen Sensortechniken. Kapitel 2 beschreibt die in dieser Arbeit eingesetzten Messaufbauten.

Kapitel 3 behandelt die Herstellung eines referenzierten optischen Sensors zur hochauflösenden zweidimensionalen Darstellung von pH-Gradienten *in vivo*. Das Messschema beruht auf der über die Zeitdomäne ausgelesenen „Dual Lifetime Referencing“-Methode. Der Sensor beinhaltet ein pH-sensitives Fluoreszein-Derivat und einen Ruthenium-Komplex als Referenzfarbstoff. Die Biokompatibilität ist über einen dreistufigen Sicherheitsmechanismus gewährleistet. In einem ersten Schritt sind die Farbstoffmoleküle entweder chemisch an Mikropartikeln gebunden, oder durch hydrophobe Wechselwirkungen in Partikel eingebettet, was direkten Kontakt von Wunde und Sensorchemie verhindert. Zweitens erschwert die Größe der Mikropartikel eine eventuelle zelluläre Aufnahme. Alle Partikel wurden danach in einer biokompatiblen Hydrogel-Matrix immobilisiert, die ein Austreten der Partikel aus der Sensorschicht unterbindet. Der Messbereich des Sensors umspannt den physiologisch wichtigen Bereich

von pH 3 bis pH 9. Tests für Zytotoxizität, die Aufnahme durch Zellen, sowie die Produktion des Zellgifts Singulett-Sauerstoff zeigten die Unbedenklichkeit der verwendeten Materialien. Mehrere *in vivo* Studien in menschlichem Gewebe validierten die Ergebnisse. Mithilfe des Sensors konnten die pH-Wert-Verteilungen in kutanen Wunden im Verlauf des Heilungsprozesses dargestellt werden. Die Visualisierung einer heterogenen pH-Verteilungen innerhalb eines chronischen Ulcus demonstriert das volle Potenzial des pH Sensors.

Ein Sensor zur Visualisierung der physiologischen Sauerstoffversorgung in Wunden ist in Kapitel 4 beschrieben. Das Messprinzip basiert auf der Bestimmung der sauerstoffabhängigen Lumineszenzlebenszeit eines Palladium Porphyrins. Der Farbstoff, eingebettet in teilweise sauerstoffblockende Polymerpartikel, besitzt einen Messbereich der im physiologisch wichtigen Bereich (0 bis 100 mmHg) liegt. Der Sensor wurde sowohl für Studien an Spalthautentnahmestellen als auch zur Untersuchung der Sauerstoffbarriere des Stratum Corneum benutzt.

Die Sensorpartikel aus Kapitel 3 und 4 dienen in Kapitel 5 zur Herstellung eines Dual-Sensors für die gleichzeitige Messung von pH/pO₂. Die Signaltrennung der jeweiligen Sensorantworten geschieht über unterschiedliche Emissionsfilter. Mit dem Hybridsensor wurden zum ersten Mal gleichzeitig die pH- und pO₂-Verteilungen auf Spalthautentnahmetellen und chronischen Ulcera visualisiert.

In Kapitel 6 wird ein einfaches Konzept für das Auslesen ratiometrischer Fluoreszenzbildgebungsverfahren vorgestellt. Es beruht auf der Verwendung von Daten digitaler Kameras, die farbige Bilder in 3 Farbkanälen (rot, grün und blau) aufzeichnen. Die Kamera wird als rudimentäres „Spektrometer“ benutzt, das drei spektral verschiedene Bilder gleichzeitig aufnimmt. Das grundlegende Prinzip der Messung ist anhand der Entwicklung einer passenden Sauerstoff-Messmembran erläutert. Des Weiteren wurden ein intrinsisch referenzierter Sensor für die zweidimensionale Abbildung von CO₂-Verteilungen und ein pH-Sensor hergestellt.

Zum Abschluss beschreibt Kapitel 7 die Entwicklung eines auf der RGB-Technik basierenden Dual-Sensors für pH/pO₂ *in vivo*. Das Sensormaterial verwendet alle drei Farbkanäle der Kamera (blauer Kanal: Referenz; grüner Kanal: pH abhängiges Signal; roter

Kanal: pO_2 abhängiges Signal). Das biokompatible Material wurde ausführlich *in vitro* charakterisiert und klinisch *in vivo* angewendet, um simultan die Analytverteilungen in menschlichem Gewebe während der Wundheilung zu untersuchen.

10. Curriculum Vitae

PERSONAL DATA

Name: Robert Johannes Meier
Date of birth: April 3th 1982
Place of birth: Deggendorf, Germany
Nationality: German
Marital status: unmarried
Address: Seifensiedergasse 2a, 93059 Regensburg

EDUCATION

09/1988 - 07/1992 Grundschule St. Martin 2, Deggendorf
09/1992 - 06/2001 Robert-Koch-Gymnasium, Deggendorf
06/2001 Graduation (Abitur)

CIVILIAN SERVICE

07/2001 - 03/2002 Malteser Hilfsdienst, Deggendorf

STUDIES

10/2002 - 12/2006 Studies of chemistry (Diploma) at the University of Regensburg
01/2007 – 09/2007 Diploma Thesis at the University of Regensburg (Supervisor Prof. Dr. Otto S. Wolfbeis) Title: Pre-staining in SDS-PAGE
10/2007 – present Ph.D. Thesis at the University of Regensburg (Supervisor Prof. Dr. Otto S. Wolfbeis)

11. List of Publications and Presentations

Diploma thesis

Meier, R. J., Pre-staining in SDS-PAGE, (2007) Institute for Analytical Chemistry, Chemo- and Biosensors, University of Regensburg

Papers

(*Authors are contributed equally)

**Meier, R. J.*, *Schreml, S., Wang, X.-D., Landthaler, M., Babilas, P., and Wolfbeis, O. S. (2011) Photographing of oxygen and pH in vivo, *submitted*.

Schreml, S., *Meier, R. J.*, Abels, C., Albert, A. G., Seidl, U., Landthaler, M. and Babilas, P. (2011) The impact of topical alpha hydroxy acid on skin pH, *submitted*.

Ali, R., Lang, T. Saleh, S. M., *Meier, R. J.* and Wolfbeis, O. S., (2011) Optical sensing scheme for carbon dioxide using a solvatochromic probe, **Analytical Chemistry** 83, 2846–2851.

Wang, X.-D., Gorris, H. H., Stolwijk, J. A., *Meier, R. J.*, Groegel, D. B. M., Wegener, J., and Wolfbeis, O. S. (2011) Self-referenced RGB colour imaging of intracellular oxygen, **Chemical Sciences**, 2, 901-906.

*Schreml, S., **Meier, R. J.*, Wolfbeis, O. S., Landthaler, M., Szeimies, R.-M., and Babilas, P. (2011) 2D luminescence imaging of pH in vivo, **Proceedings of the National Academy of Sciences of the United States of America** 108, 2432-2437.

Schreml, S., *Meier, R. J.*, Wolfbeis, O. S., Landthaler, M., Szeimies, R., and Babilas, P. (2011) 2D Luminescence Imaging of Physiological Wound Oxygenation, **Experimental Dermatology** *in press*. (Cover article) DOI: 10.1111/j.1600-0625.2011.01263.x

Achatz, D. E., *Meier, R. J.*, Fischer, L. H., and Wolfbeis, O. S. (2011) Luminescent Sensing of Oxygen Using a Quenchable Probe and Upconverting Nanoparticles, **Angewandte Chemie International Edition** 50, 260-263.

*Wang, X. D., **Meier, R. J.*, Link, M., and Wolfbeis, O. S. (2010) Photographing Oxygen Distribution, **Angewandte Chemie International Edition** 49, 4907-4909.

Steiner, M. S., *Meier, R. J.*, Duerkop, A., and Wolfbeis, O. S. (2010) Chromogenic Sensing of Biogenic Amines Using a Chameleon Probe and the Red-Green-Blue Read-out of Digital Camera Images, **Analytical Chemistry** 82, 8402-8405.

Ali, R., Saleh, S. M., *Meier, R. J.*, Azab, H. A., Abdelgawad, I. I., and Wolfbeis, O. S. (2010) Upconverting nanoparticle based optical sensor for carbon dioxide, **Sensors and Actuators B-Chemical** 150, 126-131.

Steiner, M. S., *Meier, R. J.*, Spangler, C., Duerkop, A., and Wolfbeis, O. S. (2009) Determination of biogenic amines by capillary electrophoresis using a chameleon type of fluorescent stain, **Microchimica Acta** 167, 259-266.

Meier, R. J., Steiner, M. S., Duerkop, A., and Wolfbeis, O. S. (2008) SDS-PAGE of proteins using a chameleon-type of fluorescent prestain, **Analytical Chemistry** 80, 6274-6279.

Abstracts and Posters

Luminescent Photographing of Oxygen, *Meier R. J., Wolfbeis, O.S., Kaiser Friedrich Forschungspreis*, Kaiserpfalz Goslar, Germany, 2011.

Two-dimensional luminescence imaging of pH in vivo, *Schreml, S., Meier, R. J., Wolfbeis, O. S., Szemies, R.-M., Landthaler, M., Babilas, P.*, **38. Jahrestagung der Arbeitsgemeinschaft dermatologische Forschung ADF**, Tübingen, Germany, 2011.

2D luminescence imaging of pH in wound healing, *Schreml, S., Meier, R. J., Wolfbeis, O. S., Szemies, R.-M., Landthaler, M., Babilas, P.*, **21st Conference of the European Wound Management Association EWMA**, Brussels, Belgium, 2011.

2D Luminescence imaging of pH in vivo, *Meier, R. J., Schreml, S., Babilas, P., Wolfbeis, O. S.*, **European Conference on Optical Chemical Sensors and Biosensors, Europtrode X**, Prague, Czech Republic, 2010.

Wound surface pO₂ imaging during physiological cutaneous wound healing, *Schreml, S., Meier, R. J., Wolfbeis, O. S., Babilas, P.*, **20th Conference of the European Wound Management Association EWMA**, Genf, Switzerland, 2010.

pO₂ imaging of split-thickness graft donor sites using two-dimensional oxygen sensors: a new insight into tissue oxygenation during physiological wound healing, *Schreml, S., Meier, R. J., Wolfbeis, O. S., Landthaler, M., Szeimies, R.-M., Babilas, P.* **18th congress of the European Academy of Dermatology and Venereology EADV**, Berlin, Germany 2009.

Two-dimensional fluorescent sensors for pH and pO₂ in dermatological purpose, *Meier, R. J., Schreml, S., Kochmann, S., Babilas, P., Wolfbeis, O. S.*, **2nd Japanese/German on new prospects of molecular imaging technology in interdisciplinary research**, Regensburg, Germany, 2009.

12. Appendix

12.1 Partial pressure – a conversion table for oxygen at 1 atm

Oxygen [vol %]	pO ₂ [torr] or [mmHg]	O ₂ [mbar]	O ₂ [Pa]	Oxygen [vol %]	pO ₂ [torr] or [mmHg]	O ₂ [mbar]	O ₂ [Pa]
0	0,0	0,0	0	0	0	0	0
1	7.6	10.1	10100	1.3	10	13.3	13300
2	15.2	20.3	20300	2.6	20	26.7	26700
4	30.4	40.5	40500	3.9	30	40.0	40000
5	38.0	50.7	50700	5.3	40	53.3	53300
7	53.2	70.9	70900	6.6	50	66.6	66600
10	76.0	101.3	101300	7.9	60	80.0	80000
12	91.2	121.6	121600	9.2	70	93.3	93300
14	10.4	141.8	141800	10.5	80	106.6	106600
16	121.6	162.1	162100	11.8	90	120.0	120000
18	136.8	182.3	182300	13.2	100	133.3	133300
20	152.0	202.6	202600	26.3	200	266.6	266600
30	228.0	303.9	303900	39.5	300	399.9	399900
50	380.0	506.5	506500	65.8	500	666.4	666400
100	760.0	1013.0	1013000	98.7	750	999.7	999700

12.2 Source code for the ImageJ RGB macro

```

Open("all.tif");

run("Split Channels");

imageCalculator("Divide create 32-bit", "C1-all.tif","C3-all.tif");

run("Interactive 3D Surface Plot");

imageCalculator("Divide create 32-bit", "C2-all.tif","C3-all.tif");

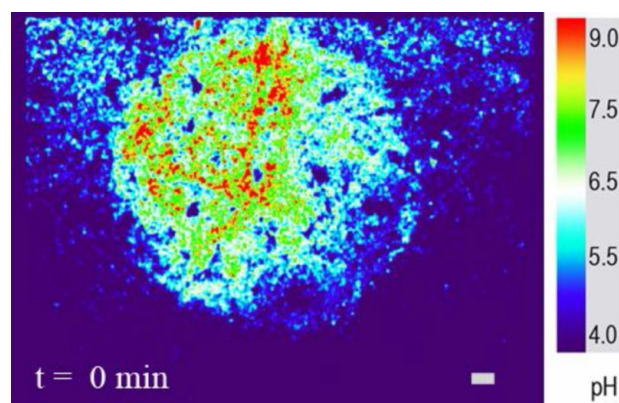
run("Interactive 3D Surface Plot");

run("Save", "save=[C:\\Dokumente und
Einstellungen\\Administrator\\Desktop\\Surface_Plot_of_Result pH.tif]");

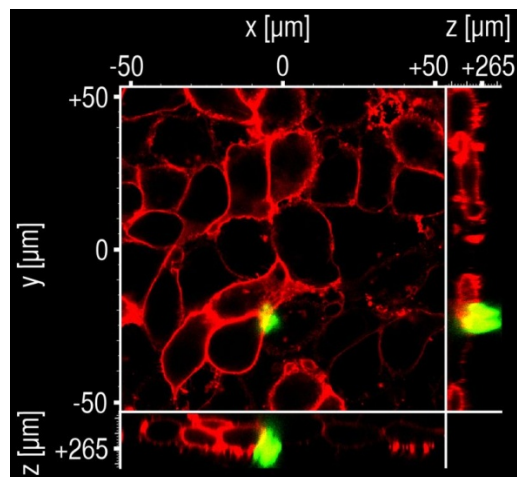
run("Save", "save=[C:\\Dokumente und
Einstellungen\\Administrator\\Desktop\\Surface_Plot_of_Result po2.tif]");

```

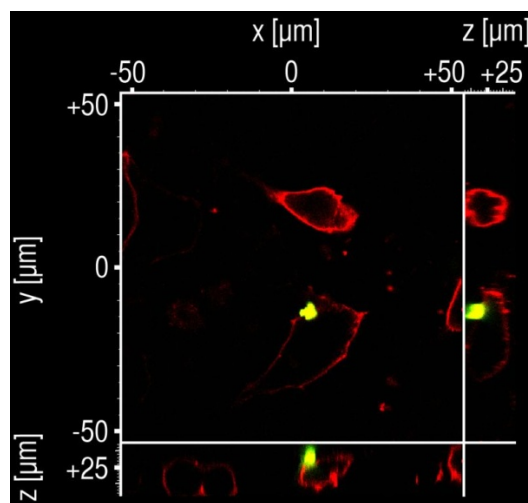
12.3 Video stills (videos on the on the enclosed CD)



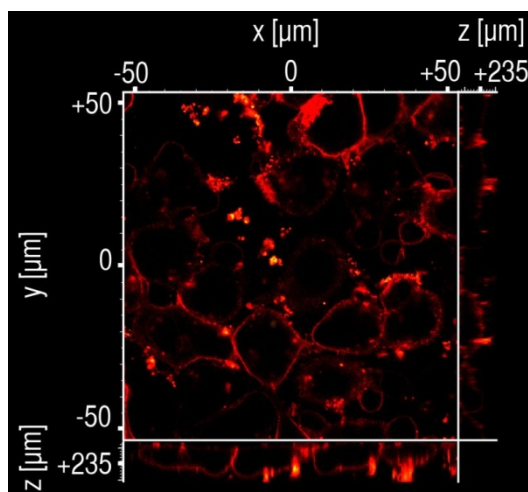
Video IV.1 | Spatiotemporal resolution shown by real-time microscopic 2D-pH imaging. Spatial resolution shown by a representative visualization of a drop (pH 8) on a sensor foil impregnated in a solution of pH 4 after connecting the CCD camera to a microscope. To assess whether significant horizontal proton diffusion exists affecting spatial resolution, continuous imaging was conducted (2 min intervals in first 20 min, then after 30 min). No significant change was found in the spatial aspect of pH values. Resolution was found to be $< 5 \mu\text{m}$. (Scale bar, $10 \mu\text{m}$).



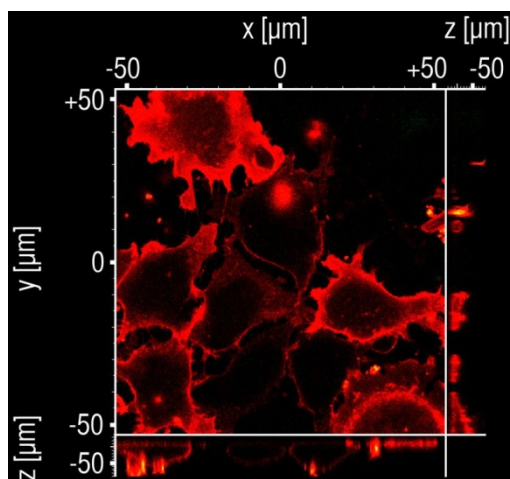
Video IV.2 | Confocal microscopy of cells exposed to FITC-AC (1 h). Confocal microscopic image stack of L929 fibroblasts exposed to FITC-AC for 1 h. FITC-AC (green) are only found on the cell surface, not inside live L929 fibroblasts. In the static z-scale, the location of the particle is additionally visualized.



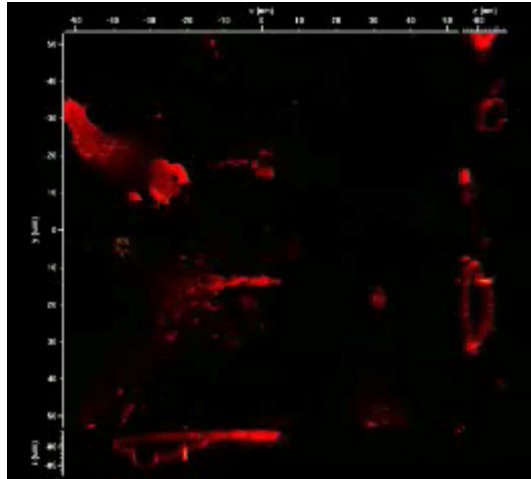
Video IV.3 | Confocal microscopy of cells exposed to FITC-AC (24 h). Confocal microscopic image stack of L929 fibroblasts exposed to FITC-AC for 24 h. FITC-AC (green) are only found on the cell surface, not inside live L929 fibroblasts. In the static z-scale, the location of the particle is additionally visualized.



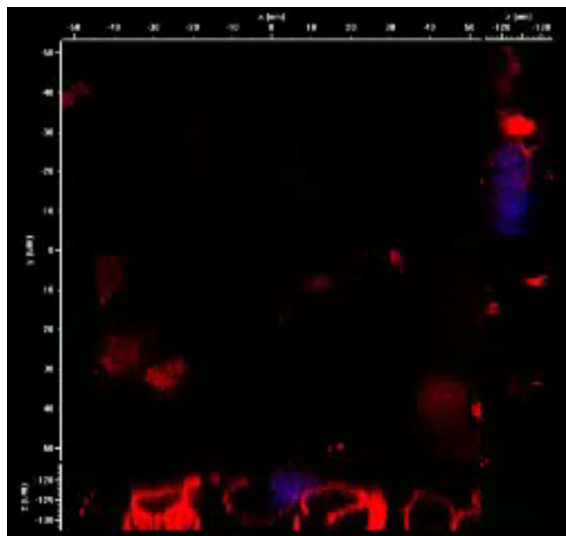
Video IV.4 | Confocal microscopy of cells exposed to $Ru(dpp)_3$ -PAN (1 h). Confocal microscopic image stack of L929 fibroblasts exposed to $Ru(dpp)_3$ -PAN for 1 h. $Ru(dpp)_3$ -PAN (yellow to orange) are only found on the cell surface, not inside live L929 fibroblasts. In the static z-scale, multiple particles on the cell surfaces are additionally visualized.



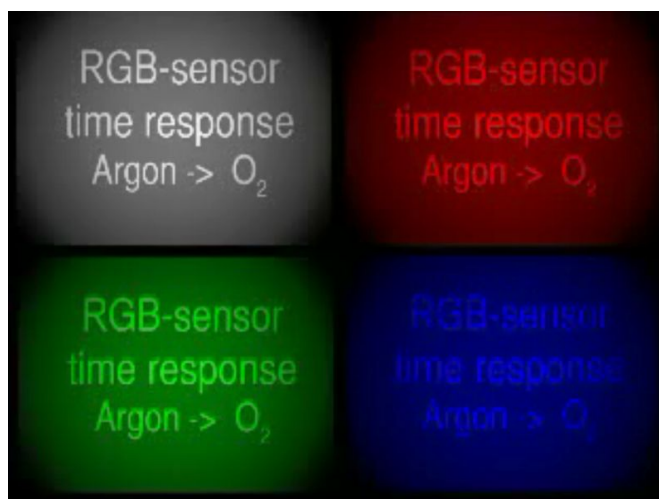
Video IV.5 | Confocal microscopy of cells exposed to $Ru(dpp)_3$ -PAN (24 h). Confocal microscopic image stack of L929 fibroblasts exposed to $Ru(dpp)_3$ -PAN for 24 h. $Ru(dpp)_3$ -PAN (yellow to orange) are only found on the cell surface, not inside live L929 fibroblasts. In the static z-scale, multiple particles on the cell surfaces are additionally visualized.



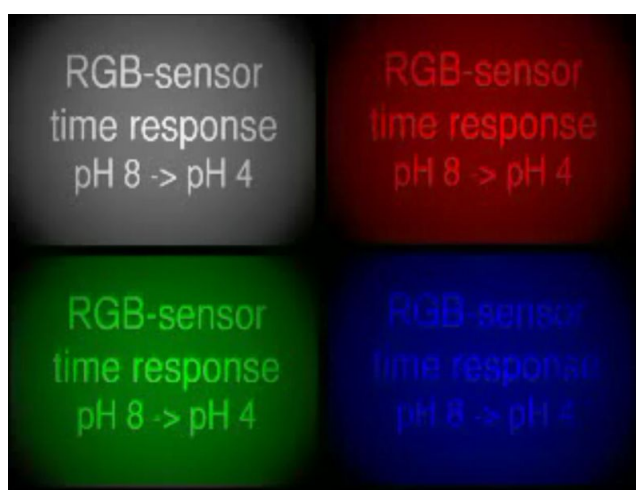
Video VII.1 | Confocal microscopy of cells exposed to Pt-PS (24 h). Confocal microscopic image stack of L929 fibroblasts exposed to Pt-PS for 24 h. Pt-PS (red spots) are only found on the cell surface, not inside live L929 fibroblasts. In the static z-scale, the location of the particle is additionally visualized.



Video VII. 2 | Confocal microscopy of cells exposed to DPA-PAN (24 h). Confocal microscopic image stack of L929 fibroblasts exposed to DPA-PAN for 24 h. Agglomerates of DPA-PAN particles (blue) are only found on the cell surface, not inside live L929 fibroblasts. In the static z-scale, the location of the particle is additionally visualized.



Video VII.3 | Time response oxygen. Time response of the sensor (incubated in buffer pH 4, "Ox" is written with buffer pH 8) starting from argon gas and switching towards oxygen and back. Top left: RGB video; Top right: Response of the red channel; Bottom left: Response of the green channel; Bottom right: Response of the blue channel;



Video VII.4 | Time response pH. Time response of the sensor incubated in buffer pH 8 by writing the letters "pH" using buffer of pH 3. Top left: RGB video; Top right: Response of the red channel; Bottom left: Response of the green channel; Bottom right: Response of the blue channel;